A transient steam reforming process to produce hydrogen from methane for use in fuel cells

Shirley, Alexander

Award date:
2005

Awarding institution:
University of Bath

A TRANSIENT STEAM REFORMING PROCESS TO PRODUCE HYDROGEN FROM METHANE FOR USE IN FUEL CELLS

Alexander Shirley

A thesis submitted for the degree of Doctor of Philosophy

University of Bath

Department of Chemical Engineering

June 2005

ProQuest LLC
789 East Eisenhower Parkway
P.O. Box 1346
Ann Arbor, MI 48106-1346

Abstract

Accepting the long term vision of the use of hydrogen as an energy vector, the design of a compact reformer to produce hydrogen from natural gas provides the backdrop for the work in this thesis. To become familiar with the thermodynamic constraints, chemical equilibrium calculations were performed using Aspen. It is shown that the reaction is favoured by low pressure and high temperature, with conversions approaching 100% at 900°C. High steam to methane ratios improved methane conversion and reduced carbon formation, but decreased hydrogen yield and process efficiency. In order to investigate these phenomena experimentally, a novel transient approach was adopted.

The experimental reactor comprised a cylindrical brass block length 110 mm, diameter 64 mm, with two 12.7 mm diameter stainless steel tubes passing through. The tubes would house the catalysts and perform the reactions, one catalytic combustion (for use in future work), one steam reforming. A cartridge heater was also fitted to provide initial heating. A system of valves was used to control the reforming reaction in a batchwise manner at temperatures ranging from 500 to 800°C and pressures from 2 to 9.5 bar g.

The results from the experiments were encouraging, with hydrogen production being observed in all experiments and varying with pressure, temperature and steam to methane ratio as expected. However, the absolute values of hydrogen produced did not match thermodynamic equilibrium. The proportion of hydrogen in the product was between one third and one tenth of the equilibrium value after a reaction time of 10 minutes. After 20 minutes, the hydrogen proportion was still increasing roughly linearly with time. Kinetic models suggested that the reaction should proceed far faster, obtaining equilibrium in 10 seconds or so.

Increasing the dead volume above the reactor was found to have a marked negative effect on the rate of reaction. Doubling the dead volume approximately halved the hydrogen yield for a given reaction time. It is postulated that cold spots in this area may have caused temporary condensation of steam from the feed, which would then have slowly evaporated as the reaction proceeded. In order to test this theory, further experiments using the transient reactor should be carried out with the dead volume minimised and with improved trace heating and insulation.

Acknowledgements

I gratefully acknowledge the support and goodwill of my friends and family and of my supervisor, Professor Stan Kolaczkowski, without which I could not have completed this Ph.D.

My gratitude is especially extended to my colleague Liang Chen for his help and support during the experimental phase of my work.

I am also very grateful towards Synetix for supplying the catalyst for my experiments and towards the EPSRC for their financial support.

Contents

List of figures

List of tables

Nomenclature

a_i	Activity of chemical species i	
A_{peak}	Area of a peak on gas chromatogram, determined by integration [1]	
A_i	Pre-exponential factor for species i, in Equation (4.48)	
A_n	Pre-exponential factor for reaction n, in Equation (4.49)	
A	Parameter in *Cp* function	
A'	Variable in reaction extent calculation	mol
B	Parameter in *Cp* function	
B'	Variable in reaction extent calculation	
C	Parameter in *Cp* function	
C'	Variable in reaction extent calculation	mol
$C_{1\text{-}5}$	Coefficients in expression for vapour pressure of a liquid	
C_A	Concentration of species A	mol/m³
Cp	Specific heat capacity at constant pressure	J/mol.K
D	Parameter in *Cp* function	
D'	Variable in reaction extent calculation	
D_A	Diffusivity for species A between points z_i and z_{i+1}	m²/s
D_A'	Diffusivity for species A between points z_{i-1} and z_i	m²/s
$D_{A,B}$	Binary diffusivity of species A in species B	cm²/s or m²/s
$D_{A,mix}$	Diffusivity of species A in a mixture	m²/s
E_n	Activation energy for reaction n	
E'	Variable in reaction extent calculation	mol
f	Function for equilibrium constant	
$\bar{f}_i$	Fugacity of component i in solution	bar
f_i°	Fugacity of component i in the standard state (= 1)	bar
F'	Variable in reaction extent calculation	
G'	Variable in reaction extent calculation	mol
ΔG_R°	Standard Gibbs energy change of reaction	kJ/mol
ΔG_f°	Standard Gibbs energy change of formation	kJ/mol
H'	Variable in reaction extent calculation	

[1] Units for peak area are arbitrary units used by Chrompack Maestro

ΔH_R°	Standard enthalpy change of reaction	kJ/mol
J'	Variable in reaction extent calculation	
k_n	Reaction rate constant for reaction n	[2]
K	Thermodynamic equilibrium constant	
K'	Variable in reaction extent calculation	mol
K_i	Adsorption coefficient for species i	[3]
K_p	Partial pressure thermodynamic equilibrium constant	$(kPa)^{\nu}$
M_A	Molecular mass of species A	g/mol
n	Number of moles	mol
P	Pressure	bar or kPa
P_v	Vapour pressure	Pa
P_i	Partial pressure of species i	Pa
r_i	Response factor for species i	[4]
r_n	Rate of reaction n	mol/g cat.s
R	Universal gas constant = 8.314	J/mol.K
ΔS_R°	Standard entropy change of reaction	kJ/mol.K
T	Temperature	K
V_A	Molecular volume of species A	
X	Variable in Newton's method for solving simultaneous equations	
y_i	Mole fraction of component i in the gas phase	
Y_i	Molar percentage of component i in the gas phase	
z	Distance along tube	m
Z	Coefficient in equation for approximating K	10^3/K

[2] (kmol/kg cat.s).$(kPa)^{0.25}$ for reactions 1 and 3, (kmol/kg cat.s).(kPa) for reaction 2

[3] $(kPa)^{-1}$ for CH_4 and CO, dimensionless for H_2O

[4] Units are the same as those of A_{peak}

Greek characters

α	Stoichiometric coefficient	
ε	Extent of reaction	mol
ϕ_i	Fugacity coefficient	
κ	Coefficients in expressions for response factor	
ν	Stoichiometric sum of species for a reaction	
θ	Reaction progress co-ordinate	
τ	Tortuosity factor	
υ_A	Atomic diffusion volume of species A	

Subscripts

i	incremental value or chemical species i
i,j	at position i and time increment j
k	for chemical species k
n	for reaction n
P	at pressure P
t	after elapsed time *t*
T	at temperature *T*
TOTAL	sum for all species
0	initially
298	at 298.15 K

Abbreviations

ATR	Autothermal reforming	
CAR	Combined autothermal reforming	
CNG	Compressed natural gas	
CPR	Catalytic plate reactor	
CRM	Combined reforming of methane	
CWI	Catalyst weight index	
CWR	Catalytic wall reactor	
DEN	Denominator in rate equation	
FBMR	Fluidised bed membrane reactor	
GC	Gas chromatograph	
GHR	Gas heated reforming	
HC	Unburned hydrocarbon emissions	
HHV	Higher heating value	
ICE	Internal combustion engine	
NK	Numaguchi and Kikuchi kinetic model	
PEM	Polymer electrolyte membrane	
POX	Partial oxidation	
ppm	Parts per million	
PSA	Pressure swing adsorption	
RESC	Reformer sponge iron cycle	
RVI	Reactor volume index	
SEM	Scanning electron microscopy	
SERP	Sorption enhanced reaction process	
SIR	Sponge iron reactor	
SMR	Steam to methane molar ratio	mol/mol
SMR	Steam methane reforming	
XF	Xu and Froment kinetic model	

Chapter 1 - Introduction

Hydrogen is currently produced by many large-scale plants, which use it as a feedstock for other industrial processes, such as ammonia production, methanol synthesis and catalytic cracking of hydrocarbons. In the US alone, chemical processing demands over 120 billion cubic feet (3.4 billion m^3) per year.

There are also many smaller scale industrial applications for hydrogen, such as pharmaceutical production, food processing *etc.* These applications are typically supplied with hydrogen in small gas bottles, transported by road or rail.

There is an emerging market for hydrogen to power motor vehicles. Companies such as *BMW, Daimler-Chrysler, Honda, Mitsubishi, Ford and Toyota* are all developing vehicles that use hydrogen fuel. The development of fuel cells for mobile and stationary electricity production is also creating a market for hydrogen.

For these growing markets and for the smaller scale industry, there are two methods of supplying the required hydrogen:

- The current system of transporting hydrogen from existing production plants to where it is needed.
- To manufacture the hydrogen locally at the point of use.

There is no current, large-scale transportation infrastructure for hydrogen. This will become more of an issue in the future as the market increases in size. Transportation by small cylinders of compressed gas is not very efficient, since most of the energy used is consumed in moving the cylinders themselves. One solution would be to build a pipeline network to transport the gas, in much the same way that natural gas is currently distributed. The problem with this approach is obviously the cost of building such a network and deciding who should pay for its development.

An alternative solution is to generate the hydrogen at the point of use, in only the quantity required for the application. This is the challenge that is addressed by this thesis. Natural

gas already has a fully developed supply infrastructure and has, therefore, been chosen as the feedstock for this research.

A review of the literature is presented in Chapter 2, covering hydrogen, its properties, methods of production and purification and the requirements for various applications. The review focuses on previous work on compact reformers and methods of modelling the various processes involved in reforming.

Having selected a concept for a compact reformer, the process was simulated using Aspen, as detailed in Chapter 3. Aspen's results were checked by performing a manual calculation of the equilibrium composition under various conditions. The purpose of the simulations was to indicate the feasibility of the concept and to determine the sensitivity of the system to various parameters. This led to the publication of the paper in Appendix A.

Chapter 4 covers the design and operation of the experimental reactor, which was developed as a result of the findings of the Aspen simulations. The material balance calculations and estimates of precision are fully explained, along with example data. Experimentation verified the viability of the transient reformer concept and provided the data and experience to improve future experimental procedures.

The final conclusions and recommendations drawn from the thesis are presented in Chapter 5.

Chapter 2 - Literature Review

2.1 Problems with current road vehicle fuels

Current technology for powering cars is almost exclusively based on internal combustion engines. These are heat engines which convert the chemical potential energy of their fuels first into heat, then from heat into work. Due to the second law of thermodynamics, there is a limit to the maximum efficiency of such a process which is set by the compression ratio of the engine. Modern engines have a compression ratio of around 10 to 1. Given an idealised Otto cycle, this would limit the efficiency to around 54%. That is an absolute maximum efficiency which could never be obtained in practice. In fact, internal combustion engines are rarely more than 35% efficient (Smith, Van Ness and Abbott, 1996).

Most of the fuels used in transportation are fossil fuels such as petroleum and natural gas. These are finite resources and their combustion leads to the formation of polluting by-products such as oxides of nitrogen (NO_x), carbon monoxide (CO), carbon dioxide (CO_2) and unburned hydrocarbons (HC).

2.2 The hydrogen alternative

Stebar and Parks (1974) reported on the use of hydrogen as a fuel supplement for standard petrol fuelled internal combustion engines. Hydrogen addition allows the engine to run on much leaner fuel/air mixtures than operation on petrol alone. It was found that a mass fraction of 0.1 of hydrogen in the fuel input (an energy fraction of 0.23) would allow the engine to run at an equivalence ratio as low as 0.55. At this ratio, NO_x and CO emissions are minimised while hydrocarbon emissions are reduced, compared to stoichiometric running (equivalence ratio of 1).

In order to further reduce the pollutants produced by an ICE, hydrogen may be used in place of petrol (Peña, Gómez and Fierro, 1996). A hydrogen powered ICE produces no CO, CO_2 or hydrocarbons, although it does produce some NO_x if air is used as the

oxidant. In fact, under stoichiometric operation, NO_x production was twice as high for the H_2 fuelled engine. However, hydrogen's wide flammability limits permit a very lean mixture to be used, which reduces the combustion temperature and thereby reduces NO_x formation.

Hydrogen may be used in several different ways as a fuel for internal combustion engines (Peschka, 1998). It may be either injected into the air intake or injected directly into the cylinders. If the hydrogen is stored as a liquid, then cryogenic gas may be used to fuel the engine. The cooling effect of using the cryogenic hydrogen is beneficial in reducing NO_x emissions and increasing power output. Problems such as backfiring and poor control over mixture preparation are removed by using direct injection. If cryogenic hydrogen is injected directly into the cylinders late in the compression cycle, performance similar to that of an equivalent petrol powered engine can be obtained.

A higher compression ratio may be used with H_2 fuel and the fuel itself will weigh less, so hydrogen vehicles are, on average, 22% more efficient than petrol vehicles (Veziroğlu and Barbir, 1992).

If advanced power trains with internal combustion engines (ICEs) running on conventional fuels can fulfil future energy demand and emission standards, and if sufficient conventional fuels will be available world-wide on a long term basis, then industry will continue to use these conventional systems for passenger cars. However, it is unlikely that these conditions will continue to be met in the future. Höhlein, Biedermann, Grube and Menzer (1999) compare the potential efficiencies of various fuel supply systems, from oil well to filling station in Germany. Their comparison is given in Table 2.1. These efficiencies have to be taken into account when comparing different drivetrain technologies. There is no point in improving drivetrain efficiency if the subsequent effect on fuel supply efficiency reduces the overall efficiency.

Using a best case scenario, Höhlein *et al.* (1999) ran a simulation to determine the energy requirements per 100 km for a passenger car, as well as the emissions per 100 km for a number of different combinations of technology. Their analysis shows that using compressed hydrogen (generated on a large scale from natural gas) in a PEM fuel cell is the most efficient solution (87 MJ/100 km). The gasoline fuelled ICE is shown to be the least efficient solution (152 MJ/100 km).

Table 2.1 – Efficiencies of energy supply from oil well to filling station in Germany (adapted from Höhlein *et al.*, 1999)

Fuel Supplied	Path 1	Efficiency	Path 2	Efficiency
Gasoline	Crude oil to refinery	97 %	Gasoline at filling station	88 %
Diesel	Crude oil to refinery	97 %	Diesel at filling station	91 %
CNG	Natural gas to high pressure grid	90 %	CNG (250 bar) at filling station	81 %
Compressed Hydrogen	Natural gas to high pressure grid	90 %	Compressed H_2 at filling station	63 %
Methanol	Natural gas to high pressure grid	90 %	Methanol at filling station	58 %

This analysis takes into account the fuel supply efficiency, but it does not consider any other factors affecting the choice of fuel and engine technology. Also, it considers a best case situation where weight of a fuel cell powered car is equivalent to that of a conventional vehicle and the efficiency of the various components is at a level predicted by manufacturers for the future (after 2005). This level of efficiency may not be achievable in practice. Guy (2000) has performed a simple analysis of two alternative routes from energy source to work output. By considering the efficiency of each stage of the route, it has been shown that, using current technology, the crude oil to internal combustion engine route is more efficient than the natural gas to fuel cell route.

Ogden, Williams and Larson (2004) evaluated the lifecycle costs of cars with various alternative fuels and engines. There is great uncertainty as to the cost associated with various pollutants or with insecurity in future oil supplies, therefore a precise and definitive analysis is impossible. However, it was found that the lifecycle costs of current cars powered by conventional petrol engines were higher than many of the alternatives. If the cost of externalities such as air pollutants are assumed to be high, then the hydrogen fuel cell car stands out as that with the lowest societal lifecycle costs.

A recent study by MIT (Weiss, Heywood, Drake, Schafer and AuYeung, 2000) focussed on the wells-to-wheels efficiency of various fuel/engine systems. It found that, if hydrogen is not generated by renewable power, petrol/electric hybrids, such as the Toyota Prius are more efficient than hydrogen powered alternatives. Transporting and storing the

hydrogen are the critical problems. Hydrogen gas compressed to 5000 psi (*ca.* 350 bar) can give vehicles such as the Honda FCX prototype a range of only 150-200 miles.

DaimlerChrysler has a $1 billion budget over 5 years to develop alternatives to petroleum fuelled vehicles. They believe fuel cell technology will become dominant in 30 to 40 years.

2.2.1 Fuel cells

A block diagram of a typical automotive fuel cell power train is shown in Figure 2.1.

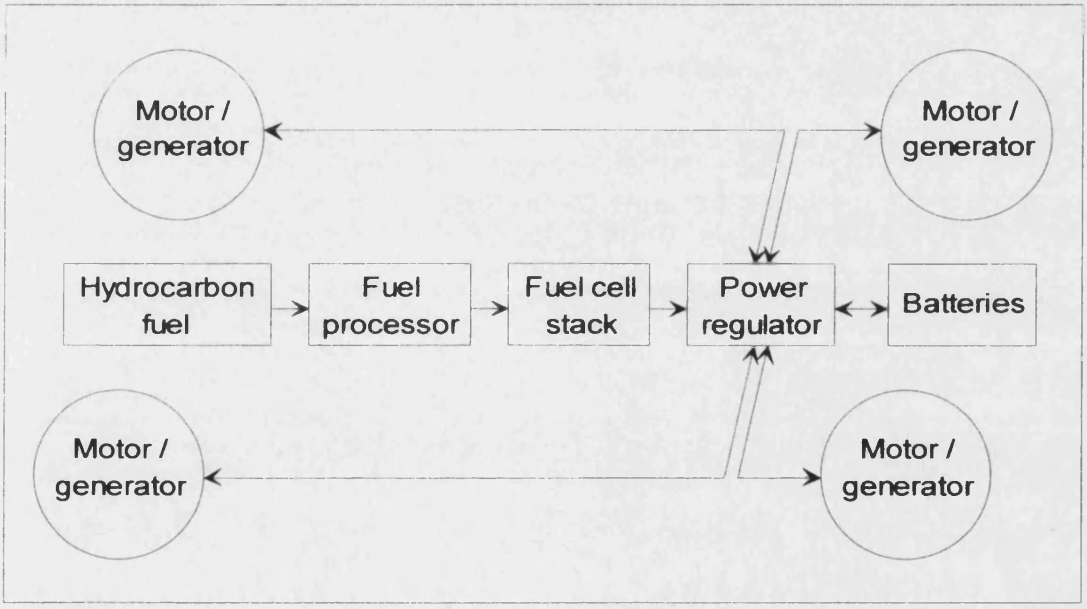

Figure 2.1 – Block diagram of a typical automotive fuel cell power train.

Different fuel cells are usually characterised by the electrolyte they use. Table 2.2 is a comparison of different types of fuel cell, taken from Kalhammer, Prokopius, Roan and Voecks (1998). Their report for the Fuel Cell Technical Advisory Panel was written in consultation with many leading companies in automotive fuel cell research.

Requirements of an automotive fuel cell power plant

In order for a fuel cell system to be considered for production cars it must meet the requirements of the driver for cost, drivability, and usability. It must also have a lower impact upon the environment than an equivalent car with conventional internal

combustion technology, otherwise there would be no point in choosing the fuel cell at all! Kalhammer *et al.* (1998) describe the considerations that must be taken into account when choosing a particular fuel cell technology for use in cars. One important factor is operating temperature. This should be as low as possible to minimise both start-up times, and the cost and bulk of high performance insulation required. This rules out the Molten Carbonate and the Solid Oxide fuel cells for practical automotive use.

Fuel and air compatibility

In order to reduce the cost and complexity of the processing system, the fuel cell must be compatible with air and processed fuel. The Aqueous Alkaline fuel cell has no tolerance for CO_2, which reacts with the electrolyte to form a solid carbonate, causing irreversible damage to the cell. It is not practical to remove all CO_2 from the processed fuel. Therefore, this technology is not practical for automotive use (Kalhammer *et al.*, 1998).

Transient operating conditions

Rapid start-up, response to rapid load changes and high power density are also important requirements. The Phosphoric Acid fuel cell is tolerant to around 1% of CO in the processed fuel stream, reducing the complexity of the required fuel processor (Kalhammer *et al.*, 1998). However, it must be operated at above 100 °C and less than 0.8 V per cell, so it does not meet the rapid start-up or load response requirements. Also, the power density is only modest. This technology is being commercialised for stationary applications, however.

Durability and current density

This leaves the Proton Exchange Membrane fuel cell (PEMFC) and the Direct Methanol fuel cell (DMFC). Both of these technologies use a proton exchange membrane electrolyte, but the PEMFC requires a hydrogen rich fuel, whereas the DMFC can run on methanol fuel. The DMFC has no requirement for a fuel processor, thus reducing the cost and complexity of the system. However, there are two major problems with the technology. Firstly, the current density is well below the levels that would be required for car use. Secondly, the methanol can diffuse through the electrolyte and oxidise on the air electrode reducing performance and efficiency (Kalhammer *et al.*, 1998).

Table 2.2 – Comparison of the characteristics of various types of fuel cells (adapted from Kalhammer *et al.* (1998))

Cell Type	Electrocatalyst Type	Operating Temp. (°C)	Current Density	Need Fuel Processor?	Compatible with CO_2?	Stage of Development	Prospects For	
							High Efficiency	Low Cost
PEMFC	Proton Exchange Membrane	70 – 80	High	Yes	Yes	Early prototypes	Good	Good
AFC	Aqueous Alkaline	80 – 100	High	Yes	No	Space application	Good	Good
PAFC	Phosphoric Acid	200 – 220	Moderate	Yes	Yes	Early commercial applications	Good	Fair
MCFC	Molten Carbonate	600 – 650	Moderate	Yes[5]	Yes	Field Demonstrations	Good	Fair
SOFC	Solid Oxide	800 – 1000	High	Yes[5]	Yes	Laboratory demonstrations	Good	Fair – Good
DMFC	Proton Exchange Membrane	70 – 80	Moderate	No	Yes	Research	Poor	Poor – Fair

[5] Except for natural gas fuel

Conclusion

The PEMFC currently comes closest to meeting the criteria for automotive use. It operates at relatively low temperatures, can use air, has excellent performance with hydrogen and the potential for cost effective mass production. If carbonaceous fuels are to be used, a fuel processor is required to produce a hydrogen rich gas for the fuel cell. In doing this, a certain amount of carbon monoxide will be produced. The system has to be able to reduce the CO in the product gas down to a concentration of around 10 ppm to avoid damage to the fuel cell.

Current state of research

A lot of current research by car manufacturers is in methanol fuelled fuel cell systems that replace the conventional ICE. Currently, PEM fuel cells are around 50 – 60% efficient (Kalhammer *et al*, 1998). Methanol fuel processors are around 85% efficient. Therefore, overall efficiency is 43 – 51%. This is greater than the 35% efficiency of an internal combustion engine, however it does not take into account the relative efficiencies of fuel production or vehicle drivetrain. There are also some obstacles in the way of these systems' development. According to Kalhammer *et al*, (1998), turbo machinery for fuel cell power plants is not currently sufficiently developed, and manufacturers are not investing enough in this research. Machinery that meets the required performance criteria is too expensive to mass-produce. Another area in which research is not far enough progressed is the area of catalytic combustion. This is required to efficiently and cleanly supply heat to the reforming reaction and to recover chemical energy from the fuel cell exhaust gas. It is also important that the various parts of the system are optimally integrated in order to obtain the highest efficiency. Few manufacturers (only Daimler Chrysler and Toyota) have the capability of testing water and thermal energy integration in a rolling test bed.

The cost of fuel cell vehicles that use hydrogen fuel is significantly lower than that of vehicles with on-board conversion of methanol or petrol (Thomas, James, Lomax, and Kuhn, 2000). This may outweigh the cost per vehicle of developing a hydrogen supply infrastructure, based on localised generation of hydrogen from natural gas. Thomas *et al.* (2000) have calculated that a hydrogen fuel cell vehicle may have the lowest fuel cost per mile, compared with gasoline or methanol fuel cell vehicles. This assumes that the

hydrogen fuel cell vehicle achieves a fuel economy of 66 miles per US gallon gasoline equivalent. If this is the case, the cost per mile could be lower than that of a conventional vehicle with a petrol fuelled internal combustion engine.

2.2.2 Hydrogen storage

One of the major obstacles to overcome, if hydrogen is to be used to fuel cars, is that of storing the hydrogen on board the car.

Carbon nanotubes

One hydrogen storage medium that is attracting some interest is carbon nanotubes. Nanotubes can be made in several different ways, including the carbon arc-discharge method and the catalytic method (Wu, Chen, Lin and Tan, 2000). It has been observed that, under certain circumstances, hydrogen can be taken up by these microscopic structures and can then be rejected later by heating. Dillon, Jones, Bekkedahl, Kiang, Bethune and Heben (1997) used co-evaporation of cobalt and graphite in an electric arc to form single walled carbon nanotubes. Iijima (1991) describes how multi-walled graphitic carbon tubes can be formed by carbon arc-discharge evaporation, similar to the method used to form C_{60} fullerenes.

Compression

The energy required to liquefy hydrogen is roughly one third of its energy content. On the other hand, compression to 5000 psi (roughly 350 bar) takes only one tenth (Farrell, Keith and Corbett, 2003).

Cryogenic storage

Hydrogen liquefies at about 20 K and 2 bar and is stored in double-walled, super-insulated vessels to minimise boil-off (DeLuchi, 1989). It takes 2 to 5 days for pressure in a liquid hydrogen tank to reach 3 to 5 bar, at which point the tank must be vented. In vehicles using internal combustion engines, the vented hydrogen may be disposed of safely using a small fuel cell, which can generate electricity to charge the vehicle's starting battery (Peschka, 1998).

Liquefaction is an energy intensive process that is only economical in large scale. Current liquid hydrogen plants are about 27 tonnes per day capacity (Moore and Ramen, 1998).

Comparison of storage methods

Dillon *et al.* (1997) compare nanotubes with the following methods of storing hydrogen.

- Carbon/polymer
- Fibreglass/aluminium
- Iron oxide reduction
- Liquid hydrogen
- Activated carbon

The storage of H_2 in single-walled carbon nanotubes is shown to exceed the volumetric energy density of all of the alternative technologies, including liquid H_2 and commercially available carbon/polymer storage units. This would appear to make the carbon nanotube technology very attractive. It does, however, assume that the storage system contains virtually pure nanotubes, properly aligned and bundled, something which may be difficult to achieve in practice. There is no indication of what temperature or pressure would be required for H_2 adsorption and desorption in such a system, or the time that these processes would take in practice. Iijima (1991) found that total hydrogen uptake was only 0.25% of the weight of the multi-walled carbon nanotubes. Obviously, a lot more work will be necessary if this technology is to be useful for storing hydrogen in cars. It does seem that the single walled, straight tubes have a greater potential for hydrogen storage.

Safety concerns

There is a perception by the public that hydrogen is far less safe than conventional transportation fuels. However, hazards associated with hydrogen storage and use are different from, but not necessarily worse than other fuels (DeLuchi, 1989). Hydrogen gas is invisible and odourless, so an odorant must be added to enable detection of leaks. Hydrogen has wide flammability limits (4% to 74% by volume) and requires little energy to ignite. However, the risk of ignition would probably be similar to that for methane, since the lower volumetric ignition limits are similar for the two gases. Hydrogen has a relatively high lower volumetric detonability limit (18.3% compared to 6.3% for methane,

for example). Volumetric limits are more pertinent to storage safety than mass limits. This means that hydrogen has a lower explosive potential than other gaseous fuels when not in a confined space. Hydrogen fires burn very rapidly and radiate little heat, so they are relatively short-lived. A person can be closer to a hydrogen fire than to a petrol fire without being burned. If liquid hydrogen should leak after a crash, it would evaporate and disperse very quickly.

If equipment containing hydrogen is to be operated at very high pressures, one has to take into account the effect hydrogen has on the material strength of the equipment. Hydrogen will embrittle certain materials (*e.g.* pearlitic stainless steel) over a number of temperature and pressure cycles. This effect is discussed by Panasyuk, Andreykiv and Gembara (2000), who propose a kinetic model to describe the effect of hydrogen on crack propagation in a hydrocracking reactor. Fortunately, the equipment used in a fuel cell power plant is not likely to be run at a pressure which would make this effect significant.

2.3 Developing a hydrogen fuel supply infrastructure

2.3.1 The hydrogen economy

In many people's ideal vision of the future, there would be a hydrogen economy. The vision would include hydrogen production from water using renewable energy sources and its return to water to produce work. This would generate no polluting by-products. Unfortunately, there is currently no infrastructure to supply hydrogen to the public in sufficient volume or at sufficiently low cost to be used as an automobile fuel. Guy (2000) discusses this hydrogen economy and its potential importance in the future. It is noted that Japan and America in particular are currently investing millions of dollars in pursuit of this ideal vision. He concludes that, using current technology, hydrogen is not economically viable as a major energy vector and can have greater environmental load then fossil fuels. However, it presents potentially large environmental benefits and could in the medium term play a significant part in reducing local urban emissions from transport.

In the US, one of the main reasons for developing hydrogen as a transportation fuel is to reduce the country's dependence on imported oil, since there is a large supply of natural

gas available from which the hydrogen could be manufactured (Moore and Ramen, 1998, Thomas *et al.*, 2000).

The method of hydrogen storage chosen for use onboard cars will affect the development of the supply infrastructure. If cars use liquid hydrogen, the current US infrastructure will expand to meet demand (Moore and Ramen, 1998). A market base of 25,000 hydrogen powered cars will be required to support the investment in a 27 tonne per day liquid hydrogen plant. If cars use gaseous hydrogen, initial supplies may be from existing local facilities. In remote locations, it would be more cost effective to use on-site reformers or electrolysis units. Reformers would produce hydrogen at nearly half the cost of electrolysis units (Moore and Ramen, 1998).

Farrell, Keith and Corbett (2003) believe that the best way to introduce hydrogen to the fuel market is through a single mode or application, such as commercial shipping or long-haul freight trucks, or into a geographically restricted area. This would make it easier to create significant market penetration in that area. Before commitments are made for a wide range of transportation modes, it would be better to start small, to let innovation and competition weed out lower-performance technologies, before risking broader disruptions of the transportation system. A protected niche would allow for companies to learn by doing in the design and operation of hydrogen fuelled vehicles. The immediate environmental benefits of introducing hydrogen fuel will occur in modes that have little or no pollution regulations applied to them. Therefore, heavy-duty modes would be a less costly way to introduce hydrogen fuel and a more effective way to advance hydrogen related technologies so that they could be used widely in light-duty vehicles.

2.3.2 Hydrogen filling stations

In 1999, Shell UK Ltd announced that they would be developing the world's first hydrogen economy in Iceland as a consortium joint venture. Iceland has recently received its first hydrogen automotive fuel station (Eisenstein, 2003). The Shell station is the first one in the world to be supplied with hydrogen generated entirely from renewable energy. This is possible due to Iceland's abundant supply of geothermal and hydroelectric energy. Although there are currently no hydrogen powered cars on the island, 3 Citaro urban buses will shortly be supplied by DaimlerChrysler, replacing 4% of Iceland's mass-transit

fleet. These buses store hydrogen on board at 5000 psi (*ca.* 350 bar). This is supplied to a fuel cell capable of producing 250 kW of electrical power. The buses perform as well as ones with a conventional powertrain. This is all part of a project run by an industry/government consortium called Icelandic New Energy (INE), which includes Shell, DaimlerChrysler, Norsk Hydro and various Icelandic partners. INE believes that, using existing renewable energy available in Iceland, it can produce enough hydrogen to meet both Iceland's needs, plus those of another country the size of Denmark.

2.3.3 Importance of oil companies to the hydrogen economy

More than 8.5 million tonnes per year of hydrogen is commercially produced in the US (Moore and Ramen, 1998). Only a tiny fraction of this is currently used as a transportation fuel. However, in the US there is a well developed infrastructure for the distribution of liquid hydrogen by over-the-road tankers. Current US installed capacity for liquid hydrogen production is over 80,000 tonnes per year, which is distributed in around 20,000 tanker loads per year.

Shell Global Solutions has suggested that oil companies hold the key to the future development of hydrogen as a clean energy source (Webb, 2002). The technology to produce hydrogen from hydrocarbons cheaply and efficiently already exists in the industry. This production could bridge the gap between current technology and the clean future, encouraging investment in research and development of hydrogen technology.

2.4 Approaches to hydrogen production

2.4.1 Sustainable production

Thermochemical water splitting

Producing hydrogen from hydrocarbons will always produce carbon-containing by-products. Since one of the aims of the hydrogen economy is to reduce global CO_2 production, this is obviously not desirable. An alternative is to produce hydrogen from water, with the energy supplied by a renewable source such as solar energy or nuclear

fusion. Thermochemical water splitting produces hydrogen from water using high quality heat. There are two reaction options, or a combination may be used (Peña *et al.* 1996). The first is to convert the heat to electricity (which is about 40% efficient) and then use this electricity for hydrolysis of water. The other is to use the heat for several endothermic reactions yielding products which, when reacted, will result in the products H_2 and O_2 from molecular H_2O. Which method is favourable will depend upon the cost of each method in the desired application.

Photocatalysis

Production of hydrogen from water by the direct action of solar energy on a suitable catalyst would be a very clean way to provide fuel in the future. This process is the cleavage of the water molecule over a semiconductor. The substance used as a photocatalyst is most often based on TiO_2 (Duonghong, Borgarello and Gräzel, 1981, Karakitsou and Verykios, 1993). The process may be assisted by the dispersal of metal particles on the TiO_2 surface. One of the problems facing many of the materials currently under consideration is that they only respond to UV radiation (Shangguan and Yoshida, 2001). CdS has been found to overcome this problem, but it is not stable in aqueous solutions under irradiation. Although Shangguan and Yoshida (2001) have managed to stabilise CdS in a layered composite, the rate of hydrogen evolution under irradiation by 300 W xenon lamp is not very high ($<5\times10^{-3}$ mol/m^2.h).

Duonghong *et al.*, (1981) investigated the properties of a colloidal sol of TiO_2 coated with Pt and RuO_2. The effectiveness of the photocatalyst was tested under UV light and under visible light irradiation. The quantum yield was found to be 30% ± 10% for irradiation at 310 nm. This is very high (the theoretical maximum is 50%).

Visible light experiments showed that, with no sensitiser present in the reaction mixture, not even a trace of hydrogen was produced. Addition of $Ru(bpy)_3^{2+}$ and methyl viologen (MV^{2+}) to the solution allows hydrogen to be formed at a rate of 0.14 ml/h. This was the highest production rate obtained for irradiation with visible light. This is clearly far slower than the former reaction under UV irradiation. However, this may not be a significant problem in the long term since industrial processes would be using sunlight to promote the reaction and this contains significant proportions of UV light.

Karakitsou and Verykios (1993) also investigated the use of TiO_2 as a photocatalyst for water cleavage. In this case, the effect of doping the TiO_2 with various cations was investigated. It was found that the effectiveness of the catalyst was enhanced when doped with cations of a valence greater than that of the parent cation (Ti^{4+}), *e.g.* W^{6+}, Ta^{5+} or Nb^{5+}.

Hydrogen from biomass

One renewable resource, which may be used more in the future is biomass. In the USA, 43% of renewable energy is supplied by biomass, second only to hydro-power at 51% (Chum and Overend, 2001). Hydrogen can be produced from biomass via gasification with efficiencies of up to 60% (HHV), although reforming of natural gas was found to possibly be a more efficient source of vehicle fuel when compared with gasification of municipal solid waste (Björklund, Melaina and Keoleian, 2001).

Alternatively, hydrogen can be produced via bacterial action on waste material. Hydrogen is a key intermediate in the mineralisation of organic mater by anaerobic bacterial action (Nielsen, Amandusson, Bjorklund, Dannetun, Ejlertsson, Ekedahl, Lundström, and Svensson, 2001). The production of hydrogen by bacteria is thermodynamically unfavourable unless the hydrogen partial pressure is kept low. The hydrogen can be separated from the other gases produced (mainly CO_2) by a palladium-based membrane.

Phototropic purple bacteria can convert carbon substrates such as lactate into hydrogen and CO_2 using light as the energy source. He, Bultel, Magnin, Roux and Willison (2005) tested four different mutant strains of *Rhodobacter capsulatus*, a photosynthetic, purple, non-sulphur bacterium, for their ability to produce hydrogen in a 3 L photobioreactor coupled to a small PEM fuel cell. The most preferment strain, IR3, showed a substrate conversion efficiency of 84.8% and a hydrogen yield of 3.9 L/L of culture. The relative hydrogen content of the biogas was greater than 90%. The maximum current produced by the fuel cell was similar to that observed using pure hydrogen.

Green algae can be made to produce hydrogen (Ghirardi, Zhang, Lee, Flynn, Seibert, Greenbaum and Melis, 2000). There is a need to increase the yield of hydrogen production by a factor of ten or more and to develop a protocol that works with minimal media before the process becomes commercially viable.

Photosynthesised hydrocarbons

Another method utilising solar energy to produce hydrogen is to take advantage of the natural solar energy collection performed by plants. Photosynthesis uses solar energy to produce carbohydrates from CO_2 and water. These carbohydrates may then be converted to H_2 and CO_2. This can be done indirectly, via fermentation of the carbohydrate, or it may be carried out directly. Kawai and Sakata (1980) investigated the direct conversion of carbohydrate and water to H_2 and CO_2 using a $RuO_2/TiO_2/Pt$ photocatalyst, and light energy.

$$6nH_2O + 6nCO_2 \xrightarrow{h\upsilon,\ \text{green plant}} (C_6H_{12}O_6)_n + 6nO_2 \quad (2.1)$$

$$(C_6H_{12}O_6)_n + 6nH_2O \xrightarrow{h\upsilon,\ RuO_2/TiO_2/Pt} 6nCO_2 + 12nH_2 \quad (2.2)$$

$$12nH_2O \rightarrow 6nO_2 + 12nH_2 \quad (2.3)$$

The average efficiency of photosynthesis in plants is around 0.1%, but corns and sugar cane grow rapidly and utilise solar energy with an efficiency of roughly 1%. Unfortunately though, the carbohydrates they produce are sugars and cellulose, which cannot be directly used as fuel. Kawai and Sakata (1980) have shown that it is possible to convert the carbohydrates directly to hydrogen, using Reaction (2.2) above. In their experiments, the highest hydrogen production rate measured was 341 μmol/20h for the sugar in 6M NaOH solution. This represents a quantum yield of 1.5%. Obviously, this is not a very high production rate, and the possibility of scale up has not been discussed by the authors.

2.4.2 Production from fossil fuels

Given fossil fuels' inherent advantages, such as their availability, relatively low cost and the existing infrastructure for delivery and distribution, they are likely to play a major role in energy and hydrogen production in the near to medium-term future (Muradov and Veziroğlu, 2005).

Hydrogen is used mainly for ammonia production and in petroleum refining for hydrotreating and hydrocracking, methanol production, methanol-to-gasoline and

hydrocarbon synthesis via Fischer-Tropsch processes (Adris, Pruden, Lim and Grace, 1996). More than 80% of world ammonia production is based on the steam reforming of hydrocarbons. Hydrogen is produced as a by-product during naphtha reforming, but not in large enough quantity to cover the needs of refineries.

Steam-iron process

The steam-iron process is one of the oldest methods of producing hydrogen (Hacker, Fankhauser, Faleschini, Fuchs, Friedrich, Muhr and Kordesch, 2000). It is a cyclic process for water cleavage, whereby coal is consumed. Coal is gasified to a lean reducing gas, containing CO and hydrogen. This gas reacts with iron oxides (haematite Fe_2O_3, magnetite Fe_3O_4 and wuestite FeO) to produce a reduced form of iron oxide (wuestite FeO, iron Fe). The reduced iron oxide is re-oxidised with steam to form magnetite and hydrogen. Hydrogen produced by a small-scale Sponge Iron Reactor was shown to be sufficiently pure for fuel cell use (CO < 10 ppm). Since the steam-iron process operates at high temperature (800 – 900 °C) the hydrogen is best utilised by a high temperature fuel cell, closely coupled for enhanced energy recovery. A 10 MW (power input) plant coupled with a solid oxide fuel cell was simulated by Hacker *et al.* (2000). Biomass gas formed by gasification of wood was utilised as feedstock. The simulation predicted an electricity output of 2.5 MW, and a heat output of 1 MW at 200 °C from the SOFC. This is an overall efficiency of 35 %.

The sponge iron process can be combined with a reformer to convert natural gas to hydrogen (Hacker, 2003). Efficiency can be improved by using syngas produced by SMR as feedstock for the SIR. This combined process is known as the reformer sponge iron cycle (RESC). Essentially, the reduction step of the SIR replaces the shift conversion and any downstream cleanup processes, such as PSA. Steam for the reforming process is supplied, potentially in full, by off gas from the SIR, around 40-45 % of which is recycled into the reformer. However, the CO_2 content of the off-gas can increase carbon deposition in the SMR if no additional steam is used. The rest of the off gas is used to fuel the burner that heats the SMR.

Steam reforming of methane

Natural gas will remain the major feedstock for the production of hydrogen via syngas, despite the low price and wide availability of coal. This is because the cost of coal based syngas plant is roughly 3 times that of natural gas based plant (Peña *et al.*, 1996). The following reactions are used to produce syngas from methane:

$$CH_4 + H_2O \Leftrightarrow CO + 3H_2 \quad (2.4)$$

$$CH_4 + \frac{1}{2}O_2 \Leftrightarrow CO + 2H_2 \quad (2.5)$$

$$CH_4 + CO_2 \Leftrightarrow 2CO + 2H_2 \quad (2.6)$$

Reaction (2.4) is the methane steam reforming (SMR) reaction. This is the established process for converting methane to syngas and has been used for several decades since it was first developed in 1926. It has been substantially improved over the years. The usual process comprises feed gas preheating and pre-treatment, reforming, high and low temperature shift reactions, CO_2 removal and methanation. A diagram of this process is shown in Figure 2.2.

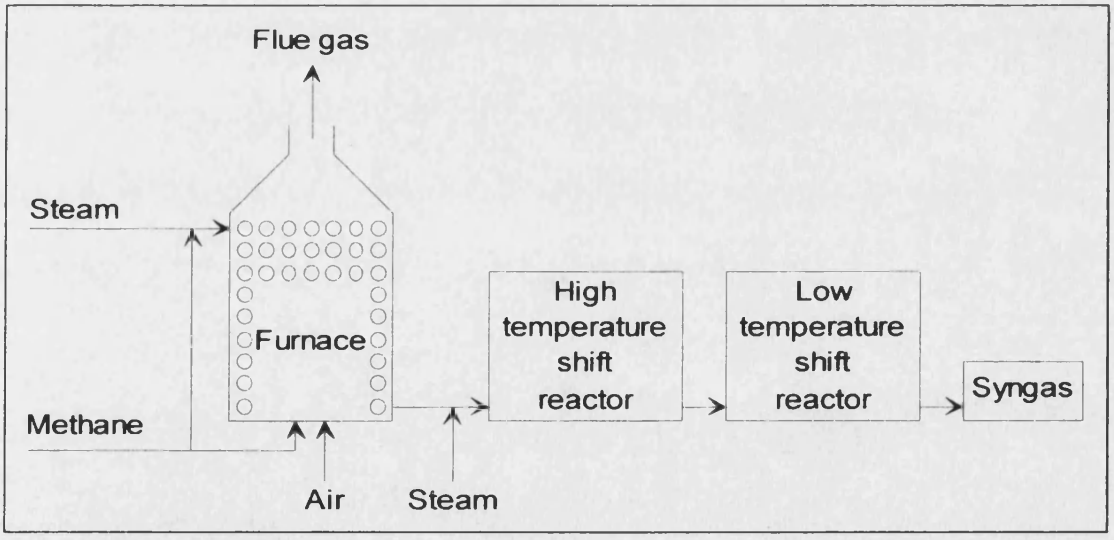

Figure 2.2 – Diagram of a standard industrial steam reforming process.

The steps of the reforming process differ, depending upon the intended use of the product. If hydrogen production is the goal, it is desirable to produce as few impurities as possible. There is no secondary reforming process and no air is added. Typically, the reaction

temperature is high, with an outlet temperature of over 800°C. Steam to carbon molar feed ratio is typically around 3.0 (Adris *et al.*, 1996)

The shift reaction, (2.7) below, is used to increase the H_2:CO ratio in the syngas.

$$CO + H_2O \Leftrightarrow CO_2 + H_2 \qquad (2.7)$$

The product stream from an SMR process is conventionally treated by high and low temperature shift reaction, a CO_2 absorption process and then methanation to remove traces of CO. More recent plants employ a pressure swing adsorption (PSA) process to purify the product stream. This replaces the low temperature shift, CO_2 removal and methanation steps of the conventional process. Using PSA, product purity can be over 99.99% (Adris *et al.*, 1996).

Partial oxidation of methane

The non-catalytic partial oxidation of methane (reaction (2.5)) is used by Texaco and Shell to produce hydrogen (Peña *et al.*, 1996). This process has the advantage that it can be run at high pressures, saving on costly downstream compression. The downside is that an oxygen plant is required. The process involves pre-heating a mixture of oxygen and natural gas and then igniting it in a burner. Reaction (2.5) is not the only reaction taking place. Complete combustion also occurs, producing H_2O and CO_2, which can subsequently be involved in steam reforming and other reactions. The outlet temperature is typically 1300 to 1400 K and the gas is near thermodynamic equilibrium at that point. A ratio of O_2:CH_4 of around 0.7 is required in the feed. Carbon formed by thermal cracking of methane has to be removed from the reactor by washing.

Reaction (2.5) can also be carried out on metal catalysts supported on refractory oxides in order to enhance reactor performance. Extensive work has been carried out in recent years on catalytic partial oxidation of methane in order to provide an alternative to steam reforming which is less energy intensive. The reaction is favoured by temperatures greater than 1100 K and an excess of CH_4. It produces syngas with the desired H_2:CO molar ratio for methanol production or Fischer-Tropsch synthesis. Because reaction (2.5) is slightly exothermic ($\Delta H°_R$ = -36 kJ/mol) it is more energy efficient to use than steam reforming. It

should be noted, however, that more CH_4 is consumed to produce the same amount of H_2 or CO and this can be weighed against the reduced energy consumption (Seo, Shirley and Kolaczkowski, 2002). The partial oxidation reaction is also faster than the steam reforming reaction allowing smaller reactors to be used and increasing productivity.

Catalytic partial oxidation has not been developed industrially due to the problems inherent to feeding CH_4/O_2 mixtures to the reactor under flammable conditions. Namely, the risk of explosion, the formation of local hot spots which could damage the catalyst and carbon formation on the catalyst (Peña *et al.*, 1996). Early work on partial oxidation of methane was carried out on a 10% Ni catalyst with $CH_4:O_2$ = 2:1 mixtures at atmospheric pressure in the temperature range 1000 to 1170 K. The temperature profile along the reactor suggested an exothermic reaction was taking place followed by an endothermic one. It is believed that the O_2 is initially completely consumed in a combustion reaction. Following this, steam and CO_2 reforming reactions take place, allowing almost complete CH_4 conversion at temperatures above 1100 K. Some subsequent research has suggested a different mechanism (Peña *et al.*, 1996), involving the direct formation of H_2, initiated by the pyrolysis of methane on the catalyst surface. There remains some debate as to which mechanism is correct.

Steam reforming reactors typically have superficial contact times of the order of 1 s (based on the feed gases at STP) while a direct oxidation process could have superficial contact times of 10^{-2} s or less. Experiments by Hickman, Haupfear and Schmidt (1993) on autothermal direct oxidation to synthesis gas of fuel rich CH_4/air and CH_4/O_2 mixtures were carried out using Rh-coated Al_2O_3 foam monoliths. The results were compared with previously reported data for Pt-coated monoliths. Rh was found to be a significantly better catalyst for partial oxidation of methane than Pt. Selectivity for hydrogen and CO were both improved and 100 % conversion of methane was achieved with around 22 % methane in the feed (with air). Pre-heating the reactants significantly improved reactor performance. Using O_2 instead of air in the feed had an effect similar to pre-heating the feed to 460 °C. Formation of hydrocarbon by-products was also reduced by using Rh catalyst and reduced further by increasing the catalyst loading. By-product selectivity was reduced to <0.01 at atmospheric pressure by using a Rh loading of 9.38 %. The short residence times indicate that the hydrogen is mainly formed by direct oxidation rather than by reforming of the products of complete oxidation.

Autothermal reforming

Autothermal reforming of methane is a combination of non-catalytic partial oxidation (reaction (2.5)) and steam reforming (reaction (2.4)). It was developed in the 1950s by Haldor Topsøe (Peña *et al.*, 1996) with the aim of performing the reforming process in a single reactor. The reactor basically comprises a ceramic lined tube for the POX reaction followed by a fixed catalyst bed to bring the gas mixture to equilibrium. The reactor has two pre-heated feed streams, one containing CH_4 and H_2O, the other containing H_2O and O_2. These are mixed in a burner at the top of the oxidation tube at approximately 2200 K. Equilibration takes place in the catalytic zone at 1200 to 1400 K. The higher temperatures help to reduce oxygen consumption, but a certain amount of steam has to be added to the feedstock to avoid carbon formation.

Combined reforming

Combined reforming of methane refers to any process where the steam reforming, CO_2 reforming and partial oxidation reactions are used in combination to produce syngas with the desired composition (Peña *et al.*, 1996). Thus there are several different variations. The combined reforming of methane (CRM) process uses a primary steam reformer and a secondary oxygen reformer in series, which allows the steam reformer to be reduced in size. This process requires an oxygen plant. ICI has patented a variation on this design named gas heated reforming (GHR), where the heat required by the steam reforming reaction in supplied directly by heat exchange with the reformed gas from the secondary reformer. This reduces the overall size of the reactor unit by around 25%. In newer ammonia plants, the secondary reactor is an autothermal reactor. Around 75% of the methane is reacted in the GHR, the remainder being reacted in the ATR with air rather than oxygen. This introduces the nitrogen necessary for ammonia synthesis and supplies the heat required for the GHR. Because the pressure is high on both sides of the tubes in the GHR (in contrast to old SRM furnaces) the heat transfer is much better.

Combined autothermal reforming

Another variation is the combined autothermal reforming process (CAR) in which steam reforming is combined with partial oxidation within a single fluidised bed reactor (Peña *et*

al., 1996). In pilot plant studies, the methane and steam are introduced at the bottom of the reactor (with steam to carbon ratios as low as 0.5), while the oxygen is introduced part way up the reactor. The catalyst is Ni on α-alumina. Carbon which forms on the catalyst due to the low steam to carbon ratio is burned off by the oxygen.

This process may be carried out in a fixed bed reactor. It is possible to use the same catalyst for both the combustion and reforming reactions, but the use of separate catalysts is more effective (Ma and Trimm, 1996). The two types of catalyst can be arranged in 2 separate beds, or sequentially in a single bed, or they can be intimately mixed in a single bed. It is also possible to deposit the two active catalyst components on the same support. These different configurations have been investigated experimentally. Higher methane conversions at a given temperature were observed with the single bed approaches. The best results were produced when both catalyst functions were available on the same support. This was achieved by impregnating a Ni/Al_2O_3 steam reforming catalyst with platinum.

Catalytic cracking of methane – on a nickel gauze

One of the drawbacks of using steam reforming or partial oxidation of methane to form hydrogen for fuel cells is that these reactions produce CO and CO_2. The CO has to be removed if the hydrogen is to be used in a PEM fuel cell. An alternative process is the catalytic cracking of methane:

$$CH_4 \rightarrow C + 2H_2 \qquad (2.8)$$

This reaction produces no CO or CO_2 and therefore saves on costly downstream cleaning processes. Monnerat, Kiwi-Minsker and Renken (2001) describe a cyclic process whereby the carbon is periodically removed from the reactor by reaction with oxygen:

$$C + \tfrac{1}{2}O_2 \rightarrow CO \qquad (2.9)$$

$$C + O_2 \rightarrow CO_2 \qquad (2.10)$$

These reactions can be carried out separately from the cracking reaction (2.8). Monnerat *et al.* (2001) have carried out experiments using a nickel gauze as the catalyst. An

advantage of the gauze structure is the low pressure drop in the reactor. A Raney-type layer was formed on the surface of the gauze to increase the surface area. Before experiments commenced, the catalyst was pre-treated with hydrogen, heating from ambient temperature to 600°C at 5°C/minute. During experiments, either methane or oxygen were fed to the reactor in an Argon carrier gas. Methane partial pressure was 30 kPa and oxygen partial pressure was 12 kPa.

It was found that some loss of catalyst occurred over time – about 10% of catalyst mass after 70 hours of operation. The most efficient temperature range for hydrogen production was found to be 540 to 560°C. In this range, hydrogen selectivity was maximised. Unfortunately, at temperatures over 500°C, hot spots formed during the oxidation process which damaged the catalyst structure. A cycle time of 4 minutes was found to give maximum conversion, but longer cycle times improved the hydrogen selectivity. A study of cracking time/cycle time split for a cycle time of 8 minutes was carried out. Increasing the split in favour of the cracking reaction improves the hydrogen selectivity, but decreases the methane conversion. The best time-average hydrogen production rate was obtained for a split of 0.5, *i.e.* equal time for the cracking and oxidisation reactions. Running the reactor at the optimum conditions for hydrogen production rate causes the production of significant amounts of H_2O and CO_2 and a small amount of CO, so downstream clean up would still be necessary if the product were to be used as fuel for a PEM fuel cell.

Catalytic cracking of methane – in parallel fixed-bed reactors

A hydrogen production system utilising catalytic decomposition of methane to hydrogen has been proposed by Poirier and Sapundzhiev (1997). A two-step process is proposed. In the first, endothermic step, CH_4 is decomposed to hydrogen and solid carbon in a fixed bed reactor. In the second, exothermic step, the catalyst is regenerated by flowing air through the reactor and combusting the carbon. The amount of energy released from burning the carbon is 4 times that required for the decomposition, so autothermal operation is possible.

High conversions in this process require high temperatures (>800 °C) during the decomposition step. The proposed system uses 2 reactors running in parallel. While one reactor is performing the decomposition, the other is being regenerated. There is a bed of

inert material at either end of each catalyst bed, the function of which is to store thermal energy. During the decomposition step, CH_4 is fed up through the reactor. The lower inert bed pre-heats the CH_4. A low temperature front moves up through the catalyst bed. When the top of the bed reaches around 800 °C, the CH_4 flow is switched to the other reactor and the regeneration step is initiated. During regeneration, air flows down through the reactor. The inert material at the top of the reactor pre-heats the air and combustion is initiated when the hot air meets the carbon in the catalyst bed. This step not only regenerates the catalyst, but also increases the reactor temperature to around 1000 °C, supplying enough thermal energy to support the following decomposition step. The off-gas may be combusted to remove any CO present and heat may be recovered from the stream. No purge step is required. The gas initially produced at the start of the decomposition step will contain some CO and other combustion products, but can be directed to the off-gas burner.

Some CO is always present in the product (ca. 1 vol. %) due to some reduction of the catalyst, which is oxidised to some extent during the regeneration step. Methanation is suggested as a possible cleanup process. PSA would also be a good alternative

Catalytic cracking of methane – catalysts

Catalysts for methane decomposition reactions were studied by Nakagawa, Nishitani-Gamo and Ando (2005). They found that nickel and palladium both showed good activity when supported by oxidised diamond, with nickel showing the greatest activity. This catalyst support was compared with various metal oxides using a nickel catalyst. The oxidised diamond support had superior activity to the other materials.

An alternative method of achieving catalytic decomposition of methane is in a fluidised bed reactor. Such a reactor, using an activated carbon catalyst is proposed by Lee, Han, Yoon and Lee (2004). The carbon particles formed in the reactor can be separated from the product gas stream by a cyclone, theoretically removing the requirement of a regeneration step and avoiding any introduction of oxygen to the system. Unfortunately, during experiments on a pilot-scale reactor, catalyst activity (and thus methane conversion) fell rapidly during experiments as carbon deposition occurred on the catalyst particles.

2.5 *Efficiency of various hydrogen production methods*

Rosen and Scott (1998) compare several different hydrogen production processes in terms of their energy efficiency and their exergy efficiency. The processes considered were steam reforming of methane, coal gasification, current and advanced technology water electrolysis and thermochemical water decomposition. Also considered were hybrid processes where oxygen from the electrolysis processes and the thermochemical water decomposition was used to enhance the combustion in the steam reforming furnace. These comparisons were made using the process simulator, Aspen Plus, enhanced for exergy analysis. The following assumptions were made:

- Combustion was assumed to occur in 40% excess air
- Hydrocarbons were considered sulphur free
- Natural gas was modelled as pure methane
- Coal was modelled as pure carbon
- Air was modelled as 79% nitrogen and 21% oxygen by volume

According to the authors, the assumptions regarding the composition of the fossil fuels affect the efficiencies calculated by only about 2% compared with exact fuel models. This is not significant. The results of the analysis are given in Table 2.3. The steam methane reforming process is shown to be the most efficient, both in terms of the energy and the exergy consumption. Most of the energy losses are due to waste emissions, specifically cooling water and stack gas. The exergy losses are mainly due to internal consumption in the burner. Exergy is the maximum amount of work that can be produced by a stream or system as it is brought into equilibrium with a reference environment. It can be thought of as the usefulness or quality of energy. Exergy is conserved during ideal processes and consumed during real processes. Its consumption during a real process is proportional to the entropy created by process irreversiblities.

Table 2.3 – Comparative efficiencies of various hydrogen production processes (Rosen and Scott, 1998)

Process	Efficiency (%)	
	Energy	Exergy
Steam methane reforming (SMR)	86	78
Coal gasification	59	49
Current technology water electrolysis	30	26
Advanced technology water electrolysis	49	41
Thermochemical water decomposition	21	19
SMR & current technology water electrolysis	55	48
SMR & advanced technology water electrolysis	70	62
SMR & thermochemical water decomposition	45	40

The integrated SMR & current technology water electrolysis process is shown to be less efficient than the standalone SMR process. However, the integrated process has several advantages over the standalone process. Firstly, the methane fuel requirement is reduced, due to oxygen being used instead of air in the burner, meaning that no nitrogen is present to require heating. Secondly, if the methane supply is relatively pure, the stack gas will be relatively pure CO_2, which can be contained as an additional by-product. This would also eliminate the stack gas, making the process very clean.

The various methods of hydrogen production have been reviewed and compared economically by Peña *et al.* (1996). They conclude that, for hydrogen production from light hydrocarbons, steam reforming of methane will continue to be the technology of choice. It is simple, efficient and well proven technology.

2.6 Recent enhancements to the steam reforming process

2.6.1 Linking combustion and reforming in a monolith

Experiments were performed on a novel reactor utilising alternate channels in a ceramic monolith for steam reforming and catalytic combustion of methane (Frauhammer, Eigenberger, Hippel and Arntz, 1999). A one-dimensional model was also created to investigate the coupling of the reactions. Reforming and combustion reactants are fed counter-currently in alternate channels. Palladium was used as the catalyst for both

reactions, since this simplified the coating of the monolith. The model showed that maximum peak temperature would be obtained when each stream carries half of the heat of reaction out of the reactor. This can be achieved by leaving an inert zone at the beginning of the combustion channel, which causes the internal temperature to rise more sharply to a higher peak value. Conversion in the reforming channel can be improved by leaving an inert zone at the end of the channel. In this zone, the temperature falls rapidly due to heat transfer to the incoming combustion gas stream. If reforming catalyst is present in this zone, the equilibrium is shifted back towards the reactants as the temperature falls. With these enhancements, conversion in the reforming reactor is increased from 74 to 100 % and efficiency is improved from 48 to 76 %. There is the added benefit that the amount of catalyst required is below 60 % of that required to coat the entire monolith. 100 cpsi alumina monoliths were used for the experiments. Constructing the gas manifolds was not a trivial task. Although the reactions proceeded as expected, with a conversion of 95 % at 800 °C, there were problems with the monolith cracking in the hot region. Tests using a mullite monolith material are ongoing.

2.6.2 Catalytic wall reactors

The intimate linking of catalytic combustion heat source with an endothermic reaction process significantly reduces the overall heat transfer resistance. A catalytic plate reactor for the steam reforming of methane would be two orders of magnitude smaller than a conventional steam reforming reactor (Zanfir and Gavriilidis, 2001). However, catalyst deactivation can have severe consequences on the operation of the reactor.

Folded plate reactor

A possible configuration is the so-called "folded plate reactor" (Kolios, Frauhammer and Eigenberger, 2002). Here, the walls separating the two reactions are formed by folding a single sheet of metal into channels with rectangular cross-section. Spacers made from further sheets of metal folded into a corrugated shape are placed between the walls to improve heat transfer, flow distribution and provide extra catalyst support area. Kolios *et al.* (2002) modelled different flow regimes and found that counter-current flow of the reactants in opposing channels led to temperature instability and possible runaway of the combustion reaction. Co-current schemes were found to be more stable.

Catalytic wall reactor

Venkataraman, Wanat and Schmidt (2003) conducted experiments on parallel plate CWRs of different configurations. The plates used in the experiments were 8 cm × 5 cm × 0.1 mm corrugated fecralloy sheets with corrugations perpendicular to the direction of flow. A washcoat was applied directly to the plates after they had been oxidised in air at 900 °C for *ca.* 5 h to improve adhesion. The washcoat was an aqueous suspension of ~ 10 wt. % γ-alumina powder having 3 μm particles and contained 1 wt. % Cr_2O_3 and 0.1 wt. % Y_2O_3. One or two coatings were used to leave a layer ~ 10 μm thick. The γ-alumina was partially converted to α-alumina, which has a less porous structure, when the washcoat was briefly fired to ~ 1000 °C during preparation. Platinum and rhodium were used as the combustion and reforming catalysts, respectively. In one reactor configuration, water gas shift was enhanced using a platinum-ceria catalyst. The system was found to operate stably at 800 to 1000 °C for long periods without deactivation, indicating that both the catalysts and the metal walls were stable. Conversions of fuel were 90 % or greater on the combustion side and 90 to 99 % on the reforming side. Water gas shift reactions were possible, resulting in $H_2/CO = 42/1$ in the best case.

Modelling

A theoretical study of methane steam reforming coupled with methane catalytic combustion in a catalytic plate reactor (CPR) based on a two-dimensional model was carried out by Zanfir and Gavriilidis (2003). This is in contrast to the one-dimensional model used by other authors. It has the advantage of being able to take factors such a wall thickness and channel height into account. Reactor volume index (RVI) represents the ratio between the volume of the conventional reformer and the CPR volume to convert the same amount of methane. Catalyst weight index (CWI) represents the ratio between the amount of catalyst used in the conventional process and that used in a CPR to convert the same amount of methane. Calculations indicate that, for a low pressure (ca. 1 bar) CPR, the RVI = 150 and the CWI = 85. The temperature difference between wall and process gas phase is reduced from about 250 K to a maximum of 35 K (at 1 bar).

2.6.3 Oxygen enriched feed

Thermodynamic analysis has shown that fuel consumption in a conventional steam methane reformer can be reduced by enhancing the oxygen content in the combustion air (Lambert, Sorin and Paris, 1997). It was found that peak efficiency occurred when the proportion of O_2 in the air was increased to 29 % using a semi-permeable membrane separator. This allowed fuel consumption to be reduced by 8.4 % without altering the rate of hydrogen production.

Roy, Pruden, Adris, Grace and Lim (1999) investigated the feeding of oxygen into a fluidised bed steam reforming reactor. This was able to provide autothermal operation of the reactor, at temperatures below the auto-ignition temperature of the steam / methane / oxygen mixture (up to 675 °C). The product gas did not reach equilibrium composition, but this was ascribed to the lack of heating in the upper end of the fluidised bed causing the reverse reactions to take place. Later results using a heated upper section (not reported in this paper) were said to show equilibrium conversion.

2.6.4 Micro-reactors

Compact methane steam reformers based on microchannel technology are being developed by Velocys (Tonkovich, Perry, Wang, Qui, LaPlante and Rogers, 2004). Channel dimensions in microchannel reactors range from 50 to 5000 μm and flow regimes are usually laminar. Heat and mass transfer rates can be improved by one or two orders of magnitude. The demonstration reactor was constructed by welding Inconel plates and shims. The individual pieces were made using conventional machining, wire electro-discharge machining and laser cutting. The Velocys reformer achieved > 90 % conversion of methane at > 150 kPa, approaching equilibrium conversion at 850 °C and higher with contact times of 6 ms or less. Natural gas was used as the feedstock for 40 h with similar performance. During typical operation, around 700 W of heat were produced by combustion. Of this, 311 W were consumed by the SMR reaction and around 314 W were heat losses. This is not surprising for a device of this size, with a high surface area to volume ratio. A commercial device would be expected to suffer only 5 % thermal losses. Very low amounts of NO_x were formed during combustion (< 10 ppm). Heat transfer rates to the endothermic reaction exceeded 65 W/cm^3 total reaction volume. This greatly

exceeds the process intensity of conventional steam reformers, which typically have a volumetric heat flux below 1 W/cm³.

2.6.5 Sorption enhanced SMR

Hufton, Mayorga, and Sircar (1999) describe how their Sorption Enhanced Reaction Process (SERP) can be applied to the steam reforming of methane. The SERP uses a selective adsorbent mixed with the catalyst in the reactor to remove selected reaction products. This forces the equilibrium further to the product side, producing more of the desired product under conditions that would not usually be favourable for the reaction. Periodically, the adsorbent is regenerated by a pressure swing process.

For SMR, Hufton *et al.* (1999) show that removal of CO_2 from the reaction zone drastically improves the thermodynamic performance of the reactor. Removal of CO_2 causes the water-gas shift reaction to proceed essentially to completion, which removes most of the CO from the reaction zone. In turn, this causes the steam reforming reaction to approach completion also, even at relatively low temperatures and high pressures. For example, if 99.9% of the CO_2 that is produced by the water-gas shift reaction is removed from the reaction zone, then an equilibrium conversion of >80% is possible at a temperature of 450°C and a pressure of 50 psig with a steam to methane ratio of 6:1. This results in an equilibrium mixture containing >95% H_2 and <100 ppm of CO and CO_2 on a dry basis. The equilibrium conversion under these conditions when there is no CO_2 removal is only 28%.

Hufton *et al.* (1999) describe the properties of a potential adsorbent that they have developed for SMR, which is a potassium carbonate promoted hydrotalcite in pellet form. Testing indicated that the adsorbent exhibited substantial and reversible CO_2 sorption capacity in the presence of steam, fast kinetics and desorption of CO_2 by pressure reduction and purge with non-adsorbing gas.

The cyclic steps for the SERP process for SMR are as follows (Hufton *et al.*, 1999):

1. *Sorption-reaction step:* A mixture of steam and methane at reaction temperature and pressure is passed through a tubular reactor containing an admixture of CO_2 adsorbent

and SMR catalyst. An effluent gas containing mainly H_2 and CH_4 (on a dry basis) is produced. This step is continued until the CO, CO_2 or CH_4 levels in the effluent gas reach pre-set levels. At this point, the adsorbent will have become saturated with CO_2.

2. *Depressurisation step:* The reactor is depressurised in a direction counter-current to that of the feed gas flow. A gas mixture containing H_2O, H_2, CO_2, CO and CH_4 is produced. This is primarily inter-particle-void gas, with some desorbed CO_2. The pressure can be atmospheric or sub-atmospheric.
3. *Purge step I:* The reactor is purged in a counter-current direction at the reduced pressure with a relatively non-adsorbing gas such as CH_4 or steam. The effluent gas contains the major part of the desorbed CO_2 from the adsorbent.
4. *Purge step II:* The reactor is purged in a counter-current direction with some of the H_2 enriched effluent produced during *step 1*.
5. *Pressurisation step:* The reactor is now re-pressurised up to the reaction pressure in a counter-current direction with part of the H_2 enriched effluent produced during *step 1*. The cycle then restarts at *step 1*.

At least two parallel reactors would be needed for continuous operation. Presumably, the process could be made more efficient by using multiple reactors and de/re-pressurisation stages in the manor of some PSA unit designs (*e.g.* Batta, 1971, Fuderer and Rudelstorfer, 1976).

Hufton *et al.* (1999) performed bench-scale tests to evaluate the performance of the SERP concept for SMR. Experiments were carried out in a stainless steel reactor 106.7 cm in length and 3.8 cm internal diameter. It was packed with a 1:1 weight ratio mixture of CO_2 chemisorbent and a commercial SMR catalyst. The total amount of adsorbent and catalyst loaded was 1.86 kg. Particle diameters of both were around 0.3 cm. The reactor tube was suspended in a furnace that allowed the reactor temperature to be maintained at 450±10°C during all steps of the process. A steam to methane ratio of 6:1 was used, with a reaction pressure of 55 psig (3.9 bar g) and a purge pressure of approximately 2 psig (0.14 bar g). The feed gas flow rate was 3.0×10^{-5} mol/cm².s. The results of the SERP experiment are compared with those of a standard SMR reaction at 450°C and 645°C in Table 2.4.

Table 2.4 – Performance comparison of SERP with SMR at moderate temperatures (adapted from Hufton *et al.*, 1999)

Process type	Conditions	Product purity (dry basis)	CH_4 conversion
SERP	450°C, 55 psig	96 mol % H_2, 4 mol % CH_4, <50 ppm ($CO + CO_2$)	82 %
SMR	450°C, 55 psig	53 mol % H_2, 34 mol % CH_4, 13 mol % ($CO + CO_2$)	28 %
SMR	645°C, 55 psig	75.5 mol % H_2, 4.4 mol % CH_4, 20.1 mol % ($CO + CO_2$)	82 %

Xiu, Li and Rodrigues (2002) discuss improvements to the work of Hufton *et al.* (1999) on SERP. Instead of using CH_4 or steam as the purge gas, a mixture of 10 % hydrogen in nitrogen is used. The hydrogen in the purge gas will react with the CO_2 in the adsorbent, increasing the rate of desorption. A short steam purge step is then required to remove the nitrogen. The process was modelled mathematically in order to determine the optimum temperature for this process. Lower temperatures favour the reaction, but inhibit the desorption. At 400 °C, regeneration times can be considerably shortened whilst maintaining high hydrogen product purity and production rate.

2.6.6 Fluidised bed membrane reactor

A fluidised bed membrane reactor (FBMR) combines the advantages of a fluidised bed (catalyst uniformity, improved heat transfer and elimination of diffusional limitations) with those of a membrane reactor (shifting the thermodynamic equilibrium and *in situ* separation of the desired product). Adris, Lim and Grace (1994) constructed an experimental steam reforming FBMR using thin walled palladium membrane tubes (4.7 mm outside diameter, 0.2-0.28 mm nominal wall thickness) installed vertically within the fluidised bed. Hydrogen product was removed from within these tubes. The catalyst used was a nickel oxide reforming catalyst supported on α-alumina, supplied by United Catalysts Inc. Entrained catalyst particles were separated from the by-product gas by an internal, centrally-located cyclone and returned to the bottom of the bed. Membrane throughput was found to limit the capacity of the reactor, but improvements in steam and methane conversion were observed, compared to a conventional fluidised bed reactor.

2.6.7 Supercritical water reactor

Taylor, Herdman, Wu, Wally and Rice (2003). Hydrocarbons such as methanol and ethanol may be reformed in a supercritical water reformer, running at very high pressures (around 27 MPa) and high temperatures (up to 700 °C). This is possible in very compact tubular reactors with small internal volumes. The reaction can be catalysed by the tube material itself (Inconel 625), thus simplifying the reactor. A reactor of this type was shown to achieve near-equilibrium conditions.

2.7 Hydrogen purification processes

The fuel gas produced by any reforming system must have a composition that ensures sufficient service life of the fuel cell at high efficiency (Höhlein *et al.*, 1996). Several post-reforming gas conditioning steps were considered:

- CO shift conversion
- selective CO methanation
- preferential CO oxidation
- adsorption processes
- membrane processes

The first three processes are chemical reactions. The shift conversion is not capable of obtaining a CO content lower than 6000 ppm with the conditions used in this study. CO methanation and CO oxidation can produce fuel gas with CO concentrations of < 100 ppm. The final two processes are separation processes capable of producing a stream containing >99.99% H_2.

2.7.1 CO oxidation

Selective CO oxidation requires very good control of oxygen (air) feed and thus temperature in order to ensure good selectivity (Höhlein *et al.*, 1996). Obviously, oxidation of the hydrogen is undesirable. Assuming equilibrium can be established, a CO content of <100 ppm is only achievable at temperatures below 120°C.

PEM fuel cells require <30 ppm CO in the hydrogen-rich gas input to prevent damage to the anode. In order to increase the fuel cell's tolerance to CO, Rohland and Plzak (1999) have investigated the application of a catalytic layer to the cell which oxidises CO from the stream before it reaches the anode. The catalyst they have tested is an Au/Fe_2O_3 catalyst, impregnated into a Ni foam sheet. This can then be placed in the fuel cell, separated from the anode by a carbon-paper sheet, which provides electrical contact between the catalyst sheet and the anode, but does not allow the Ni foam to come into contact with the acidic anode itself.

If such a catalyst sheet could be integrated into every cell in a stack, the reformate could be allowed to contain up to 1000 to 2000 ppm of CO. This would significantly cut down on the complexity and cost of the fuel gas treatment system and increase the dynamic performance of the fuel cell plant. The system would have a number of drawbacks, however. Firstly, a gold-based catalyst is not going to be cheap. The cost of integrating such a catalyst into every cell in a stack may outweigh the savings made on the rest of the plant. Rohland and Plzak (1999) do not provide information on the selectivity. The durability of the catalyst layer is also not discussed. Any system that is to be integrated into a car must be able to run for years without major overhaul and replacing the catalyst layers would be a time-consuming, tricky and expensive process.

Dudfield, Chen and Adcock (2001) have investigated preferential oxidation systems to remove CO from the fuel gas stream by oxidising the CO to CO_2. Conventional packed-bed type reactors may be too bulky for automotive applications and suffer from slow warm-up and poor thermal management. Therefore, the focus of their research was on the determination and integration of a suitable CO oxidation catalyst with a lightweight, compact and high surface area heat transfer technology. The aim was to produce a reactor that could supply sufficient fuel for a 20 kW PEM fuel cell stack.

Dudfield *et al.* (2001) considered several designs of reactor. These were the shell and tube heat exchanger, porous metallic substrates and a plate-fin heat exchanger. The plate-fin heat exchange was found to offer the lowest pressure drop, the best thermal management and the lowest CO output for a given fuel flow rate. This design also required a lower catalyst loading. Therefore, the plate-fin heat exchanger was chosen as the design to use for the 20 kW application. A duel stage reactor was built (effectively 2 reactors in series).

At the fuel flow rates required for 20 kW operation, this system was able to reduce CO levels from 2.7% to <20 ppm.

2.7.2 Membranes

Membrane separation using suitable materials can separate pure hydrogen from the reformate. The possible hydrogen yield is around 90% (Höhlein *et al.*, 1996). A pressure difference across the membrane is required to produce a driving force for the diffusion of hydrogen through it. Thus, an energy loss is introduced into the system. When polymer membranes are used, a trade-off between H_2 yield and CO content in the permeate has been observed. Ag/Pd membranes are better at performing the separation, but cost may be prohibitive. Such a membrane was tested by the authors and was found to produce a permeate of 99.999% H_2 by volume at a flowrate of 4 m^3 (at STP) H_2 per hour per m^2 membrane.

Pd and its alloys are only permeable to H_2, so they are the obvious choice for a hydrogen-producing membrane (Peña *et al.*, 1996). The membrane allows hydrogen to be removed from the reaction mixture so that the reaction is driven to a new steady state extent. For example, for the cyclohexane dehydrogenation reaction, at 473 K and 1 bar, the equilibrium conversion is 18.7%. Using a 0.5% Pt/Al_2O_3 catalyst packed in a 0.2 mm thick Pd tubular membrane reactor, a conversion of 99.7% was obtained, for high permeate side sweep rates. Unfortunately, there are some problems associated with using membranes in this way. Firstly, carbon dissolves into the Pd lattice, causing deactivation. Another cause of deactivation is chemisorbtion of the dehydrogenated species onto the membrane surface. Eventually, these phenomena cause the membrane to become impermeable to hydrogen.

Pd-Ag membranes were tested by Nielsen *et al.* (2001). The H_2 is adsorbed on one side of the membrane where it becomes dissociated. The H atoms dissolve into the Pd lattice before diffusing through to the other side, driven by the concentration gradient. Here they re-associate to H_2 which is desorbed. The membrane unit used by Nielsen *et al.* (2001) was a 4 standard litres per minute unit, at 273 K and 1 atm. The membrane was in the form of a cylinder through which the gas from the sulphide trap passed. The outside of the cylinder (permeate side of the membrane) was kept at a pressure of 10^{-2} Torr. The

operating temperature was around 350°C. Membrane performance was good, removing 85-90% of the hydrogen from the bioreactor product stream. Performance was not seen to decrease as the experiment progressed, with membrane efficiency still high after 22 hours. This was attributed to the operation of the sulphide trap, which probably protected the membrane from potentially damaging sulphur-containing species.

2.7.3 Methanation

CO methanation is thermodynamically feasible. It is important to find a selective catalyst that avoids the undesirable CO_2 methanation process (Höhlein *et al.*, 1996), which could lead to temperature runaway and significant H_2 loss. At temperatures below 240°C, CO methanation can produce fuel gas with less than 10 ppm CO content.

2.7.4 Adsorption

The impurities can be removed from the hydrogen stream by adsorption. Typically, this is carried out using a process called pressure swing adsorption (PSA). Several variations on the theme of PSA have been proposed (*e.g.* Batta, 1971, Fuderer and Rudelstorfer, 1976) but the basic principle remains the same throughout: The product gas stream is passed at high pressure through a packed bed of adsorbent, which removes the impurities from the stream. Once the adsorbent has become saturated with impurities, the pressure is reduced and the bed is flushed to return the adsorbent to its original state. The bed is then re-pressurised and the process is repeated. This is clearly a discontinuous process, so several beds must be used in parallel in order to provide a continuous flow of product gas.

2.8 Current work on compact hydrogen production systems

2.8.1 Mobile production

There are many references in the literature to compact hydrogen production processes. Many of these involve hydrogen produced from hydrocarbons. The most common processes under consideration are steam reforming of methane, propane or methanol,

thermal or catalytic cracking of methane, catalytic partial oxidation of methane and autothermal reforming of methane.

Comparison of mobile hydrogen generation technologies

Ledjeff-Hey, Formanski, Kalk and Roes (1998) have compared a methanol steam reforming process with thermal and catalytic cracking of propane as compact methods of producing hydrogen for solid polymer fuel cells. They do not come to a conclusion on which is the superior technology, but it is noted that the hydrocarbon decomposition route has the lowest energy consumption. Systems based on this technology can also be very small, simple and inexpensive, since no further gas purification is necessary.

The cost of a reforming technology is a major factor in whether it will be chosen as the optimum solution in any given situation. In order to achieve the widespread commercialisation of fuel cells in transport applications, costs of equipment must be reduced by at least an order of magnitude (Teagan, Bentley and Barnett, 1998). Teagan *et al.* (1998) have investigated the impact of factors such as fuel choice and fuel processor technology selection on fuel cell power plant costs. An analysis of the cost of building the infrastructure to replace 10% of the USA's gasoline demand with various alternative fuels was performed. It was found that the cost of developing such an infrastructure would be around $50 billion for compressed natural gas, $65 billion for methanol and $95 billion for hydrogen. This equates to approximately $50, $65 and $95 per kW generated for CNG, methanol and hydrogen, respectively. This means that a power plant utilising hydrogen will need to be around $95/kW cheaper than one utilising gasoline to make the construction of the infrastructure worthwhile. A fuel processor which is capable of processing a range of alternative fuels is the ideal compromise. Although the authors state that they have demonstrated such a processor, they clearly have commercial interests in mind and have not compared the performance of their processor with any others. Specific details about the construction of Arthur D. Little's fuel processor are also not given, although it is stated that partial oxidation technology is used rather than steam reforming. This allows the elimination of high temperature heat exchangers and makes fabrication cheaper.

Fixed-bed partial oxidation reactors

Adiabatic fixed-bed reactors for the partial oxidation of methane to synthesis gas were modelled by de Smet, de Croon, Berger, Marin and Schouten (2001). Ni catalysts produce synthesis gas by indirect partial oxidation, *i.e.* by total combustion of part of the methane followed by reforming of the remaining methane. At high temperatures and pressures hot-spot formation due to exothermal oxidation reactions can lead to severe catalyst deactivation. For that reason, the choice of suitable operating conditions and problems related to catalyst stability and process safety during scale-up still require considerable attention before this process can become industrially valid. Therefore, de Smet *et al.* (2001) have modelled the process for application to the production of methanol as well as to production of hydrogen for fuel cells. The principle differences between the two models were the capacity, the feed composition and the operating pressure. The full specifications for the hydrogen-for-fuel-cells model are given in Table 2.5.

Table 2.5 - Specification for methane partial oxidation reactor (adapted from de Smet *et al.*, 2001)

Parameter	Value	Units
Reactor and catalyst		
Capacity	10	kW
Reactor diameter	0.1	m
Reactor length	0.5	m
Void fraction of packing	0.43	$m^3_{gas}/m^3_{reactor}$
Pellet radius	2.5×10^{-3}	m
Operating conditions		
Pressure	1	bar
Temperature	773	K
Superficial mass flow velocity	0.15	$kg/m^2.s$
Feed composition		
CH_4/O_2	2.0	
H_2O/CH_4	1.5	
Oxygen source	Air	
Equilibrium conditions		
Temperature at equilibrium	971.7	K
H_2/CO at equilibrium	4.23	
$\chi_{CH_4,eq}$	98.5	%

For the hydrogen-for-fuel-cells case, a capacity of 10 kW was used. This seems a little modest since any car will require at least 50 kW electrical power in order to meet performance targets.

A steady state, one dimensional heterogeneous reactor model was used. Intra-particle concentration gradients as well as external concentration and temperature gradients were taken into account. Two alternative sets of kinetic equations were used to model the reforming reaction. Xu and Froment (1989a) (XF model) and Numaguchi and Kikuchi (1988) (NK model). While the reforming rate was seen to increase with decreasing pressure in the former case, the latter indicated a decrease in the reforming rate with decreasing pressure. Therefore, under the low pressure conditions of the hydrogen-for-fuel-cells case, the XF model predicted a higher endothermic reforming rate then the NK model. This meant that, while the NK model predicted a hot spot near the entrance of the reactor, the XF model did not. The maximum temperature predicted by the NK model was 1003 K. This would not lead to excessive catalyst de-activation. In order to determine whether gas phase reactions would be significant, the residence time for complete homogeneous conversion of all the oxygen present was compared with that for complete heterogeneous conversion. In the hydrogen-for-fuel-cells case, the time required for complete heterogeneous conversion was found to be 0.21 s, while that for homogeneous conversion was found to be 0.57 s. Therefore, the homogeneous gas-phase combustion reaction is not likely to play a significant part in the reaction scheme. This implies safe and stable reactor operation, something which was not found for the syngas-for-methanol case.

On board methanol conversion

One of the options for fuel cell vehicles is to store energy on board the car in the form of methanol. This can be converted to hydrogen using a steam reforming process, in order to supply the fuel cell. A lot of work has been done in this area. Höhlein, Boe, Bøgild-Hansen, Bröckerhoff, Colsman, Emonts, Menzer and Riedel (1996) investigated the general feasibility of such a system. Within the framework of a European Union JOULE II project, work was carried out to design a compact methanol reformer for use in fuel cell powered vehicles. In addition to this, Emonts, Bøgild-Hansen, Lœgsgaard Jørgensen, Höhlein, and Peters (1998) built and tested a compact steam reforming system, including a catalytic burner described by Emonts (1999). Wiese, Emonts, and Peters (1999) carried

out further analysis to investigate the production feasibility of compact methanol reforming systems.

2.8.2 Stationary production

Experimental reactors

In an effort to provide maximum efficiency and minimum emissions from a compact steam reformer, Polman, Der Kinderen and Thuis (1999) have designed an integrated steam reformer and catalytic combustion reactor. Their integrated reactor concept was to use metal monoliths to support the catalysts for the reforming and combustion reactions. These could be placed in contact with one another in a sandwich formation ensuring good heat transfer and a compact design. A coil was placed around the reactor to supply inductive heating for start-up and to compensate for load changes.

The experimental reactor used two reforming sections, sandwiched between two outer combustion sections. The monoliths had 250 channels per inch and were coated in precious metal catalyst by Degussa AG. The exact composition of the catalysts is not given. Catalyst activity was reduced over time if water was present in the feed, however operation of the compact reformer was still possible for up to 30% water in the feed. Initial activity levels could be restored by exposing the catalyst to a dry feed. Heat transfer between the two reactions was shown to be good, with the temperatures in the combustion and reforming parts of the reactor measured as being equal a short distance into the reactor. The conversion of the combustion and reforming reaction were greater than 99.98% and 97% respectively. NO_x levels were found to be in the ppb range, although actual data were not presented.

Reformer system efficiency

Thermal integration is a key issue for the design of a fuel processing system. The system design has to fulfil many different requirements, many of which are conflicting. For example, high system efficiency requires a sophisticated thermal integration, but this will tend to result in a complex and, therefore, large and heavy system, which is not desirable for a mobile system. The system must also operate safely and reliably, with minimal coke formation. In choosing a reforming technology, an important criterion is the thermal

efficiency (Docter and Lamm, 1999). This describes the relation of the lower heating value of the hydrogen produced to the lower heating value of the fuel processed. Of all the technologies available, steam reforming offers the highest efficiencies. The reason for this is obvious, however, as it is an endothermic reaction, so heat is supplied to the fuel as it is converted to hydrogen, therefore the energy available from the hydrogen will be greater than that available from the original fuel. According to Docter and Lamm (1999), no sulphur-tolerant steam reforming catalyst has been found, resulting in the need for a very efficient and probably large (for gasoline feedstock) unit for removing sulphur from the fuel. Since this paper has been written, however, ultra low sulphur fuels have been made widely available, so this may not be such a problem. Of more concern is the slow response of the steam reformer to transient conditions. The simpler, faster responding alternative is the partial oxidation process, but this is less efficient. A good compromise is the autothermal system.

The efficiency of the reformer is improved by increasing the temperature to which the feed streams are pre-heated. In an autothermal system, heat which would have been wasted in a partial oxidation system can be used to pre-heat the steam stream, thus providing better energy integration. The calculations of Docter and Lamm (1999) are purely thermodynamic and do not take into account the kinetics of the reactions. They are, therefore, only useful as a starting point for more in-depth simulations and experiments.

Thermal integration of reformer with fuel cell

Aguiar, P., Lapeña-Rey, N., Chadwick, D. and Kershenbaum, L. (2001) investigated the linking of a methane steam reformer to a solid oxide fuel cell. The solid oxide fuel cell uses a solid ceramic membrane for an electrolyte. It operates at a high temperature (700 to 1000°C) and can use hydrogen and carbon monoxide, as well as hydrocarbons as fuel. Methane may be converted directly to hydrogen in the anode by use of a suitable catalyst. Heat from the fuel cell would supply the energy for the endothermic reforming reaction. This can be done either directly, where methane is fed straight into the anode, or indirectly where the reformer is separate but adjacent to the fuel cell anode. The direct approach has the advantage that hydrogen consumption by the electrochemical reactions promotes the reforming reactions. The anode must have both good catalytic properties for the reforming reactions and good properties for promoting the electrochemical reactions

on the fuel cell anode. Nickel-yttria stabilised zirconia cements have been reported to be a promising material for this purpose. The indirect approach has the advantage that the catalyst can be better matched to the task of steam reforming and less carbon deposition occurs, meaning that catalyst de-activation is less of a problem. It has been shown that the heat available from the fuel cell is sufficient for complete conversion of the methane at the anode.

Aguiar *et al.* (2001) investigated the indirect approach to internal reforming. One of the major problems with this approach is caused by the mismatch between the activity of the steam reforming catalyst at solid oxide fuel cell operating temperatures and the heat available from the outer cells. This leads to extremely rapid kinetics for the steam reforming reaction which reduces the temperature of the fuel cell and prevents proper operation. Four methods for solving this problem were considered:

a) Catalysts with much lower metal surface area
b) Catalysts sintered at high temperature to reduce internal surface area
c) Catalysts with a non-uniform distribution of the active metal
d) Catalysts with a diffusive barrier placed around the outer surface of the pellets

The methods all aim to reduce the activity of the catalysts. Methods a) and b) above are unlikely to guarantee long catalyst life. a) would lead to a high loss of activity whenever deactivation occurs. b) can lead to complete pore blockage, reducing the overall reaction rate to an unacceptable level. Methods c) and d) offer a better solution – a reduced reforming reaction rate, whilst maintaining catalyst performance in the face of possible deactivation. These methods were studied by Aguiar *et al.* (2001) by modelling a catalyst particle with various catalyst activity profiles and diffusivity profiles. Another approach which is not considered is the recycling of anode off gas to reduce the rate of reaction. This would also allow better heat transfer.

Further modelling was performed (Aguiar, Chadwick and Kershenbaum, 2002) using the kinetics of Xu and Froment (1989a). The model comprised two coupled models: one for the steam reforming reactor and one for the solid oxide fuel cell. Several configurations are possible for the design of the system. The model used by Aguiar *et al.* (2002) was a simple annular design, where the fuel cell anode, electrolyte and cathode are constructed around a tubular packed-bed steam reforming reactor. The fuel was first fed to the inner

reformer, whose exit gases are then fed into the anode. The cathode was fed with air in a counter-current flow scheme. The steam reformer model was a conventional heterogeneous two-dimensional one, accounting for intra-particle mass gradients and inter-particle thermal gradients. As there was thermal contact between the steam reformer and the fuel cell, the boundary condition accounted for the overall heat transfer between the fuel stream in the fuel cell and the fuel stream in the reformer, as well as the radiation between the solid structure of the fuel cell and that of the reformer. The were used in the reformer model. The shift reaction was assumed in equilibrium in both the reformer model and the fuel cell model.

The heat released in the fuel cell can provide the heat required by the reforming reaction, which can vary from 40% to 70% of the total heat produced by the cell, depending on operating conditions. This increases overall system efficiency. It also reduces the requirement for fuel cell cooling, which is usually achieved by flowing excess air through the cathode. The problem of localised cooling due to high catalyst activity was investigated. This cooling effect can cause thermally induced fractures of the ceramic components of the fuel cell.

2.8.3 Generating heat for the reforming reaction

Solar furnace

One method for supplying the heat required for the steam reforming of methane is to use a solar furnace. This device collects and concentrates sunlight to provide high quality heat to a small area. Yokota, Oku, Sano, Hasegawa, Matsunami, Tsuji and Tamaura (2000) have studied the process by simulating the solar furnace on a bench scale using a Xe lamp. The experiments were all conducted at a temperature of 650±17°C, the heat being supplied by a Xe lamp. The steam to methane molar ratio in the feed was maintained at 1 to 1 and a Ni/Al_2O_3 catalyst was employed. The catalyst was prepared from $Ni(NO_3)_2 \cdot 6H_2O$ and Al_2O_3 powder. 0.149 g of Al_2O_3 powder was made into a suspension with ~10 ml of water. 1.01 g of the $Ni(NO_3)_2 \cdot 6H_2O$ was dissolved into the suspension, which was then evaporated to dryness at 110°C for 12 hours. The dried powder was then mixed in a mortar and calcined at 750°C for 1 hour before being reduced by H_2 at 450°C for 30 minutes. The reaction took place in a quartz tube, packed with the catalyst.

Product gases were analysed by gas chromatography, using Poropak Q or molecular sieve 13X columns.

The product composition was found to closely match the composition predicted by thermodynamic analysis. It was therefore assumed that the reaction mixture effectively reached equilibrium in the reactor. During the 230 minute study, catalyst deactivation was not found to be a problem. Considering that this experiment uses a very low steam to methane ratio and a relatively low temperature, it is surprising that carbon formation was not more notable.

Catalytic burners

If steam reforming is to be used to produce hydrogen, a source of heat is required. In a fuel cell drive system, this will be provided by burning a small amount of the fuel (either petrol, natural gas or methanol), perhaps mixed with the exhaust from the fuel cell, which may contain some hydrogen. If this mixture is to be burnt completely in air with a minimum of NO_x formation, a homogenous combustion process is not suitable. Instead, catalytic combustion must be used to improve efficiency and reduce emissions. One of the major challenges in coupling an endothermic reaction to an exothermic one is how to control the rate of the reactions so that the heat demands are evenly matched. If this is not achieved, the temperature will either rise or fall. This could slow or stop either one of the reactions, or cause undesirable side reactions, damage to catalysts and fluctuations in the product quality, with subsequent effects on downstream processes. Emmonts (1999) describes the catalytic burners developed at the Research Centre Jülich for both stationary and mobile use. These burners utilise a platinum catalyst on aluminium oxide. This is attached to a wire mesh which surrounds a fibrous support structure. This support structure acts as thermal insulation between the reaction zone and the cold feed gas and equalises the speed or the fuel/air mixture throughout the burner, ensuring uniform combustion. The experimental burner is cooled by a water jacket and a flue gas heat exchanger.

Experiments were carried out using methanol as the main fuel. The following parameters were varied during the experiments:

- air/fuel ratio
- amount of hydrogen in the fuel
- CO_2 contnet in the fuel
- power density (burner load relative to the area of the outer surface of the support structure)
- start-up procedures.

CO emissions were found to be virtually unaffected by CO_2 concentration in the feed, except at very low power density. CO emissions increased with power density. NO_x emissions were very low (0.4 mg/kWh) and were found to be virtually independent of power density or H_2O concentration in the feed.

An alternative design of catalytic burner was described by Höhlein *et al.* (1996). This consisted of a fibrous support structure surrounded by a wire mesh. The catalyst, platinum on an alumina support, was placed on the mesh. Fuel gas and air were supplied through the support structure, which served to even out the gas flow to the catalyst and to prevent the hot reaction zone igniting the gas mixture homogeneously. The experimental burner was cooled by a water jacket and a flue gas heat exchanger in order to determine its heating performance. For use in the vehicle, the burner would have to operate in basically one of two modes. Firstly, at start-up, pure methanol from the fuel tank would have to be used as the burner fuel. Once the rest of the power plant is operating, the methanol would be mixed with retentate from the membrane separation unit and anode off-gas in order to maximise efficiency and minimise emissions.

2.9 Modelling the steam reforming process

2.9.1 Kinetics of reaction

Despite the steam reforming process having been used to produce hydrogen for many years, the kinetics of the process have not always been well understood. According to Xu and Froment (1989a), the industrial process is a large-scale operation carried out in numerous tubular reactors contained within a gas-fired furnace. Temperatures in the tubes reach 675 to 1000 K and pressures are in the region of 30 bar. Because of the cost involved in building and running such a reactor, accurate simulations of the process are very desirable and much research has been done in this area in recent years. This is illustrated by providing an extended discussion of papers published by:

- Xu and Froment (1989a)
- Hou and Hughes (2001)
- Soliman, Adris, Al-Ubaid and El-Nashaie (1992)

Xu and Froment (1989a)

Xu and Froment (1989a) carried out experiments using a $Ni/MgAl_2O_4$-spinel catalyst with the aim of deducing the most likely reaction mechanism and thereby evaluating the intrinsic kinetics of the steam reforming reaction. Their apparatus consisted of a tubular preheater and reactor, made from HK 40 stainless steel of 1.07 cm inside diameter. The reaction zone was 10 cm in length, heated by 2 heaters of 5 cm length each. The reactor contained a central tube of 0.35 cm outside diameter into which a thermocouple could be placed. There were 4 further thermocouples welded to the external reactor wall. The preheating and post reaction sections of the reactor were packed with pure α-alumina spheres. The catalyst bed was also diluted with pure α-alumina spheres. Flows of methane and hydrogen were measured by rotameters and that of carbon dioxide by a mass flow meter. De-ionised water was fed by a volumetric pump. Hydrogen, methane and carbon dioxide were of N40, N35 and N25 purity respectively. Reactor back pressure was regulated by means of a membrane pressure regulator. Effluent analysis was performed

by 2 gas chromatographs (GCs). One of the GCs used a 15 m column packed with Porapak Q and hydrogen as the carrier gas. The other GC, which was used to measure hydrogen concentration, contained a column with 10 m of Porapak Q and 5 m of Porapak N and used nitrogen as the carrier gas.

The catalyst contained 15.2% nickel, had a BET-surface area of 58 m^2 and a nickel surface area of 9.3 m^2/g of catalyst. The void fraction was 0.528. The original ring-shaped catalyst was crushed into particles of 0.18-0.25 mm. It was found that catalyst activity dropped very rapidly during the first 24 hours of use, but thereafter much more gradually. Their kinetic study was started after some 70 hours on stream, by which time the deactivation rate was so slow that only minor corrections to their experimental data were required to take account of it. They suggest that the deactivation could be caused by sintering of the catalyst.

The experimental conditions used are given in Table 2.6. It was found that higher pressures, temperatures and steam to methane molar ratios increased the deactivation rate. In order to limit the reaction rate, to avoid measuring only equilibrium conversions, the temperature range used in their experiments was well below that which is used industrially. Hydrogen was added to the feed stream to avoid re-oxidation of the catalyst by steam. Experiments were carried out using different catalyst sizes to ensure that internal diffusion did not limit the rate of reaction. This objective was met for catalysts particles in the size range 0.17-0.25 mm.

At 10 to 15 bar pressure, the water-gas shift reaction was found to be close to equilibrium. This was not the case at 3 and 5 bar.

Table 2.6 – Comparison of experimental conditions for various steam reforming experiments found in the literature

	Pressure /kPa	Temperature /K	H_2O:CH_4:H_2 molar ratio	H_2/CO_2 molar ratio	Reference
1.	Steam reforming				Xu and Froment (1989a)
	500		5:1:1.25		
	500		3:1:1.25		
	1000	773, 798, 823, 848	3:1:1.25		
	1500		5:1:1.25		
	300		5:1:1.25		
	300		3:1:1.25		
	Reverse of water gas shift				
	800, 1000, 300, 1000	573, 598, 623, 648, 673		1.0, 0.5	
2.	Steam reforming				Hou and Hughes (2001)
	120	748, 773, 798, 823	4.0:1:1		
	120	748, 773, 798, 823	5.5:1:1		
	300	748, 773, 798, 823	5.5:1:1		
	450	798, 823	5.5:1:1		
	600	748, 773, 798, 823	5.5:1:1		
	120	748, 773, 798, 823	7.0:1:1		
	Reverse water gas shift				
	120	598, 623, 648, 673		0.75	
	120	598, 623, 648, 673		0.5	
3.	Steam reforming				Soliman *et al.* (1992)
	100-300	748-823	2.739-5.855:1:0.316-		

Pressure /kPa	Temperature /K	$H_2O:CH_4:H_2$ molar ratio	H_2/CO_2 molar ratio	Reference
Methanation and shift reaction 223-239	598, 623, 648, 673	0.593	0.55-0.971	

Table 2.7 – Comparison of rate equations for steam reforming reactions

	Catalyst Type	Rate Equations	Notes	Reference
1.	$Ni/MgAl_2O_4$ 15.2 % Ni 9.3 $m^2/g_{catalyst}$	Steam Reforming $r_1 = \frac{k_1}{P_{H_2}^{2.5}}\left(P_{CH_4}P_{H_2O} - \frac{P_{H_2}^3 P_{CO}}{K_1}\right)\Big/(DEN)^2$ Water-Gas Shift $r_2 = \frac{k_2}{P_{H_2}}\left(P_{CO}P_{H_2O} - \frac{P_{H_2}P_{CO_2}}{K_2}\right)\Big/(DEN)^2$ Reverse Methanation $r_3 = \frac{k_3}{P_{H_2}^{3.5}}\left(P_{CH_4}P_{H_2O}^2 - \frac{P_{H_2}^4 P_{CO_2}}{K_3}\right)\Big/(DEN)^2$	$DEN = 1 + K_{CO}P_{CO} + K_{H_2}P_{H_2} + K_{CH_4}P_{CH_4} + \frac{K_{H_2O}P_{H_2O}}{P_{H_2}}$	Xu and Froment (1989a)
2.		$r_I = \frac{k_I}{E^2 y_{H_2}^{2.5}\sqrt{P}}\left(y_{CH_4}y_{H_2O} - \frac{P^2 y_{H_2}^3 y_{CO}}{K_I}\right)$ $r_{II} = \frac{k_{II}P}{E^2 y_{H_2}}\left(y_{CO}y_{H_2O} - \frac{y_{H_2}y_{CO_2}}{K_{II}}\right)$ $r_{III} = \frac{k_{III}}{E^2 y_{H_2}^{3.5}\sqrt{P}}\left(y_{CH_4}y_{H_2O}^2 - \frac{y_{H_2}^4 y_{CO_2}}{K_I K_{II}}\right)$	$E = 1 + P\left(K_{CO}y_{CO} + K_{CH_4}y_{CH_4} + K_{H_2}y_{H_2}\right) + K_{H_2O}\frac{y_{H_2O}}{y_{H_2}}$	Rajesh, Gupta, Rangaiah and Ray (2000)
3.	$Ni/\alpha\text{-}Al_2O_3$ 15-17 % Ni	$r_1 = k_1\frac{P_{CH_4}P_{H_2O}^{0.5}}{P_{H_2}^{1.25}}\left(1 - \frac{P_{CO}P_{H_2}^3}{K_{p1}P_{CH_4}P_{H_2O}}\right)\Big/(den)^2$	$den = 1 + K_{CO}P_{CO} + K_H P_H^{0.5} + K_{H_2O}\frac{P_{H_2O}}{P_{H_2}}$	Hou and Hughes (2001)

	Catalyst Type	Rate Equations	Notes	Reference
	14.30 $m^2/g_{catalyst}$	$r_2 = k_2 \frac{P_{CO} P_{H_2O}^{0.5}}{P_{H_2}^{0.5}} \left(1 - \frac{P_{CO_2} P_{H_2}}{K_{p2} P_{CO} P_{H_2O}}\right) \Big/ (\text{den})^2$		
		$r_3 = k_3 \frac{P_{CH_4} P_{H_2O}}{P_{H_2}^{1.75}} \left(1 - \frac{P_{CO_2} P_{H_2}^4}{K_{p3} P_{CH_4} P_{H_2O}^2}\right) \Big/ (\text{den})^2$		
4.	Ni/Ca aluminate spinel	$r_1 = 0$	$\text{DEN} = 1 + K_{CO} P_{CO} + \frac{K_{H_2O} P_{H_2O}}{P_{H_2}}$	Soliman et al. (1992)
		$r_2 = \frac{k_2}{P_{H_2}^{2.5}} \left(P_{CO} P_{H_2O} - \frac{P_{H_2} P_{CO_2}}{K_2}\right) \Big/ (\text{DEN})^2$		
		$r_3 = \frac{k_3}{P_{H_2}^{3.5}} \left(P_{CH_4} P_{H_2O}^2 - \frac{P_{H_2}^4 P_{CO_2}}{K_1 K_2}\right) \Big/ (\text{DEN})^2$		

Thermodynamic analysis led to the conclusion that reaction schemes where all of the CO_2 is generated from CO and where CO and CO_2 are formed directly from CH_4 are not likely. Three rate determining steps were found, which led to the formation of 3 rate equations, which are summarised in Table 2.7.

In order to simulate a real steam reforming reactor, the tortuosity and effectiveness factors of the catalyst must be evaluated. Xu and Froment (1989b) experimentally studied the diffusional limitations in large catalyst particles and related them to the tortuosity factor for the catalyst. This information was then combined with the intrinsic kinetics from Xu and Froment (1989a) to simulate an industrial steam reformer. Tortuosity factors ranging from 1.5 up to 10 or more were found to have been reported elsewhere. Since the range of factors is so large, the authors measured the tortuosity factor of the catalyst which they were considering. In order to do this, the intrinsic kinetics and the diffusion aspects were combined to simulate the reactor. The calculated results were then fitted to the experimental results, allowing the tortuosity factor to be evaluated. A value of τ of 3.54 was obtained. This allowed an industrial scale reformer to be simulated.

Hou and Hughes (2001)

Hou and Hughes (2001) carried out similar experiments to Xu and Froment (1989a) using ICI catalyst 54-7, which is a Ni/α-Al_2O catalyst. Kinetic rate equations were developed using the Lanmuir-Hinshelwood-Hougen-Watson approach and Freundlich's adsorption concept.

The equipment used was similar to that used by Xu and Froment (1989a), although the reactor was somewhat larger, being 338 mm in length and 1 cm inside diameter. The evaporator/preheater took the form of a side arm, 215 mm in length. All of the gas flows were controlled by mass flow controllers, which should be more accurate than rotameters. A 2 mm outside diameter thermocouple well was placed along the axis of the reactor. Gas analysis also differed from the method of Xu and Froment (1989a). A GC with a 2 m long column packed with 5 Å molecular sieve was used to detect methane and CO_2. An infra red gas analyser was used to detect CO. The concentration of hydrogen in the effluent and the amount of H_2O consumed were determined by a hydrogen balance and an oxygen balance respectively. Overall carbon balances were better than 95%. Helium was used as the carrier gas in the GC.

Their experiments were designed to minimise the effects of diffusion limitation. This was achieved by crushing the catalyst particles to smaller sizes until no change in activity was observed for identical operating conditions. It was concluded that, for particle diameters of less than 0.15 mm, the reactions were not diffusion limited. By analysing the difference in temperature and concentration between the fluid and solid phases, they were also able to discount the affects of heat and mass transfer.

For the steam reforming reaction, 0.3 g of crushed catalyst were loaded. For the reverse water gas shift reaction, 0.1 g of catalyst were loaded. Once loaded, the catalyst had to be reduced. This was achieved using the following procedure:

- the catalyst was heated to 673 K at 3 K/min in nitrogen and maintained at this temperature for 1 hour;
- the catalyst was sustained at the same temperature for 2 hours in hydrogen, before being heated to 873 K at 2.5 K/min and kept at this temperature for a further hour in hydrogen;
- the temperature was decreased to the required operating temperature in a stream of hydrogen.

It was found that, for a steam:methane ratio of 3:1, catalyst activity decreased rapidly. It was confirmed that deactivation was caused by carbon deposition. It was considered that the small particle size chosen may have accelerated the carbon formation. This conclusion was supported by the previous work of Blue, Holm, Regier, Fast and Heckelburg (1952). However, this research into the effect of granule size was not based on steam reforming, but dehydrogenation of butane and hydrogen transfer. Thus, conditions and the catalyst used were different to the work of Hou and Hughes (2001) and may not be relevant. Nevertheless, a method of reducing carbon formation was sought. A thermodynamic analysis showed that the carbon formation was mainly due to methane decomposition. To inhibit this reaction, hydrogen, one of the products, was added in the feed. It was found that an equimolar ratio of hydrogen and methane in the feed was acceptable, allowing the other reaction parameters to be varied over relatively wide ranges. Using the hydrogen in the feed reduced the deactivation of the hydrogen so that, after 250 minutes only minor corrections would be needed to account for it. It could be possible that the rapid

deactivation of the catalyst when no hydrogen was present in the feed could be due to re-oxidation of the catalyst, rather than carbon formation. Hydrogen in the feed would also prevent this from occurring. This is the reason cited by other sources (*e.g.* Xu and Froment (1989a)) for adding hydrogen to the feed stream.

Reactions were carried out during times from 270-450 minutes on stream for the steam reforming. The water gas shift experiments were carried out at a lower temperature and deactivation was not such a problem, so data were collected from 200-400 minutes on stream.

It was found that there is a positive effect of temperature on methane conversion and this effect is augmented as temperature increases. When methane conversion is low, methane conversion is almost proportional to contact time at a constant steam:methane ratio. Methane steam reforming is sensitive to pressure. High pressure enhances both the forward and backward reaction rates, the backward one being enhanced more. However, Hou and Hughes (2001) found that there was a positive effect of pressure on methane conversion. They state that this is due to the low temperatures and consequently low product concentrations obtained in their experiments. At these temperatures, the forward reaction rate is more sensitive to pressure than the backward rate.

CO_2 selectivity was found to decrease almost linearly with increasing CH_4 conversion at a constant steam:methane ratio. Also, selectivity dropped as temperature increased. These observations were explained by CO and CO_2 both being primary product of reactions taking place, with temperature affecting the different reactions by different amounts. High concentrations of steam were found to increase CO_2 selectivity. This is due to inhibition of the reverse water gas shift reaction and promotion of reactions which for CO_2 directly from CH_4. Pressure was not found to affect CO_2 selectivity.

During methane steam reforming at high temperature, the water gas shift reaction is essentially at equilibrium (Soliman, Adris, Al-Ubaid and El-Nashaie, 1992). Therefore Hou and Hughes (2001) carried out their reverse water gas shift experiments at low temperatures in order to obtain more accurate kinetic parameters.

Increasing the steam:methane ratio was found to reduce the rate of methane disappearance. This effect was increased at higher temperatures. The reason for this is

that the increase in steam concentration reduces the partial pressure of methane, with methane disappearance rate being first order with respect to methane concentration. Also, high steam concentration inhibits the adsorption of methane onto the catalyst surface. Increased temperature favours water vapour adsorption, thus increasing this inhibition.

The kinetic rate equations obtained are given in Table 2.7 while the experimental conditions are shown in Table 2.6.

Soliman* et al. *(1992)

The kinetics of methane steam reforming have also been studied for a Ni/Ca aluminate spinel catalyst (Soliman *et al.*, 1992). This catalyst was produced by the authors in their lab. In this study, it was noted that there is a contradiction in the literature over the dependence of the rate of reaction upon steam partial pressure. In some instances, dependence was of positive order (acidic supports, *e.g.* Y-zeolite, Ni aluminate) and others negative order (less acidic supports, *e.g.* calcium aluminate).

This study used mass flow controllers to control the input flow rates. These were protected from pressure pulses by the dual-stage regulators fitted to the supply cylinders. The catalyst tube was smaller than that used by other researchers, being ¼" internal diameter. It was 12" long and heated by a furnace with 3 independently temperature controlled zones. Water was supplied by metering pump. Preheating was achieved by placing the entire apparatus (apart from control and analysis equipment) inside an enclosure that could be heated to 250°C. Feed gases flowed through coils within the enclosure before being fed to the reactor, also within the enclosure. Analysis was by GC. Hydrogen was separated from the other gases by means of a palladium tube, through which the hydrogen could permeate. It was then detected by a thermal conductivity detector (TCD) using N_2 as the carrier gas. The other gases were detected by a TCD using He carrier gas. The GC was equipped with 3 columns to perform the separation:

A 3' molecular sieve, 5 Å
B 9' Porapak Q + 5' Chromasorb 104
C 9' Porapak Q + 5' Chromasorb 104

It is claimed that this gives very good separation, although the results of the mole balance performed to verify this are not given.

It was found that the reaction step of water vapour adsorption was significant in the kinetics of the reaction with this catalyst. This is in contrast to studies by Xu and Froment (1989a) and Hou and Hughes (2001). The presence of Ca in the catalyst formulation could be the cause of this. As a result, the rate equations (shown in Table) are quite different to those of other studies. It was concluded that changing the catalyst composition clearly changes, not only the kinetic parameters of the kinetic model, but the structure of the model itself. Therefore, a different model must be developed for each different catalyst structure.

2.9.2 Reactor modelling

Several authors have used the kinetic data given in the literature to model the steam reforming process. Two such papers have been selected for this review:

- Numaguchi and Kikuchi (1988)
- Avcı, Trimm and İlsen Önsan (2001)

Numaguchi and Kikuchi (1988)

An attempt to quantify the importance of using intrinsic rather than apparent kinetics to model the steam methane reformer was made by Numaguchi and Kikuchi (1988). It was noted that, in order to design a compact reformer, the catalyst volume and heating section must be minimised. The required volume of catalyst calculated by using intrinsic vs. that using apparent kinetics was investigated. Only 5 experimental runs were made, so it is probably unsafe to place a great deal of trust in the conclusions of this study. The trends found may be of interest, however. The conclusion is that, at high inlet temperatures, or high steam to carbon ratios, the reactor may be over designed if the effects of diffusion are not considered.

Avcı* et al., *(2001)

Avcı *et al.*, (2001) have modelled autothermal steam reformers and compared the results with those of bench-scale experiments. Their reactor used Pt/δ-Al_2O_3 to catalyse the combustion of methane and Ni/MgO-Al_2O_3 to catalyse the steam reforming reactions. A one-dimensional heterogeneous reactor model was used. The reactions considered in the model were combustion of methane, steam reforming of methane, water gas shift, reverse methanation and methane cracking. Rate expressions from Ma and Trimm were used for the combustion and steam reforming reactions. For the water gas shift and reverse methanation reactions, the rate equations were taken from Xu and Froment (1989a), despite the fact that these equations were derived for a Ni/$MgAl_2O_4$ catalyst. By comparing the work of Xu and Froment (1989a) with that of Hou and Hughes (2001), it can be seen that changing the catalyst support can have a significant effect on the rate expression required. Therefore, the model of Avcı *et al.* (2001) may be flawed.

There were two alternative configurations for the reactor. In the first, the combustion catalyst was placed upstream of the reforming catalyst, so the combustion reaction occurred first, followed by steam reforming. In the second configuration, the catalysts were mixed uniformly in the same part of the reactor, so that all reactions occurred simultaneously. Initially, a bench-scale reactor was simulated, so that the results could be compared with those of an actual bench scale experiment, conducted by Ma and Trimm (1996). After that, an industrial scale reactor was simulated. For the purposes of this study on micro reactors, the bench-scale results are the most relevant.

The bench-scale experiments with a dual, sequential bed reactor were conducted with an initial feed temperature of 640-665 K and 2.5 atm pressure. The experiments with a mixed-bed reactor were carried out at an initial feed temperature of 800 K and 2.9 atm pressure. The maximum temperature was found to vary with differing inlet composition. The main trends seen in the results of the simulation agree with those found in the experimental results. These trends are:

- At constant steam to methane ratio, a decrease in the methane to oxygen ratio in the feed results in greater hydrogen yield and elevated maximum bed temperature.
- At a constant methane to oxygen ratio, an increase in the steam to methane ratio reduces the maximum temperature of the bed and increases the hydrogen yield.

The predicted maximum bed temperature agrees fairly well with experimental results, but the model over-predicts the hydrogen and CO yields. The model also appears to predict that the steam reforming reaction is inhibited by excess steam, something which is not found experimentally. The authors suggest that inclusion of the following side reaction in the model may improve it:

$$CO + H_2 \Leftrightarrow C + H_2O$$

The methane to oxygen ratios used in the dual-bed scheme experiments are different from those used in the mixed-bed scheme experiments, so it is hard to draw any conclusions about which is the superior technology. The yield of hydrogen was found to be greater in the mixed-bed scheme. It was argued that improved heat and mass transfer in the mixed-bed scheme would explain the improved hydrogen yield.

2.10 Conclusions

2.10.1 Requirements of the hydrogen market

There is at present only a small market for hydrogen as a transportation fuel, but that situation is set to change. Research into hydrogen fuelled vehicles has been extensive in recent years and many manufacturers have prototype vehicles running. The PEM fuel cell is a popular technology for hydrogen power. A PEM fuel cell requires a source of hydrogen and a source of oxygen in order to operate. Air is a suitable source of oxygen, since the fuel cell is not affected adversely by nitrogen or carbon dioxide. The hydrogen source may also contain carbon dioxide or hydrocarbon impurities, but there must be <10 ppm of carbon monoxide present in order to prevent damage to the fuel cell.

2.10.2 Existing hydrogen production

There are many different ways of generating hydrogen, but none of the established processes are ideal for an automotive or small-scale stationary application. There are several issues which must be taken into account when choosing a production technology, including process efficiency and hydrogen storage.

Of all the current hydrogen production processes, the longest established and most efficient is the steam reforming of methane. Steam reforming of methane is by far the most efficient current process for producing hydrogen, in terms of both energy and exergy recovered in the hydrogen (Rosen, 1996). Typically, the industrial process produces a product gas at around 1000-1200 K and at a pressure of 15-30 bar. The capacity of an industrial reformer is typically around 500 Nm^3/h of hydrogen. As a small scale hydrogen generation process, this has the potential advantage of using natural gas as a feedstock. Natural gas already has a fully developed supply infrastructure. There are some disadvantages to the industrial system when applied to a compact situation however. Firstly, due to the high pressure nature of the established process, equipment costs are high. Also, part of the current process uses high temperature homogeneous combustion to supply heat to the endothermic reforming reaction. This results in the formation of nitrogen oxides which have to be cleaned from the stack gas. Finally, the industrial

process can use large quantities of very high temperature steam and still be run efficiently, since excess steam will be used on other parts of the plant. This option is not available to a compact system, which must utilise its heat very efficiently. Therefore, a novel system must be developed to solve these issues, whilst maintaining the fundamental high efficiency of the steam reforming process.

2.10.3 Hydrogen purification

In order to meet the specifications of the PEM fuel cell, the hydrogen product must be purged of carbon monoxide. A suitable technology for achieving this is pressure swing adsorption (PSA). Impurities are adsorbed from the product stream at elevated pressure. Once the adsorbent is saturated, it is regenerated by flushing with an inert gas at a lower pressure.

2.10.4 Compact steam reformers

Work is progressing in this area and several of the concepts under investigation in the literature couple catalytic combustion with steam reforming. This offers the potential of an efficient, compact system which produces no nitrogen oxides due to the absence of a homogeneous flame.

Current research into compact reformers is looking at applications ranging from portable electric device power, with an output of 0.1-1 kW, to car power plants with an capacity of 50-100 kW. The scale of this micro reactor research may be too small for the applications emerging in the marketplace. Stationary generation for the fuel supply or small feedstock supply markets would have to have a capacity of around 2.7 tonnes/day to serve up to 500 cars/day (Moore and Raman, 1998).

2.10.5 Choice of catalyst

The chosen steam reforming catalyst is a nickel on alumina system. The kinetics of the reaction on Ni-Al_2O have been extensively investigated in the literature, particularly by Hou and Hughes (2001) and it is a current industrial catalyst. The catalyst used by Hou

and Hughes (2001) (ICI Katalco catalyst 57-4) is a nickel catalyst supported on calcium aluminate ceramic.

2.10.6 Kinetics of reaction

The reaction system is quite complex, with many thermodynamically feasible reactions potentially occurring in parallel. The most important reactions for the kinetics of the system are the steam reforming, the water gas shift and the reverse methanation reactions. Thus, the system may be described by three rate equations, which must be solved in parallel.

2.10.7 Operation of catalyst

Before the catalyst can be used for reforming, it must be pre-conditioned. This is to reduce the NiO surface of the catalyst and make it active. To do this, the catalyst is purged of oxygen while the temperature is raised, before having hydrogen passed over it until the exit gas reaches operating temperature. The maximum rate of temperature change during start up is 150-170°C per hour.

In order to prevent carbon formation on the catalyst, an excess of steam is used in industrial reformers. During their experiments, Hou and Hughes (2001) found that small sized catalyst particles suffered deactivation due to carbon formation on their interior. To combat this, they introduced hydrogen to the feed, giving a feed composition of 5.5:1:1 molar ratio of steam:methane:hydrogen. Rajesh *et al.*(2000) also use a hydrogen recycle in their reformer model, in this case in order to prevent the catalyst oxidising in the first part of the reformer.

It was found that intra-particle diffusion and film resistance to mass transfer were negligible for particles of 0.15 mm diameter or less. This means that, effectively, the entire active surface of the catalyst is exposed to the exterior gas concentrations. Therefore, for particles in that size range, the internal effectiveness factor is likely to be around 1, since heat transfer effects will likely be negligible as well for particles in this size range.

Chapter 3 - Simulation of steam reforming reactions

3.1 Introduction

Steam reforming reactions were investigated with the aim of developing a novel solution to the requirement for compact hydrogen production systems. Before experimental work could take place, a thorough understanding of the fundamental thermodynamics and kinetics of a steam reforming reactor were required. For this reason, various scenarios were simulated on computer and a manual check was made of the thermodynamic equilibrium calculations.

3.2 Aspen Plus

AspenTech Aspen Plus® is a commercial software tool intended for design, steady-state modelling and optimisation of petrochemicals, chemicals and speciality chemicals processes. It uses mass and energy balances, phase and chemical equilibrium and reaction kinetics to simulate plant behaviour, when supplied with reliable thermodynamic data and realistic operating conditions. A large database of thermodynamic data is supplied with the system.

3.3 Manual calculation of the equilibrium composition

3.3.1 Aim of the calculation

As with any modelling system, the data produced are only as good as the data supplied, including the thermodynamic data. In order to have maximum confidence in the model, it was necessary to manually verify that the equilibrium results are correct. The primary purpose in carrying out these calculations is to provide a check of both the output from Aspen and other published sources of thermodynamic data. This will allow a more accurate appraisal of experimental reactor performance. They will also allow evaluation

of the time taken to reach equilibrium, which is a starting point for designing the experiments.

3.3.2 Methods of determining equilibrium composition

Calculation of the composition of a gas mixture at equilibrium involves determining the composition that minimises the Gibbs free energy of the system. Two methods of doing this are described in Smith *et al.* (1996). One is based on the method of Lagrange's undetermined multipliers and requires the simultaneous solution of a set of equations, with one equation for each component in the system (*e.g.* methane, steam *etc.*), and one equation for each element (*e.g.* carbon, oxygen, hydrogen). The other method involves calculating equilibrium constants for characteristic reactions that describe the system. This method requires the simultaneous solution of a smaller set of equations – one for each independent reaction required to describe the system. For this reason, the second method was chosen, since this would facilitate solution by spreadsheet.

3.3.3 Assumptions

In analysing the thermodynamics of the system, a number of assumptions have been made in order to simplify the calculations. The main assumption is that all of the gases present in the reactor behave as an ideal gas. This assumption is reasonable, as the compressibility factor for the steam/methane mixture is approximately 0.99 at 500°C and 9.5 bar g with a steam to methane ratio of 4.

3.3.4 Reactions to describe the system

To simplify the analysis, it is assumed that no solid carbon is present in the reacting mixture. This is a reasonable assumption at this stage, since the purpose of carrying out these calculations is to verify the validity of the model used by Aspen. Later calculations carried out by Aspen can be modified to include solid carbon. It is assumed that the chemical species present in the reacting mixture are CH_4, H_2O, CO, CO_2 and H_2.

The **formation reactions** for these species are:

$$C + \tfrac{1}{2}O_2 \rightarrow CO \quad (3.1)$$

$$C + 2H_2 \rightarrow CH_4 \quad (3.2)$$

$$H_2 + \tfrac{1}{2}O_2 \rightarrow H_2O \quad (3.3)$$

$$C + O_2 \rightarrow CO_2 \quad (3.4)$$

These reactions may be combined to eliminate the elements that are assumed to be not present in the reaction mixture, C and O_2. Combining Reaction (3.1) with Reaction (3.2) and with Reaction (3.4) eliminates C and results in:

$$CH_4 + \tfrac{1}{2}O_2 \rightarrow CO + 2H_2 \quad (3.5)$$

$$CO + \tfrac{1}{2}O_2 \rightarrow CO_2 \quad (3.6)$$

Now, combining Reaction (3.3) with Reactions (3.5) and (3.6) eliminates O_2 and gives two independent reactions:

$$CH_4 + H_2O \Leftrightarrow CO + 3H_2 \quad (3.7)$$

$$CO + H_2O \Leftrightarrow CO_2 + H_2 \quad (3.8)$$

These two reactions are perfectly adequate to completely describe the reacting system for the purpose of material balance and equilibrium calculations. In reality, many different reactions may be taking place and these would have to be taken into account during an analysis of the kinetics of the system, but the net material balance is described by these two reactions. Reaction (3.7) is known as the steam reforming reaction, while Reaction (3.8) is called the water-gas shift reaction.

3.3.5 Thermodynamic data

Thermodynamic data were taken from ICI catalyst information, Hou and Hughes (2001), Smith, Van Ness and Abbott (1996), Hayes & Kolaczkowski (1997) and the JANAF tables. ICI and Hou and Hughes (2001) give an equation for calculating equilibrium constant. In the case of the other sources, the equilibrium constant was calculated from

specific heat capacity data and standard enthalpy and Gibbs energy change of formation data.

3.3.6 Determining the equilibrium constant for the steam reforming reaction

For each reaction, the value of the thermodynamic equilibrium constant, K, is dependent on the standard free energy change of reaction, which is the difference between the Gibbs free energy of the products and the reactants, with each in their standard states. K is therefore a function of temperature, but not of pressure. The relationship between K and temperature is given by:

$$\ln K = -\frac{\Delta G_R^\circ}{RT} \tag{3.1}$$

The value of ΔG_R° may be calculated from standard free energies of formation data, which are available in the literature for 1 bar and 298.15 K (or 1 atm and 298.15 K in some older sources). If the stoichiometric coefficients α_i are defined as positive for both reactants and products, the general equation normalised for species k is:

$$\Delta G_{R,298}^\circ = \frac{1}{\alpha_k}\left[\sum_{\text{products}} \alpha_i \Delta G_{f,298}^\circ - \sum_{\text{reactants}} \alpha_i \Delta G_{f,298}^\circ\right] \tag{3.2}$$

Thus, for the steam reforming reaction (Reaction (3.7)) at 298.15 K, normalised for CH_4 (data obtained from Smith *et al.*, 1996):

$$\begin{aligned}\Delta G_{R,298}^\circ &= \frac{1}{1}\left[\left(\Delta G_{f,298\,\mathrm{CO}}^\circ\right) + 3\left(\Delta G_{f,298\,\mathrm{H_2}}^\circ\right) - \left(\Delta G_{f,298\,\mathrm{CH_4}}^\circ\right) - \left(\Delta G_{f,298\,\mathrm{H_2O}}^\circ\right)\right] \\ &= [(-137.169) + 3(0) - (-50.46) - (-228.572)] \\ &= 141.863 \text{ kJ/mol}\end{aligned}$$

Therefore, the equilibrium constant at 298.15 K is given by:

$$\ln K_{298} = -\frac{\Delta G^{\circ}_{R,298}}{RT}$$
$$= -\frac{141.863 \times 1000}{8.314 \times 298.15}$$
$$= -57.230$$

Using the van't Hoff equation to calculate K

In order to compute K at other temperatures, one may use the van't Hoff equation:

$$\frac{d \ln K}{dT} = \frac{\Delta H^{\circ}_{R}}{RT^2} \tag{3.3}$$

ΔH°_{R} is the enthalpy change of reaction. Integrating Equation (3.3) gives:

$$\ln\left(\frac{K_T}{K_{298}}\right) = \int_{298.15}^{T} \frac{\Delta H^{\circ}_{R}}{RT^2} dT \tag{3.4}$$

In order to solve (3.4), it is necessary to know ΔH°_{R} as a function of temperature. The enthalpy change of reaction at 298.15 K, $\Delta H^{\circ}_{R,298}$ is the difference between the standard enthalpy changes of formation of the products and the reactants, normalised in terms of species k:

$$\Delta H^{\circ}_{R,298} = \frac{1}{\alpha_k}\left[\sum_{\text{products}} \alpha_i \Delta H^{\circ}_{f,298} - \sum_{\text{reactants}} \alpha_i \Delta H^{\circ}_{f,298}\right] \tag{3.5}$$

So, for the steam reforming reaction, normalised in terms of CH_4 (data obtained from Smith *et al.*, 1996):

$$\begin{aligned}\Delta H^{\circ}_{R,298} &= \frac{1}{1}\left[\left(\Delta H^{\circ}_{f,298\,CO}\right)+3\left(\Delta H^{\circ}_{f,298\,H_2}\right)-\left(\Delta H^{\circ}_{f,298\,CH_4}\right)-\left(\Delta H^{\circ}_{f,298\,H_2O}\right)\right] \\ &= [(-110.525)+3(0)-(-74.52)-(-241.818)] \\ &= 205.813 \text{ kJ/mol} \\ &= 2.058\times10^{5} \text{ J/mol}\end{aligned}$$

To calculate the enthalpy change of reaction at a temperature, T, it is necessary to add on the difference between the energy that would be required to heat the products from 298.15 K to T and the energy that would be released by cooling the reactants from T to 298.15 K. This difference in energy may be calculated from the specific heat capacities of the various species, Cp_i, therefore:

$$\Delta H^{\circ}_{R,T} = \Delta H^{\circ}_{R,298} + \frac{1}{\alpha_k}\left[\int_{298.15}^{T}\left(\sum_{\text{products}}\alpha_i Cp - \sum_{\text{reactants}}\alpha_i Cp\right)dT\right] \tag{3.6}$$

The bracketed expression in Equation (3.6) may be written:

$$\left(\sum_{\text{products}}\alpha_i Cp - \sum_{\text{reactants}}\alpha_i Cp\right) = \Delta Cp \tag{3.7}$$

In many cases, specific heat capacity is given as a function of temperature, such as:

$$\frac{Cp_i}{R} = A_i + B_i T + C_i T^2 + \frac{D_i}{T^2}$$

It follows that:

$$\frac{\Delta Cp}{R} = \Delta A + \Delta B T + \Delta C T^2 + \frac{\Delta D}{T^2} \tag{3.8}$$

where the coefficients, Δi are given by

$$\Delta i = \left(\sum_{\text{products}} \alpha_i i_i - \sum_{\text{reactants}} \alpha_i i_i \right) \tag{3.9}$$

For the steam reforming reaction (*Cp* data obtained from Smith *et al.*, 1996) the coefficients are calculated as follows:

$$\begin{aligned}
\Delta A &= \left(\sum_{\text{products}} \alpha_i A_i - \sum_{\text{reactants}} \alpha_i A_i \right) \\
&= (\alpha_{CO} A_{CO}) + (\alpha_{H_2} A_{H_2}) - (\alpha_{CH_4} A_{CH_4}) - (\alpha_{H_2O} A_{H_2O}) \\
&= (3.376) + (3 \times 3.249) - (1.702) - (3.47) \\
&= 7.951
\end{aligned}$$

$$\Delta B = -8.71 \times 10^{-3}$$

$$\Delta C = 2.164 \times 10^{-6}$$

$$\Delta D = 9700$$

Therefore, substituting the coefficients into Equation (3.8) gives:

$$\frac{\Delta Cp}{R} = 7.951 - 8.71 \times 10^{-3} T - 2.164 \times 10^{-6} T^2 + \frac{9700}{T^2} \tag{3.10}$$

Substituting Equation (3.10) into Equation (3.6) and integrating gives:

$$\Delta H^{\circ}_{R,T} = \Delta H^{\circ}_{R,298} + \frac{R}{1} \left[\int_{298.15}^{T} \left(7.951 - 8.71 \times 10^{-3} T - 2.164 \times 10^{-6} T^2 + \frac{9700}{T^2} \right) dT \right]$$

$$\Delta H^{\circ}_{R,T} = 189.4 + 6.61 \times 10^{-2} T - 3.62 \times 10^{-5} T^2 + 6.00 \times 10^{-9} T^3 - 80.65/T \text{ kJ/mol} \tag{3.11}$$

Now Equation (3.11) can be substituted into Equation (3.4), which may then be integrated.

Therefore, for the steam reforming reaction:

$$\ln\left(\frac{K_T}{K_{298}}\right) = \int_{298.15}^{T} \frac{\Delta H^{\circ}_{R,T}}{RT^2} dT$$
$$= \int_{298.15}^{T} \frac{1}{0.008314T^2} \begin{pmatrix} 189.4 + 6.61\times10^{-2}T - 3.62\times10^{-5}T^2 \\ + 6.00\times10^{-9}T^3 - 80.65/T \end{pmatrix} dT$$

Therefore:

$$\ln K_T = -24.9 - 2.278\times10^4 T^{-1} + 7.951\ln T - 3.354\times10^{-3}T + 3.607\times10^{-7}T^2 + 4.850\times10^3 T^{-2} \quad (3.12)$$

So, for example, at a temperature of 700 °C (973.15 K) the equilibrium constant can be computed thus:

$$\ln K_{1073} = 2.504$$
$$K_{1073} = e^{2.504}$$
$$= 12.23$$

Using the standard enthalpy and entropy changes of reaction to calculate K

An alternative way to calculate the standard change of Gibbs free energy is from the standard enthalpy change, ΔH° and standard entropy change, ΔS° using the following expression:

$$\Delta G^{\circ} = \Delta H^{\circ} - T\Delta S^{\circ} \quad (3.13)$$

Substituting this into Equation (3.1) gives:

$$-\ln K = \frac{\Delta G^{\circ}}{RT} = \frac{\Delta H^{\circ}}{RT} - \frac{\Delta S^{\circ}}{R} \quad (3.14)$$

In an expression similar to Equation (3.6), $\Delta H^{\circ}_{R,T}$ can be calculated from $\Delta H^{\circ}_{R,298}$ and ΔCp:

$$\Delta H^{\circ}_{R,T} = \Delta H^{\circ}_{R,298} + R \int_{298.15}^{T} \frac{\Delta Cp}{R} dT \tag{3.15}$$

$\Delta S^{\circ}_{R,T}$ may be calculated in the same way:

$$\Delta S^{\circ}_{R,T} = \Delta S^{\circ}_{R,298} + R \int_{298.15}^{T} \frac{\Delta Cp}{R} \frac{dT}{T} \tag{3.16}$$

Substituting Equations (3.15) and (3.16) into Equation (3.14) gives:

$$-\ln K_T = \frac{\Delta G^{\circ}_{R,T}}{RT} = \frac{\Delta H^{\circ}_{R,298}}{RT} + \frac{1}{T} \int_{298.15}^{T} \frac{\Delta Cp^{\circ}}{R} dT - \frac{\Delta S^{\circ}_{R,298}}{R} - \int_{298.15}^{T} \frac{\Delta Cp^{\circ}}{R} \frac{dT}{T} \tag{3.17}$$

The entropy change of reaction at 298.15 K and 1 bar can be calculated from Equation (3.13):

$$\Delta S^{\circ}_{R,298} = \frac{\Delta H^{\circ}_{R,298} - \Delta G^{\circ}_{R,298}}{298.15} \tag{3.18}$$

Substituting Equation (3.18) into Equation (3.17) gives:

$$-\ln K_T = \frac{\Delta G^{\circ}_{R,T}}{RT} = \frac{\Delta H^{\circ}_{R,298}}{RT} + \frac{\Delta G^{\circ}_{R,298} - \Delta H^{\circ}_{R,298}}{298.15R} + \frac{1}{T} \int_{298.15}^{T} \frac{\Delta Cp^{\circ}}{R} dT - \int_{298.15}^{T} \frac{\Delta Cp^{\circ}}{R} \frac{dT}{T} \tag{3.19}$$

This is equivalent to Equation (3.4).

3.3.7 Determining K for the water-gas shift reaction

The method used to calculate K for Reaction (3.8), the water-gas shift reaction, is the same as that used to calculate K for the steam reforming reaction.

Using data from Smith *et al.* (1996) and a temperature of 1073.15 K,

$$\ln K_{1073} = 0.495$$
$$K_{1073} = e^{0.495}$$
$$= 1.640$$

Once a value of K is obtained for both reactions at the desired reaction temperature, the equilibrium composition of the product may be calculated.

3.3.8 Calculating the composition at equilibrium

The equilibrium constant for the steam reforming reaction is related to the activity coefficients of the various components involved in the reaction by:

$$K = \frac{a_{CO} a_{H_2}^3}{a_{CH_4} a_{H_2O}} \tag{3.20}$$

where K is the equilibrium constant for the reaction and a_i is the activity for component i. The activity of a component for a gas phase reaction is defined as the ratio of its fugacity in the mixture, $\bar{f}_i$, to its fugacity in the standard state, f_i°. The fugacity of a component in the mixture can be expressed in terms of the total pressure, P, the mole fraction of the component, y_i and a fugacity coefficient, ϕ_i. Thus, for methane:

$$a_{CH_4} = \frac{\bar{f}_{CH_4}}{f_{CH_4}^\circ} = \frac{y_{CH_4} \phi_{CH_4} P}{f_{CH_4}^\circ} \tag{3.21}$$

For an ideal gas, the fugacity coefficient, ϕ_i = 1. The standard state fugacity of any gaseous species, f_i° = 1 bar (Smith *et al.*, 1996). The activity for a component, a_i is a

ratio of fugacities and is, therefore, dimensionless. This means that overall pressure, P, must be expressed in the same units as the standard state pressure in order for the units to cancel. Inserting Equation (3.21) for each component into Equation (3.20) gives the following, for an ideal gas:

$$K = \frac{y_{CO} y_{H_2}^3}{y_{CH_4} y_{H_2O}} \times \frac{P^{(1+3-1-1)}}{(1\ \text{bar})^{(1+3-1-1)}}$$

$$K = \frac{y_{CO} y_{H_2}^3}{y_{CH_4} y_{H_2O}} \times \frac{P^2}{(1\ \text{bar})^2} \tag{3.22}$$

For CH_4, the mole fraction at equilibrium, y_{CH_4} is defined as the number of moles of CH_4 present at equilibrium, n_{CH_4} divided by the total number of moles present at equilibrium, n_{TOTAL}:

$$y_{CH_4} = \frac{n_{CH_4}}{n_{TOTAL}} \tag{3.23}$$

The number of moles of CH_4 present at equilibrium can be calculated from the initial number of moles, n_{oCH_4} the molar extent of reaction, ε_1, and the reaction stoichiometry:

$$n_{CH_4} = n_{0,CH_4} - \varepsilon_1 \tag{3.24}$$

Similar expressions can be derived for the other components:

$$n_{H_2O} = n_{0,H_2O} - \varepsilon_1 - \varepsilon_2$$

$$n_{CO} = n_{0,CO} + \varepsilon_1 - \varepsilon_2$$

$$n_{CO_2} = n_{0,CO_2} + \varepsilon_2$$

$$n_{H_2} = n_{0,H_2} + 3\varepsilon_1 + \varepsilon_2$$

Substituting Equation (3.24) into Equation (3.23) gives:

$$y_{CH_4} = \frac{n_{0,CH_4} - \varepsilon_1}{n_{TOTAL}} \tag{3.25}$$

A similar expression to Equation (3.25) can be derived for each component. Where the component is involved in Reaction (3.8), the water-gas shift reaction, its mole fraction will be a function of the molar extent of Reaction (3.8), ε_2. These expressions may be substituted into Equation (3.22) to give the following equation:

$$K_1 = \left(\frac{\left(\frac{n_{0,CO} + \varepsilon_1 - \varepsilon_2}{n_{TOTAL}} \right) \left(\frac{n_{0,H_2} + 3\varepsilon_1 + \varepsilon_2}{n_{TOTAL}} \right)^3}{\left(\frac{n_{0,CH_4} - \varepsilon_1}{n_{TOTAL}} \right) \left(\frac{n_{0,H_2O} - \varepsilon_1 - \varepsilon_2}{n_{TOTAL}} \right)} \right) \times \frac{P^2}{(1\ \text{bar})^2} \tag{3.26}$$

A similar expression may be derived for the water-gas shift reaction:

$$K_2 = \left(\frac{\left(\frac{n_{0,CO_2} + \varepsilon_2}{n_{TOTAL}} \right) \left(\frac{n_{0,H_2} + 3\varepsilon_1 + \varepsilon_2}{n_{TOTAL}} \right)}{\left(\frac{n_{0,CO} + \varepsilon_1 - \varepsilon_2}{n_{TOTAL}} \right) \left(\frac{n_{0,H_2O} - \varepsilon_1 - \varepsilon_2}{n_{TOTAL}} \right)} \right) \tag{3.27}$$

The total number of moles present at equilibrium, n_{TOTAL} may be calculated from the initial number of moles of each component and the equilibrium conversion in the following manner:

$$\begin{aligned} n_{TOTAL} &= \sum n_i \\ &= n_{0,CH_4} - \varepsilon_1 + n_{0,H_2O} - \varepsilon_1 - \varepsilon_2 + n_{0,CO} + \varepsilon_1 - \varepsilon_2 + n_{0,CO_2} + \varepsilon_2 \\ &\quad + n_{oH_2} + 3\varepsilon_1 + \varepsilon_2 \end{aligned}$$

$$n_{TOTAL} = 2\varepsilon_1 + \sum n_{0,i} \tag{3.28}$$

Now, given the initial number of moles of each compound, the two equilibrium constants and the reaction pressure, Equations (3.26) and (3.27) may be solved simultaneously for ε_1 and ε_2.

The solution was performed using Newton's method. Equations (3.26) and (3.27) are re-arranged to equate to zero and then differentiated numerically with a very small step size. The partial derivatives are then used in:

$$f_1 + \left(\frac{\partial f_1}{\partial X_1}\right)\Delta X_1 + \left(\frac{\partial f_1}{\partial X_2}\right)\Delta X_2 = 0$$

$$f_2 + \left(\frac{\partial f_2}{\partial X_1}\right)\Delta X_1 + \left(\frac{\partial f_2}{\partial X_2}\right)\Delta X_2 = 0$$

In this case, $X_1 = \varepsilon_1$ and $X_2 = \varepsilon_2$, while f_1 and f_2 are the functions obtained from Equations (3.26) and (3.27).

For the example system, at 700°C and 6 bar g, with a steam to methane ratio of 2 (so initial moles of CH_4 = 1 mol and initial moles of H_2O = 2 mol), the iterations in the solution of Equations (3.26) and (3.27) are given in Table 3.1.

Table 3.1 – Iterations in solution for ε_1 and ε_2

Iteration	ε_1	ε_2	$\Delta\varepsilon_1$	$\Delta\varepsilon_2$
0	0.600	0.400	-3.32×10^{-2}	-7.98×10^{-2}
1	0.567	0.320	-5.01×10^{-3}	-3.65×10^{-2}
2	0.562	0.284	-4.24×10^{-5}	-6.78×10^{-3}
3	0.562	0.277	3.14×10^{-6}	-2.04×10^{-4}
4	0.562	0.277	3.06×10^{-9}	-1.77×10^{-7}
5	0.562	0.277	1.76×10^{-14}	-1.10×10^{-13}
6	**0.562**	**0.277**	$0.00\times10^{+0}$	$0.00\times10^{+0}$

It can be seen that the solution converges rapidly. Now that the extents of reaction at equilibrium have been calculated, it is a simple matter to calculate the number of moles of each species at equilibrium, and hence the equilibrium mole fractions. These results are given in Table 3.2.

Table 3.2 – Example results – composition at equilibrium

Component	Moles at equilibrium	Equilibrium mole fraction
CH_4	0.438	0.106
H_2O	1.162	0.282
CO	0.285	0.069
CO_2	0.277	0.067
H_2	1.962	0.476
Total	4.123	1.000

3.3.9 Alternative methods of calculating K

There are several alternative formulae for calculating K for various reactions available in the literature. Hou and Hughes (2001) have the following equation for the steam reforming reaction:

$$K_p = 1.198 \times 10^{17} e^{(-26830/T)} \quad \text{kPa}^2$$

This value is probably calculated with a standard state pressure of 1 atm, or 101.3 kPa, so it follows that:

$$K = \frac{K_p}{(101.3\ \text{kPa})^2}$$

The following equation is given for the water gas shift reaction:

$$K = K_p = 1.767 \times 10^{-2} e^{(4400/T)}$$

ICI use the following method for calculating K for the steam reforming reaction:

$$K = \frac{1}{K_p \times (1\ \text{atm})^2}, \text{ where } K_p = e^{\{Z[Z(Z(0.2513Z - 0.3665) - 0.58101) + 27.1337] - 3.2770\}}$$

and $Z = \frac{1000}{T} - 1$

The equilibrium composition was calculated over a range of conditions using several different sources of thermodynamic data. The results for the example conditions (700 °C, 6 bar g and *SMR* = 2) are given in Table 3.3. The results calculated from data given in Smith *et al.* (1996) and Hou and Hughes (2001) are in almost complete agreement with those generated by Aspen, to a precision of 3 s.f. The results calculated from data given in the JANAF tables are also in agreement with the Aspen-generated results, to a precision of 2 s.f. A similar agreement was observed over a range of temperatures (from 500 to 800 °C) and pressures (from 2 to 9.5 bar g) and for steam to methane ratios of 2 and 4.

3.4 Effect of varying temperature and pressure on reforming equilibrium

Aspen was used to investigate the effect of temperature and pressure on the equilibrium of the reforming reaction. In this simulation, the chemical species included were CH_4, H_2O, CO, CO_2 and H_2. A simple model was set up using the RGibbs equilibrium reactor. The feed was specified as 1 kmol/h CH_4 and 3 kmol/h H_2O. Simulations were run for various temperatures from 500 to 900 °C and pressures from 2 to 10 bar a. The equilibrium fractional conversion of CH_4 is shown against temperature in Figure 3.1 and against pressure in Figure 3.2. The mol fraction of H_2 at equilibrium is shown against temperature in Figure 3.3 and pressure in Figure 3.4.

Table 3.3 – Summary of equilibrium composition calculations using various alternative data sources (T = 700 °C, P = 6 bar g, initial SMR = 2)

	K calculated from $\Delta G_R°$			K approximated by equation		Aspen equilibrium calculation
Data source	Smith *et al.* (1996)	JANAF (2003)	Hayes & Kolaczkowski (1997)	Hou and Hughes (2001)	ICI data sheet	
K_1	12.23	14.17	6.786	12.41	12.54	-
K_2	1.640	1.598	1.191	1.625	1.541	-
ε_1 /mol	0.562	0.576	0.503	0.566	0.566	-
ε_2 /mol	0.277	0.275	0.233	0.276	0.270	-
y_{CH_4}	0.106	0.102	0.124	0.105	0.105	0.105
y_{H_2O}	0.282	0.277	0.315	0.280	0.282	0.281
y_{CO}	0.069	0.072	0.067	0.070	0.072	0.070
y_{CO_2}	0.067	0.066	0.058	0.067	0.065	0.067
y_{H_2}	0.476	0.483	0.435	0.478	0.476	0.477

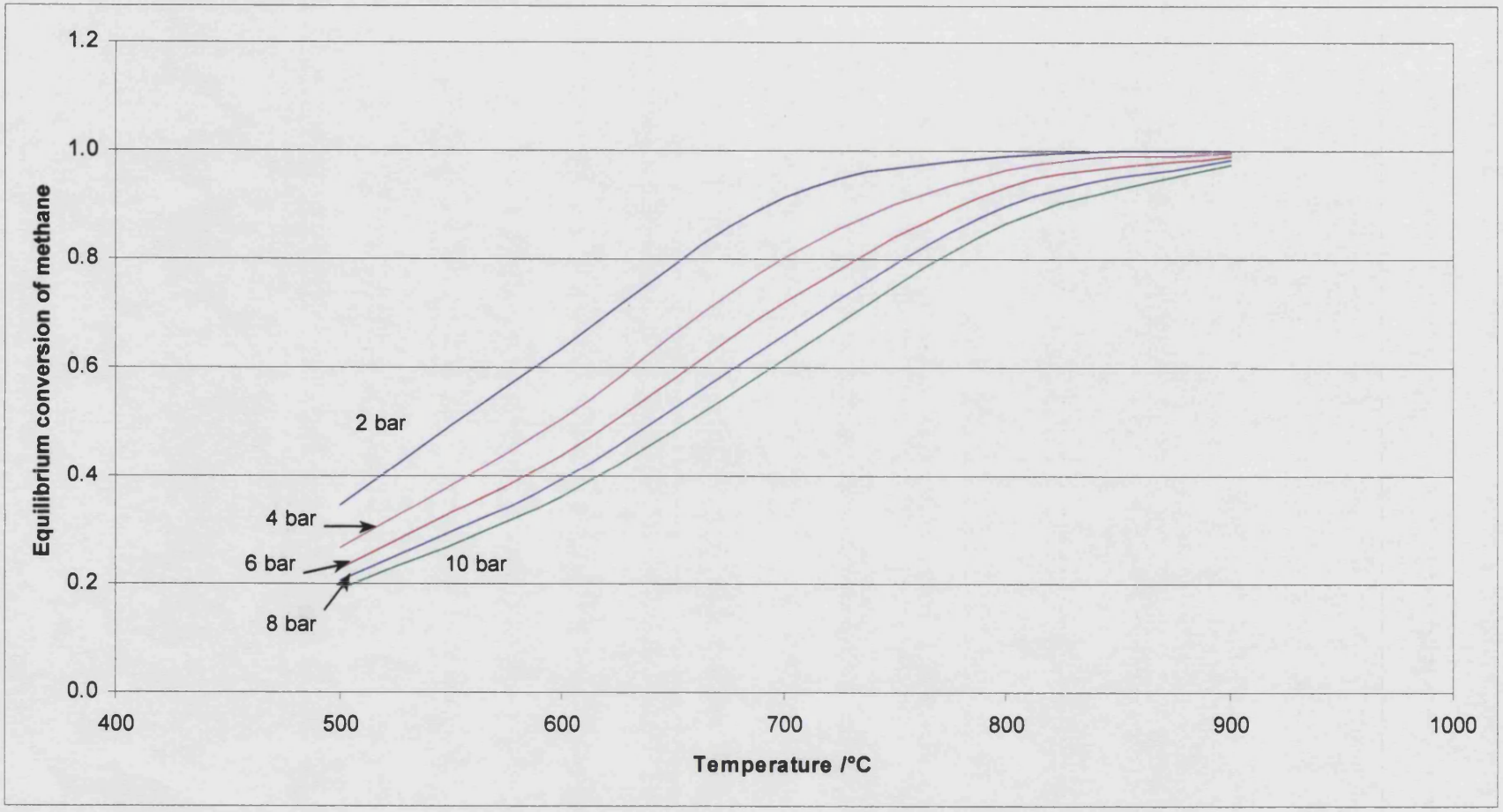

Figure 3.1 – Results of initial Aspen model: CH_4 equilibrium conversion against temperature at various pressures (in bar absolute), initial *SMR* = 3

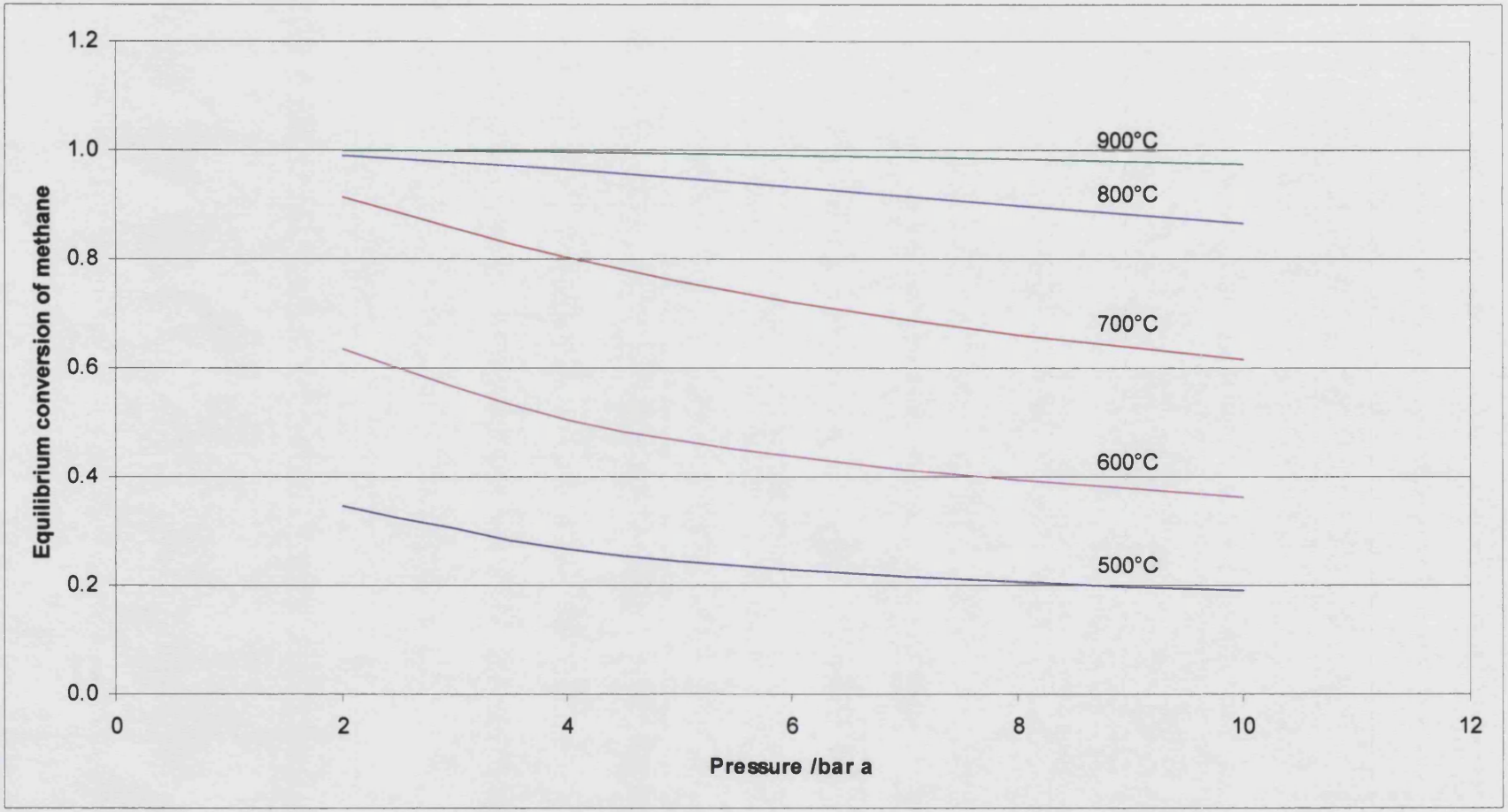

Figure 3.2 – Results of initial Aspen model: CH_4 equilibrium conversion against pressure at various temperatures (in °C), initial *SMR* = 3

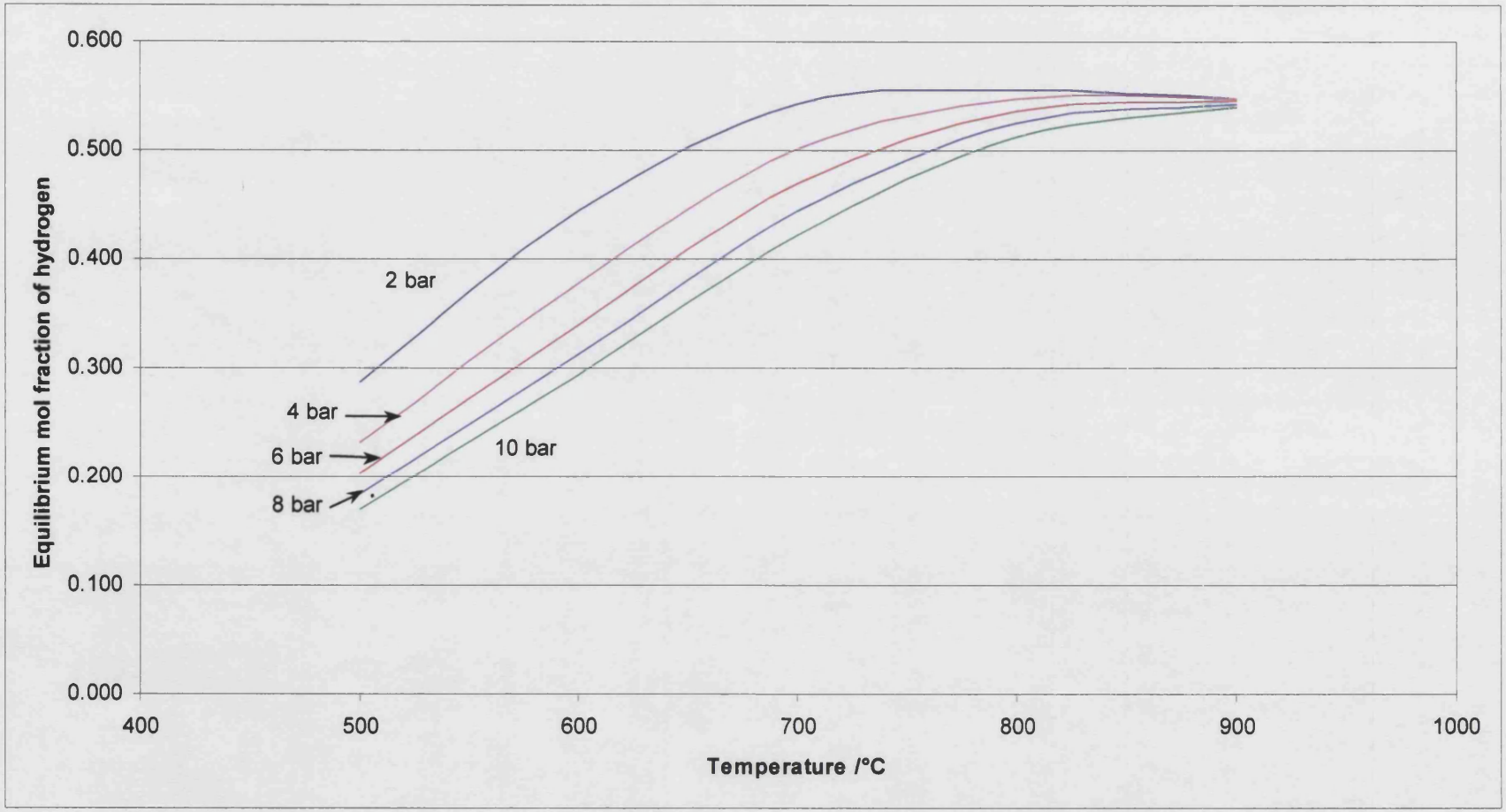

Figure 3.3 – Results of initial Aspen model: H_2 equilibrium mol fraction against temperature at various pressures (in bar absolute), initial *SMR* = 3

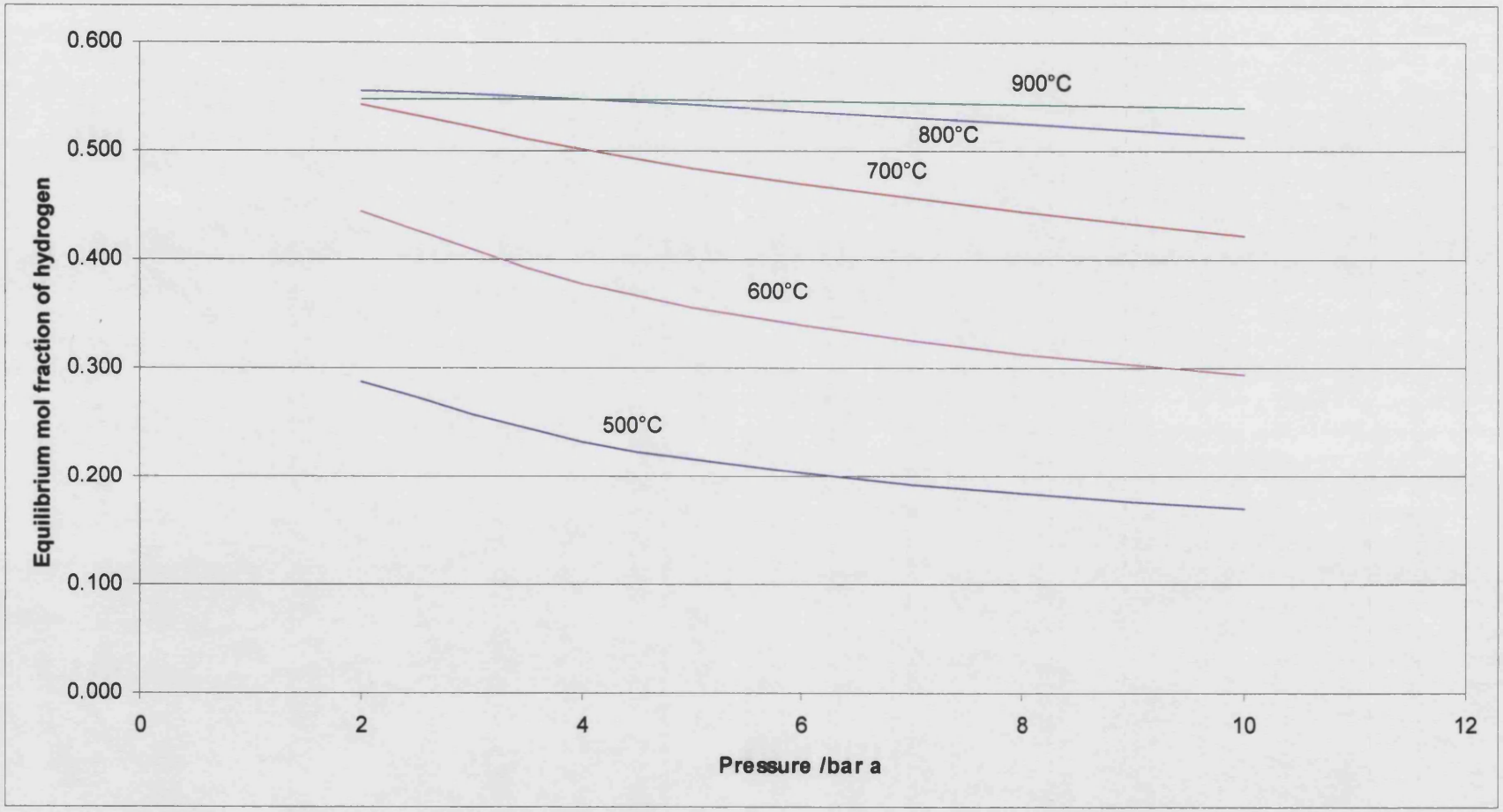

Figure 3.4 – Results of initial Aspen model: H_2 equilibrium mol fraction against pressure at various temperatures (in °C), initial *SMR* = 3

3.5 Simulation of different reforming technologies

In order to develop a deeper understanding of alternative reforming technologies, three processes were simulated in Aspen. To determine the optimum operating conditions for different types of reforming reactor, a number of processes were simulated using Aspen, which led to the publication of Seo *et al.* (2002) (included in Appendix A). Steam reforming of methane, partial oxidation of methane and autothermal reforming of methane were studied. Each process was set up in Aspen to include a reforming reactor, water-gas-shift reactor, steam generator and heat exchanger. For the sake of simplicity, a de-sulphurisation plant was not used in the model, although one would be needed in a real application due to the sulphur content of natural gas and its potential to poison the reforming catalyst. The model used for the reactors was a steady state equilibrium reactor model, the chemical equilibrium being calculated by the minimisation of the Gibbs free energy. The composition of air was assumed to be 20.95% oxygen and 79.05% nitrogen.

3.5.1 Thermodynamic equilibrium

The first objective was to study the thermodynamic equilibrium under different operating conditions, *i.e.* reactor temperature and pressure, steam to carbon ratio and (for the autothermal and partial oxidation systems) the air ratio. The optimum operating conditions were thereby determined. In this case, the steam to carbon ratio (S:C) was defined as (molar flow of H_2O)/(molar flow of CH_4) and the air ratio was defined as (molar flow of O_2)/(2×molar flow of CH_4).

Steam reforming process

The following chemical species were included in the model: CH_4, H_2O, H_2, CO, CO_2, C(s), *H*, *O*, *OH*, HO_2, *HCO*, *CH* and CH_2, where C(s) is solid carbon and those species in *italics* are radicals. S:C ratios from 0.6 to 3.0 were studied at temperatures ranging from 500 to 1000°C and pressures from 1 to 25 bar a. The reactor was modelled as an isothermal reactor, the required heat duty being calculated by Aspen. In a real system, the temperature would have to be kept below 800°C in order to maintain the effectiveness of the catalyst and pressures may be dictated by downstream processes.

It was found that increasing the pressure reduced the conversion and the H_2 yield, so low pressures are desirable. However, C(s) formation (coking) was eliminated by running at >10 bar. Increasing the temperature was found to improve the conversion and above 600°C to reduce C(s) formation. Ideally, the highest temperature possible should be used, and this is around 800°C for real catalysts. It was found that C(s) formation could be eliminated at lower temperatures by increasing the S:C ratio. This also had the effect of increasing the conversion, so ideally this should be set as high as possible. It will be limited in reality by the cost of steam generation. As such the ideal operating conditions for a steam reformer were found to be low pressure (around atmospheric pressure) high temperature (around 800°C) and a S:C ratio of 1.9-3.0. These will give a conversion of 0.9, so long as the reactants have sufficient time to reach equilibrium in the reactor. Obviously, the reaction speed will also be increased by operating at high temperature.

Partial oxidation process

The optimal reactor temperature was also found to be 800°C. However, this reactor was modelled adiabatically, so the pre-heat temperature was the parameter that was adjusted. An optimum air ratio of 0.3 was obtained. At air ratios higher than this, conversion reduced rapidly, while lower air ratios resulted in C(s) formation. The maximum pre-heat temperature, 312°C for an adiabatic reactor, is set by the maximum reactor temperature of 800°C. If it were necessary to use a higher pre heat temperature, the air ratio would have to be reduced, inevitably resulting in coke formation.

Autothermal process

It was found that C(s) formation could be eliminated, either by using S:C ratio of 1.2 or greater, or an air ratio of 0.3 or greater. This reactor was also modelled as an adiabatic reactor. For a pre-heat temperature of 400°C, the optimum conditions were found to be an air ratio of 0.29 and a S:C ratio of 0.35. The air ratio has a marked effect on reactor temperature and should be kept close to the optimum value. Conversely, the S:C ratio could be increased significantly above 0.35, however this would be undesirable in reality due to the increased steam generation costs.

3.5.2 *Thermal energy requirements*

The second objective of the study was to determine the thermal energy requirements of each process. An energy balance was performed for each system running in the most favourable operating conditions. The energy required as heat input to the system was calculated as an equivalent quantity of CH_4 that would have to be burned to produce the heat. Each system comprised a number of heat exchangers, including the isothermal steam reforming reactor. The efficiency assumed for these had a large impact on the relative efficiency of the three systems. If the heat exchangers were assumed to be perfectly efficient, the most efficient process was found to be steam reforming. If the heat transfer efficiency was assumed to be only 80%, the steam reforming process became the least efficient, due to the large heat duty required to support the endothermic reaction. In this case the partial oxidation reactor was found to be the most efficient system.

3.6 Conclusions

3.6.1 Reliability of results generated by Aspen

Thermodynamic equilibrium analysis of the steam reforming reactions using various sources of data show good agreement with data produced by Aspen.

3.6.2 Feasibility of reforming system

The simulations set up in Aspen have shown that the low pressure compact system is a feasible one. System efficiency was shown to be high, as long as the best use was made of the heat supplied to the system.

3.6.3 Operating pressure

High pressures were shown to be unnecessary. In fact, the simulations showed an increase in equilibrium conversion at lower pressures. It may be concluded that existing processes operate at high pressures primarily due to a high pressure requirement downstream, rather than to improve the efficiency of the steam reforming process itself.

3.6.4 CO reduction

Despite the use of both low and high temperature water gas shift reactions in the process, the concentration of CO in the product stream was found to be too high for direct use in a PEM fuel cell. For this purpose, ideally, <10 ppm CO should be present in the product gas. Therefore, an extra separation step is necessary. A review of the literature has shown that there are essentially 4 different processes which could provide this step. These are methanation, PSA, preferential oxidation and membrane separation. The best choice for this application was found to be PSA, due to its relatively low material cost and pumping requirements and minimal loss of hydrogen product.

3.6.5 *Steady state or transient process*

The disadvantage of PSA is that it is a cyclical process. Therefore, in order to connect it to a continuous production process would require either intermediate product storage, or multiple PSA units operating in parallel. A more elegant solution would be to develop a transient reforming system, which would be matched to a PSA unit providing synchronous operation. Another potential advantage of this approach would be to allow the reactants to approach closer to equilibrium and possibly to reduce carbon deposits on the reforming catalyst. Therefore, it was decided that a transient reactor system should be constructed to test the feasibility of the concept.

3.6.6 *Potential advantages of transient approach*

- A smaller reactor may lend itself to modular design, allowing easy scaling for different applications
- May be easier to control than a continuous system
- Residence time can be adjusted to improve conversion (get closer to equilibrium than continuous process)
- It may be possible to reduce catalyst deactivation (*e.g.* by carbon deposition) without using high steam to methane ratios

Chapter 4 - Research into a transient mini-reactor concept

4.1 Aim of the experimental work

The aim is to obtain some preliminary fundamental data on this kind of transient system. Some of the unknowns are listed below:

- How long would such a reactor require to reach equilibrium? Do the kinetic models in the literature apply well in this case?
- How will reaction conditions affect coking of the catalyst?
- What are the optimum conditions for effective operation?
- How effectively can the reforming reaction be linked with a combustion reaction?

4.2 Design of apparatus

4.2.1 Design of reactor

For ease of control, the steam reforming reaction should not be too closely coupled with the combustion reaction that is supplying the required heat. If an injection of reforming reactants was to cause the temperature of the combustion reaction to drop significantly, this could cause the combustion reaction to cease. In order for a steam reforming reactor to operate in transient mode without causing a large change in reactor temperature, the reactor itself should have a high heat capacity compared to the quantity of reactants injected in each reaction cycle. This could be achieved by making the reactor out of a large mass of metal or ceramic, with the combustion and reforming reactions taking place inside tubes that are alternately placed inside the block.

Since the demand on the reactor could be quite varied depending on location and variable depending on demand, the design should be capable of scaling easily. If the design were modular, one could increase the output by adding more units and, if demand fell

temporarily, a number of units could be switched off. The reaction should take place in tubes of relatively small diameter to ensure good heat transfer from the heat source, outside, to the catalyst at the centre. During scale-up, the diameter of tubes should not be increased, but the length and number of tubes could be.

Initial heat up could be achieved by electrical heating. Heating elements evenly spaced throughout the reactor block could be used to raise the temperature high enough to initiate the catalytic combustion reaction.

If modules were of a square-block design (*e.g.* Figure 4.1) then they would be easy to pack together to form a reactor of the required capacity.

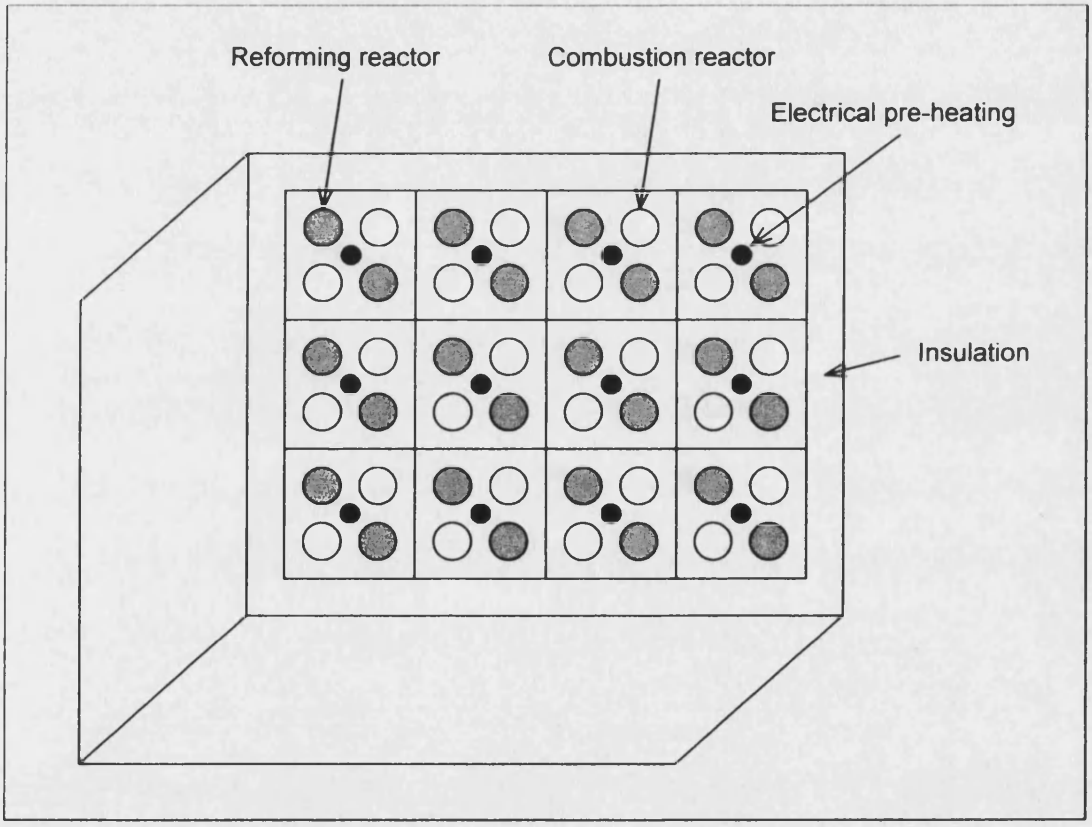

Figure 4.1 – Diagram of a hypothetical modular reactor

When designing the experimental reactor, there were several other considerations. The materials and facilities available had to be taken into account. The purpose of the first experimental reactor was to investigate whether or not the features proposed above for a commercial reactor are feasible in practice. The experimental reactor did not need to have a very large capacity. A cylindrical block of brass was available to form the heat store.

Brass has a high specific heat capacity and can withstand temperatures of up to 800°C and was, therefore suitable for use in the reactor. The reactions would take place inside a pair of ½ inch (12.7 mm) diameter stainless steel tubes, one for the combustion reaction and one for the reforming reaction. A cartridge heater would be placed in the block to provide initial heating.

A photograph of the reactor is shown in Figure 4.2 and a diagram in Figure 4.3.

Figure 4.2 – Photograph of reactor before installation into rig

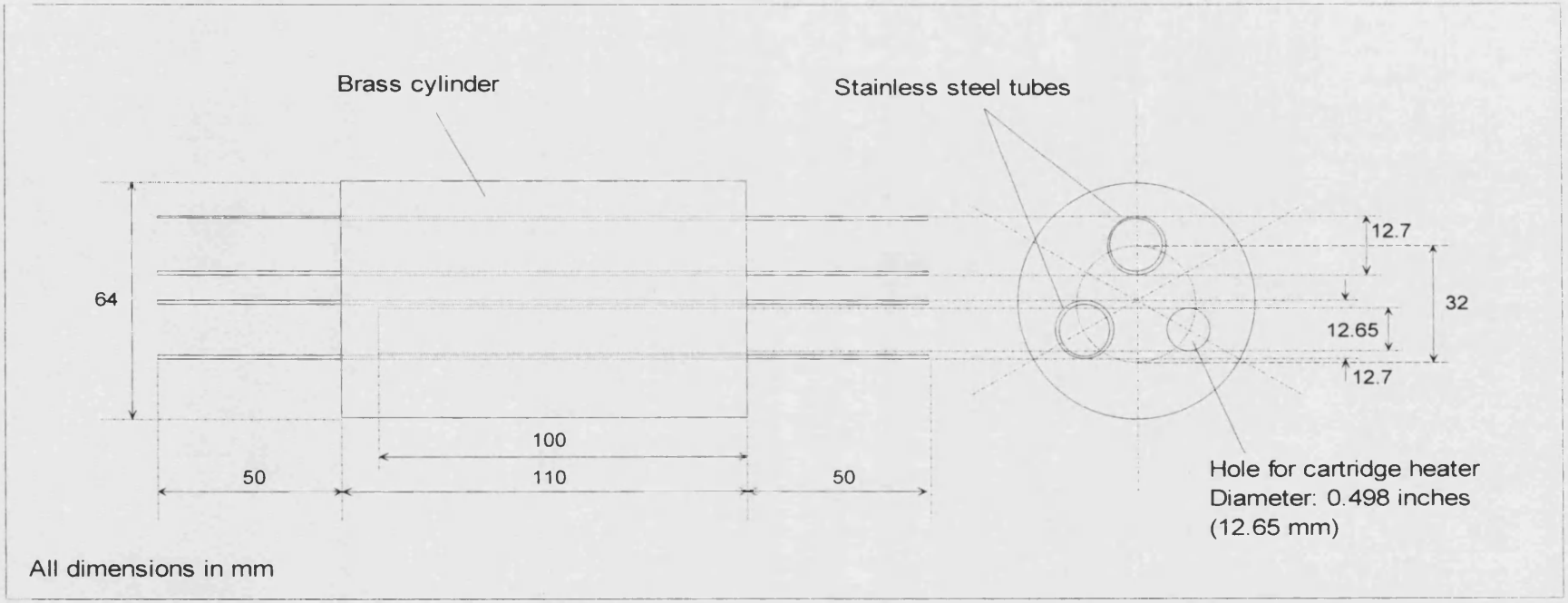

Figure 4.3 –Diagram of the experimental reactor

Calculations showed that the temperature drop of the reforming reactor caused by injecting the reactants would be less than a tenth of a degree.

4.2.2 Form/preparation of catalysts

The chosen reforming catalyst was ICI/Katalco catalyst 57-7, which is an industrial steam reforming catalyst. It consisted of nickel oxide supported on alumina pellets. The pellets were cylindrical and of 3 mm diameter and 3 mm length (see Figure 4.4 and Table 4.1).

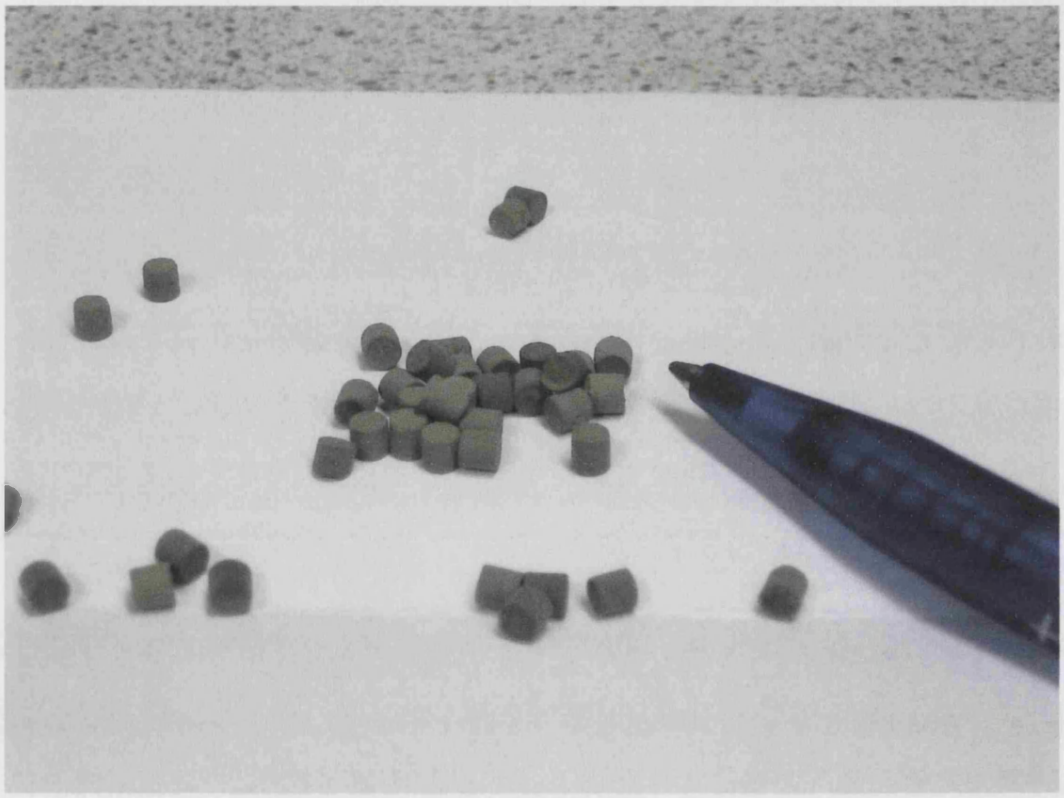

Figure 4.4 – Fresh reforming catalyst pellets

Table 4.1 – Selected catalyst properties

Length	3	mm
Diameter	3	mm
Porosity	34.68	%
Total pore area	17.757	m^2/g
Bulk Density	2.243	g/ml
Skeletal Density	3.434	g/ml

The nickel oxide catalyst had to be reduced, either prior to installation in the reactor, or after installation, but prior to going on line. It was decided to reduce it after installation, which required the reactor to be temporarily connected to a hydrogen supply. The following procedure was used:

1. The apparatus was purged with hydrogen to remove any air that might be present.
2. The reactor was brought up to 700°C.
3. The reactor was pressurised with hydrogen to 6 bar g and then left for 30 minutes before being vented and re-pressurised. This was repeated for 6 hours.
4. The reactor was left overnight at 700°C, pressurised with hydrogen.

For the catalytic combustion, a palladium catalyst on an alumina support was to have been used. Preliminary experiments showed that the combustion reaction would initiate when the catalyst particles reached a temperature of around 250°C, if the reactants had been preheated to around 400°C. Therefore, a block temperature of around 400°C to 450°C would be required prior to catalytic combustion taking place.

4.2.3 Specification of heater

A cartridge heater was required to heat the reactor block sufficiently to start the catalytic combustion reaction. The heater, purchased from Watlow Ltd., Nottingham, was a FIREROD (model number: J4A103). The specifications are given in Table 4.2:

Table 4.2 – Specifications of cartridge heater

Length	4 inches (101.6 mm)
Diameter	0.500 ± 0.002 inches (12.70 ± 0.05 mm)
Voltage requirement	240 V
Power	350 W
Maximum power density	65 W/in^2 (0.10 W/mm^2)
Leads	Fully swaged MGT leads

4.2.4 Insulation of block

The reactor was suspended in a vertical tube electric furnace, with the gas supply/return tubes passing through the top entrance (see Figure 4.5). The bottom end of the furnace

was sealed with a ceramic plug, while the gaps between the tubes at the top end of the furnace were packed with ceramic fibre insulation. These measures reduced heat loss sufficiently to allow the furnace to maintain a temperature of up to 800°C. The furnace could then be used to pre-heat the block, provide all the heat needed for the reforming reaction, or simply to simulate any desired level of heat loss from the reactor.

4.2.5 Reactant Preparation

For the reforming reaction, steam and methane would be required in a mixture of known composition. This mixture was prepared in a small autoclave supplied by Baskerville (Reactors & Autoclaves) Ltd., Manchester, UK.

Figure 4.5 – Furnace with reactor installed

The autoclave consisted of a 100 ml pressure vessel (shown in Figure 4.6), containing a stirrer and two thermocouples, fed by two delivery tubes at the top of the vessel and surrounded by an electrical heating jacket (see Figure 4.7). Each tube had two ¼ inch (6.4 mm) tube connections, controlled by ball valves. There was a oil-filled pressure gauge attached to one of the delivery tubes that measured the pressure inside the autoclave. The stirrer and heating jacket were controlled by a remote panel. It was found that heat loss from the outer surfaces of the autoclave prevented it from reaching temperatures much in excess of 100°C. Therefore, the entire unit was covered by an insulation blanket (see Figure 4.8), which allowed temperatures in excess of 170°C to be obtained.

Figure 4.6 – Autoclave pressure vessel

The vapour pressure (in Pa) of water at any given temperature (in K) can be calculated by the following equation (Perry and Green, 1998 p. 2-54):

$$P_V = \exp\left(C_1 + {}^{C_2}/_{T} + C_3 \ln T + C_4 T^{C_5}\right)$$

where, for water between the temperatures of 0°C and 374°C:

$C_1 = 73.649$, $C_2 = -7258.2$, $C_3 = -7.3037$, $C_4 = 4.1653 \times 10^{-6}$ and $C_5 = 2$.

Figure 4.7 – Autoclave without insulation blanket

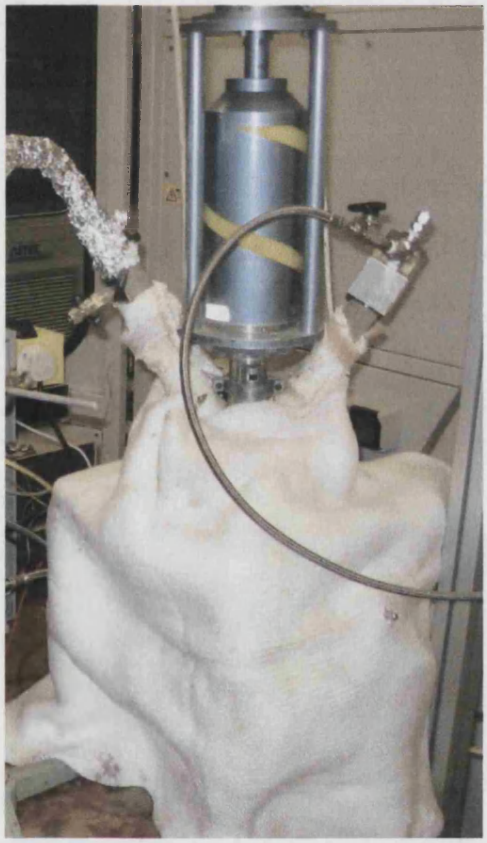

Figure 4.8 – Autoclave fully insulated

In the mixture of steam and methane in the autoclave, steam was assumed to be an ideal vapour and methane to be an ideal gas that was insoluble in the liquid water present. The partial pressure of steam was thus assumed to be equal to its vapour pressure, allowing the proportion of steam to methane to be calculated from the temperature and overall pressure in the autoclave.

In order to make sure that the reactant mixture composition was not affected by any condensation of the steam while it was transferred from the autoclave to the reactor, the delivery tube was surrounded by trace heating and insulation. The tube temperature could thereby be maintained at over 200°C, a temperature in excess of that used in the autoclave. This would also have the effect of partially pre-heating the reactants, which would reduce the thermal load on the reactor when the reactants were injected.

A simpler system was devised for preparing the methane and air mixture for the combustion reaction. The two gases were fed alternately into a mixing/storage chamber which was attached to a pressure gauge. The change in chamber pressure as each gas was added could then be used to calculate the composition of the mixture.

4.2.6 Overall experimental apparatus

A photograph of the entire rig is shown in Figure 4.9.

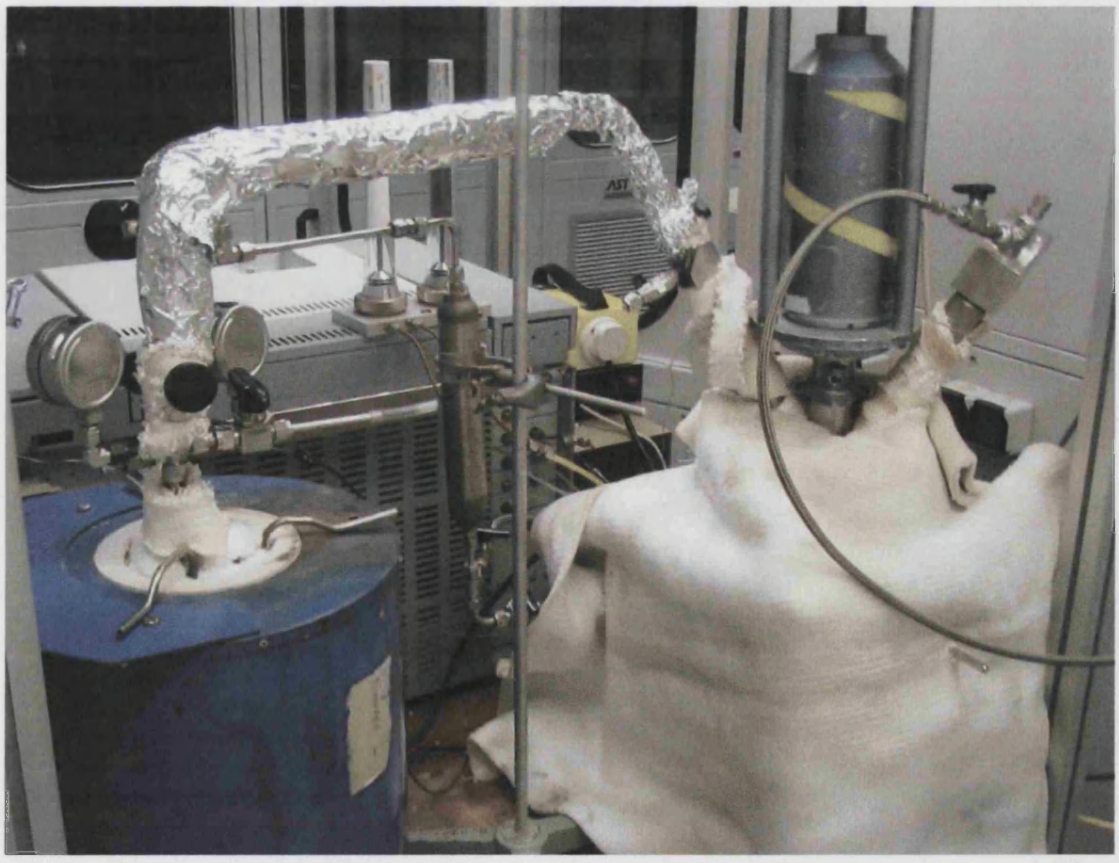

Figure 4.9 – Complete experimental rig

A diagram of the complete reaction system is shown in Figure 4.10.

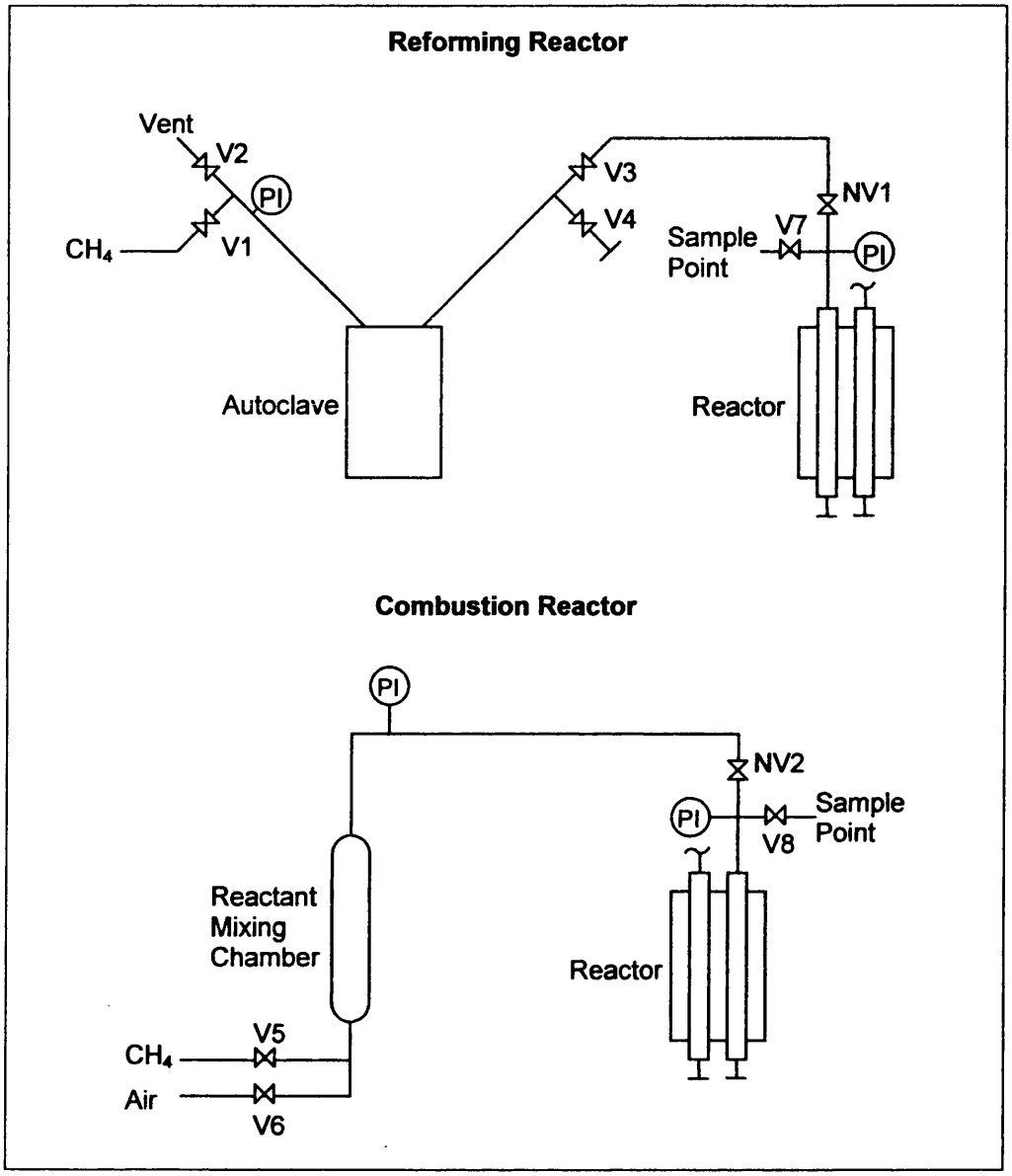

Figure 4.10 – Flow diagrams for the experimental rig

All of the pipework on the rig was in ¼ inch (6.4 mm) stainless steel. The flow of reactants into the reactors and, thereby, the reaction pressure, was to be controlled by a needle valve at the inlet of each reactor. At the end of a run, the product gases could be emptied through a ball valve into a sample bag. Reaction pressure was measured with analogue pressure gauges.

4.3 Experimental design

4.3.1 Stages of investigation

The reacting system was designed in such a manner so as to be able to explore the transient reactor concept in a number of phases. These are outlined in Table 4.3.

Table 4.3 – Experimental phases

Phase 1	Blank runs The performance of the cartridge heater could be evaluated when no catalyst is present. Running the reactors with no catalyst allows the experimental procedure to be tested and can confirm that no reactions take place in the absence of the catalyst.
Phase 2	Reforming experiments With no combustion catalyst present, experiments could be carried out on the reforming reactor. In order to simplify the procedure, the heat for these experiments could be provided by the furnace. Material and energy balances may then be performed and the results compared with those of the simulations.
Phase 3	Combustion experiments With no reforming catalyst present, the performance of the combustion reactor could be evaluated. It would be possible to ascertain whether the reactor is capable of raising the block temperature to that required by the reforming reaction and maintaining it. It would also be possible to confirm whether the cartridge heater can heat the block sufficiently to trigger the combustion reaction.
Phase 4	Combined Reforming and combustion experiments Using the data gathered in Phases 2 and 3, it would then be possible to run both reactions simultaneously, ideally with no heat input from the furnace.

This thesis concentrates primarily on a combination of Phases 1 and 2. Phases 3 and 4 would need to follow in subsequent work.

4.3.2 Range of conditions

For the reforming reaction, there were four principle variables: temperature, pressure, transient reaction time and the steam to methane ratio of the feed. The simulations in Chapter 3 showed that increasing the reaction temperature had a beneficial effect on both the reaction rate and the equilibrium conversion of methane. In order to compare the

performance of the reactor with the simulations, the temperature for the experiments was varied between 500°C and 800°C.

Industrial steam reformers are usually run at high pressures (Peña *et al.*, 1996) (greater than 10 bar), however, simulations showed that the equilibrium conversion of methane would be greatly improved at lower pressures. Therefore, the experiments were run at pressures between 2 bar g and 10 bar g. The loss of gas throughput due to lower pressures could then be compared with the improvement in equilibrium conversion to ascertain the optimum operating conditions.

Although simulations showed that the reforming reaction should reach equilibrium relatively rapidly, it was not known whether imperfections in a practical reactor would result in a reduced overall reaction rate. The experiments were, therefore, carried out with the reaction duration varying between 2 minutes and 10 minutes.

A steam to methane ratio of 2:1 in the feed represents the stoichiometric ratio when all of the steam and methane are completely converted to carbon dioxide and hydrogen. Industrially, higher steam to methane ratios are used to prevent coking of the catalyst. This phenomenon has never been investigated in a transient reactor, however. It was decided that the steam to methane ratio in the feed should be varied between 2:1 and 4:1 for the experiments.

4.3.3 Schedule of experiments

Cartridge heater performance

It was necessary to ascertain whether the cartridge heater as specified was able to heat the reactor up to a sufficient temperature to initiate a catalytic combustion reaction. If this was possible, it was also necessary to know how long the start-up procedure would be likely to take.

Reforming reaction runs

In order to investigate the complete range of conditions described above, a sequence of 96 experiments was devised. Table 4.4 gives the conditions for each of these experiments. Unfortunately, the available methane regulator could not exceed 9.5 bar g, so this was used as the maximum pressure, instead of the 10 bar g that was originally intended.

Table 4.4 – Matrix of conditions for reforming experiments

Experiment number	Steam to methane ratio	Temperature	Time	Pressure
	mol/mol	°C	minutes	bar g
1	2	500	2	2
2	2	500	2	6
3	2	500	2	9.5
4	2	500	4	2
5	2	500	4	6
6	2	500	4	9.5
7	2	500	7	2
8	2	500	7	6
9	2	500	7	9.5
10	2	500	10	2
11	2	500	10	6
12	2	500	10	9.5
13	2	600	2	2
14	2	600	2	6
15	2	600	2	9.5
16	2	600	4	2
17	2	600	4	6
18	2	600	4	9.5
19	2	600	7	2
20	2	600	7	6
21	2	600	7	9.5
22	2	600	10	2
23	2	600	10	6
24	2	600	10	9.5

Table 4.4 continued

Experiment number	Steam to methane ratio	Temperature	Time	Pressure
	mol/mol	°C	minutes	bar g
25	2	700	2	2
26	2	700	2	6
27	2	700	2	9.5
28	2	700	4	2
29	2	700	4	6
30	2	700	4	9.5
31	2	700	7	2
32	2	700	7	6
33	2	700	7	9.5
34	2	700	10	2
35	2	700	10	6
36	2	700	10	9.5
37	2	800	2	2
38	2	800	2	6
39	2	800	2	9.5
40	2	800	4	2
41	2	800	4	6
42	2	800	4	9.5
43	2	800	7	2
44	2	800	7	6
45	2	800	7	9.5
46	2	800	10	2
47	2	800	10	6
48	2	800	10	9.5
49	4	500	2	2
50	4	500	2	6
51	4	500	2	9.5
52	4	500	4	2
53	4	500	4	6
54	4	500	4	9.5
55	4	500	7	2
56	4	500	7	6
57	4	500	7	9.5
58	4	500	10	2
59	4	500	10	6
60	4	500	10	9.5

Table 4.4 continued

Experiment number	Steam to methane ratio	Temperature	Time	Pressure
	mol/mol	°C	minutes	bar g
61	4	600	2	2
62	4	600	2	6
63	4	600	2	9.5
64	4	600	4	2
65	4	600	4	6
66	4	600	4	9.5
67	4	600	7	2
68	4	600	7	6
69	4	600	7	9.5
70	4	600	10	2
71	4	600	10	6
72	4	600	10	9.5
73	4	700	2	2
74	4	700	2	6
75	4	700	2	9.5
76	4	700	4	2
77	4	700	4	6
78	4	700	4	9.5
79	4	700	7	2
80	4	700	7	6
81	4	700	7	9.5
82	4	700	10	2
83	4	700	10	6
84	4	700	10	9.5
85	4	800	2	2
86	4	800	2	6
87	4	800	2	9.5
88	4	800	4	2
89	4	800	4	6
90	4	800	4	9.5
91	4	800	7	2
92	4	800	7	6
93	4	800	7	9.5
94	4	800	10	2
95	4	800	10	6
96	4	800	10	9.5

Repeatability of experiments

In order to determine the experimental repeatability, experiment numbers 74, 77, 80 and 83 were carried out several times and the results compared. These conditions were chosen as the best compromise between the amount of hydrogen produced and the time taken to repeat the experiments.

4.3.4 Experimental procedure

Cartridge heater tests

There was no catalyst present for the cartridge heater tests and no gas connections were made to the reactor. The reactor block was suspended in the furnace, which was then sealed with insulation, but the furnace was not switched on for this experiment. Thus, all of the heat supplied to the block came from the cartridge heater. One thermocouple measured the temperature of the block, while another thermocouple was placed inside one of the reaction tubes. The power supply to the cartridge heater was turned on and the temperature of the block and reaction tube were recorded against time. The experiment would be complete when the temperatures became steady, or when the block temperature exceeded 550°C. At this point, the power to the heater would be turned off.

Reforming experiments

The following procedures refer to valve numbers which are defined on the flow diagram of the reforming system (Figure 4.11). During the experimental phase of the project, the experimental procedures were gradually modified and updated to take into account previously unforeseen factors and to produce the most reliable results in the time available. The procedures detailed below are the final procedures used for the experiments. Note that during these experiments, the cartridge heater was disconnected and the temperature of the block was controlled by the furnace temperature.

Start-up

1. Ensure that valves V1, V3, NV1 and V7 are closed.
2. Set furnace controller to required temperature and then switch on furnace. Leave for approximately 2 hours to reach the required temperature.
3. Inject approximately 60 ml of de-ionised water into the autoclave through V2 and then close it. This is sufficient for 3 to 4 days' operation.
4. Set the methane regulator to 1 bar output. Purge the autoclave with methane by opening V1 and V4. After 5 seconds, close V4 and then V1. Fix cap over V4 outlet and V2 outlet.

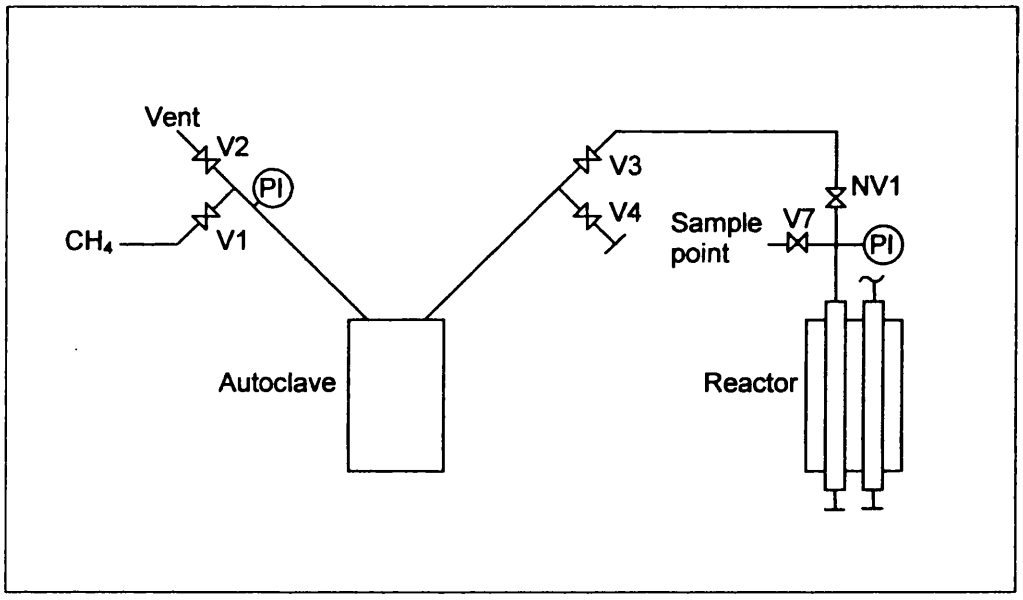

Figure 4.11 – Diagram of the reforming reactor system

5. Calculate the temperature required to achieve the desired steam to methane ratio at the desired reaction pressure[6].
6. Set the autoclave temperature controller, switch on heaters and stirrer and leave for approximately 1 hour until the temperature is within 10°C of the set point.

---

[6] It was found that the needle valve NV1 could not be shut off properly and would leak if the pressure in the autoclave was higher than that in the reactor. The leak (across the valve, not to atmosphere) would always allow the pressure in the reactor to rise up to that in the autoclave after a minute or so. Therefore, the autoclave was run at the desired reaction pressure.

7. Set the methane supply pressure to the desired reaction pressure. Open V1 to charge the autoclave with methane. Leave for approximately 30 minutes to allow the pressure and temperature to stabilise.
8. Switch on the reactant delivery tube trace heating and adjust to obtain a tube temperature of around 200°C. Open V3.
9. Open and close NV1 to charge the reactor, and then open and close V7 to discharge it. Repeat this several times to ensure that the reactant supply tube is filled with the correct reactant mixture. If necessary, wait for a few minutes for the temperature in the autoclave to stabilise at the set point. Leave the reactor in a charged condition.

Operation

1. Ensure that V3 is open. Attach a sampling bag to the output tube, but leave the valve on the bag closed.
2. Briefly open and close V7 to clear any air out of the sampling tube, then open the sample valve on the bag.
3. Record the starting reactor temperature and the temperatures of the autoclave, the reactant delivery tube and the furnace. Start logging the time, close V1 and then charge the reactor by opening NV1.
4. As soon as the reactor is charged, close NV1 and open V1 to maintain the correct system pressure[7]. Record the reaction pressure.
5. During the experiment, check that the temperatures and pressures remain steady.
6. After the required reaction time has elapsed, make sure NV1 is fully closed and briefly open and then close V7 to discharge the contents of the reactor into the sampling bag.
7. Repeat steps 3 to 6 enough times to ensure that the required amount of sample gas has been collected. Make sure the pressure, reaction time and temperatures are the same for all runs. The number of runs required varies with reaction pressure: 6 runs for 9.5 bar, 9 runs for 6 bar and 25 runs for 2 bar.
8. Close the valve on the gas sampling bag and remove it from the output tube.

---

[7] As NV1 was found to leak slightly, the pressure in the reactor was always the same as the pressure in the autoclave, despite any volume changes that may have been occurring in the reactor. Any gas formed by the reaction would flow across NV1 back into the autoclave.

9. Attach a new sampling bag and then return to step 2 for the next experiment. If a change of temperature or pressure is required, the rig will need several hours to reach steady state before the next experiment can be run.

Shut down

1. Close NV1.
2. Switch off autoclave heaters and stirrer, trace heating, cartridge heater and furnace.
3. Ensure that V1 is closed, then carefully open V2 to vent off remaining steam and de-pressurise the autoclave and the reactant delivery tube. Leave V2 open.
4. Leave V7 closed to prevent air entering the reactor while the catalyst is still hot. If the reactor must be de-pressurised during this period, do so by opening NV1.
5. Close V3.
6. Close methane valve on front of fume cupboard. Close methane regulator and shut off the cylinder.
7. Close the fume cupboard doors.

4.3.5 Safety considerations

Safety glasses were worn when working inside the fume cupboard, except for when the entire rig was cool and no section was above atmospheric pressure. When it was possible for hands to come into contact with hot materials, appropriate protection was used.

It was important not to exceed the melting point of the block material. This is 932°C for yellow brass, however it can be as low as 880°C for other types of brass. Since the exact composition of the block used in these experiments was unknown, care was taken not to exceed a block temperature of 830°C.

Care was taken not to vent excessive quantities of hydrogen or methane into the fume cupboard, in order to prevent explosions. Also, care was taken not to release large amounts of helium or argon while working in the fume cupboard although, due to airflow through the cupboard, the possibility of asphyxiation was extremely remote.

4.4 Analysis of product gas

Product gas was collected in 7" × 7" (178 × 178 mm), 1 litre capacity Tedlar sample bags, supplied by Alltech (part number: 48001). The gas was then analysed in a Chrompack CP9001 gas chromatograph (GC), fitted with one pre-column and one molecular sieve column connected in series. The specifications of the columns are given in Table 4.5:

Table 4.5 – Specifications of the columns used in the GC

	Pre-column	Molecular sieve column
Manufacturer	Chrompack	Alltech Associates, Inc.
Part number	84211	57732
Packing	Hayesep T + Hayesep Q	Molecular sieve 13X
Mesh size	80-100	80-100
Column outside diameter	1/8 inch (3.2 mm)	1/8 inch (3.2 mm)
Column length	0.5 m	6 feet (1.83 m)

A thermal conductivity detector (TCD) was used to analyse the content of the sample. The pre-column separated CO_2 from the other gases, which is necessary since the molecular sieve column would have absorbed it otherwise. The columns were connected via a pair of multi-port valves which allowed the injection of a known volume of sample gas and allowed the detector to be connected to either column. The multi-port valves were controlled by a computer in the GC, which could switch them in a timed sequence. Signals from the GC were sent to a PC running Chrompack Maestro version 2.4, which could perform the necessary integration and analysis.

4.4.1 Gas chromatograph configuration

Two alternative carrier gases (helium and argon) were fed at a pressure of 4 bar g to a two-way valve that allowed the required gas to be selected. The required gas then passed through a moisture filter before entering the GC. Helium was used to detect CO, CO_2, O_2, N_2 and CH_4. Hydrogen cannot be accurately measured using helium carrier gas due to the two gases having a very similar thermal conductivity. Argon was used to detect hydrogen. The other gases also show up on the argon chromatograms, but the response is much smaller, so the errors would be increased.

The flow of gas through the GC was controlled by two multi-port valves, Valve 1 and Valve 2. Figure 4.12 to Figure 4.15 are flow diagrams showing the flow regimes for different settings for the two valves.

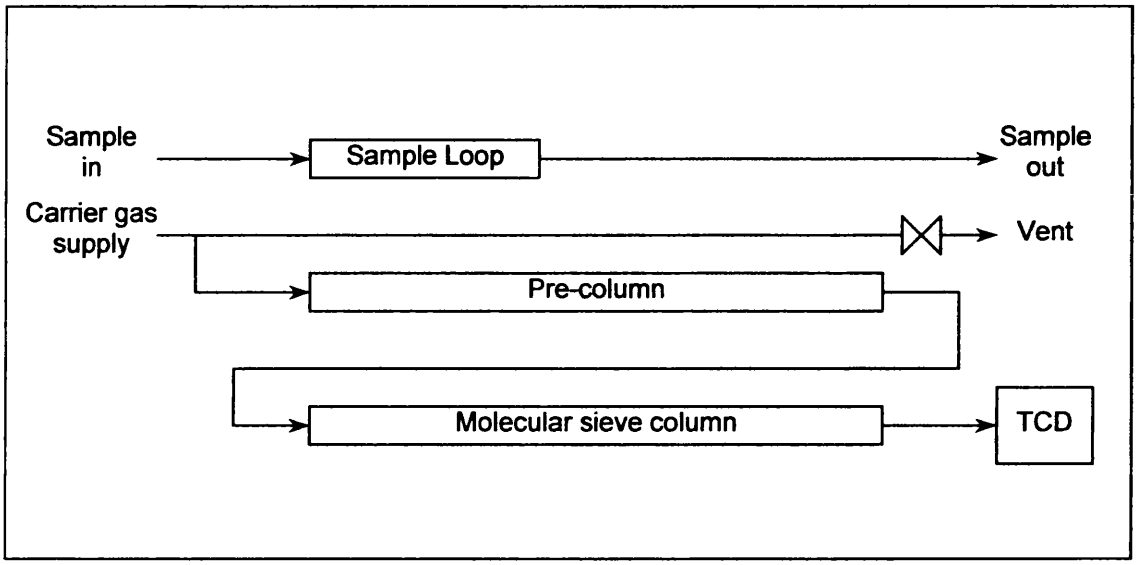

Figure 4.12 – Flow diagram for GC, Valves 1 and 2 in position 1 (initial and final condition)

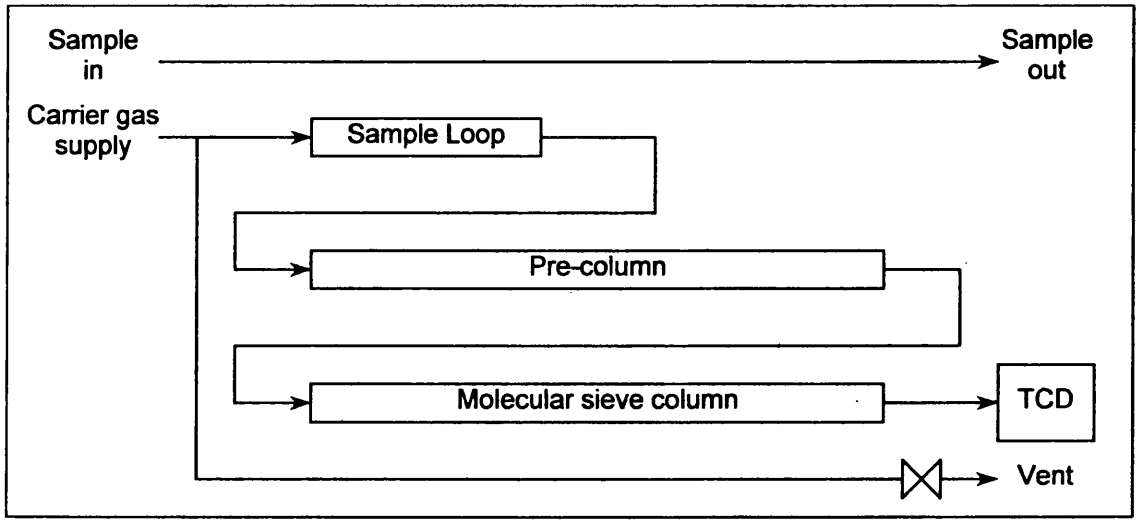

Figure 4.13 – Flow diagram for GC, Valve 1 in position 2, Valve 2 in position 1

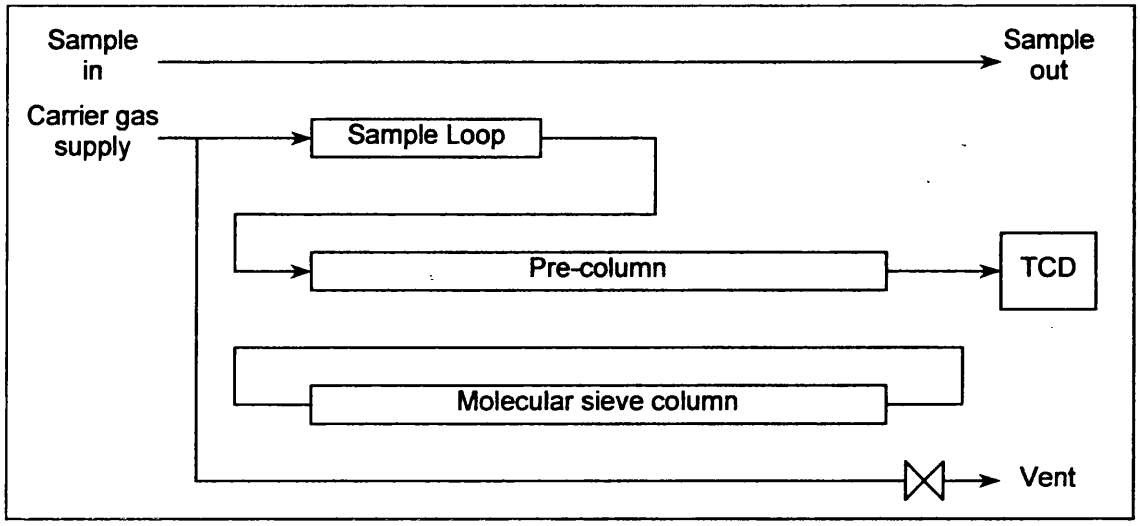

Figure 4.14 – Flow diagram for GC, Valves 1 and 2 in position 2

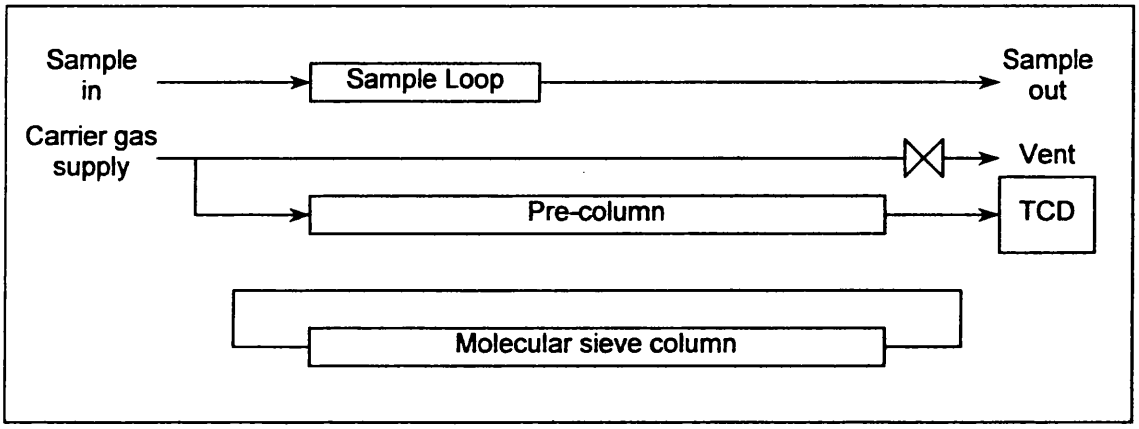

Figure 4.15 – Flow diagram for GC, Valve 1 in position 1, Valve 2 in position 2

The function of the pre-column is to separate CO_2 from the other gases in the sample so that it does not enter the molecular sieve column, where it would be absorbed. After the other gases have passed into the molecular sieve, it is isolated and the output of the pre-column is switched to the detector to allow the CO_2 content to be measured. The hydrogen passes through both columns very quickly and emerges through the detector before the other gases pass into the molecular sieve. After the CO_2 has passed through the detector, the molecular sieve column is re-connected and all of the remaining gases are sent to the detector.

Unfortunately, there is an unwanted side-effect of the pre-column. It not only separates CO_2 from the other gases, but also CH_4. This means that CH_4 enters the molecular sieve after the remaining components. However, it then passes through the molecular sieve faster than the CO and "overtakes" it, emerging slightly earlier. This leads to the peaks for

CO and CH_4 being poorly separated. If either peak is very large, the two peaks join together, the smaller one forming a shoulder on the larger one. The peaks can still be integrated separately, but it is not the ideal situation. One way to avoid this problem is to isolate the molecular sieve before the CH_4 has entered it. The CH_4 would then emerge first, before the CO_2. Unfortunately, due to an unresolved problem with Valve 2, there is always a large spike on the chromatogram as the valve is switched over that makes it impossible to take accurate CH_4 readings in this way.

4.4.2 Control of the GC valves

The computer built into the GC was programmed to alter the valve settings at specific times. Initially, both valves were set to position 1 so that sample gas entering the GC would flow through the sample loop, carrier gas would back-flush the pre-column and more carrier gas would flow through the molecular sieve column to the detector. After the sample loop was charged with sample gas, the program was started. The program that was used is outlined in Table 4.6.

Table 4.6 – Valve control sequence for the GC

Time	Action	Effect
Start	Valve 1 to position 2	Connect sample loop to pre-column and carrier gas flow to sample loop to inject sample
After all gases apart from CO_2 have passed into mol sieve and H_2 has passed through detector	Valve 2 to position 2	Connect pre-column output to detector and isolate mol sieve, preventing CO_2 from entering mol sieve
After CO_2 has passed out of pre-column	Valve 1 to position 1	Set pre-column and sample loop back to initial condition
After CO_2 has passed through the detector	Valve 2 to position 1	Re-connect mol sieve to detector and carrier gas supply in order to feed remaining components to the detector and set system back to initial state

The specific timings were adjusted to suit the flowrate of carrier gas through the system. Argon flowed at a slower rate than helium, necessitating a longer delay between each step of the program.

4.4.3 Recording and analysing signal data

Signals from the GC were sent by serial connection to a PC running Chrompack Maestro version 2.4. This software records the data in a chromatogram and can perform integration and multi-level calibration operations on the data. Maestro does not perform statistical analyses or estimate data errors. After completion of the experiments, the calibration was performed manually in order to gain a better understanding of the precision of the results.

4.4.4 Gas chromatograph calibration

Calibration gas samples

It is necessary to know for each component what quantity is represented by the area under the corresponding peak on the chromatogram. The peaks represent a certain quantity of material, rather than a proportion. However, the total volume of sample gas present is always the same (the volume of the sample loop) and the pressure is always the same. Therefore, the peaks can be calibrated for a molar percentage, or fraction, of each component present in the sample.

For the runs using helium as the carrier gas, 3 different gas standards were run through the GC to ascertain the response to methane, carbon monoxide, carbon dioxide, oxygen and nitrogen:

1. Matheson Tri-Gas, Microsol CTR I calibration gas, Alltech part number 9799
2. Scott Speciality Gases, Mixture 234, Alltech part number 19792 (discontinued)
3. Pure methane from cylinder.

The composition of each standard is given in Table 4.7 below.

Table 4.7 – Composition of calibration gas standards

Standard	1	2	3
Methane	4.50 %	4.00 %	100 %
Carbon monoxide	7.00 %	4.99 %	-
Carbon dioxide	15.0 %	5.00 %	-
Oxygen	7.00 %	5.09 %	-
Nitrogen	Balance (66.5 %)	5.09 %	-
Hydrogen	-	4.00 %	-
Helium	-	Balance	-

The precision of the specifications for Standard 2 was given as ± 2 %. This was taken to be the proportional error of the specification, *i.e.* the quantity of methane was 4.00 ± 0.08 %. It was assumed that the specifications for Standard 1 had the same proportional error, since no precision was specified on the canister.

Calibration runs were carried out every day that the GC was used, prior to running that day's samples through the GC. Figures 4.16 to 4.18 show the areas measured for each gas standard each day for the duration of the experimental work. They show that the response factor did not drift appreciably during the course of the experimental work. This large number of readings allowed the calibration for helium carrier gas to be carried out to a relatively high precision, as described below.

For the runs that used argon as the carrier gas, there was no fixed standard available. Standard 2 could not be used, since it contained helium as well as hydrogen and these could not be separated in the GC. Because of this, various different mixtures of hydrogen and methane were made up and stored in sample bags. The bags were analysed using helium as the carrier gas, the proportion of hydrogen present being calculated by difference. As well as this, pure hydrogen from a cylinder was used to give an area for 100%. As with the helium carrier gas runs, calibration runs were carried out each day prior to the sample runs. If the carrier gas was switched over during the day, calibration runs were carried out prior to any sample runs using the new carrier gas.

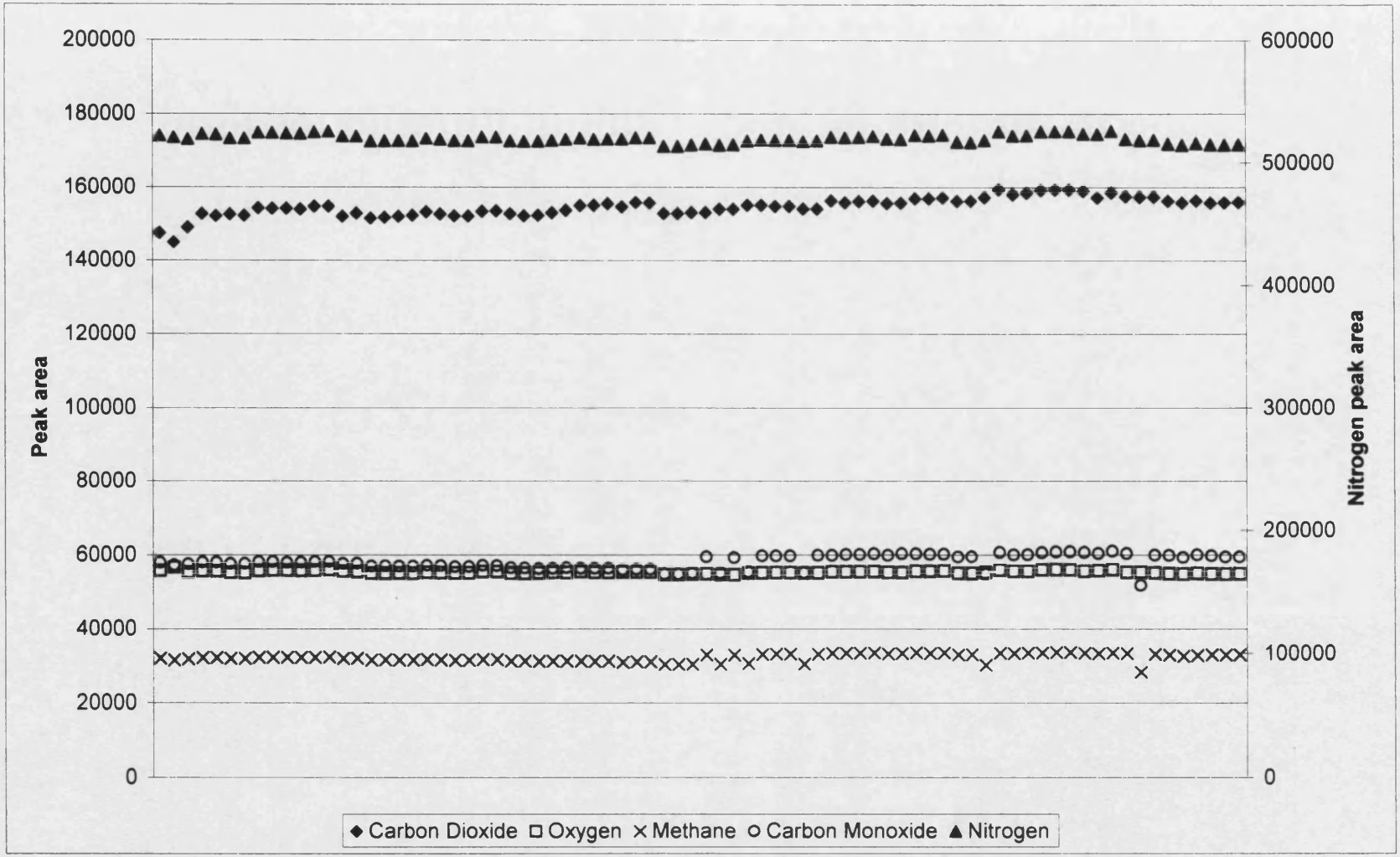

Figure 4.16 – Calibration runs with Standard 1

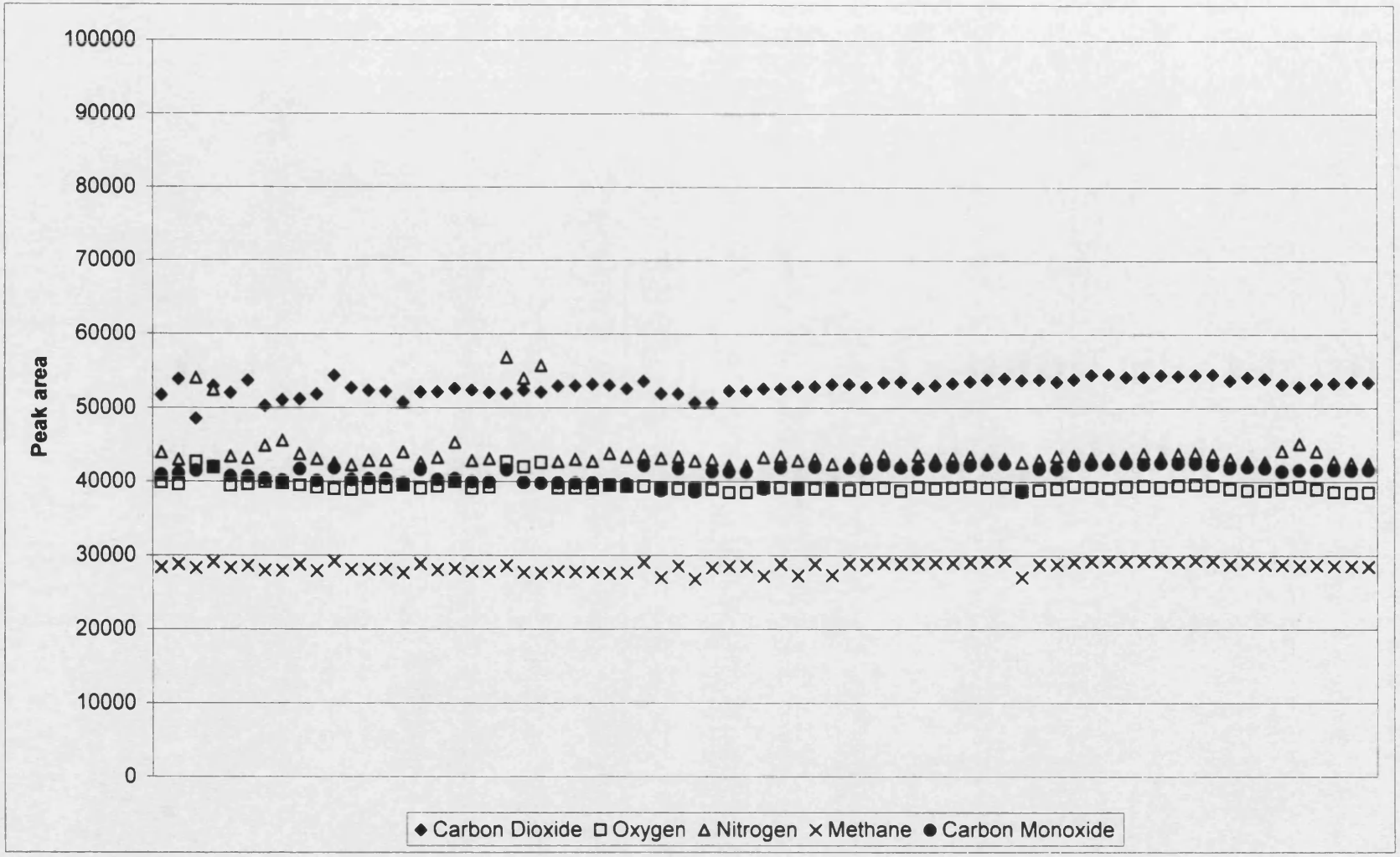

Figure 4.17 – Calibration runs with Standard 2

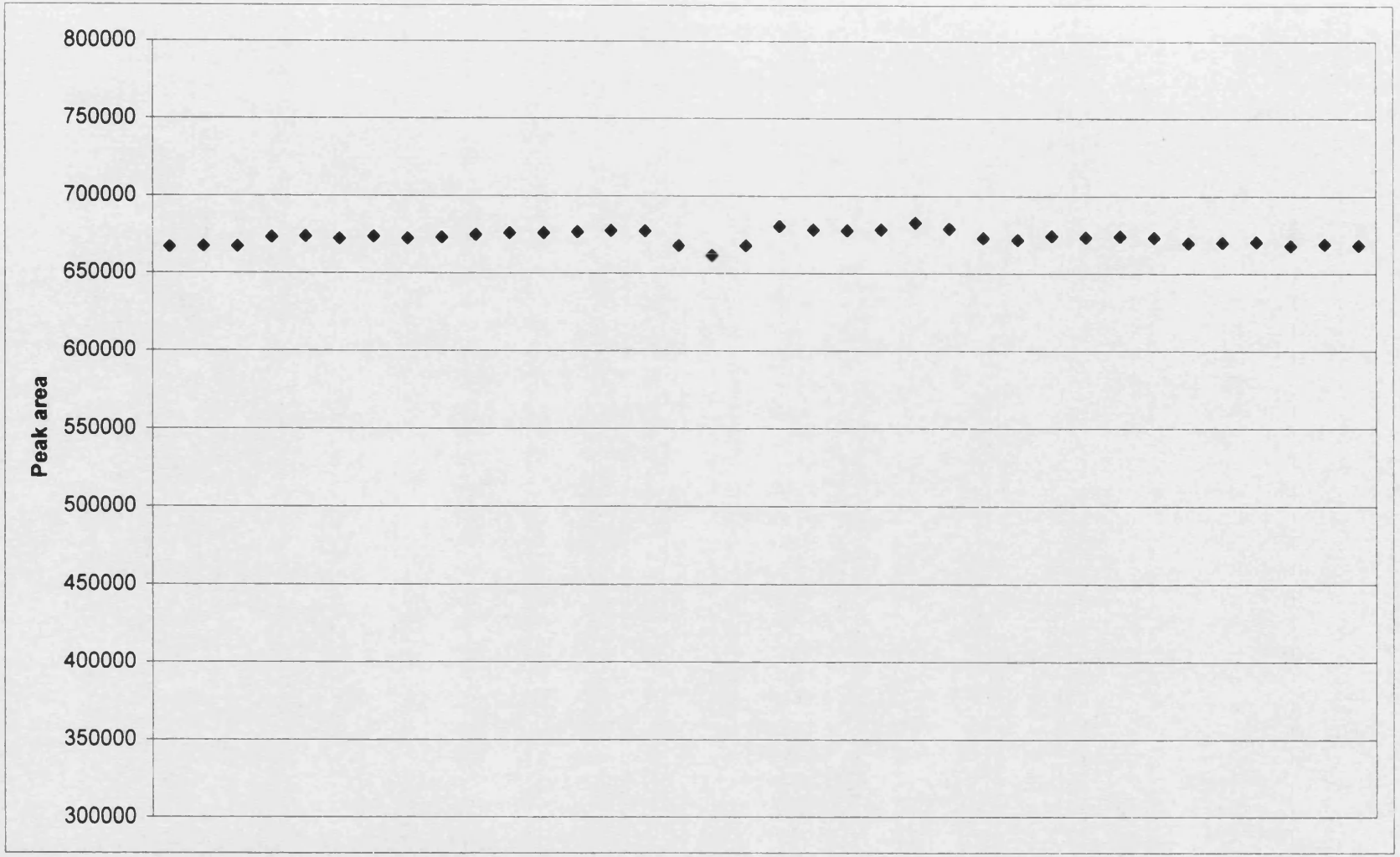

Figure 4.18 – Calibration runs with 100 % methane

Response factor for carbon dioxide

The response factor for component i, r_i, is defined as the peak area, $A_{peak,i}$ divided by the molar percentage of component i, Y_i. The error in r_i, δr_i is given by the following equation, derived from the general relationship for uncertainty in a product or quotient of values with independent uncertainties, given by Taylor (1997) p. 61:

$$\delta r_i = r_i \left[\left(\frac{\delta Y_i}{Y_i} \right)^2 + \left(\frac{\delta A_{peak,i}}{A_{peak,i}} \right)^2 \right]^{1/2} \tag{4.1}$$

The results for CO_2 of the calibration runs are given in Table 4.8. Although the results given in the table have been rounded in line with the magnitude of the errors, non-rounded values were used in all subsequent calculations. It can be seen that, within the experimental error, the two values agree with one another. Over this range of areas, the response may therefore be treated as linear.

Table 4.8 – CO_2 calibration results

Standard	1	2
Mean area	154703	52881
Number of samples	78	71
Standard deviation of mean area	293	136
Calibration amount	15.0 %	5.0 %
Calibration amount error	± 0.3 %	± 0.1 %
Response factor	10300	10600
Response factor error	± 200	± 200

The final value for the response factor was taken to be the weighted average of the two values in Table 4.8. So, for CO_2, $r_{CO_2} = 10440 \pm 150$.

Response factor for oxygen

The results for O_2, calculated in the same manor as those for CO_2 are given in Table 4.9 below:

Table 4.9 – Calibration results for O_2

Standard	1	2
Mean area	55285	39350
Number of samples	78	71
Standard deviation of mean area	43	105
Calibration amount	7.0 %	5.1 %
Calibration amount error	± 0.1 %	± 0.1 %
Response factor	7900	7700
Response factor error	± 200	± 200

In this case, the values for response factor also show good agreement, the final value being $r_{O_2} = 7800 \pm 100$.

Response factor for nitrogen

Table 4.10 gives the results for the calibration of the N_2 peak:

Table 4.10 – Calibration results for N_2

Standard	1	2
Mean area	519745	44012
Number of samples	78	71
Standard deviation of mean area	376	361
Calibration amount	67 %	5.1 %
Calibration amount error	± 1 %	± 0.1 %
Response factor	7800	8600
Response factor error	± 200	± 200

It can be seen from Table 4.10 that the two computed values for response factor do not agree with one another. This indicates that the response to N_2 over this range is slightly non-linear. However, the amounts of N_2 in the experimental product samples are very low

and the values are not used in subsequent calculations, so it is reasonable to use the response factor computed from the Standard 2 runs. Therefore, $r_{N_2} = 8650 \pm 200$.

Response factor for methane

Table 4.11 – Calibration results for CH_4

Standard	1	2	3
Mean area	32207	28445	672896
Number of samples	78	71	36
Standard deviation of mean area	124	77	755
Calibration amount	4.50 %	4.00 %	100 %
Calibration amount error	± 0.09 %	± 0.08 %	± 0 %
Response factor	7160	7110	6729
Response factor error	± 100	± 100	± 8

The response factors from Standard 1 and Standard 2 (low levels of CH_4) agree well with one another, but are not in good agreement with the response factor for 100 % CH_4. Therefore, the response over the full range was slightly non-linear. From a CH_4 concentration of zero to 4.5 %, the response was treated as linear, with a response factor of $r_{CH_4} = 7100 \pm 100$.

For CH_4 concentrations between 4.5 % and 100 %, the response was also treated as linear, but with a different gradient. The concentration of CH_4 in the sample, Y_{CH_4} was calculated by the following equation:

$$Y_{CH_4} = \kappa_1 A_{peak,CH_4} + \kappa_2 \qquad (4.2)$$

where $\kappa_1 = 1.49 \times 10^{-4}$ and $\kappa_2 = -0.28$

At a concentration of 4.5 % (peak area of 32102), Equation (4.2) gives the same result as calculating Y_{CH_4} from the initial response factor.

Response factor for carbon monoxide

Table 4.12 – Calibration results for CO

Standard	1	2
Mean area	58091	41090
Number of samples	78	71
Standard deviation of mean area	221	133
Calibration amount	7.0 %	5.0 %
Calibration amount error	± 0.1 %	± 0.1 %
Response factor	8300	8200
Response factor error	± 200	± 200

These results agree well with one another, within experimental error. Therefore, the final value for the response factor was the weighted average of the two results in Table 4.12 calculated in the same way as those for CO_2 and O_2, so $r_{CO} = 8270 \pm 100$.

Response factor for hydrogen

The calibration results for H_2, measured using argon carrier gas, are shown in Figure 4.19 below. The figure shows that a linear response passing through the origin is not a good match to the data. The calibration curve must pass through the origin, since an area of zero (no peak) would indicate a hydrogen proportion of zero. Perhaps the best approximation would be to use two linear functions in the same way that the response to CH_4 was modelled. However, it is difficult to choose where to change from one function to the next. In this case, a least squares quadratic fit was used. This line is shown on the figure. The sample concentration of H_2 may then be calculated using Equation (4.3) below:

$$Y_{H_2} = \kappa_3 A^2_{peak,H_2} + \kappa_4 A_{peak,H_2} \qquad (4.3)$$

where $\kappa_3 = -5.79\times10^{-10}$ and $\kappa_4 = 4.76\times10^{-4}$

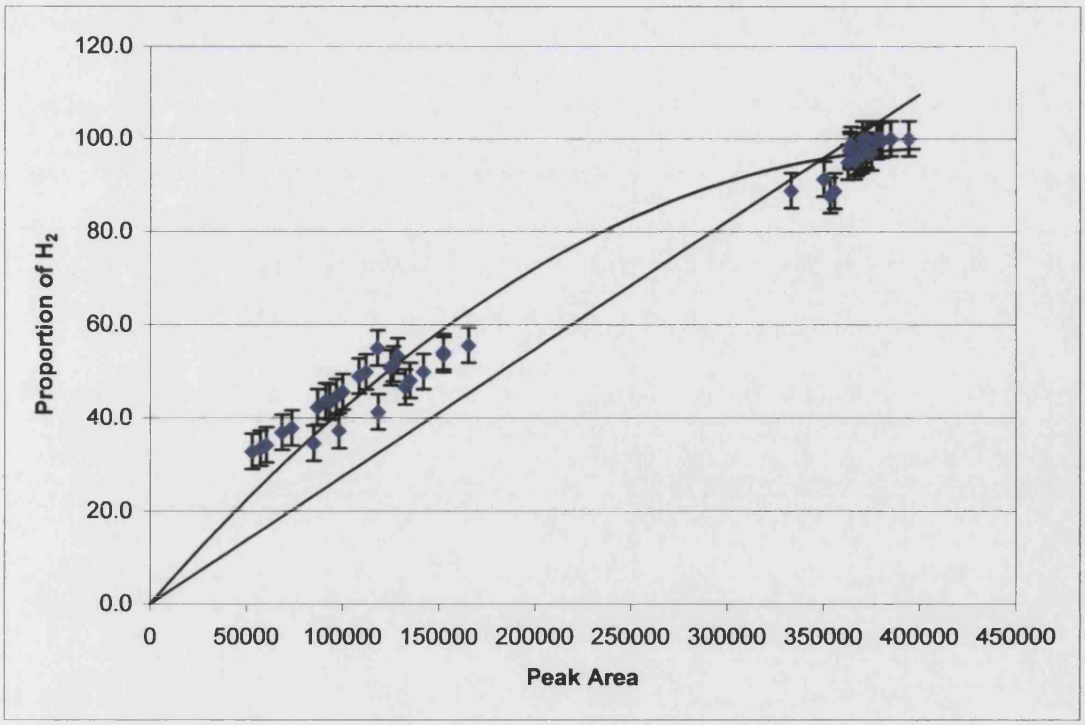

Figure 4.19 – Calibration plot for H_2

4.4.5 Calculation of sample composition

For CO_2, O_2, N_2, CH_4 (for areas below 32102) and CO, the concentration of the components in the samples were calculated using Equation (4.4) below:

$$Y_i = A_{peak,i} r_i \tag{4.4}$$

For CH_4 peak areas above 32102, the concentration in the sample was calculated using Equation (4.2). For H_2, the concentration in the sample was calculated using Equation (4.3).

4.4.6 Estimating precision of results

Each sample was run through the GC several times, producing several different areas. The mean area was used in the calculations, and its precision was estimated from the scatter of the readings.

For CO_2, O_2, N_2, CH_4 (for areas below 32102) and CO, the uncertainty in the proportion of each component was estimated using Equation (4.5) below:

$$\delta Y_i = Y_i \left[\left(\frac{\delta A_{peak,i}}{A_{peak,i}} \right)^2 + \left(\frac{\delta r_i}{r_i} \right)^2 \right]^{1/2} \tag{4.5}$$

For CH_4 peak areas above 32102 the uncertainty in the proportion of CH_4 was estimated using Equation (4.6) below. This equation was derived from the general relationship for uncertainty in a function of several variables, each with random, independent uncertainty (Taylor, 1997, p. 75).

$$\left(\delta Y_{CH_4}\right)^2 = \left(\frac{\partial Y_{CH_4}}{\partial A_{peak,CH_4}} \delta A_{peak,CH_4} \right)^2 + \left(\frac{\partial Y_{CH_4}}{\partial \kappa_1} \delta \kappa_1 \right)^2 + \left(\frac{\partial Y_{CH_4}}{\partial \kappa_2} \delta \kappa_2 \right)^2 \tag{4.6}$$

Differentiating Equation (4.2) and substituting into Equation (4.6) gives:

$$\left(\delta Y_{CH_4}\right)^2 = \left(\kappa_1 \delta A_{peak,CH_4}\right)^2 + \left(A_{peak,CH_4} \delta \kappa_1\right)^2 + \left(\delta \kappa_2\right)^2 \tag{4.7}$$

where $\delta \kappa_1 = 20.6 \times 10^{-7}$ and $\delta \kappa_2 = 0.18$

4.4.7 Example results

The complete set of area data recorded for all experiments are listed in Appendix B. A typical set of results (for Experiment number 35) are given in Table 4.13 along with the computed molar percentages and the estimated uncertainties. Experiment number 35 was run with a nominal *SMR* of 2:1, at 700°C and 6 bar g, with a reaction period of 10 minutes.

Table 4.13 – Sample gas composition for Experiment number 35

	CO_2	O_2	N_2	CH_4	CO	H_2
Mean $A_{peak,i}$	20140	6294	22130	439700	25500	54940
$\delta A_{peak,i}$	20	8	40	2000	2000	80
Y_i	1.93 %	0.806 %	2.56 %	65.3 %	3.1 %	24.4 %
δY_i	0.03 %	0.01 %	0.06 %	0.35 %	0.3 %	

4.5 Material balance

4.5.1 Presence of air in the samples

All of the samples were found to contain small, but measurable amounts of oxygen and nitrogen. There are two possible sources for these. The first is that air may have been present in the autoclave and been fed to the reactor, despite the precautions taken to purge the autoclave prior to use. The other source is air in the product vent tube and/or the sample bag tube prior to the first time the reactor was vented during each experiment. The second source is more likely.

More evidence for this is given by the ratio of N_2:O_2 measured in the samples. If air was present in the reactant feed, it would be expected that the oxygen would react entirely in the reactor and, therefore, that the N_2:O_2 ratio in the product would be greater than that of air (3.71:1). In fact, in the majority of cases there is less N_2 than expected. Clearly, O_2 cannot have been generated in the reactor, so this discrepancy is most likely due to small errors in the calibration at these low measured values of N_2.

It is reasonable to assume that a negligible amount of air was present in the autoclave, and thereby the reactant feed. Therefore, the oxygen and nitrogen found in the samples may be discounted in the calculation of the material balance.

4.5.2 Water vapour

Even if the reactions were to proceed to equilibrium, a large proportion of the product would be steam. As soon as the product gas enters the sample bag, it begins to cool and the steam condenses to a small amount of liquid water. It is then very difficult to measure the amount of water present. In addition, any water vapour that enters the GC is absorbed by the molecular sieve column. Therefore, the proportion of steam in the product gas has to be estimated by the material balance.

4.5.3 Normalising the results

The material balance was carried out using the composition of the dry product gas, which is the mixture of just CO, CO_2, CH_4 and H_2 in the product. The O_2, N_2 and any H_2O must be discounted. To do this, the results were normalised by dividing each measured mole percentage by the sum of the measured data for CO, CO_2, CH_4 and H_2.

4.5.4 Basis of calculations

The basis for the material balance was 1 mol of methane in the feed. The quantity of steam was then calculated from the steam to methane ratio (*SMR*).

The reacting system can be described by two independent reactions, as explained during the equilibrium calculations in Chapter 3. There may be many other reactions taking place in the reactor, but the net result of these, for material balance and equilibrium purposes, may be described by the following pair of reactions:

Reaction 1: $CH_4 + H_2O \Leftrightarrow CO + 3H_2$

Reaction 2: $CO + H_2O \Leftrightarrow CO_2 + H_2$

Thus, there are two unknown values, ε_1 and ε_2, the extents of Reactions 1 and 2. For a given quantity of methane in the feed, these may be calculated from two independent equations in ε_1 and ε_2. Since there are 4 components in the dry gas, there are 4 known mole fractions, which allow 4 different equations in ε_1 and ε_2 to be formed, therefore the problem is over-specified. The mole fractions of any pair of components may be used to estimate the extents of the reactions and, thereby, the mole fractions of the remaining components. If the assumptions about the components present in the reaction mixture are correct, and the measurement of the product composition is perfectly accurate, the choice of components should not matter. The estimated extents of reaction would be the same for any pair and the estimates for the remaining mole fractions would equal the measured values. The extents of reaction were, therefore, estimated using several different pairs of measured mole fractions. Comparing these estimates would then provide evidence for which pair were the most reliable.

4.5.5 *Determining the extent of reaction*

The number of moles of each species present in the product gas may be calculated from the number of moles present in the reactant feed and the extents of the two reactions by the following equations:

$$n_{CO_2} = n_{0,CO_2} + \varepsilon_2$$

$$n_{CH_4} = n_{0,CH_4} - \varepsilon_1$$

$$n_{CO} = n_{0,CO} + \varepsilon_1 - \varepsilon_2$$

$$n_{H_2} = n_{0,H_2} + 3\varepsilon_1 + \varepsilon_2$$

$$n_{H_2O} = n_{0,H_2O} - \varepsilon_1 - \varepsilon_2$$

Given the basis of 1 mole of methane in the feed, these equations may be re-written for each component in the dry gas in the following way:

$$n_{CO_2} = \varepsilon_2 \tag{4.8}$$

$$n_{CH_4} = n_{0,CH_4} - \varepsilon_1 \tag{4.9}$$

$$n_{CO} = \varepsilon_1 - \varepsilon_2 \tag{4.10}$$

$$n_{H_2} = 3\varepsilon_1 + \varepsilon_2 \tag{4.11}$$

$$n_{H_2O} = n_{0,H_2O} - \varepsilon_1 - \varepsilon_2 \tag{4.12}$$

Thus, the total number of moles in the **dry gas** is given be Equation (4.13) below:

$$n_{TOTAL,dry} = n_{0,CH_4} + 3\varepsilon_1 + \varepsilon_2 \tag{4.13}$$

The mole fractions of component *i* in the dry gas are given by the following equation:

$$y_{i,dry} = \frac{n_i}{n_{TOTAL,dry}} \tag{4.14}$$

Equation (4.14) may be written in terms of the number of moles of the component:

$$n_i = y_{i,dry} n_{\mathrm{TOTAL},dry} \tag{4.15}$$

Substituting Equations (4.8), (4.9), (4.10), (4.11) and Equation (4.13) into Equation (4.15) gives the following set of equations:

$$y_{\mathrm{CH_4},dry}\left(n_{0,\mathrm{CH_4}} + 3\varepsilon_1 + \varepsilon_2\right) = n_{0,\mathrm{CH_4}} - \varepsilon_1 \tag{4.16}$$

$$y_{\mathrm{CO_2},dry}\left(n_{0,\mathrm{CH_4}} + 3\varepsilon_1 + \varepsilon_2\right) = \varepsilon_2 \tag{4.17}$$

$$y_{\mathrm{CO},dry}\left(n_{0,\mathrm{CH_4}} + 3\varepsilon_1 + \varepsilon_2\right) = \varepsilon_1 - \varepsilon_2 \tag{4.18}$$

$$y_{\mathrm{H_2},dry}\left(n_{0,\mathrm{CH_4}} + 3\varepsilon_1 + \varepsilon_2\right) = 3\varepsilon_1 + \varepsilon_2 \tag{4.19}$$

Any pair of these equations may be solved for ε_1 and ε_2. Initially, Equation (4.16) was written in terms of ε_1:

$$\varepsilon_1 = A' - B'\varepsilon_2 \tag{4.20}$$

where $A' = n_{0,\mathrm{CH_4}} \dfrac{\left(1 - y_{\mathrm{CH_4},dry}\right)}{3y_{\mathrm{CH_4},dry} + 1}$ and $B' = \dfrac{y_{\mathrm{CH_4},dry}}{3y_{\mathrm{CH_4},dry} + 1}$

In a similar fashion, Equations (4.17), (4.18) and (4.19) were written in terms of ε_2:

$$\varepsilon_2 = C' + D'\varepsilon_1 \tag{4.21}$$

where $C' = \dfrac{y_{\mathrm{CO_2},dry} n_{0,\mathrm{CH_4}}}{1 - y_{\mathrm{CO_2},dry}}$ and $D' = \dfrac{3y_{\mathrm{CO_2},dry}}{1 - y_{\mathrm{CO_2},dry}}$

$$\varepsilon_2 = E' + F'\varepsilon_1 \tag{4.22}$$

where $E' = -\dfrac{y_{\mathrm{CO},dry} n_{0,\mathrm{CH_4}}}{y_{\mathrm{CO},dry} + 1}$ and $F' = \dfrac{1 - 3y_{\mathrm{CO},dry}}{y_{\mathrm{CO},dry} + 1}$

$$\varepsilon_2 = G' + H'\varepsilon_1 \tag{4.23}$$

where $G' = \dfrac{y_{H_2,dry} n_{0,CH_4}}{1 - y_{H_2,dry}}$ and $H' = -3$

Now, Equations (4.20) and (4.21) may be solved simultaneously for ε_1, with ε_2 being obtained directly from Equation (4.21):

$$\varepsilon_1 = \frac{A' - B'C'}{B'D' + 1} \tag{4.24}$$

Similar solutions may be written for the other pairs of equations:

$$\varepsilon_1 = \frac{A' - B'E'}{B'F' + 1} \tag{4.25}$$

$$\varepsilon_1 = \frac{A' - B'G'}{B'H' + 1} \tag{4.26}$$

In addition, Equation (4.17) was written in terms of ε_1:

$$\varepsilon_1 = J'\varepsilon_2 - K' \tag{4.27}$$

where $J' = \dfrac{1 - y_{CO_2,dry}}{3y_{CO_2,dry}}$ and $K' = \dfrac{n_{0,CH_4}}{3}$

Equation (4.27) and Equation (4.22) were solved for ε_1:

$$\varepsilon_1 = \frac{J'E' - K'}{1 - J'F'} \tag{4.28}$$

4.5.6 Estimating the product composition

For each pair of values for ε_1 and ε_2, the composition of the product gas can be calculated from Equations (4.8), (4.9), (4.10) and (4.11).

This allows the mole fractions of the components in the dry product and wet product to be estimated.

4.5.7 Comparison of estimates using different known parameters

For each pair of values for ε_1 and ε_2, the estimates for the mole fractions of the components in the dry gas were compared with the measured values. For those mole fractions that were used in the calculation of ε_1 and ε_2, the estimates were obviously equal to the measured values. For the other species, however, the predicted values did not match up with the measured ones. This is illustrated in Figure 4.20, Figure 4.21, Figure 4.22, Figure 4.23, Figure 4.24, and Figure 4.25 below.

It is immediately apparent that using the measured value for H_2 is not a good idea. The predicted values for CO and CO_2 are very different from the measured values and, in the case of CO, mostly negative. The balance is clearly very sensitive to changes in H_2 mole fraction, and it would appear that the measured values are too high. This could be caused by problems with the calibration.

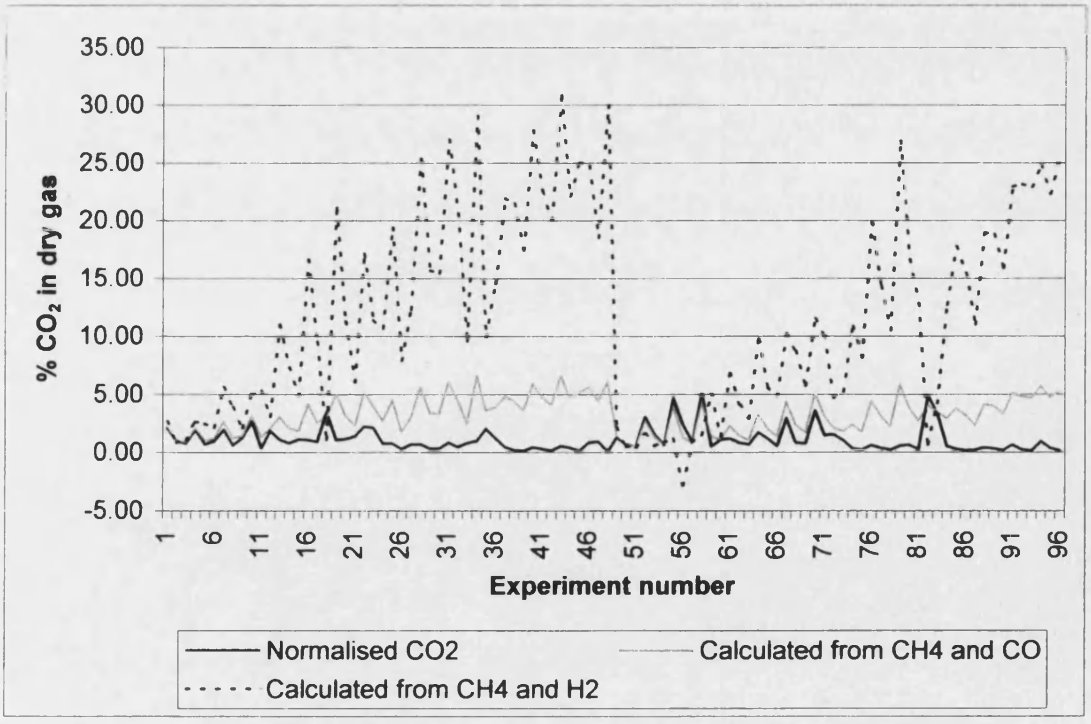

Figure 4.20 – Proportion of CO_2 in the dry product gas – Comparison of measured and calculated values

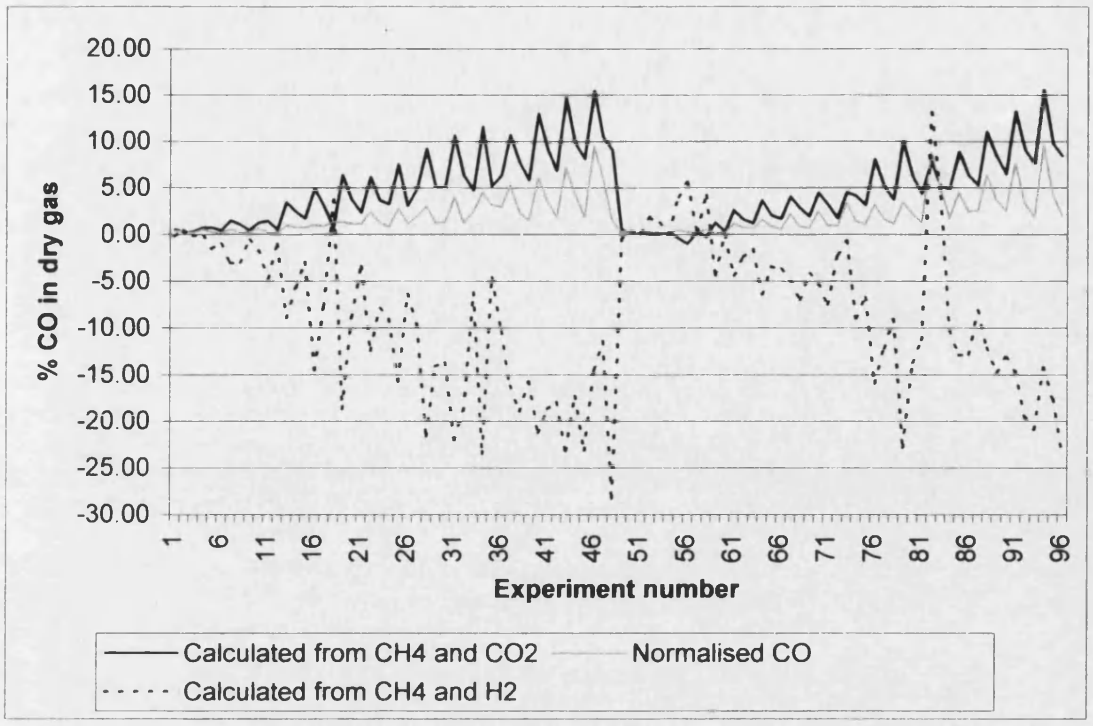

Figure 4.21 – Proportion of CO in the dry product gas – Comparison of measured and calculated values

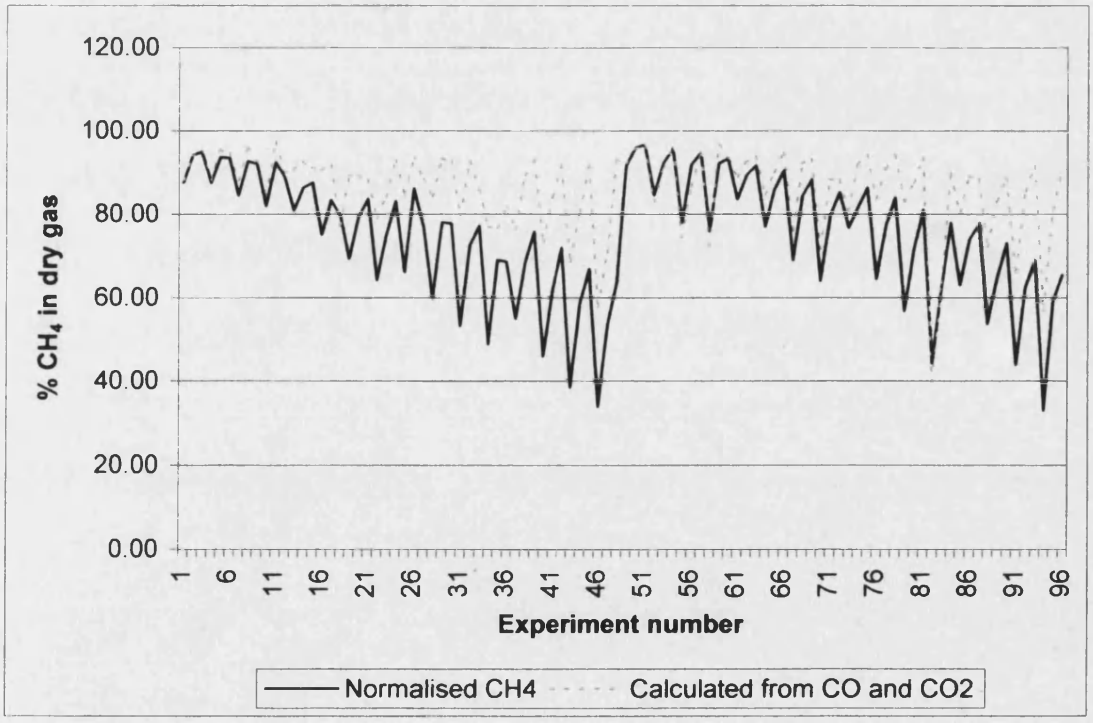

Figure 4.22 – Proportion of CH4 in the dry product gas – Comparison of measured and calculated values

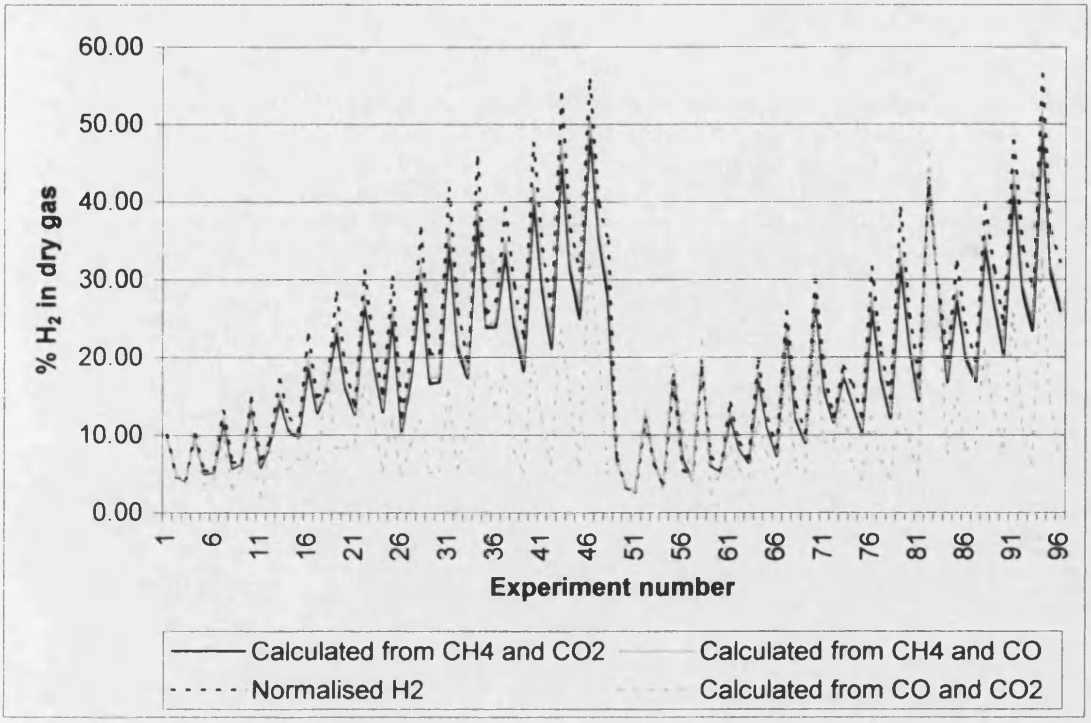

Figure 4.23 – Proportion of H_2 in the dry product gas – Comparison of measured and calculated values

When CO and CH_4 mole fractions are used to estimate the extents of reaction, the predicted value of CO_2 does not closely follow the measured value. The prediction for H_2 is fairly good though. When the measured mole fractions of CO and CO_2 are used, the predicted values for H_2 and CH_4 do not match up well with the measured values.

Generally, when the measured mole fraction of CH_4 is used, the prediction of H_2 is fairly good. CH_4 is a comparatively large peak on the chromatograms and has a relatively high precision, which makes it a suitable measurement on which to base the calculation of the material balance.

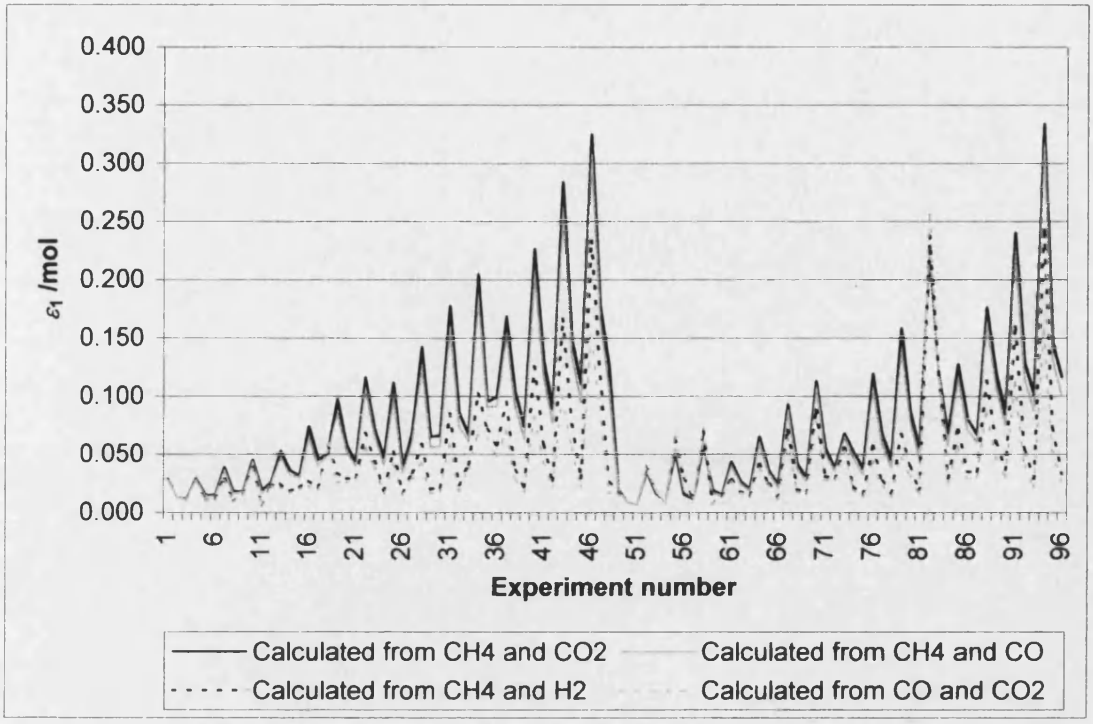

Figure 4.24 – Molar extent of Reaction 1 calculated from various pairs of measured mole fractions

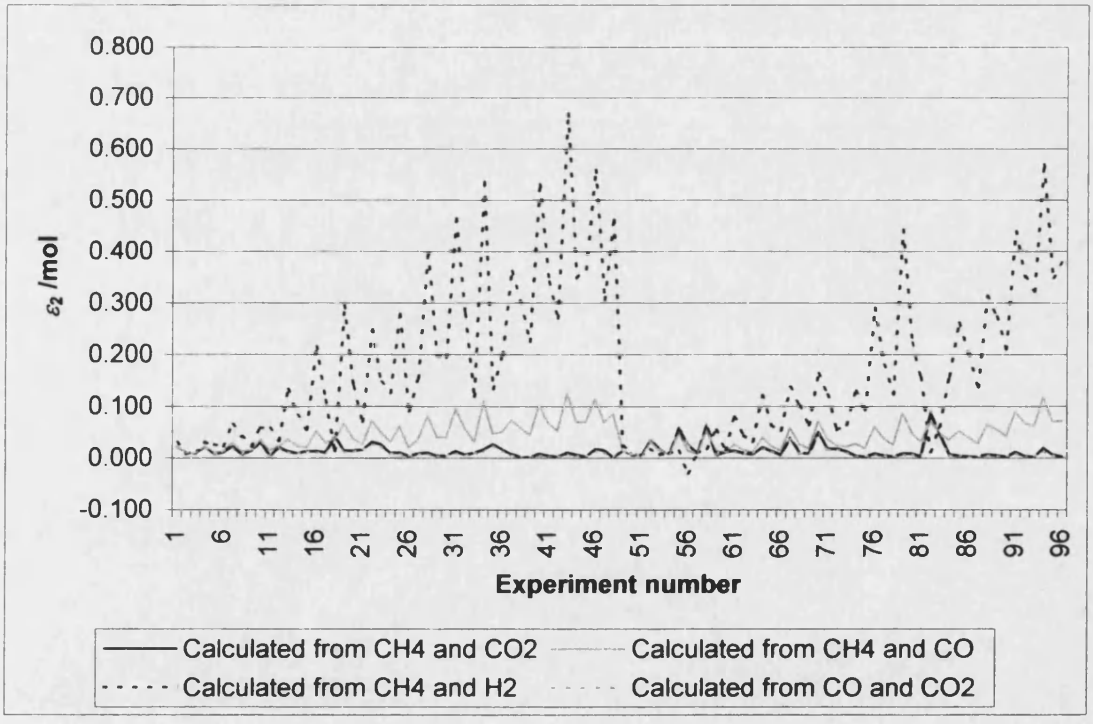

Figure 4.25 – Molar extent of Reaction 2 calculated from various pairs of measured mole fractions

When CO_2 and CH_4 are used to calculate ε_1 and ε_2, the predicted values of CO are generally higher than the measured values. However, the trend from experiment to experiment is similar. This suggests that there was some systematic error in the measurement of CO that caused it to be under-valued.

In conclusion, the best measured mole fractions to use in the calculation of the material balance are those of CO_2 and CH_4. There is likely to have been a systematic error in the measurement of CO by the GC. Although the method of calibration and sampling used have largely eliminated any random errors, it is always possible for an unforeseen systematic error to occur. This could be due to the CO peak being a shoulder on the CH_4 peak for most of the samples. If that is the case, it is likely that the values for CH_4 were also under-valued, although the effect would not have been so marked since the peak was always so much larger. CO_2's separate peak should have ensured that there was no such systematic error present in its readings.

The readings for H_2 would appear to have been too high, suggesting a problem with the method of calibration used. It should be noted that, during the normalisation calculation, the values for the other components would have been all reduced slightly relative to that for H_2 if the H_2 reading was too high. To prevent this problem occurring in the future, the sample gas should be properly dried before injection into the GC. Then it would be unnecessary to measure the value for H_2 at all.

4.5.8 Estimating precision of normalised data

The normalised values for the components in the dry gas are effectively calculated by multiplying all of the measured values by a conversion factor. The errors in the normalised values are, therefore, simply calculated from the errors in the measured values, multiplied by the same factor:

The errors in the mole fractions are simply $1/100^{th}$ of the those of the mole percentages.

4.5.9 *Estimating precision of the extents of reaction*

The error in the initial number of moles of CH_4 is zero, since this was specified as the basis of the calculation. Therefore, the error in A', $\delta A'$, is given by the following equation, which was derived from the general relationship for uncertainty in a function of one variable (Taylor, 1997, p. 65):

$$\delta A' = \left|\frac{\partial A'}{\partial y_{CH_4,dry}}\right| \delta y_{CH_4,dry} = \delta y_{CH_4,dry} \left|-\frac{n_{0,CH_4}}{3y_{CH_4,dry}^2}\right| \tag{4.29}$$

Similarly, the errors in B', C' and D' are given by:

$$\delta B' = \left|\frac{dB'}{dy_{CH_4,dry}}\right| \delta y_{CH_4,dry} = \delta y_{CH_4,dry} \left|\frac{1}{(3y_{CH_4,dry}+1)^2}\right| \tag{4.30}$$

$$\delta C' = \left|\frac{\partial C'}{\partial y_{CO_2,dry}}\right| \delta y_{CO_2,dry} = \delta y_{CO_2,dry} \left|\frac{n_{0,CH_4}}{(1-y_{CO_2,dry})^2}\right| \tag{4.31}$$

$$\delta D' = \left|\frac{dD'}{dy_{CO_2,dry}}\right| \delta y_{CO_2,dry} = \delta y_{CO_2,dry} \left|\frac{3}{(1-y_{CO_2,dry})^2}\right| \tag{4.32}$$

ε_1 is a function of A', B', C' and D'. It is reasonable to say that the errors in these coefficients are random and independent, so the error in ε_1, $\delta\varepsilon_1$, can be estimated using Equation (4.33):

$$(\delta\varepsilon_1)^2 = \left(\frac{\partial\varepsilon_1}{\partial A'}\delta A'\right)^2 + \left(\frac{\partial\varepsilon_1}{\partial B'}\delta B'\right)^2 + \left(\frac{\partial\varepsilon_1}{\partial C'}\delta C'\right)^2 + \left(\frac{\partial\varepsilon_1}{\partial D'}\delta D'\right)^2 \tag{4.33}$$

where $\dfrac{\partial\varepsilon_1}{\partial A'} = \dfrac{1}{B'D'+1}$

$$\frac{\partial\varepsilon_1}{\partial B'} = -\frac{C'+A'D'}{(B'D'+1)^2}$$

$$\frac{\partial\varepsilon_1}{\partial C'} = -\frac{B'}{B'D'+1}$$

and $\dfrac{\partial\varepsilon_1}{\partial D'} = B'\dfrac{B'C'-A'}{(B'D'+1)^2}$

ε_2 is a function of C', D' and ε_1 and its error, $\delta\varepsilon_2$, is estimated by Equation (4.34):

$$(\delta\varepsilon_2)^2 = (\delta C')^2 + (\varepsilon_1 \delta D')^2 + (D' \delta\varepsilon_1)^2 \tag{4.34}$$

4.5.10 Precision of estimates of product composition

The errors in the number of moles of CO_2 and CH_4 are given by:

$$\delta n_{CO_2} = \delta\varepsilon_2 \tag{4.35}$$

$$\delta n_{CH_4} = \delta\varepsilon_1 \tag{4.36}$$

The number of moles of CO and H_2 are functions of both ε_1 and ε_2, which are not independent of one another. Therefore the errors in the number of moles of CO and H_2 are given by:

$$\delta n_{CO} = \delta\varepsilon_1 + \delta\varepsilon_2 \tag{4.37}$$

$$\delta n_{H_2} = 3\delta\varepsilon_1 + \delta\varepsilon_2 \tag{4.38}$$

The error in the initial number of moles of H_2O is estimated from the error in the *SMR* by the following equation:

$$\delta n_{0,H_2O} = n_{0,CH_4} \delta SMR \tag{4.39}$$

The number of moles of H_2O in the product is given by Equation (4.12) and is a function of the initial number of moles, ε_1 and ε_2. ε_1 and ε_2 are not independent of one another, but they are independent of the initial number of moles of H_2O, so the error in the number of moles of H_2O in the product is given by:

$$\delta n_{H_2O} = \left[(\delta n_{0,H_2O})^2 + (\delta\varepsilon_1 + \delta\varepsilon_2)^2\right]^{1/2} \tag{4.40}$$

The mole fraction of each component is a function of the number of moles of that component and the total number of moles. The error in the total number of moles is clearly not independent of the errors in the individual numbers of moles. Therefore the error in the mole fraction of component *i* is given by:

$$\delta y_i = y_i\left(\frac{\delta n_i}{n_i} + \frac{\delta n_{\text{TOTAL}}}{n_{\text{TOTAL}}}\right) \tag{4.41}$$

where $\delta n_{\text{TOTAL}} = \sum \delta n_i$

The error in the molar percentage of component *i* is simply 100 times that of the mole fraction.

4.5.11 Example results

Continuing the example calculations for Experiment number 35, Tables 4.14 to 4.16 give the results at each stage of the material balance.

Table 4.14 – Molar percentages and normalised mole fractions of components in the product gas of Experiment number 35

	CO_2	O_2	N_2	CH_4	CO	H_2
Y_i	1.93 %	0.806 %	2.56 %	65.3 %	3.1 %	24.4 %
δY_i	0.03 %	0.01 %	0.06 %	0.35 %	0.3 %	
y_i	0.0204	0	0	0.689	0.0326	0.258
δy_i	0.0003	-	-	0.004	-	-

The steam to methane ratio for Experiment 35 was calculated from the temperature and pressure in the autoclave during the experiment. The result was $SMR = 2.1 \pm 0.7$ mol/mol.

Table 4.15 – Molar extents of reaction for Experiment number 35 and the coefficients used in their calculation

	A	*B*	*C*	*D*	ε_1	ε_2
Value	0.101	0.225	0.021	0.062	**0.095 mol**	**0.0267 mol**
Uncertainty	0.003	0.0004	0.0003	0.0009	**0.003 mol**	**0.0004 mol**

Table 4.16 – Results of the material balance calculation for Experiment number 35

	CO_2	CH_4	CO	H_2	H_2O
n_i	0.0267 mol	0.905 mol	0.069 mol	0.313 mol	2.0 mol
δn_i	0.0004 mol	0.003 mol	0.003 mol	0.008 mol	0.7 mol
y_i	0.008	0.27	0.021	0.095	0.6
δy_i	0.002	0.06	0.005	0.023	0.3
Y_i	0.8 %	27 %	2.1 %	**9.5 %**	60 %
δY_i	0.2 %	6 %	0.5 %	**2 %**	30 %

4.5.12 Conclusion of reactor product analysis

Despite measuring the hydrogen concentration in the dry sample gas directly with the GC, it was found that it could be calculated more accurately by material balance using the measured concentrations of CH_4 and CO_2. Using a basis of 1 mol CH_4 in the feed, the extents of reaction were calculated, and from these the composition of the product gas was determined for each experimental run. The estimated proportional error in the calculated hydrogen concentrations ranged from 0.07 to 0.24, with the average being 0.14. The proportional errors estimated for the results of Experiment number 35, which is used as an example above, were amongst the largest recorded.

4.6 Results and discussion

4.6.1 Performance of cartridge heater

The cartridge heater was used to heat the block with the furnace switched off. The temperature of the block was recorded at regular intervals. Also recorded was the temperature of the air within the reactor tubes, which were left open. The results of this experiment are given in Figure 4.26 below.

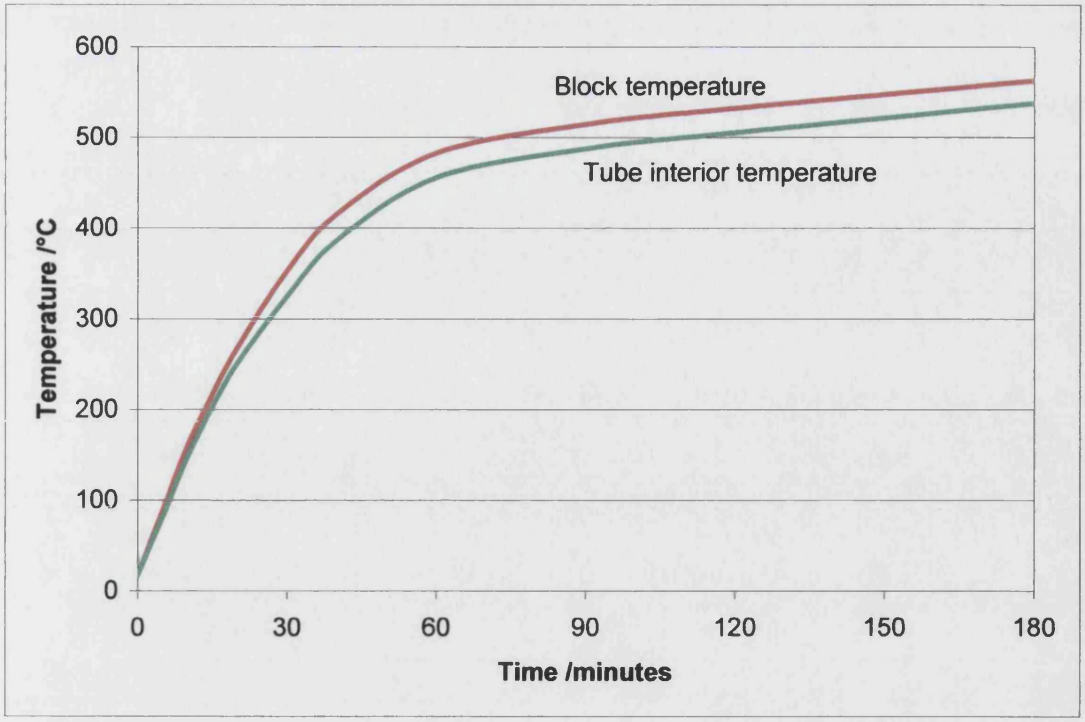

Figure 4.26 – Reactor temperature against time when heated by cartridge heater

The block temperature reached 500°C after about 70 minutes without any assistance from the furnace. The temperature inside the reaction tubes reached 450°C after about 60 minutes and 500°C after about 120 minutes. This is a sufficiently high temperature to initiate a catalytic combustion reaction in one of the reaction tubes (Ma *et al.*, 1996), so the viability of this approach has been demonstrated.

The time taken is acceptable due to fast start-up not being one of the requirements of this reactor. Also, the reactor was insulated only by being placed inside the furnace, with the ends sealed. Therefore, there would have been greater heat loss than for a well insulated system. Had there been zero heat loss (perfect insulation), the 350 W input heat would have raised the block temperature to 500°C in about 30 minutes.

One problem that was encountered was that the high furnace temperatures used for the later experiments damaged the electrical leads of the cartridge heater. This made it unsafe to use. In future, leads with a higher temperature resistance will be required.

4.6.2 Hydrogen production in the reforming reactor for steam to methane ratio of 4

The following figures show the performance of the reactor in terms of mol % of hydrogen in the **wet** product gas. The proportion of hydrogen in the wet product gas was calculated from the proportion in the sample gas for each experiment by material balance, as detailed above. There are separate data series in each figure for 2, 4, 7 and 10 minute duration experiments.

Effect of varying temperature

Figures 4.27 to 4.29 show the effect on hydrogen production of varying the reactor temperature for a given reactor pressure.

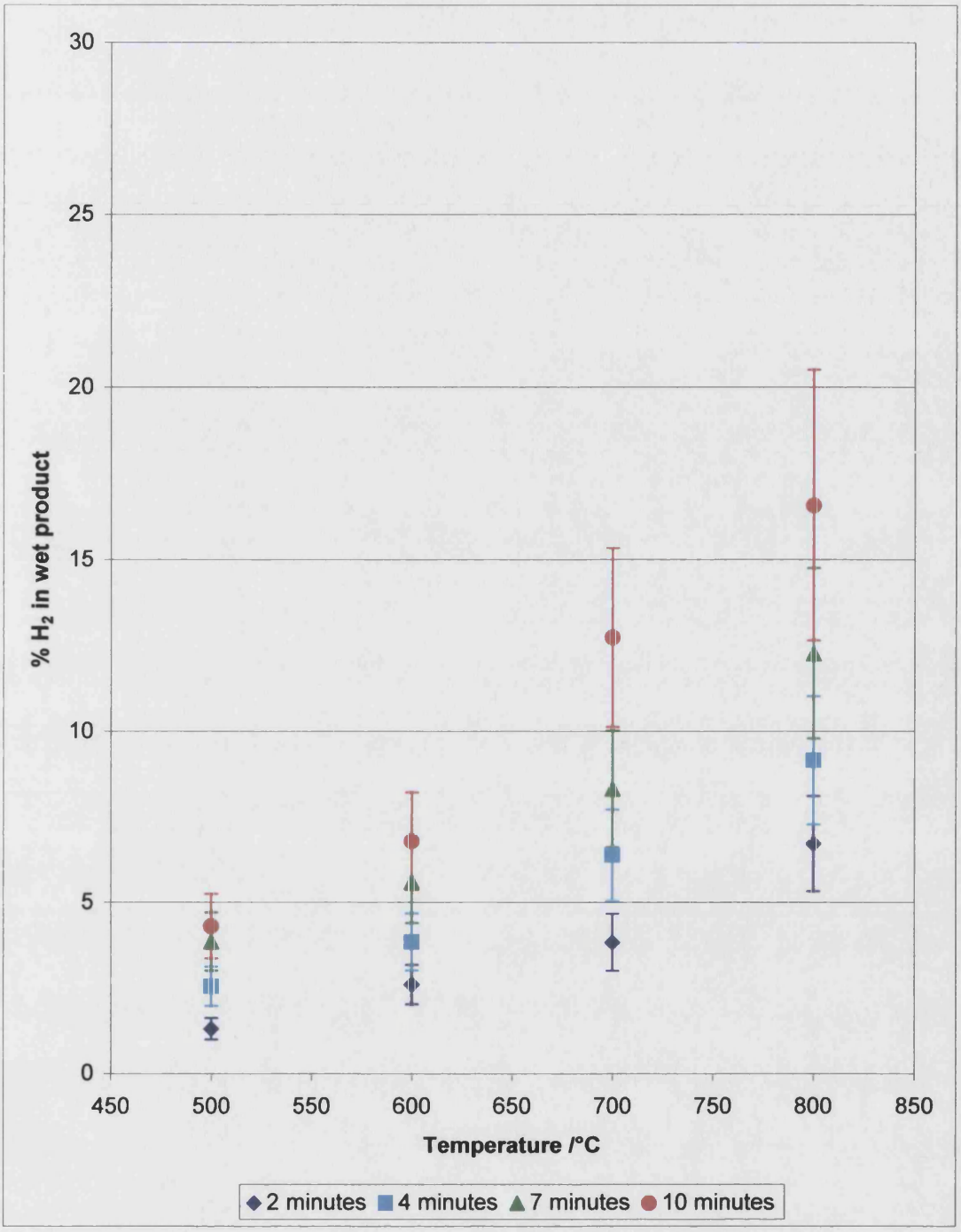

Figure 4.27 – Hydrogen in wet product gas against temperature at 2 bar, steam to methane ratio of 4

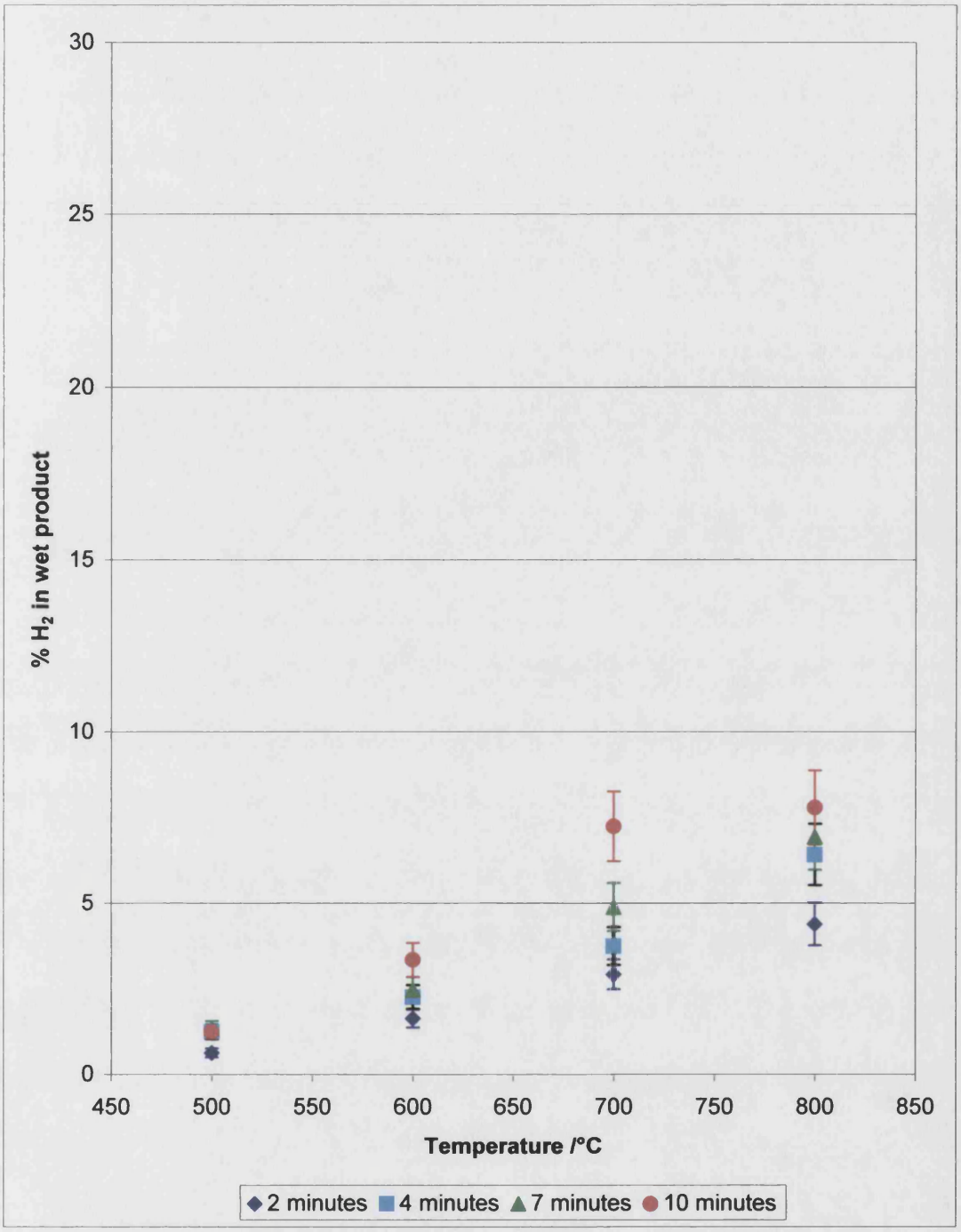

Figure 4.28 – Hydrogen in wet product gas against temperature at 6 bar, steam to methane ratio of 4

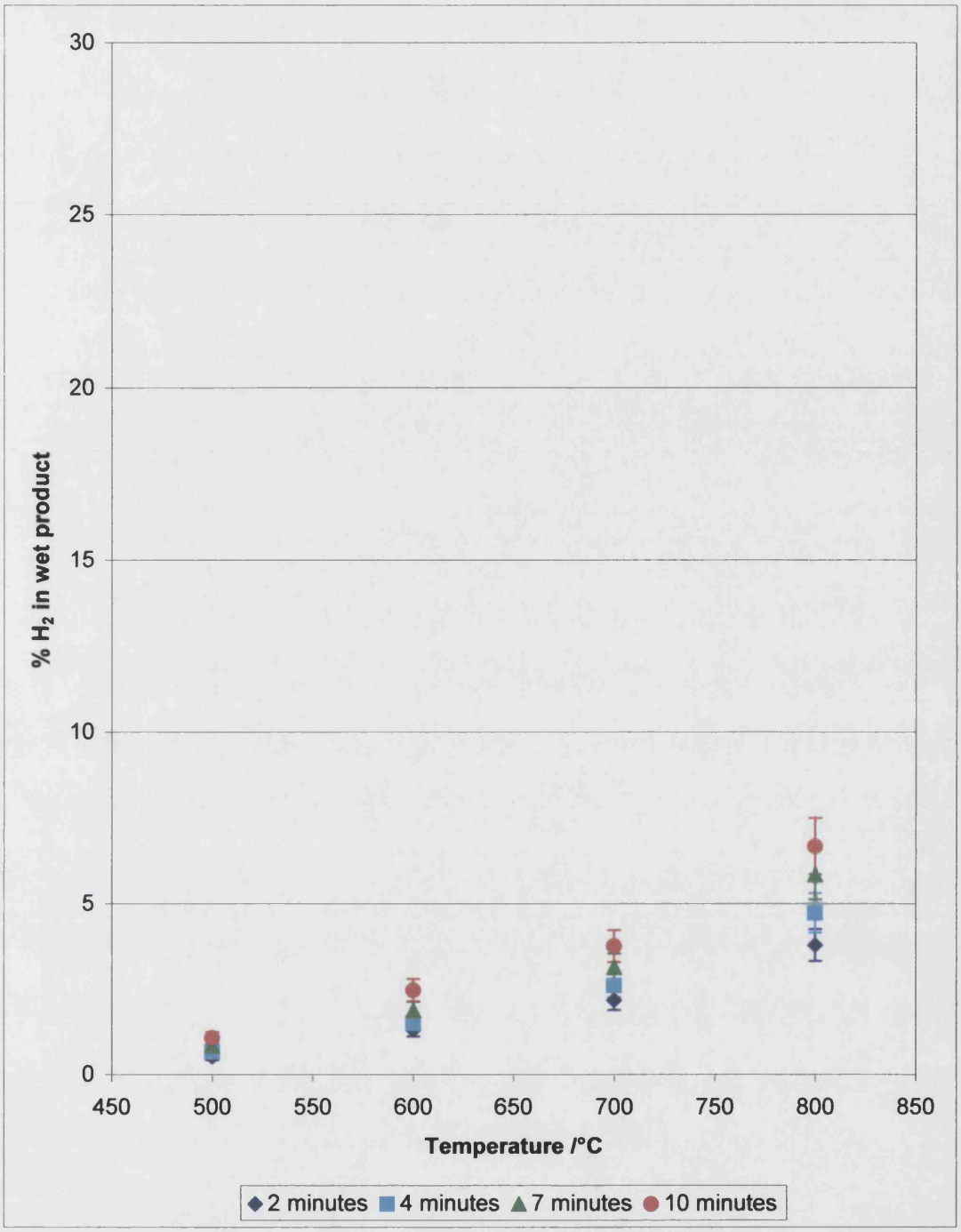

Figure 4.29 – Hydrogen in wet product gas against temperature at 9.5 bar, steam to methane ratio of 4

It is evident from the preceding figures that hydrogen yield increased with higher temperatures. This is as predicted by the thermodynamic analysis. Hydrogen yield also increased with longer residence times, indicating that equilibrium was not attained.

Effect of varying pressure

Figures 4.30 to 4.33 show the effect on hydrogen production of varying the reaction pressure for a given reactor temperature.

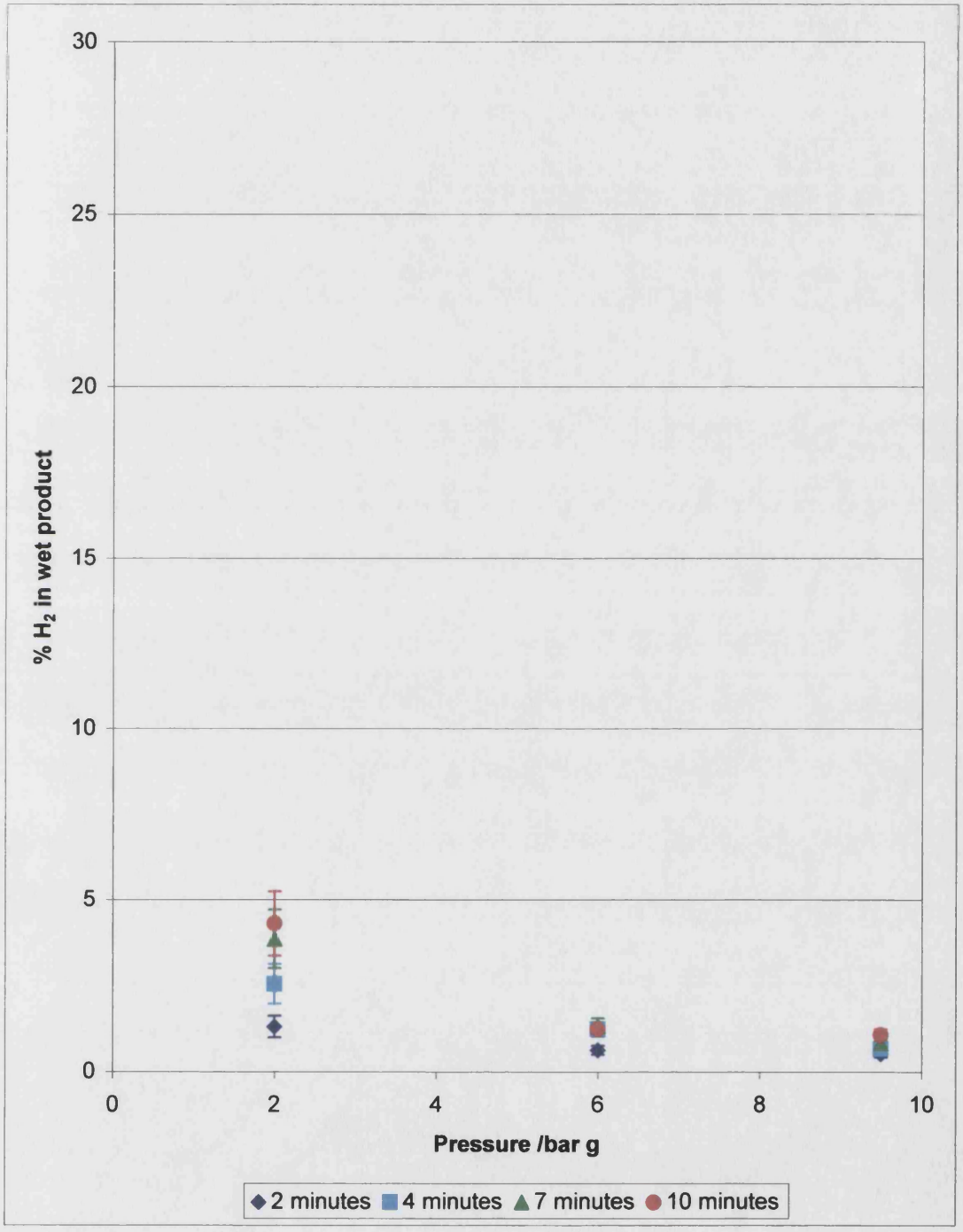

Figure 4.30 – Hydrogen in wet product gas against pressure at 500°C, steam to methane ratio of 4

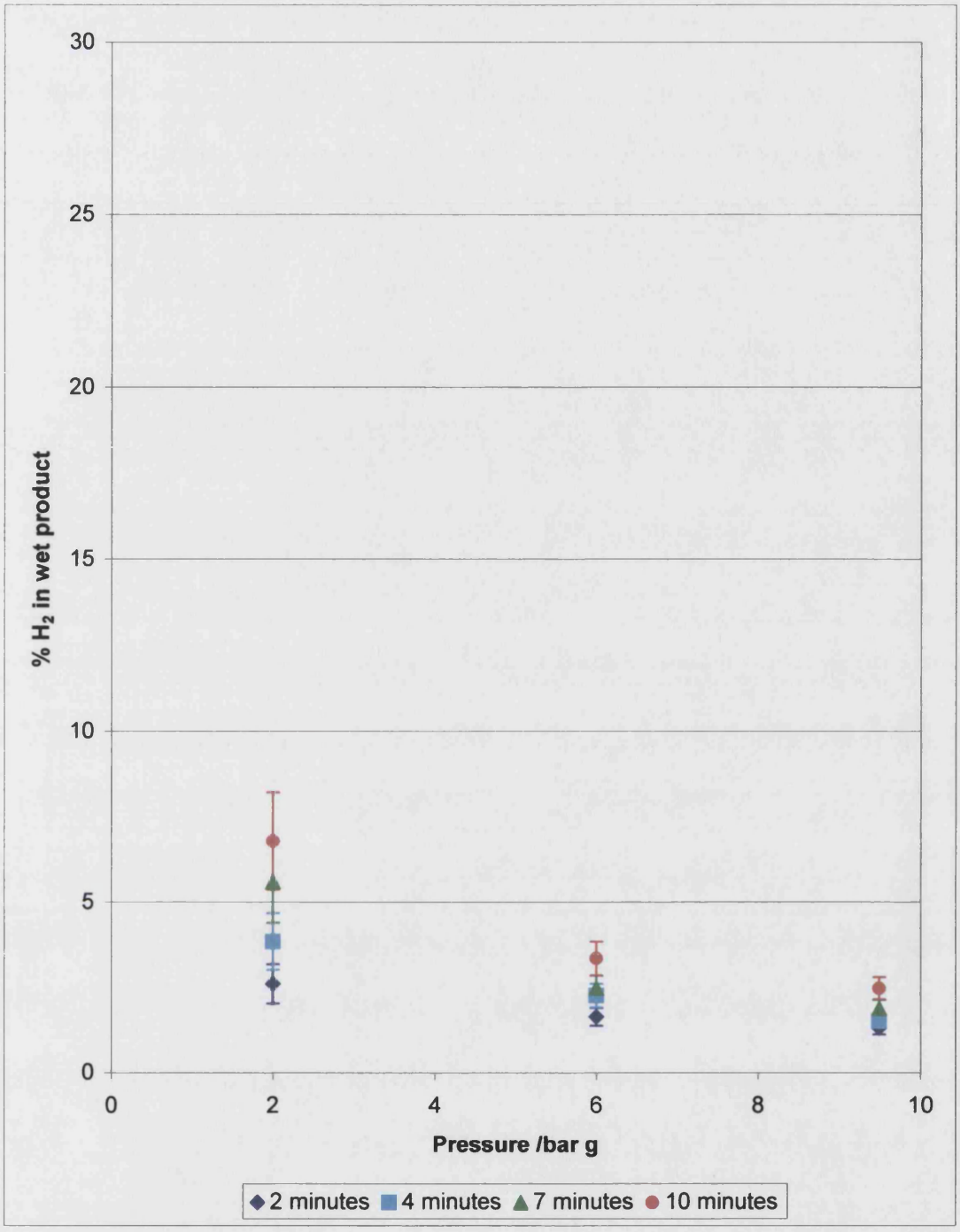

Figure 4.31 – Hydrogen in wet product gas against pressure at 600°C, steam to methane ratio of 4

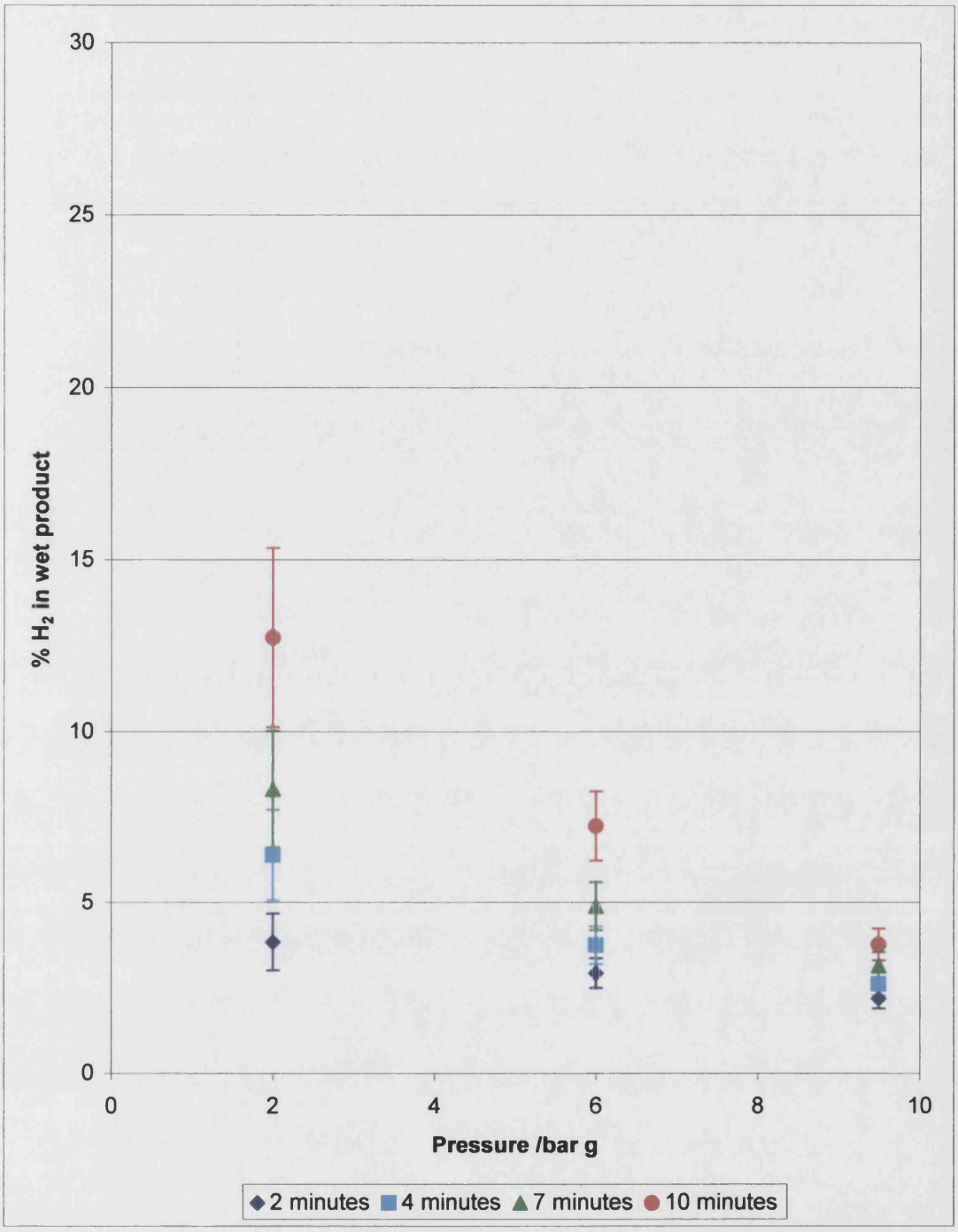

Figure 4.32 – Hydrogen in wet product gas against pressure at 700°C, steam to methane ratio of 4

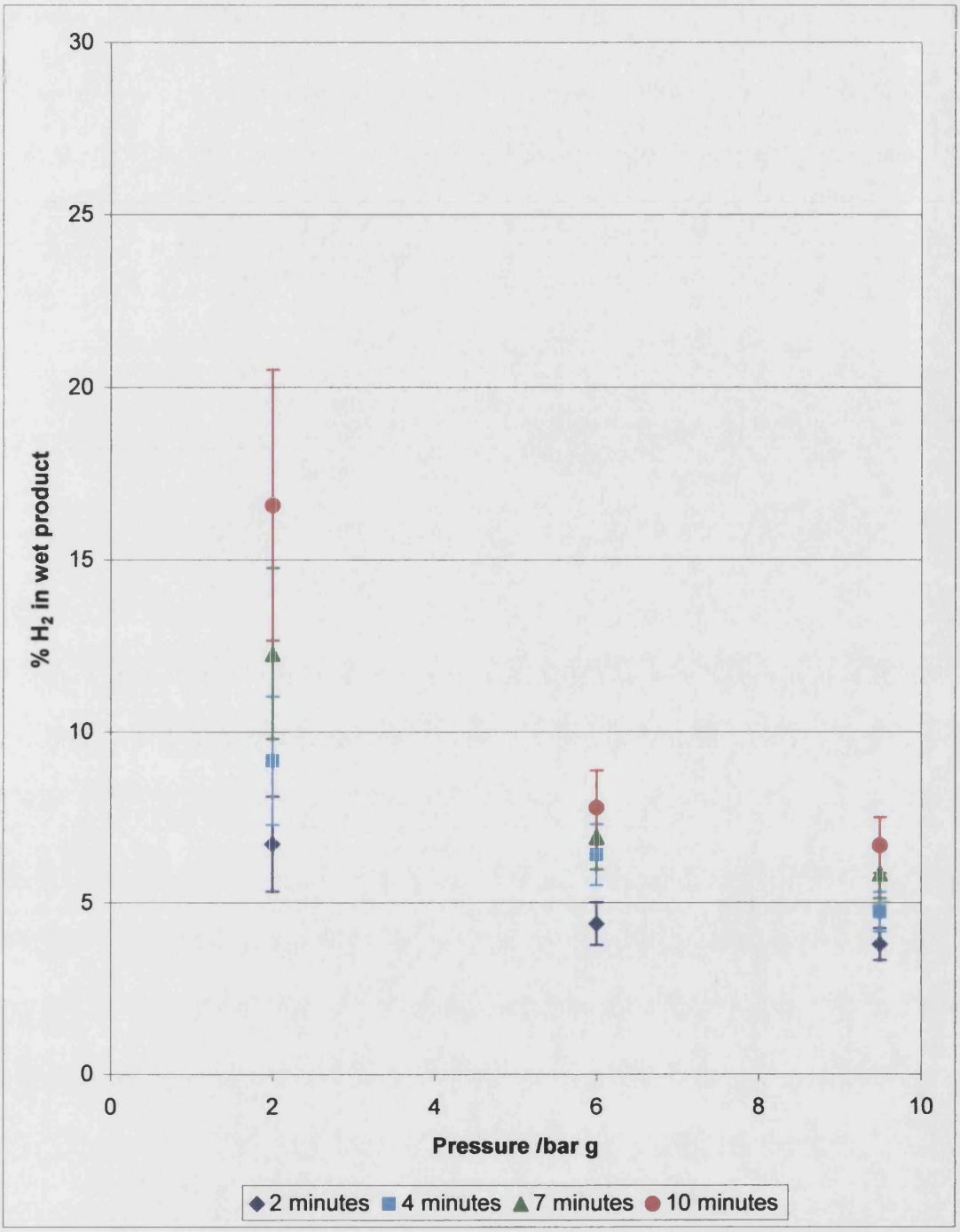

Figure 4.33 – Hydrogen in wet product gas against pressure at 800°C, steam to methane ratio of 4

As predicted by thermodynamic analysis, the hydrogen yield was reduced at higher pressures.

4.6.3 Hydrogen production in the reforming reactor for steam to methane ratio of 2

Effect of varying temperature

Figures 4.34 to 4.36 show the effect of varying the temperature on hydrogen yield, now for a steam to methane ratio of 2 in the feed gas.

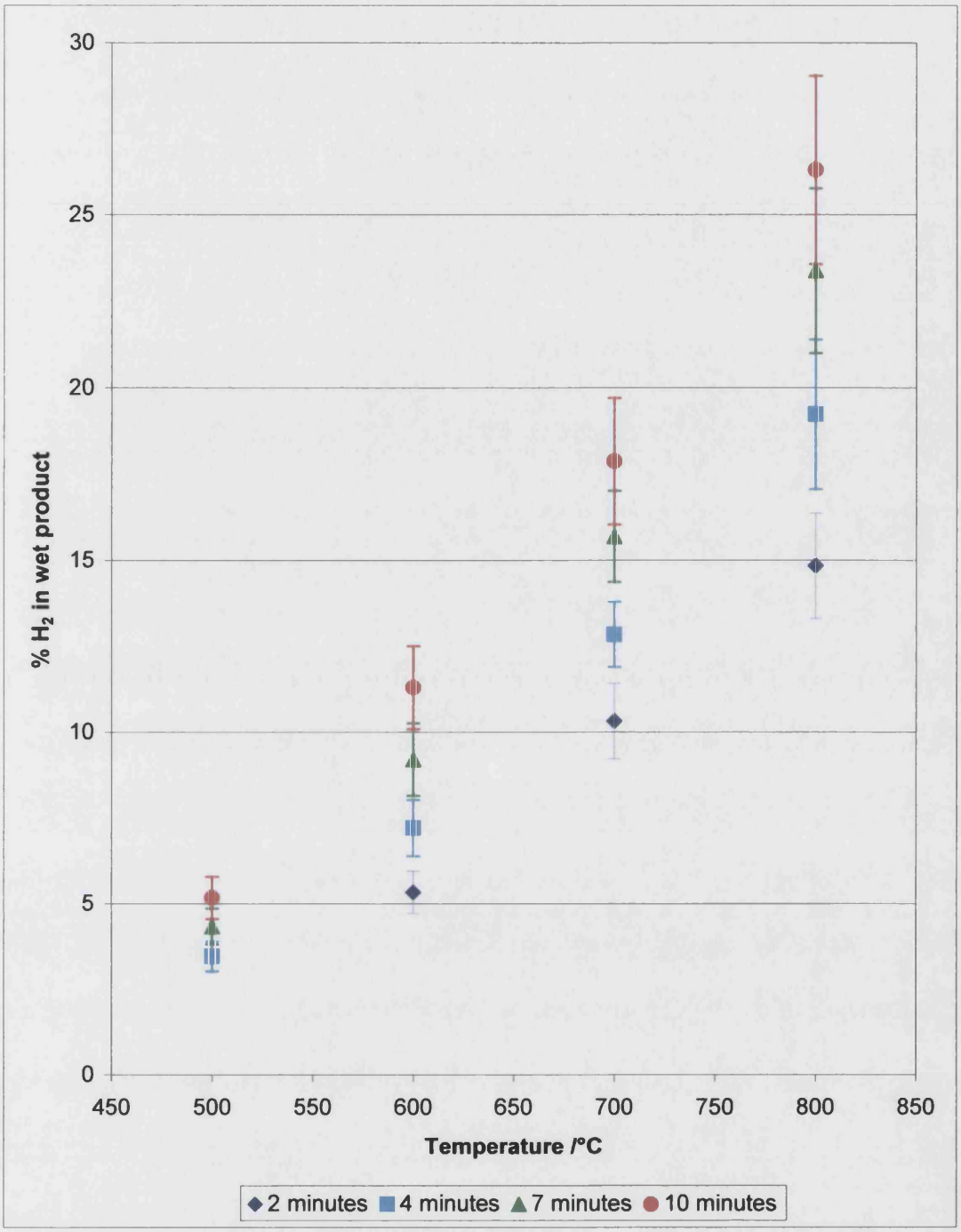

Figure 4.34 – Hydrogen in wet product gas against temperature at 2 bar, steam to methane ratio of 2

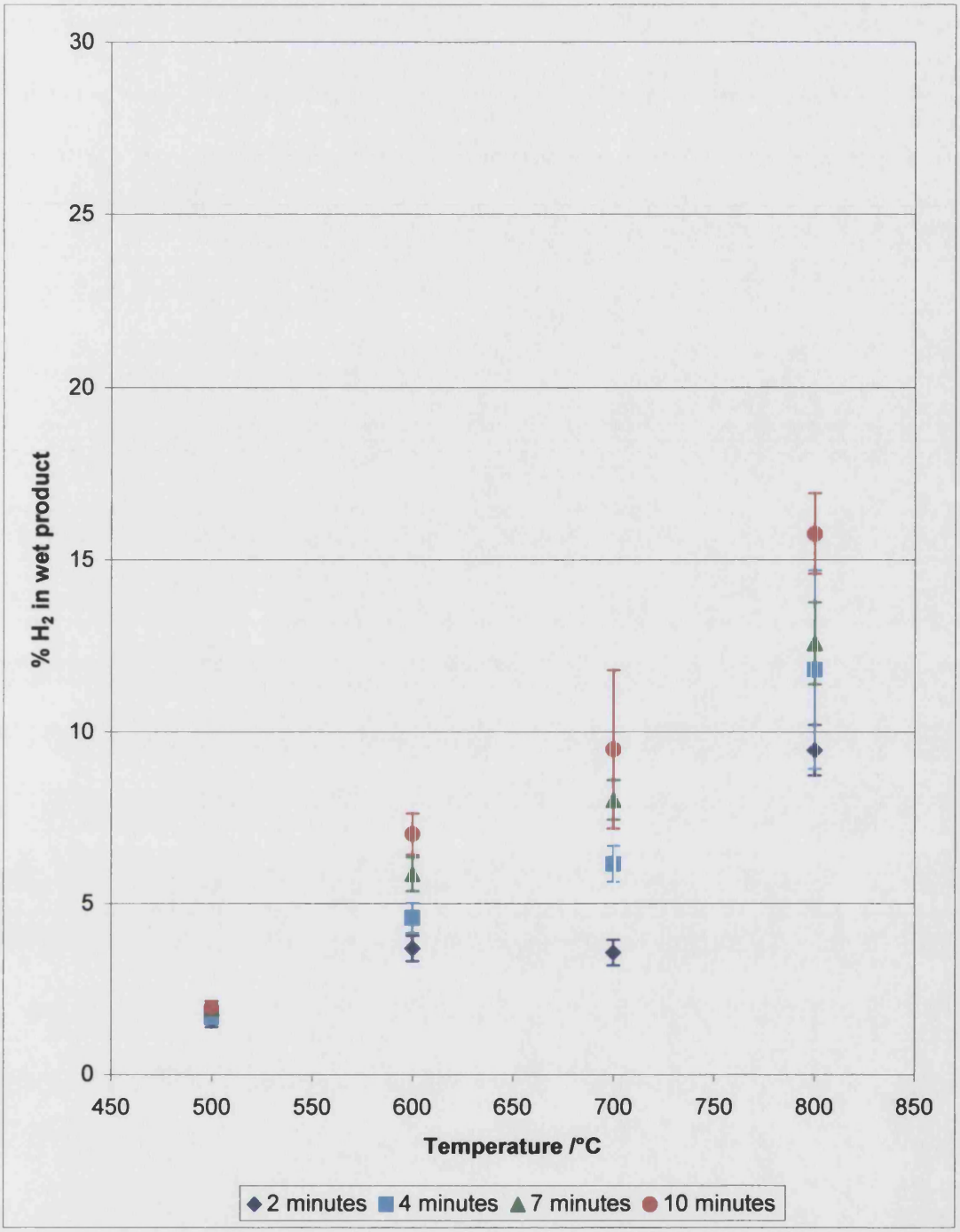

Figure 4.35 – Hydrogen in wet product gas against temperature at 6 bar, steam to methane ratio of 2

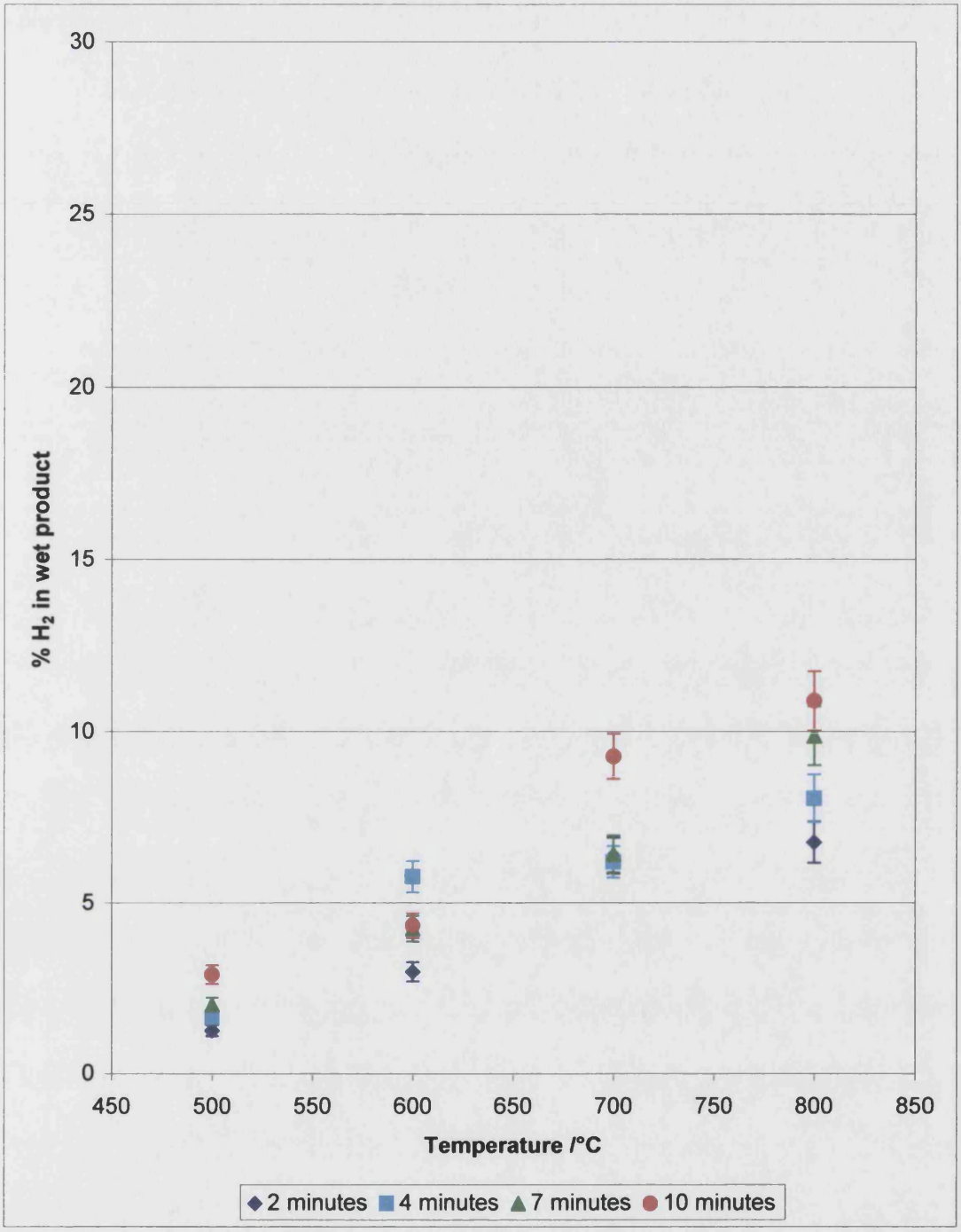

Figure 4.36 – Hydrogen in wet product gas against temperature at 9.5 bar, steam to methane ratio of 2

As was the case with a feed steam to methane ratio of 4, the preceding figures show the expected relationship between reaction temperature and hydrogen yield. The yield was significantly higher for a steam to methane ratio of 2, which is most probably due to a reduction in the excess of steam present in the product gas.

Effect of varying pressure

Figures 4.37 to 4.40 show the effect of varying the pressure for a given reactor temperature on the proportion of hydrogen in the product stream with a steam to methane ratio of 2.

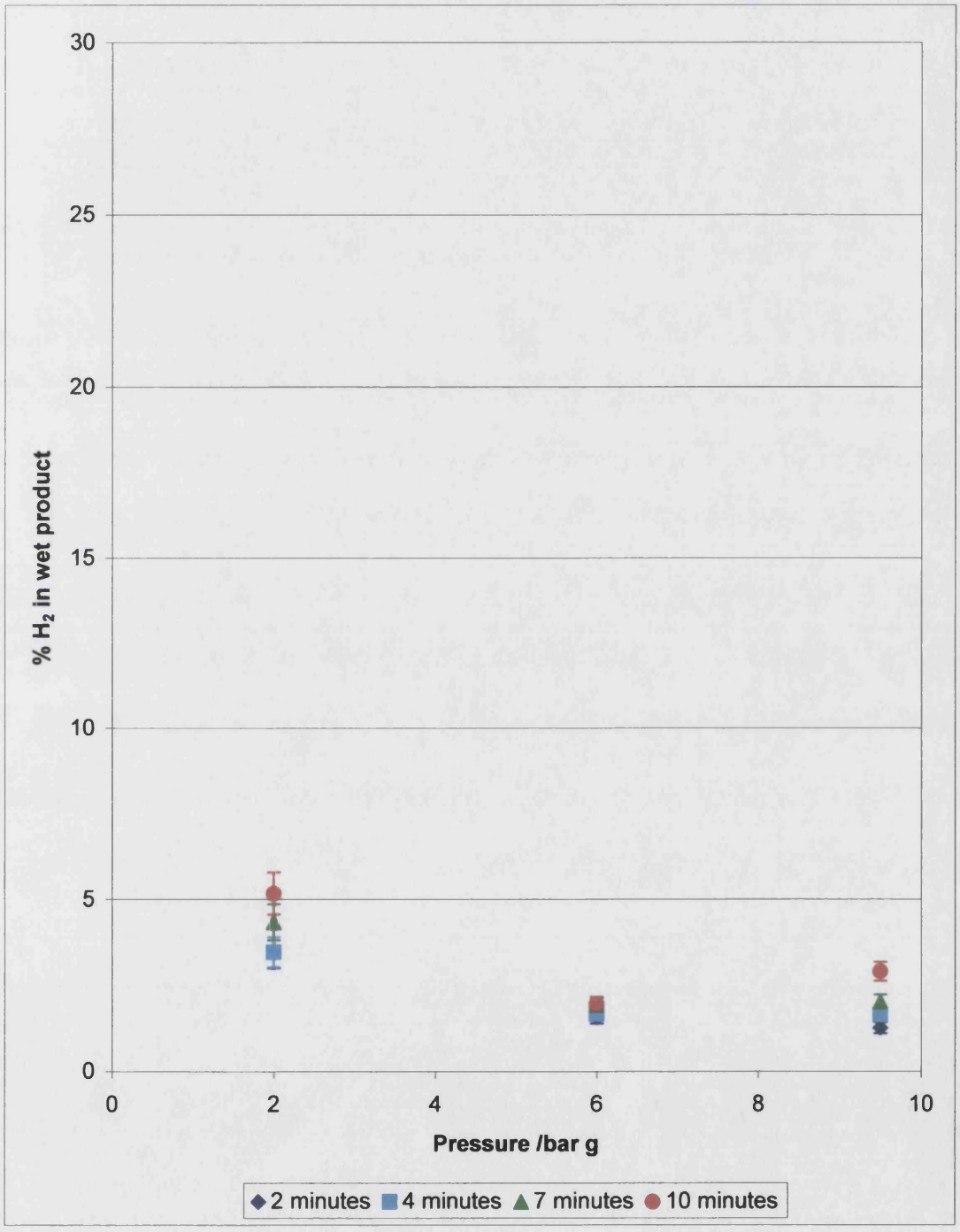

Figure 4.37 – Hydrogen in wet product gas against pressure at 500°C, steam to methane ratio of 2

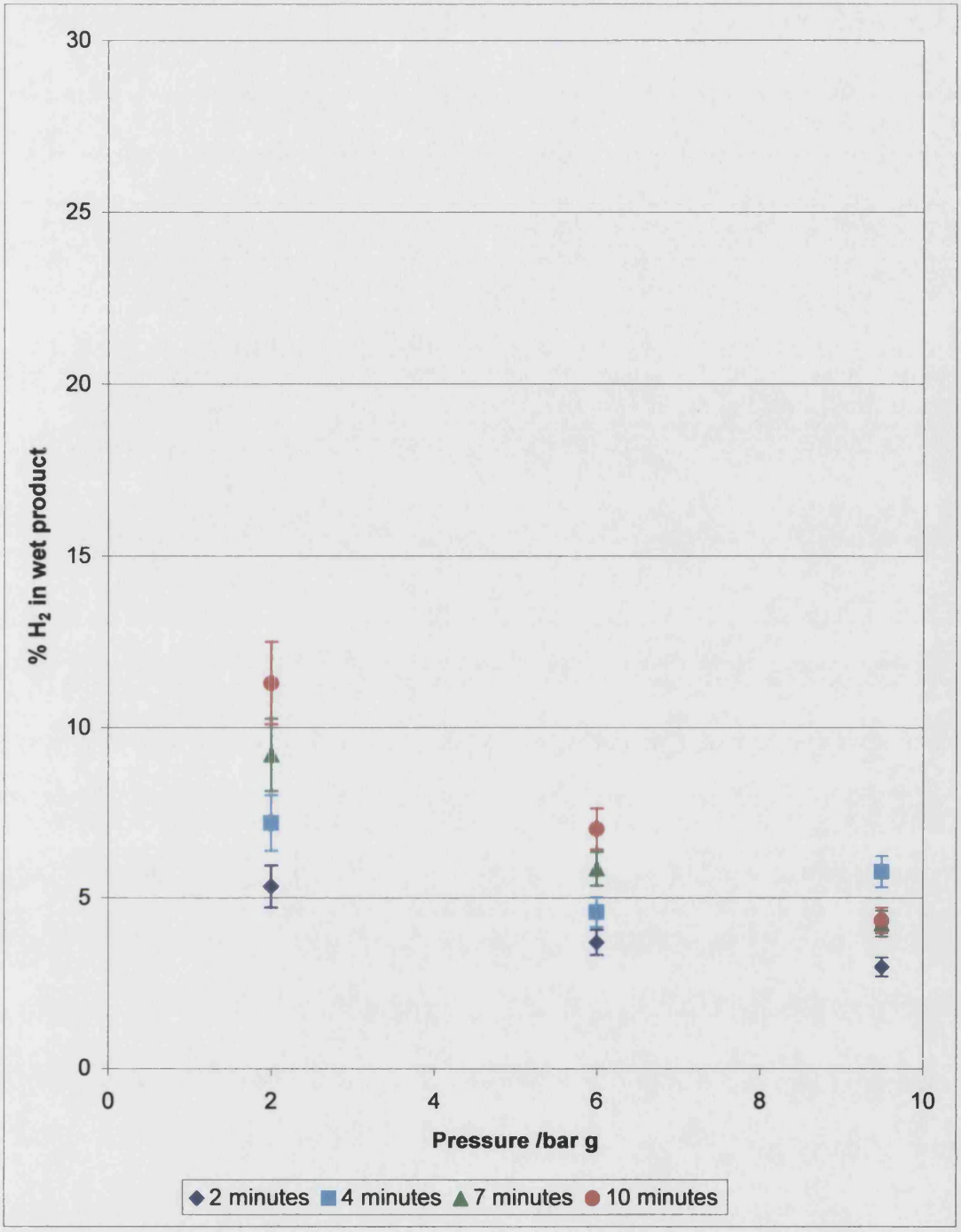

Figure 4.38 – Hydrogen in wet product gas against pressure at 600°C, steam to methane ratio of 2

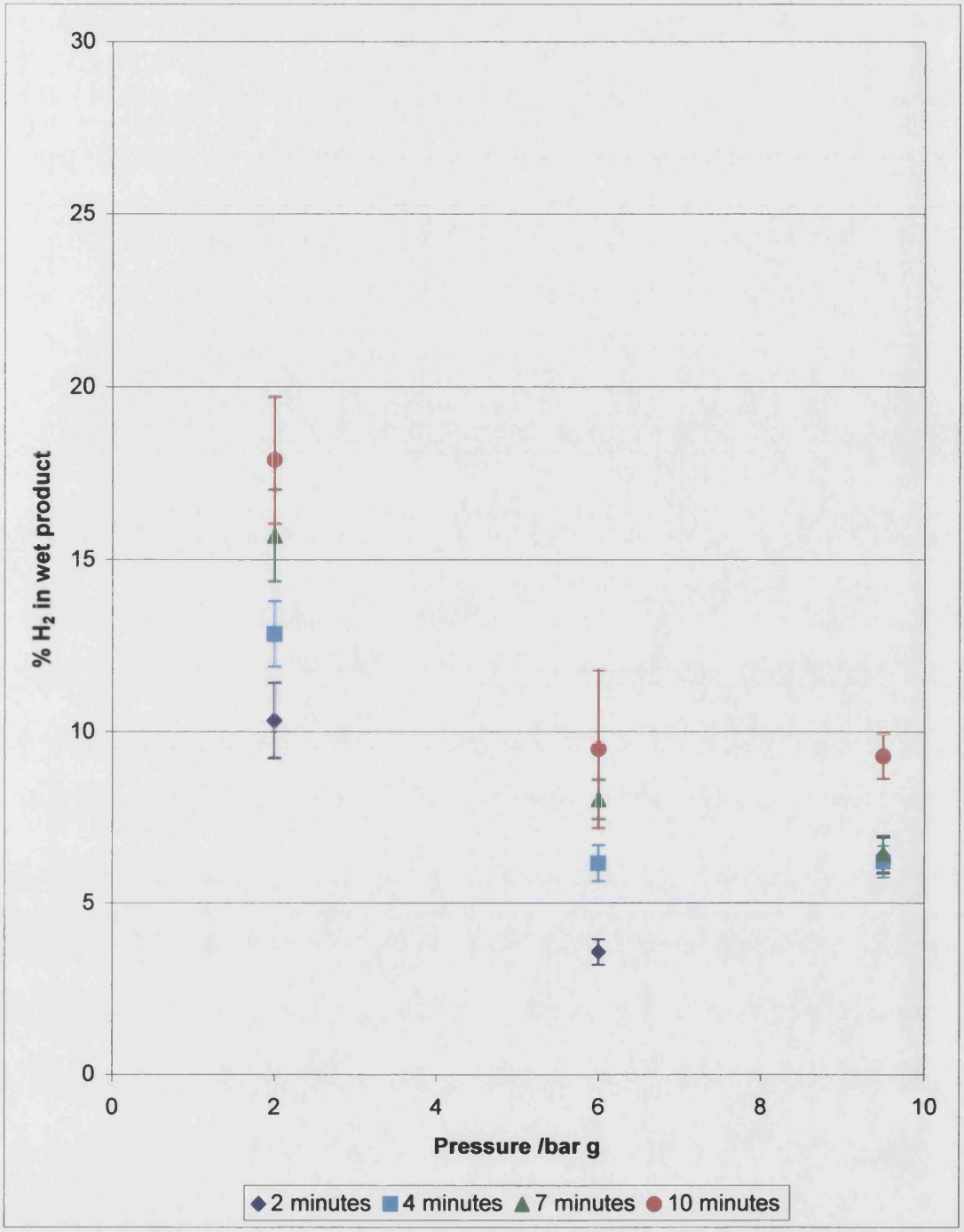

Figure 4.39 – Hydrogen in wet product gas against pressure at 700°C, steam to methane ratio of 2

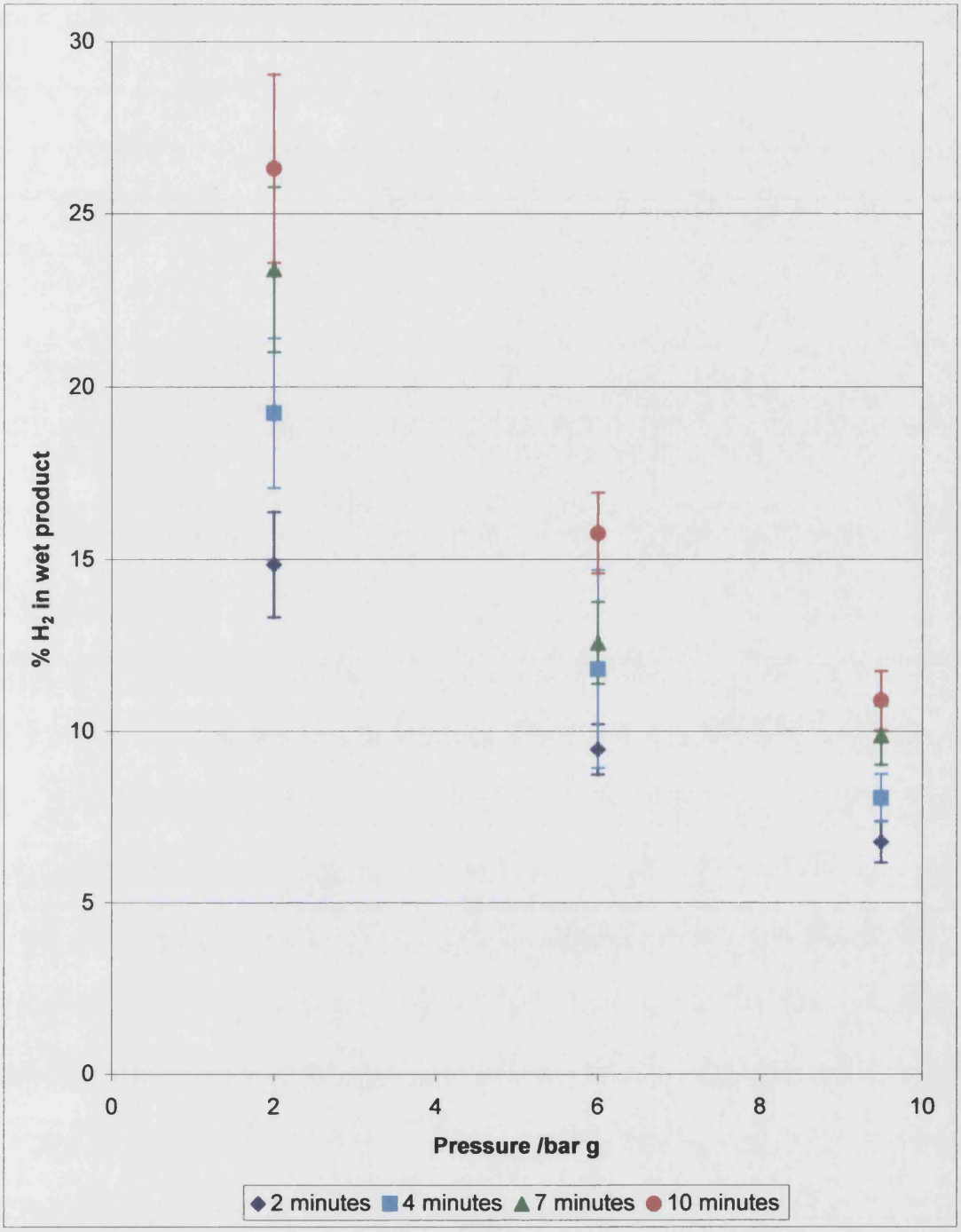

Figure 4.40 – Hydrogen in wet product gas against pressure at 800°C, steam to methane ratio of 2

Again, as expected, the hydrogen yield was reduced at higher reaction pressures. Figure 4.40 shows the highest hydrogen proportion recorded during the experiments: 26 ± 3 %.

4.6.4 Methane conversion in the reforming reactor for steam to methane ratio of 4

The fractional conversion of methane indicates the progression of the steam reforming reaction. It is equal to the molar extent of the steam reforming reaction, divided by the initial number of moles of methane. The following figures show the fractional conversion of methane against temperature and pressure. It was expected that the fractional conversion of methane would be increased by higher reaction temperatures, higher steam to methane ratios and lower reaction pressures.

Effect of varying temperature

Figures 4.41 to 4.43 show the fractional conversion of methane against reaction temperature for a given reaction pressure, with a steam to methane ratio of 4.

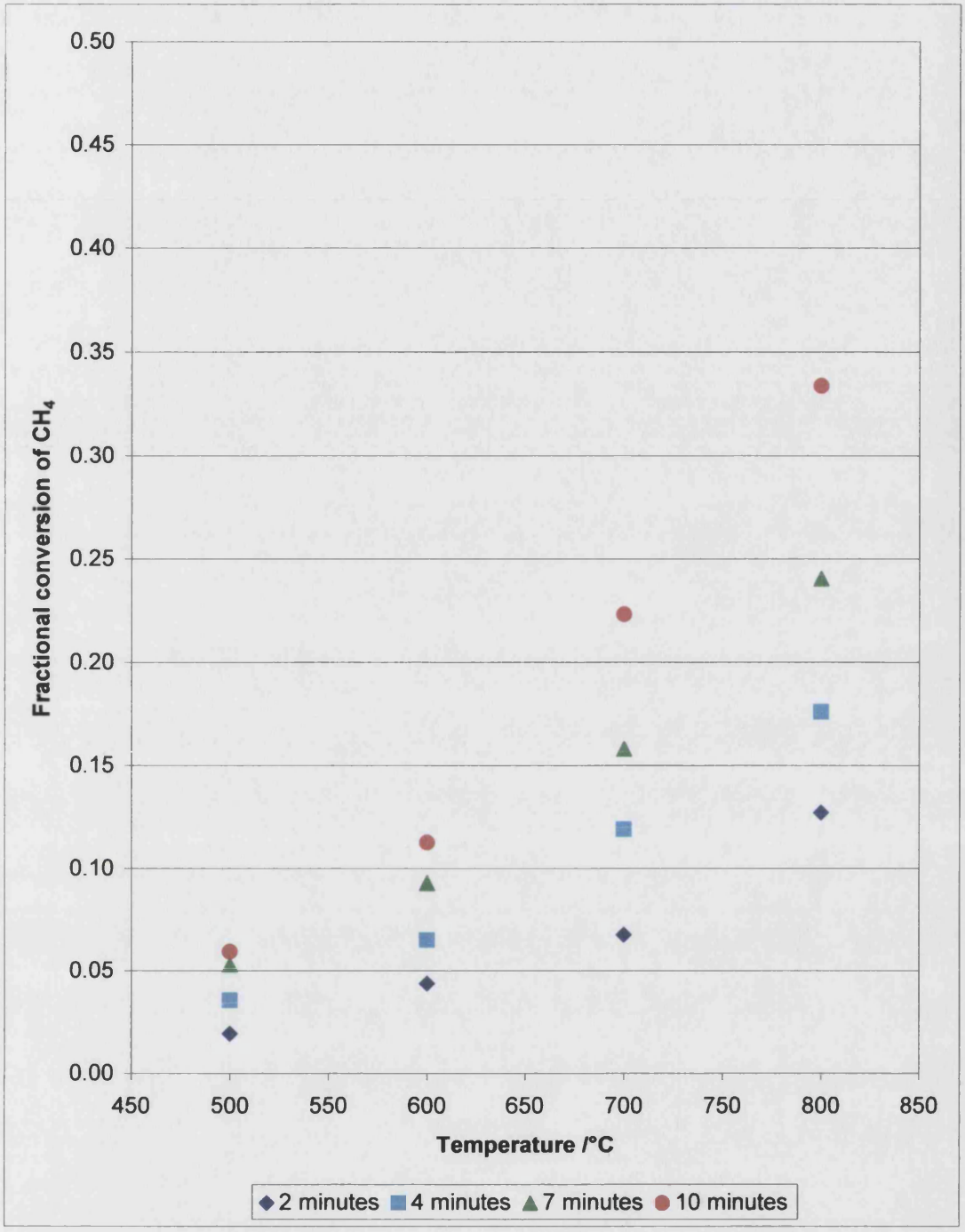

Figure 4.41 – Fractional conversion of CH_4 against temperature at 2 bar g, steam to methane ratio 4

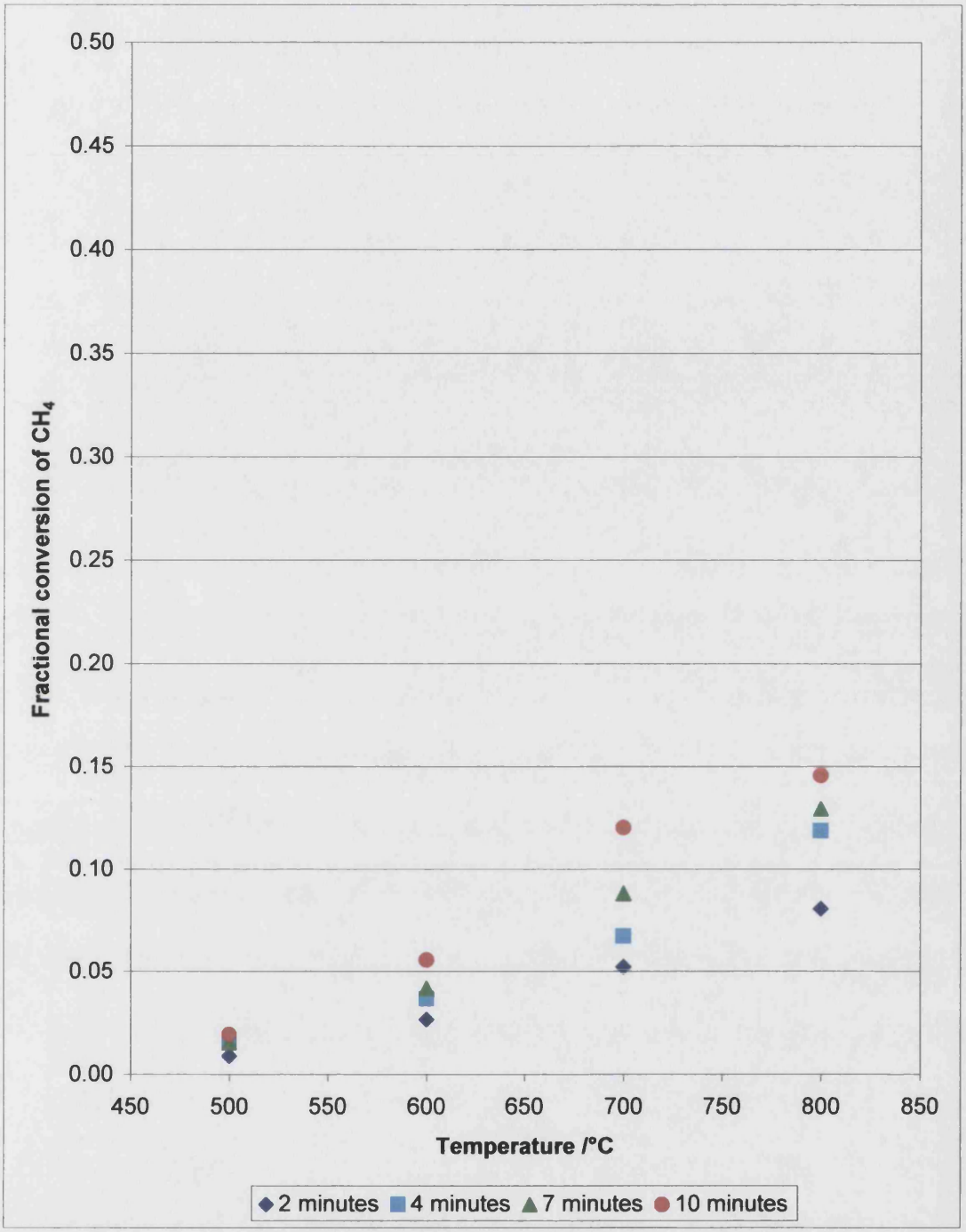

Figure 4.42 – Fractional conversion of CH_4 against temperature at 6 bar g, steam to methane ratio 4

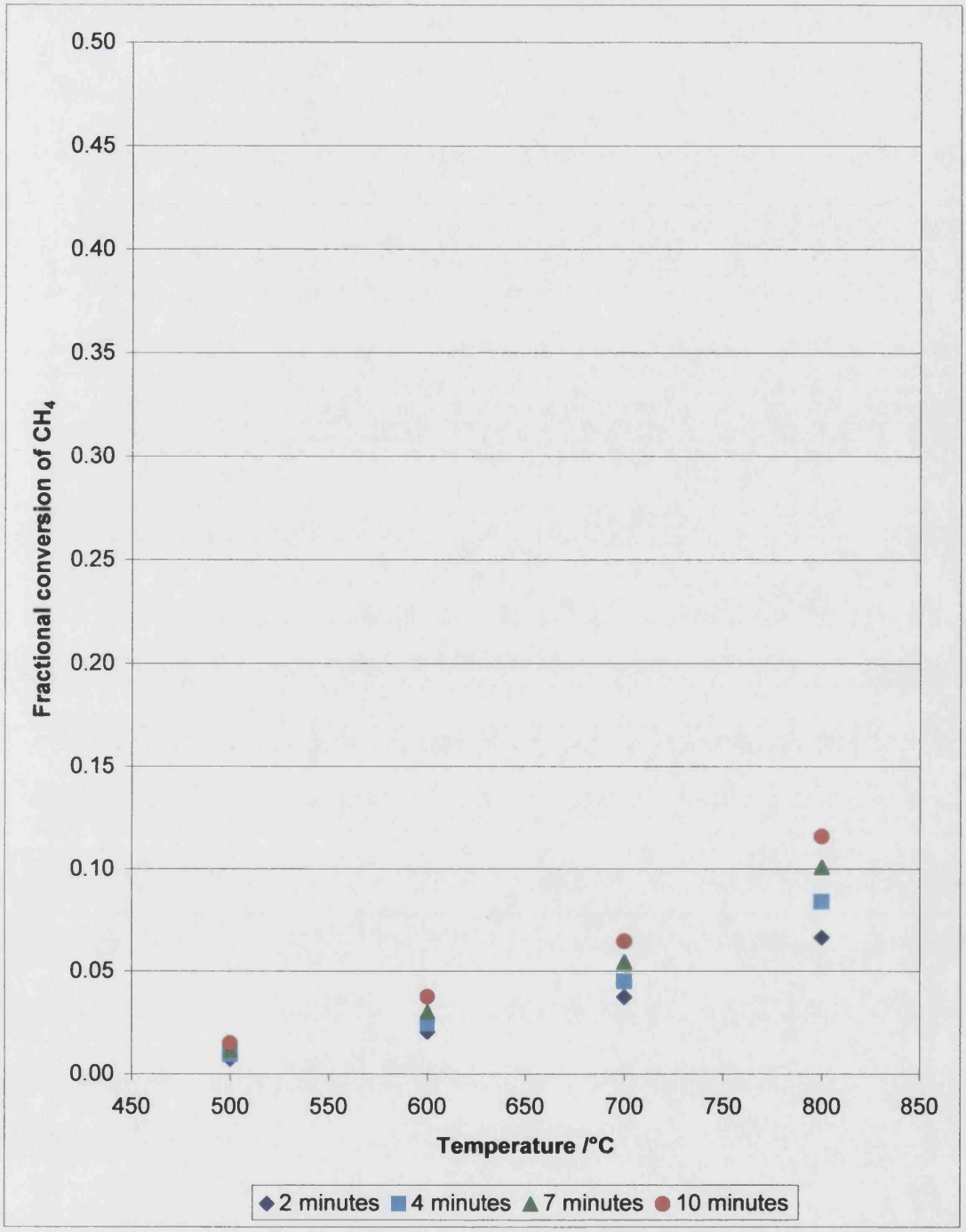

Figure 4.43 – Fractional conversion of CH_4 against temperature at 9.5 bar g, steam to methane ratio 4

The trends evident in the preceding figures are those predicted by thermodynamic analysis, although the conversion values seem a little low. Conversion increases with residence time, indicating that equilibrium has not been attained.

Effect of varying pressure

Figures 4.44 to 4.47 give the fractional conversion of methane against varying reactor pressure at a given reaction temperature.

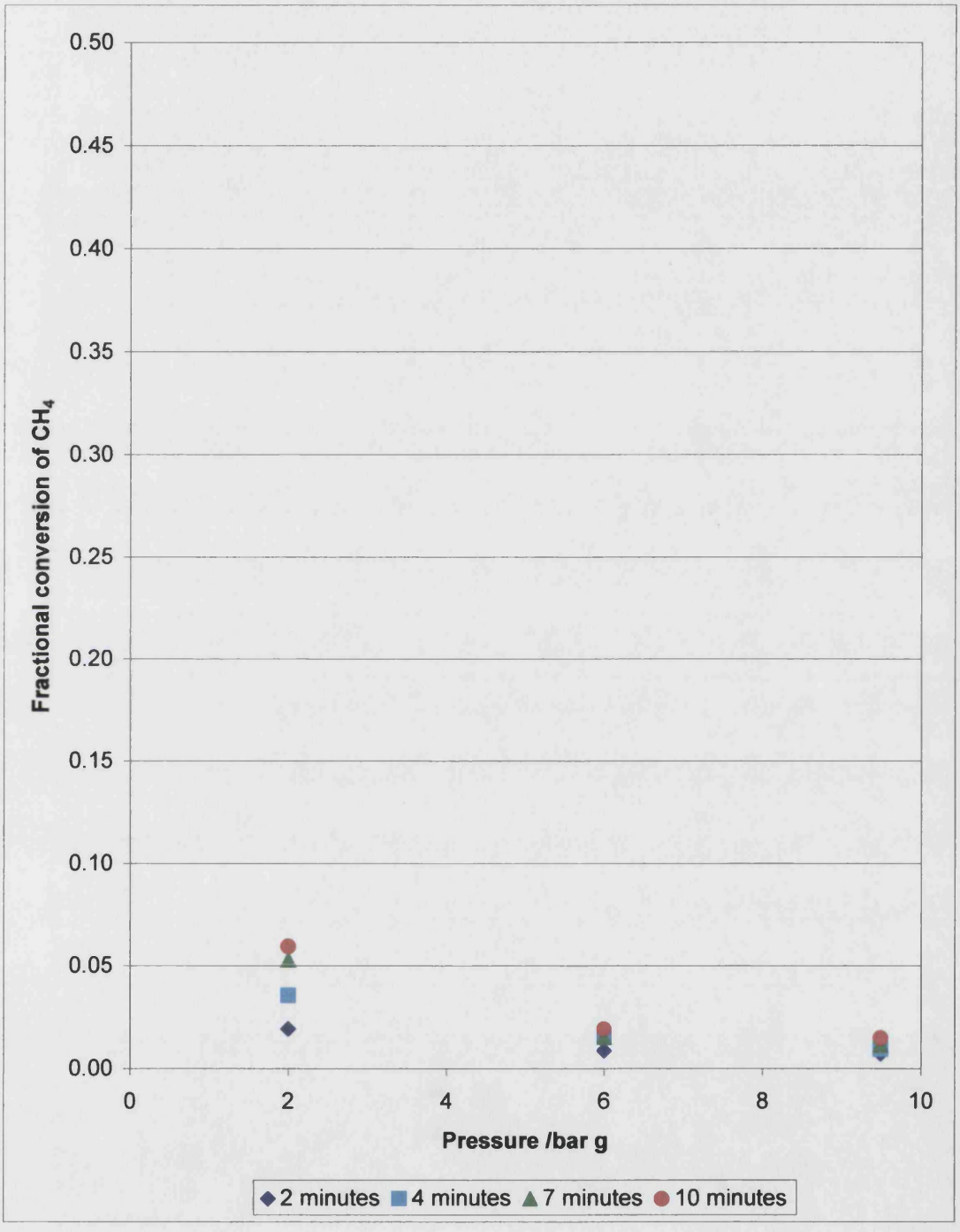

Figure 4.44 – Fractional conversion of CH_4 against pressure at 500°C, steam to methane ratio 4

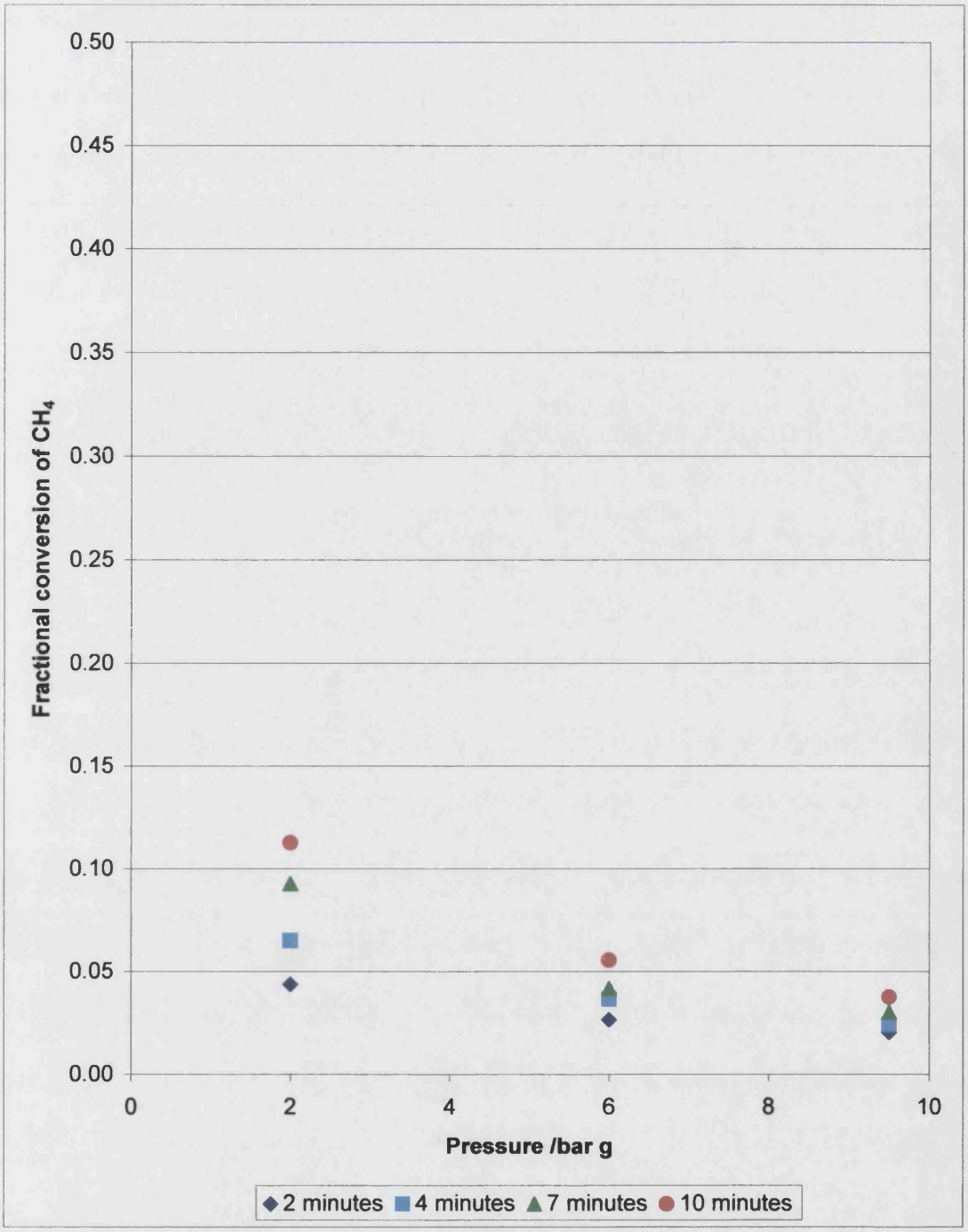

Figure 4.45 – Fractional conversion of CH_4 against pressure at 600°C, steam to methane ratio 4

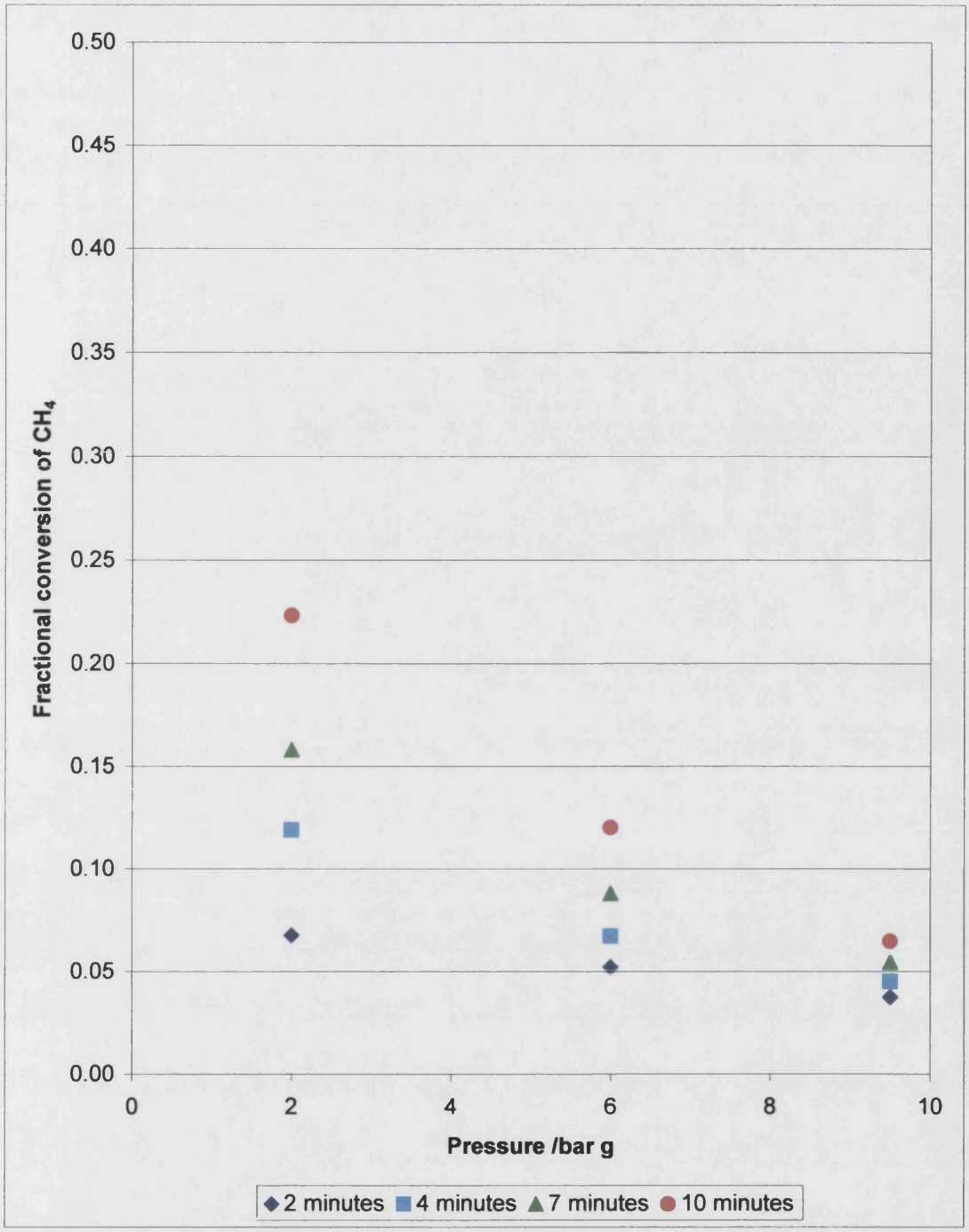

Figure 4.46 – Fractional conversion of CH_4 against pressure at 700°C, steam to methane ratio 4

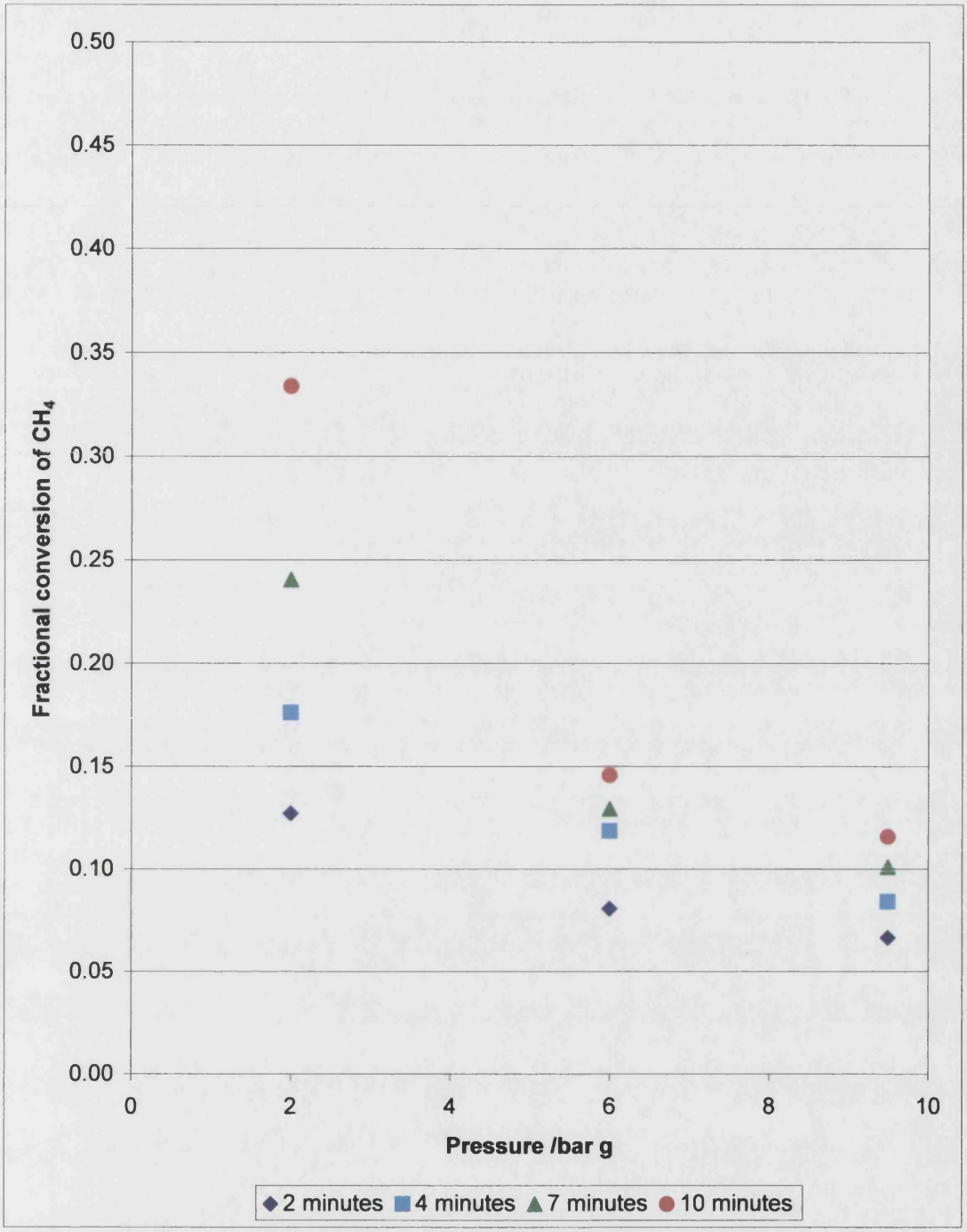

Figure 4.47 – Fractional conversion of CH_4 against pressure at 800°C, steam to methane ratio 4

Again, the trends observed are the expected ones, but the conversion values seem low.

4.6.5 Methane conversion in the reforming reactor for steam to methane ratio of 2

Effect of varying temperature

For a steam to methane ratio of 2, Figures 4.48 to 4.50 show the effect of varying the reaction temperature for a given reactor pressure on the fractional conversion of methane. It is expected that the conversion values should be lower than for a steam to methane ratio of 4.

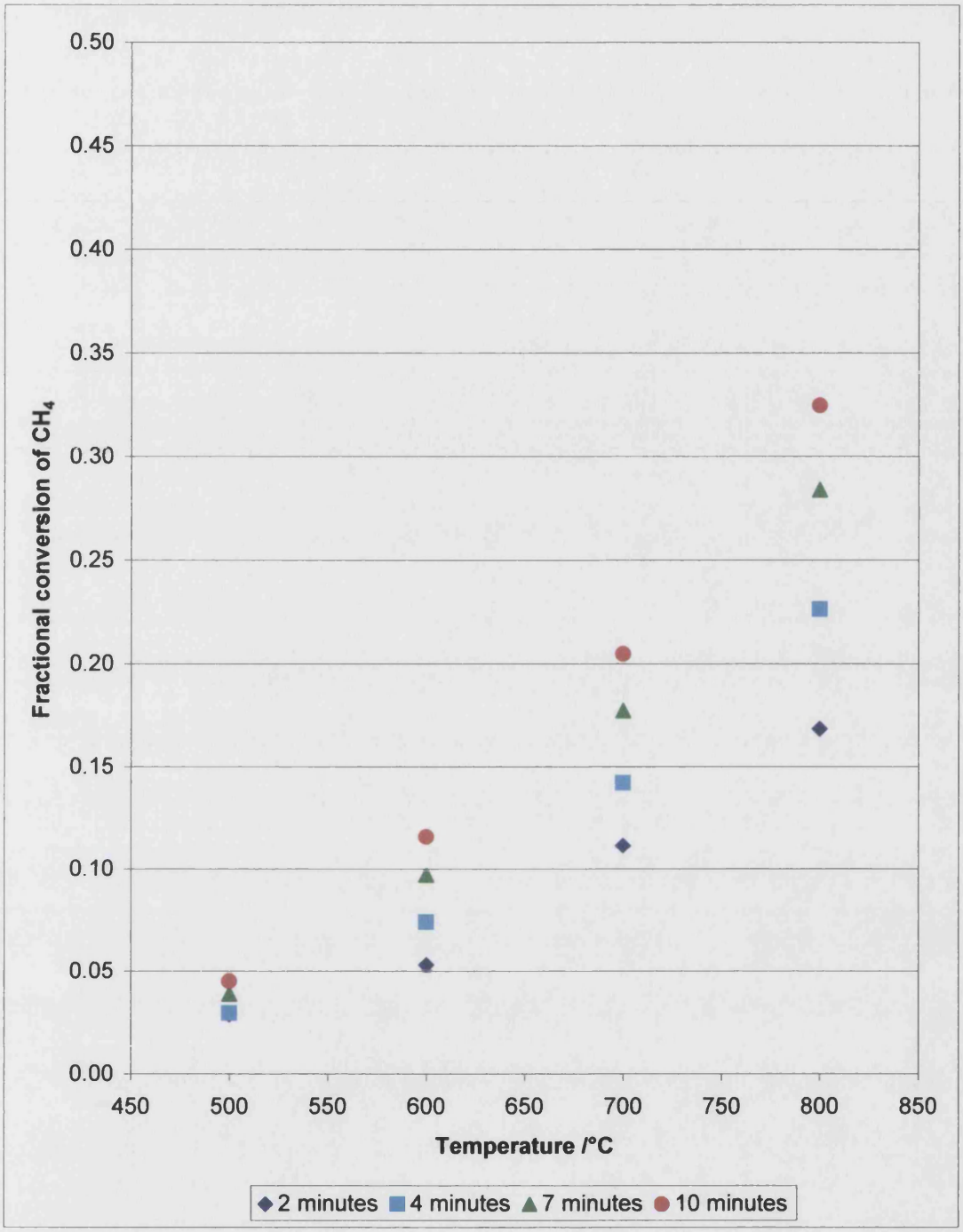

Figure 4.48 – Fractional conversion of CH_4 against temperature at 2 bar g, steam to methane ratio 2

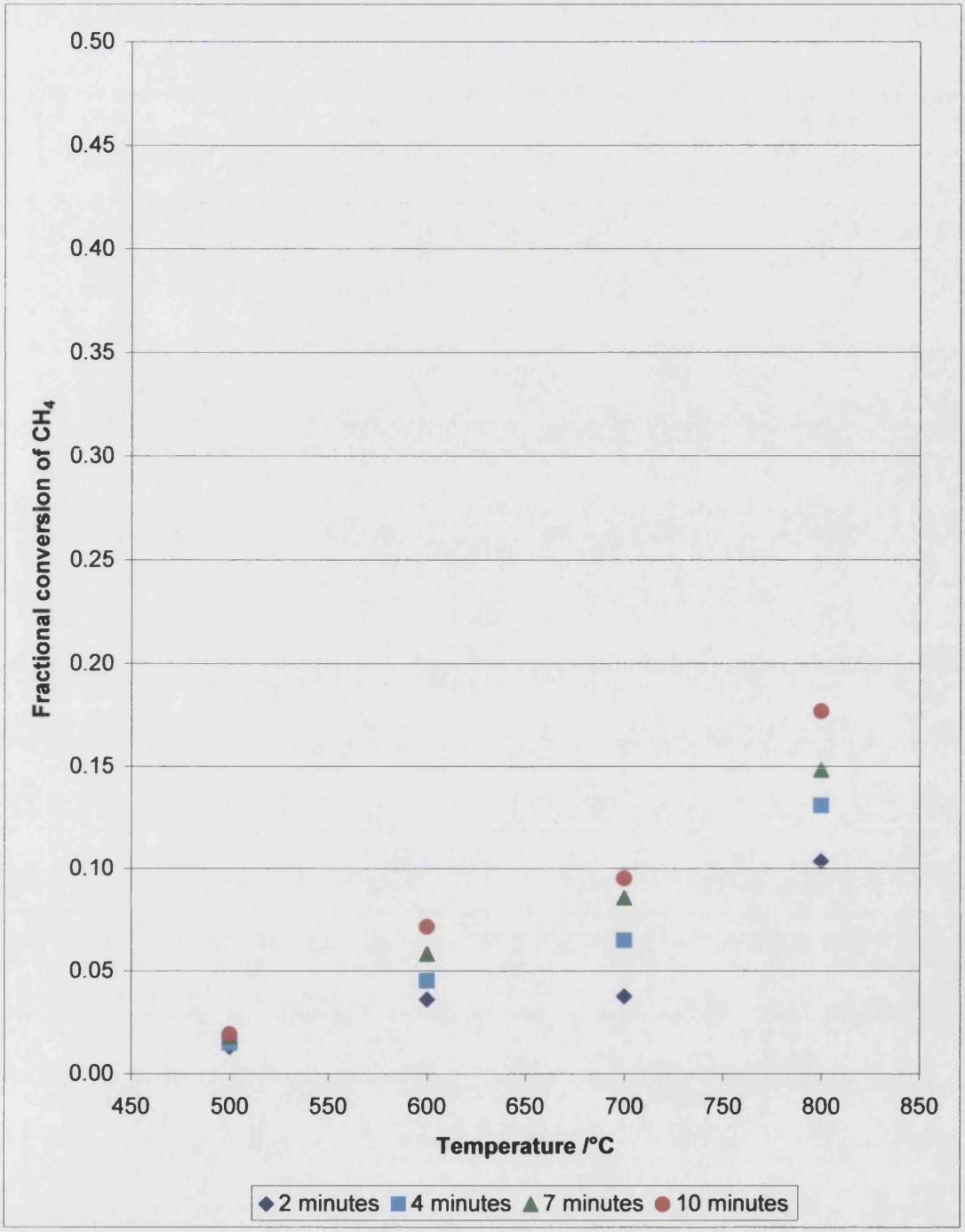

Figure 4.49 – Fractional conversion of CH_4 against temperature at 6 bar g, steam to methane ratio 2

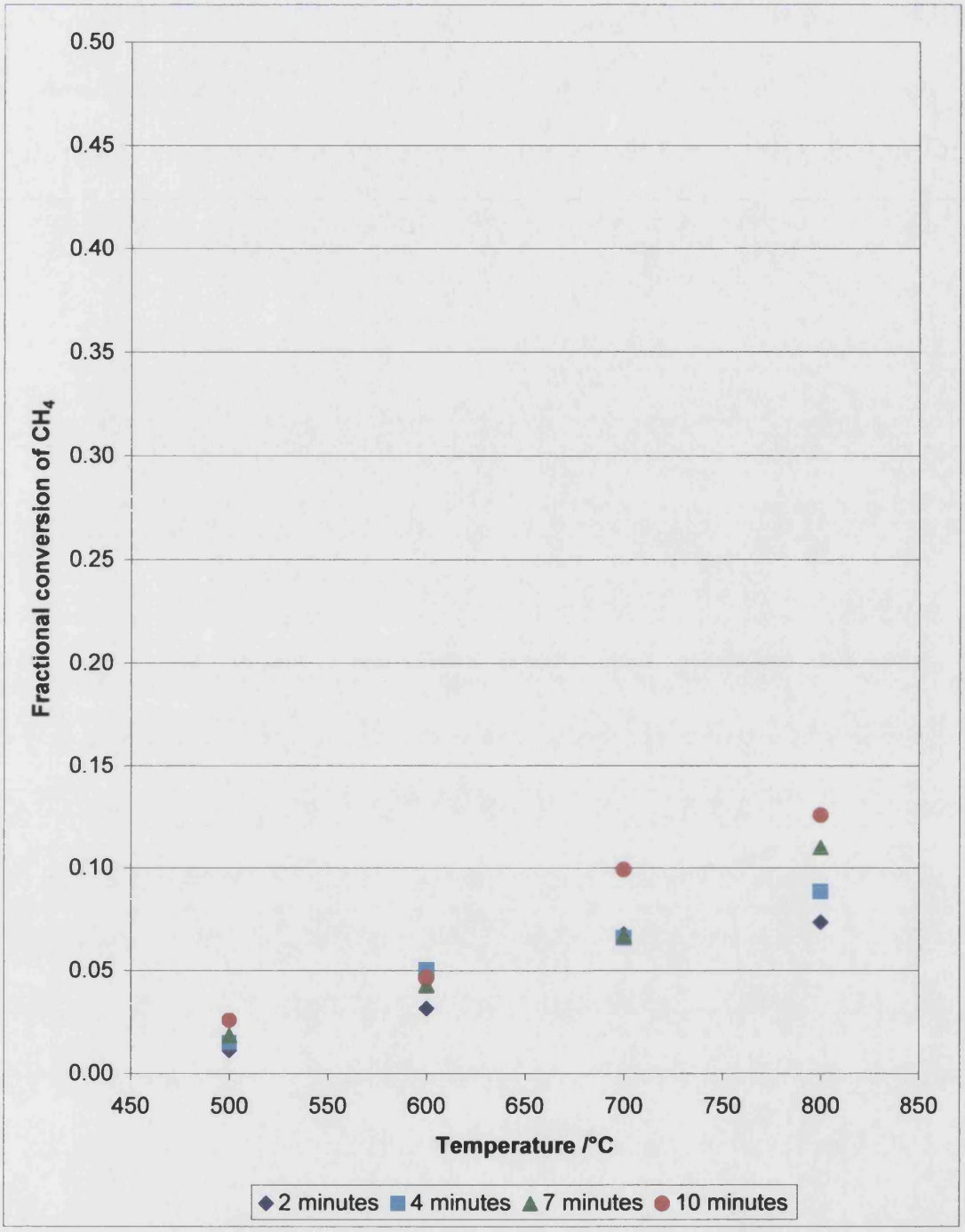

Figure 4.50 – Fractional conversion of CH_4 against temperature at 9.5 bar g, steam to methane ratio 2

The values for conversion at a steam to methane ratio of 2 appear to be very similar to those at a steam to methane ratio of 4. This is odd, since the presence of extra steam in the reactor should move the equilibrium towards the products.

Effect of varying pressure

Finally, the effect on the conversion of methane of varying the reactor pressure for a given reaction temperature is shown in Figures 4.51 to 4.54 below.

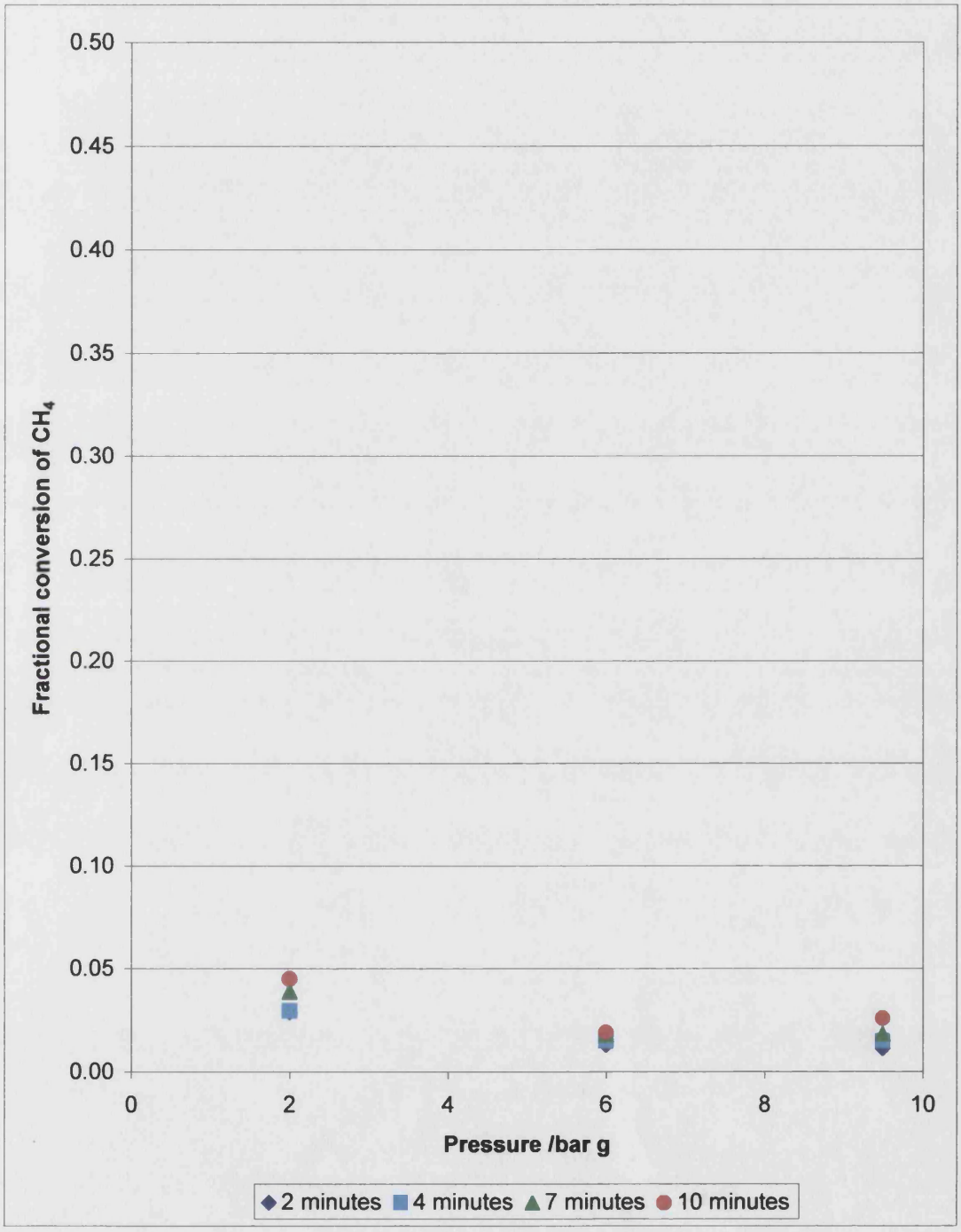

Figure 4.51 – Fractional conversion of CH_4 against pressure at 500°C, steam to methane ratio 2

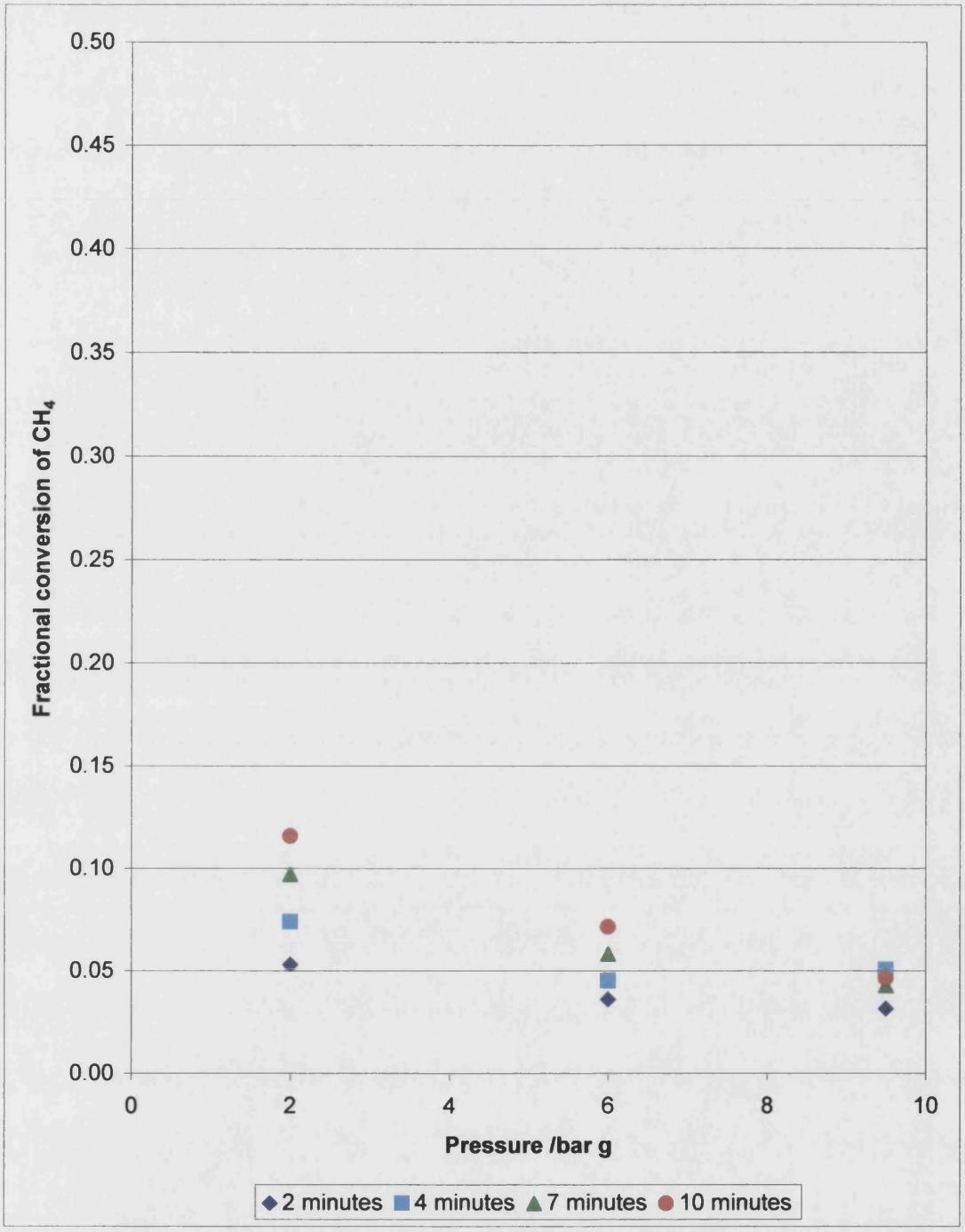

Figure 4.52 – Fractional conversion of CH_4 against pressure at 600°C, steam to methane ratio 2

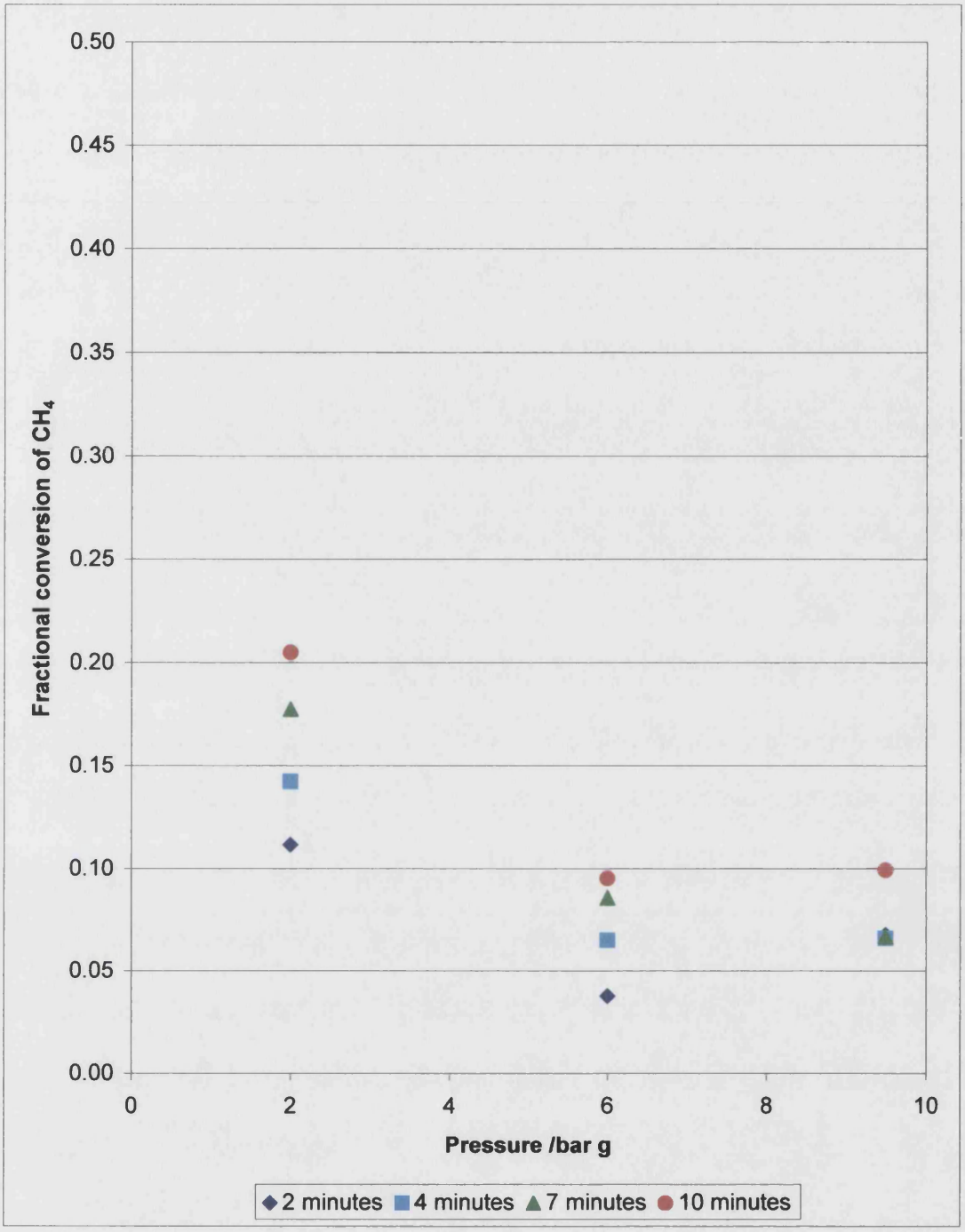

Figure 4.53 – Fractional conversion of CH_4 against pressure at 700°C, steam to methane ratio 2

Strangely, the conversion was not higher at 6 bar than at 9.5 bar for a reaction temperature of 700 °C.

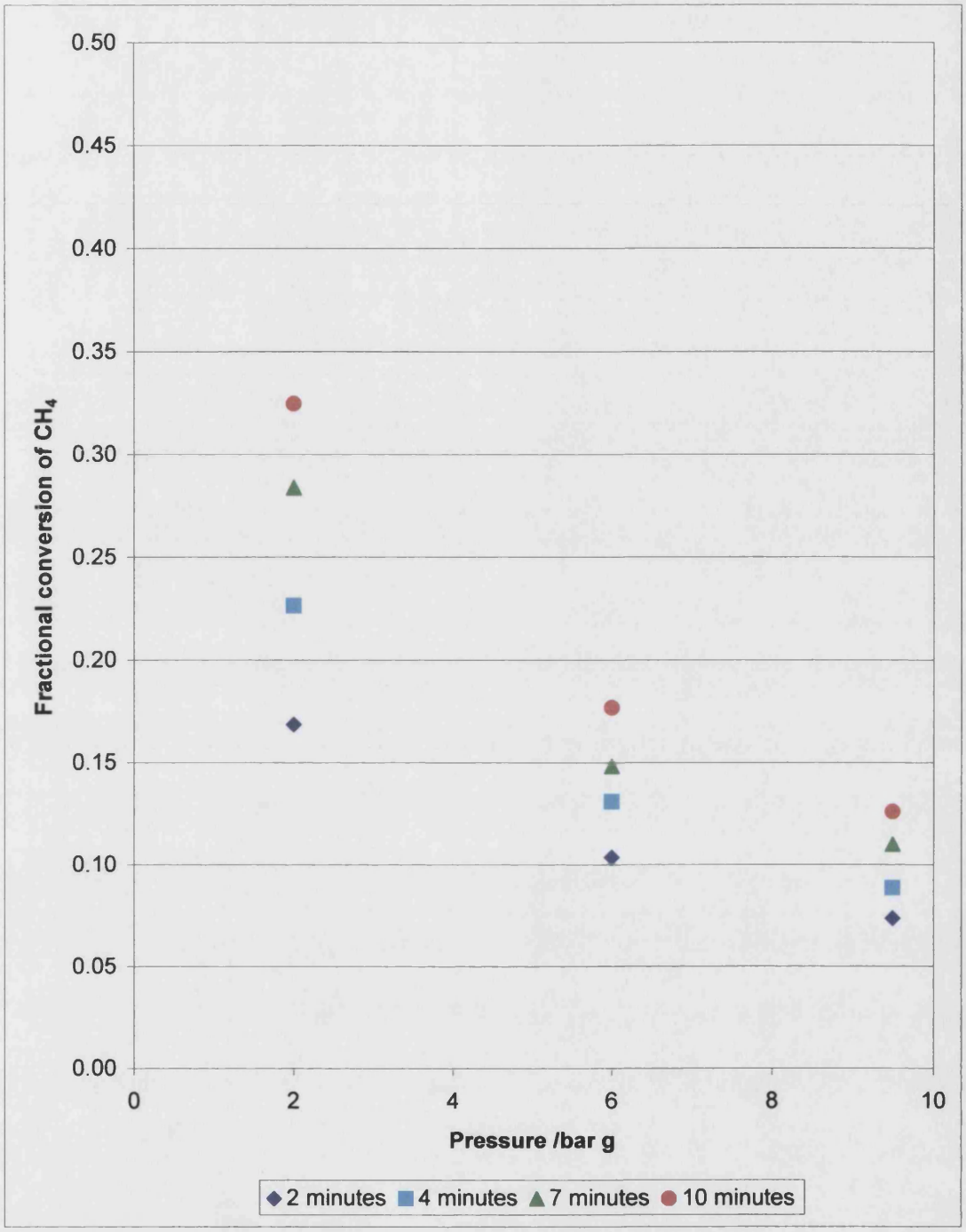

Figure 4.54 – Fractional conversion of CH_4 against pressure at 800°C, steam to methane ratio 2

Again, while the trends shown are generally as expected, the values for conversion seem low, and they are very similar to those recorded for a steam to methane ratio of 4.

4.6.6 Repeated runs of the reforming reactor

Several runs were performed under the same conditions to check the repeatability of the experiments. Run 1 was one of the earlier runs to be carried out. Runs 2 to 5 were performed over the space of a week after the other experiments had been completed. Therefore, any significant deactivation of the catalyst over the course of the experiments would be indicated by a reduction in performance between Run 1 and the other runs. The results are given in Figure 4.55 below.

The figure indicates that repeatability is very good and catalyst deactivation was not significant over the course of the experiments. For each residence time, the hydrogen proportion for all runs is equal within experimental error, with only one exception. Results for Run 1 are all a little higher than those of Runs 2 to 5, but given the relatively large experimental error, no firm conclusions can be drawn from this.

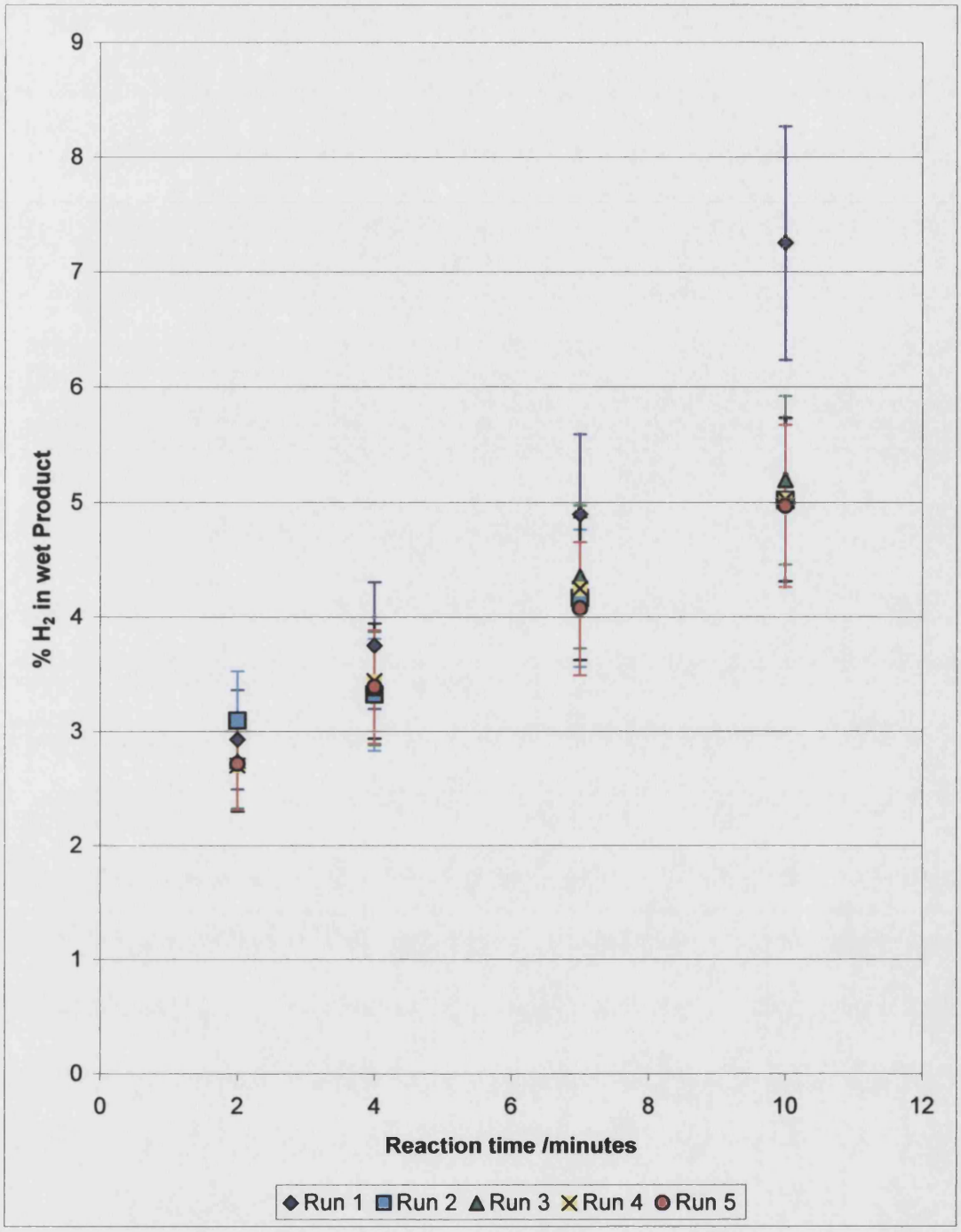

Figure 4.55 – Hydrogen production against residence time for several runs under the same conditions (*SMR* = 4, pressure = 6 bar g, temperature = 700°C)

4.6.7 Sensitivity of SMR to autoclave operating conditions

A lot of the uncertainty in the final results comes from the steam to methane ratio calculation. The *SMR* is very sensitive to changes in temperature and pressure, particularly at lower pressures. This is because, at low pressures, the partial pressure of methane in the autoclave is small so a relatively small change in either the total pressure or the vapour pressure of the water will cause a large proportional change in the partial pressure of methane. The uncertainty in the *SMR* also increases at higher *SMR* values, since the partial pressure of methane is then even smaller. Unfortunately, the temperature in the autoclave is measured by a thermocouple only to the nearest °C. The random uncertainty introduced by this is taken into account in the material balance. Any systematic error in this reading is unknown, however, so could not be included in the error analysis.

4.6.8 Comparing experimental performance with theoretical performance

Hydrogen concentration and methane conversion increased with increasing temperature, and reduced with increasing pressure, as expected from the thermodynamic analysis performed in Chapter 3. However, the experimental conversion values appear rather low compared with the results from Aspen. This impression is confirmed by Figure 4.56 and Figure 4.57, which show the same data as Figure 4.47 and Figure 4.51, but with equilibrium data included. The results recorded in Figure 4.56 are for the most favourable conditions (800 °C, *SMR* = 4), while those recorded in Figure 4.57 are for the least favourable (500 °C, *SMR* = 2). In both cases, the observed experimental conversion of methane is far lower than the equilibrium value. This is also the case for the other experimental data.

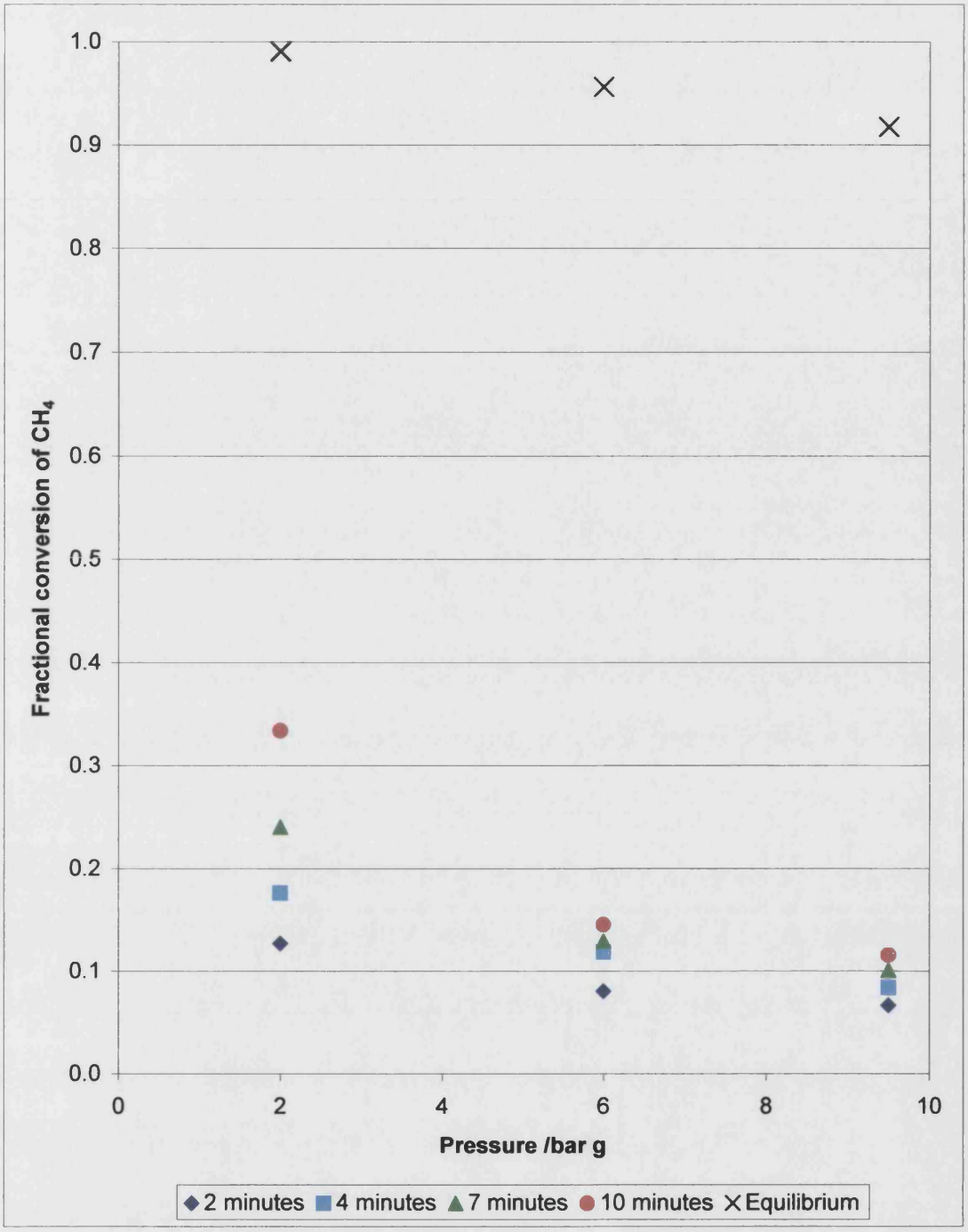

Figure 4.56 – Fractional conversion of CH_4 against pressure at 800°C, steam to methane ratio 4, showing equilibrium conversion

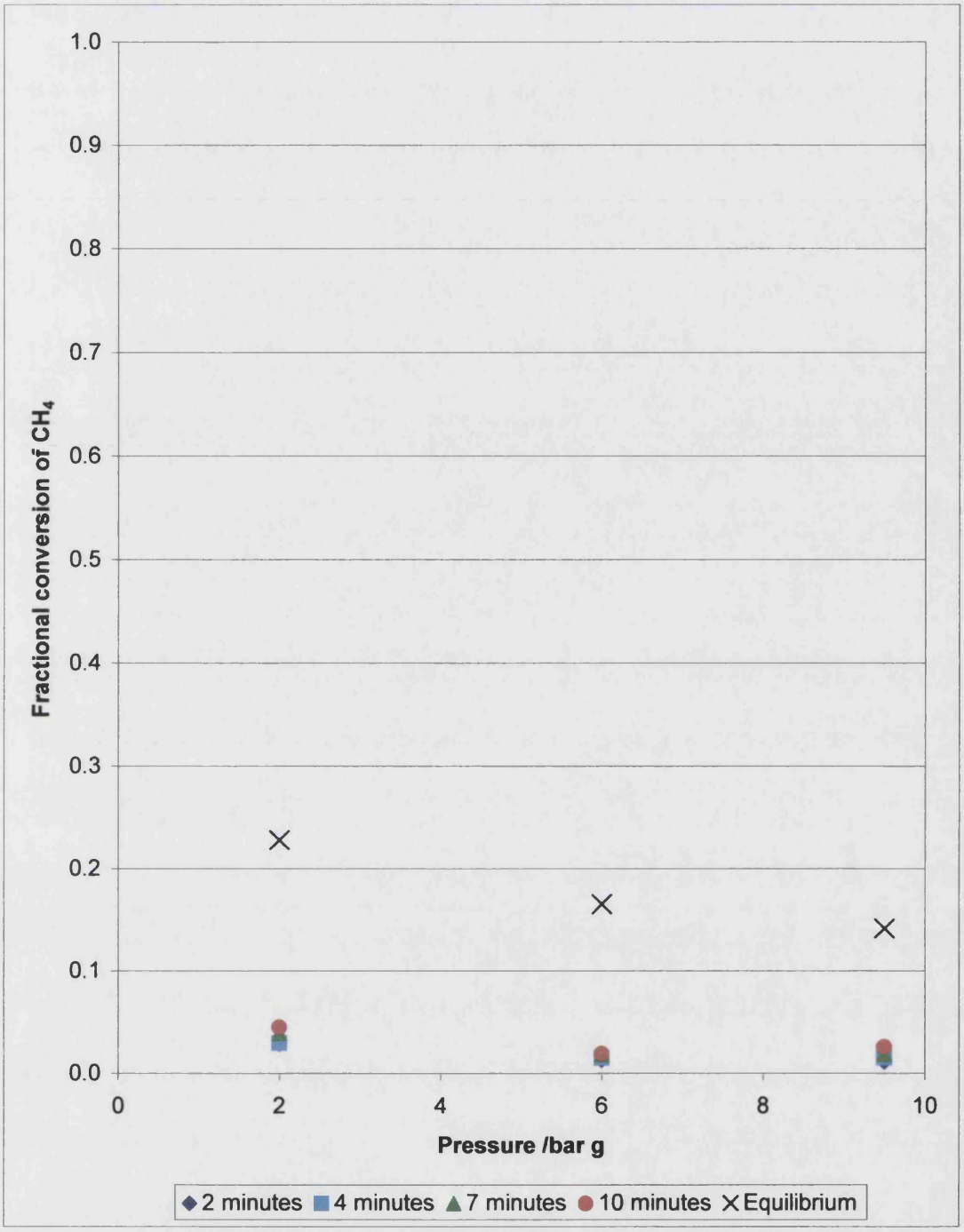

Figure 4.57 – Fractional conversion of CH_4 against pressure at 500°C, steam to methane ratio 2, showing equilibrium conversion

This result is most unexpected, since the kinetics of the steam reforming reaction are reported to be quite fast in the literature. It was expected that the components would reach a state of equilibrium in the reactor at least within a few minutes, and certainly by 10 minutes, but this is not what happened. It is unlikely that the discrepancy is caused by a mistake in the calculations, since the conversion is seen to increase with increasing residence time. This indicates that the reaction was simply proceeding at a slower rate

than expected. In order to determine the overall effectiveness factor required to produce the observed results, the kinetics of the reaction were investigated.

4.6.9 Unsteady state kinetics of the steam reforming reactions

The kinetic model

Hou and Hughes (2001) developed a set of kinetic rate equations for the steam reforming process using a similar catalyst to that which was used for the experiments in this thesis.

Hou and Hughes (2001) found that there are 3 reactions which are significant in modelling the intrinsic kinetics of the steam reforming system. The reactions are listed below.

1. $CH_4 + H_2O \Leftrightarrow CO + 3H_2$
2. $CO + H_2O \Leftrightarrow CO_2 + H_2$
3. $CH_4 + 2H_2O \Leftrightarrow CO_2 + 4H_2$

Reactions 1 and 2 are the steam reforming reaction and the water gas shift reaction, used previously for the thermodynamic equilibrium calculations. Reaction 3 is a combination of the other two reactions.

The rate expressions for these reactions are:

$$r_1 = k_1 \frac{P_{CH_4} P_{H_2O}^{0.5}}{P_{H_2}^{1.25}} \left(1 - \frac{P_{CO} P_{H_2}^3}{K_{p1} P_{CH_4} P_{H_2O}}\right) \Big/ (\text{den})^2 \qquad (4.42)$$

$$r_2 = k_2 \frac{P_{CO} P_{H_2O}^{0.5}}{P_{H_2}^{0.5}} \left(1 - \frac{P_{CO_2} P_{H_2}}{K_{p2} P_{CO} P_{H_2O}}\right) \Big/ (\text{den})^2 \qquad (4.43)$$

$$r_3 = k_3 \frac{P_{CH_4} P_{H_2O}}{P_{H_2}^{1.75}} \left(1 - \frac{P_{CO_2} P_{H_2}^4}{K_{p3} P_{CH_4} P_{H_2O}^2}\right) \Big/ (\text{den})^2 \qquad (4.44)$$

where $\text{den} = 1 + K_{CO} P_{CO} + K_H P_H^{0.5} + K_{H_2O} \frac{P_{H_2O}}{P_{H_2}}$

In these equations, P_i are the partial pressures of the various components in kPa, k_n are the reaction rate constants, K_i are the adsorption coefficients and K_{pn} are the equilibrium constants. Each rate equation is for a single reaction.

The equilibrium constants were calculated using the following equations:

$$K_{p1} = 1.198 \times 10^{17} \exp(-26830/T) \text{ (kPa)}^2 \quad (4.45)$$

$$K_{p2} = 1.767 \times 10^{-2} \exp(4400/T) \quad (4.46)$$

$$K_{p3} = 2.117 \times 10^{15} \exp(-22430/T) \text{ (kPa)}^2 \quad (4.47)$$

As explained above, the results of Equations (4.45) and (4.46) agree well with other published data and with the output from Aspen. The same was found to be true of Equation (4.47).

The adsorption coefficients and the reaction rate constants were estimated at different temperatures by comparing experimental results with predicted reaction rates using a non-linear least squares analysis. Values for k_1, k_2, k_3, K_{CO} and K_H were determined for temperatures between 598 K and 673 K. Values for k_1, k_3 and K_{H2O} were determined for temperatures between 748 K and 823 K. These data were then fitted to the following equations:

$$K_i = A_i \exp\left(-\frac{\Delta H_i}{RT}\right) \quad (4.48)$$

$$k_n = A_n \exp\left(-\frac{E_n}{RT}\right) \quad (4.49)$$

The parameters for Equation (4.48) (the van't Hoff equation) are given in Table 4.17. The parameters for Equation (4.49) (the Arrhenius equation) are given in Table 4.18.

Table 4.17 – Parameters for Equation (4.48)

	CO	H	H_2O
ΔH_i (kJ/mol)	-140.0	-93.4	15.9
A_i	5.127×10^{-13}	5.68×10^{-10}	9.251

Table 4.18 – Parameters for Equation (4.49)

	1	2	3
E_n (kJ/mol)	209.2	15.4	109.4
A_n	5.922×10^{8}	6.028×10^{-4}	1.093×10^{3}

These data allow the adsorption coefficients and rate constants to be estimated for any temperature.

Assumptions

It was assumed that the parameters for the various equations were reliable at temperatures ranging from 500 to 800 °C, despite having been extrapolated from data obtained at 325 to 400 °C and 475 to 550 °C. This is justified because the data closely fitted the equations used to model them.

The catalyst that was being modelled is in the form of cylindrical pellets, rather than the crushed particles used to form the rate equations. The rate was adjusted with an appropriate effectiveness factor.

It was assumed that the gas mixture was behaving as an ideal gas. The temperature was assumed to be constant throughout the reactor. Although the number of moles increases during the reaction, this was not allowed to affect the pressure, which was assumed to be constant. Instead, the reactor volume was effectively assumed to increase during the reaction.

Spreadsheet calculations

The initial mole fractions were calculated from the steam to methane ratio. A small amount of hydrogen had to be present initially to prevent zero values from appearing in the denominator in parts of the rate expressions. The number of moles of each gas present and the partial pressures of each component were calculated from the reactor pressure, volume and temperature.

The parameters required for the rate expressions were calculated. This allowed the three reaction rates to be calculated. These rates were assumed to remain constant for a short

time period, Δt. This allowed the change in the number of moles of each component during that time period to be calculated. The new number of moles of each component was then used as the basis for the next time period.

Example results

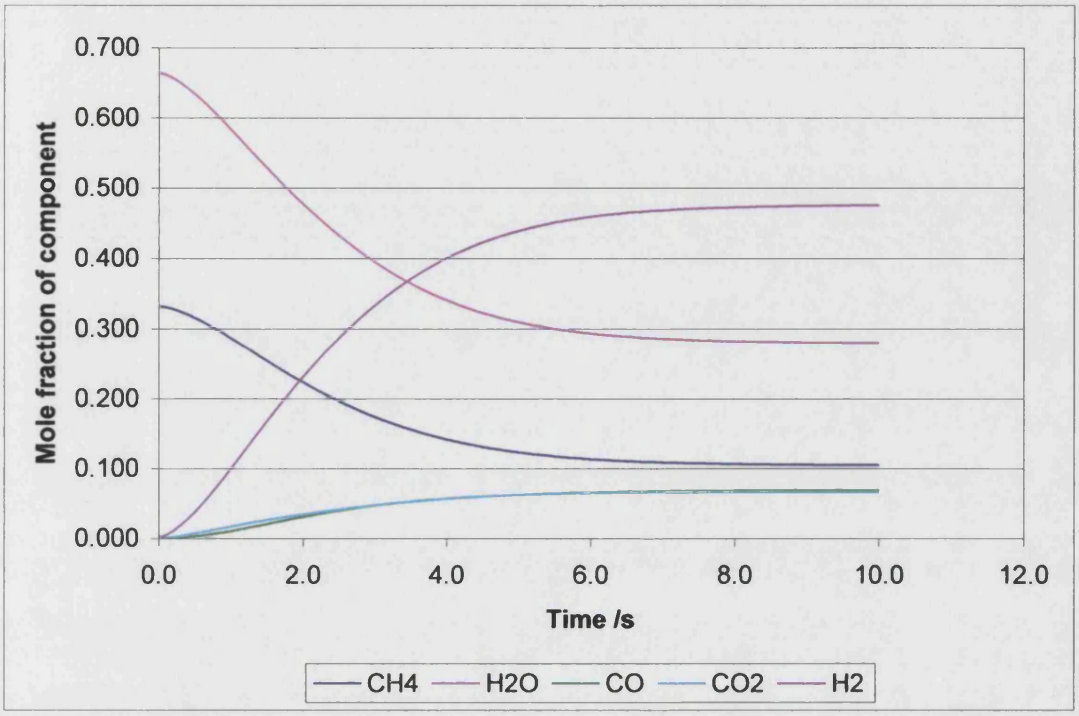

Figure 4.58 – 700°C, 6 bar g, *SMR* = 2, effectiveness factor = 0.0015

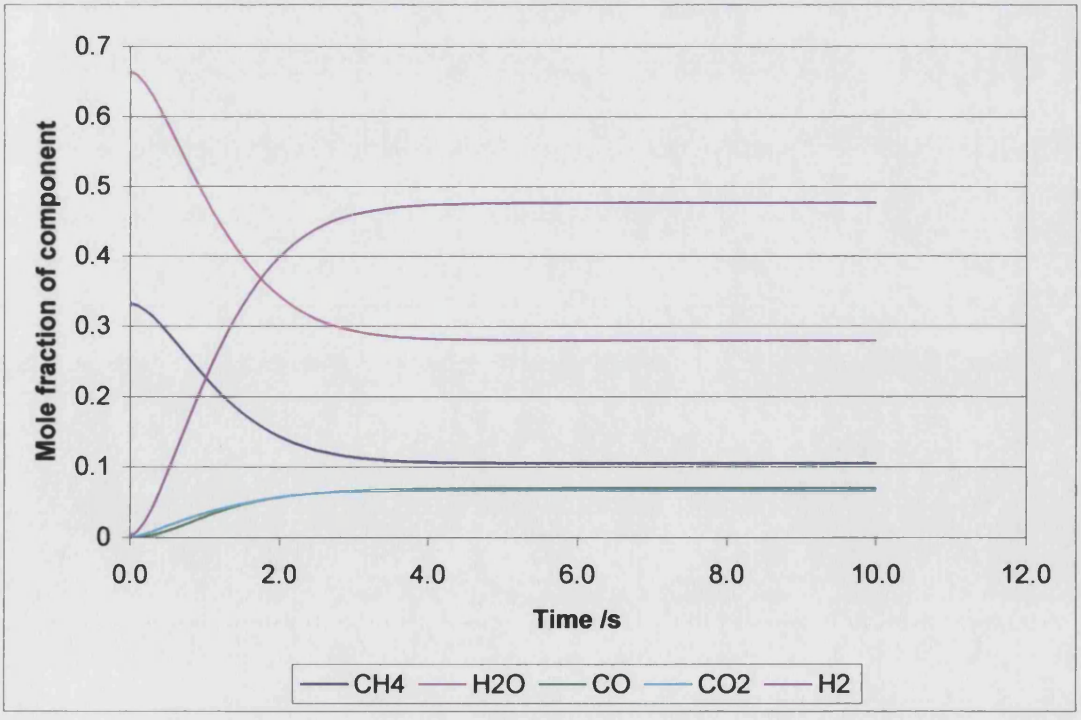

Figure 4.59 – 700°C, 6 bar g, *SMR* = 2, effectiveness factor = 0.003

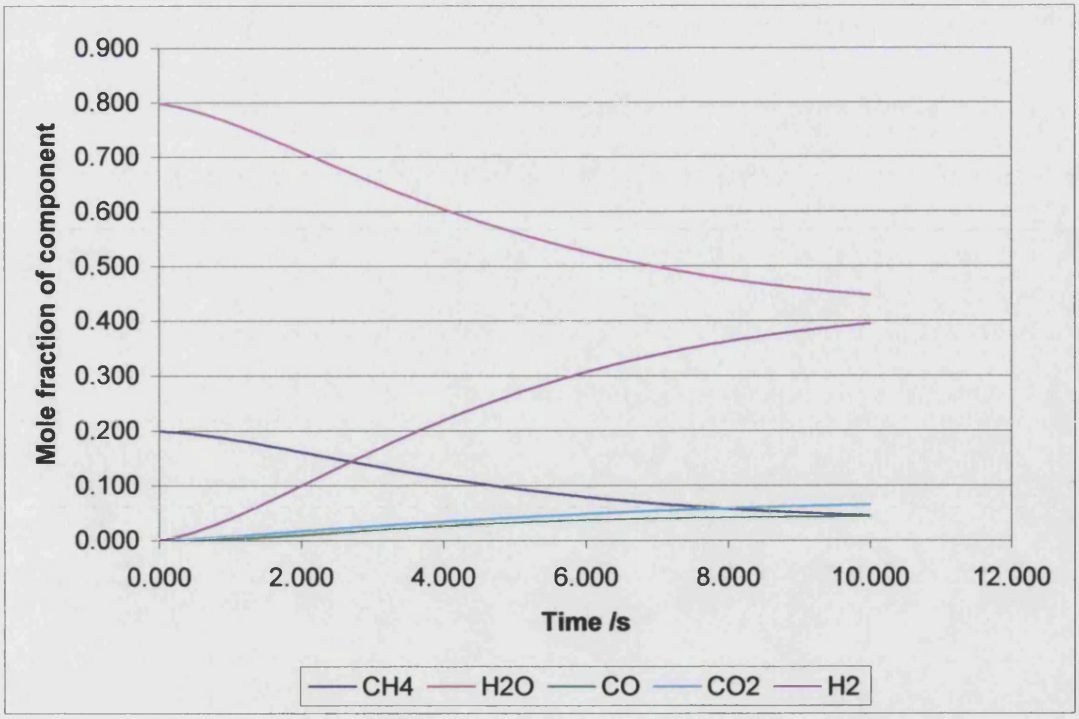

Figure 4.60 – 700°C, 6 bar g, *SMR* = 4, effectiveness factor = 0.0015

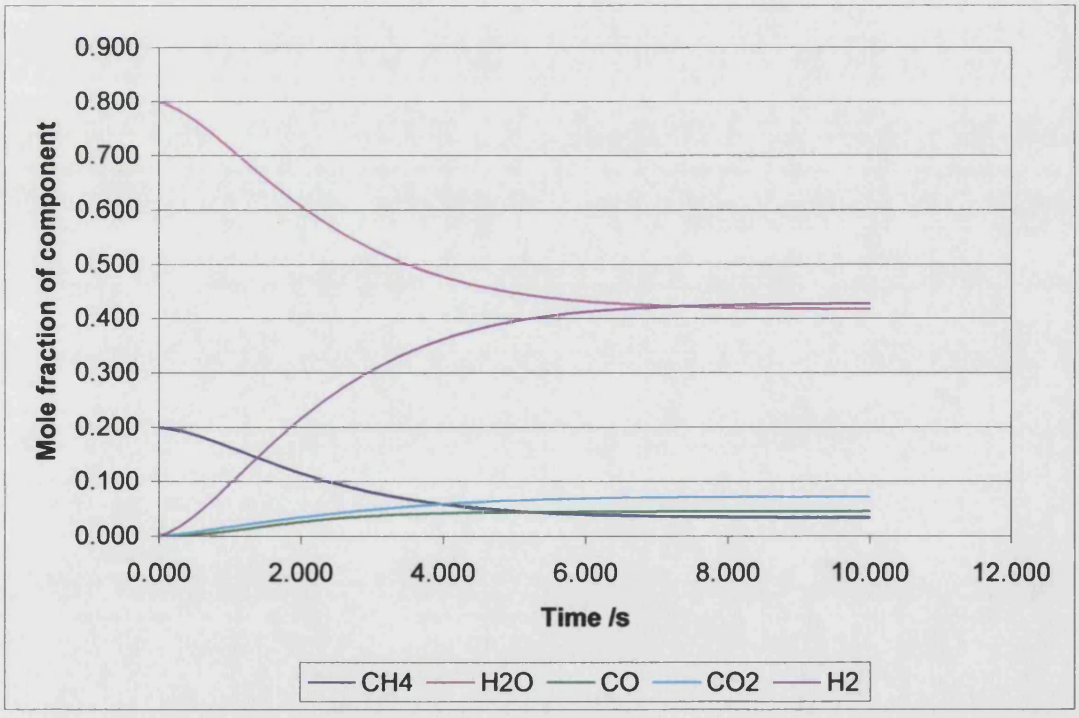

Figure 4.61 – 700°C, 6 bar g, *SMR* = 4, effectiveness factor = 0.003

4.6.10 Factors affecting catalyst effectiveness factor

One possibility is that the overall effectiveness factor of the catalyst may have been low. The kinetic model used above was developed by Hou and Hughes (2001) and is a model of the intrinsic kinetics of the catalyst, *i.e.* assuming negligible intra-particle diffusion limitations and film-resistance. For the catalyst pellets used, it is likely that these phenomena will reduce the effectiveness factor. In fact, industrial reforming catalyst has been reported to have effectiveness factors of 0.008 (Adris *et al.*, 1996). This was, however, taken into account. The model still indicated that equilibrium would be attained in 10 seconds or so even with an effectiveness factor of <0.003. It is possible that the catalyst effectiveness factor was reduced by deactivation during the preliminary experiments, caused mainly by carbon deposition. This is hard to verify, since the conditions during the first few runs were not consistent with those that followed. However, in order to generate results similar to those observed in the experiments, an extremely low effectiveness factor of the order of 10^{-6} is required. Even taking into account contamination of the catalyst with carbon, it is unlikely that the catalyst effectiveness factor would be this low.

4.6.11 Scanning electron microscopy

There was a noticeable amount of carbon inside the reforming reactor after the experiments had been completed. In order to ascertain how the catalyst surface had been affected by the experiments, fresh catalyst was compared with catalyst pellets taken from the reactor after the experiments had been completed using a scanning electron microscope. Images were taken of several samples at several different magnifications. In addition, x-ray diffraction analysis was carried out on several of the samples to determine which elements were present. Images taken of the catalyst samples are shown in Figures 4.62 to 4.65.

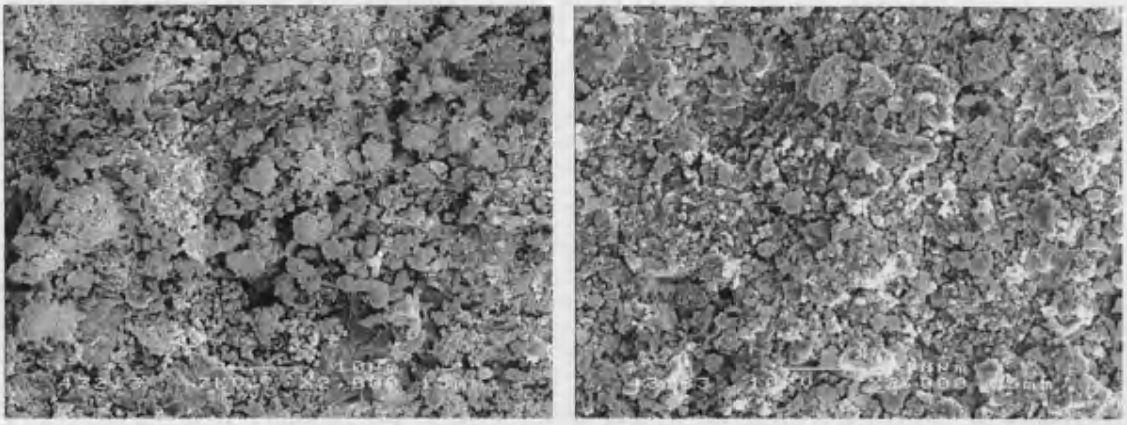

(a) Fresh **(b) Used**

Figure 4.62 – SEM image of the flat surface on the end of a catalyst pellet

There is little difference between the structure of the fresh catalyst in Figure 4.62 (a) and that of the used catalyst in Figure 4.62 (b).

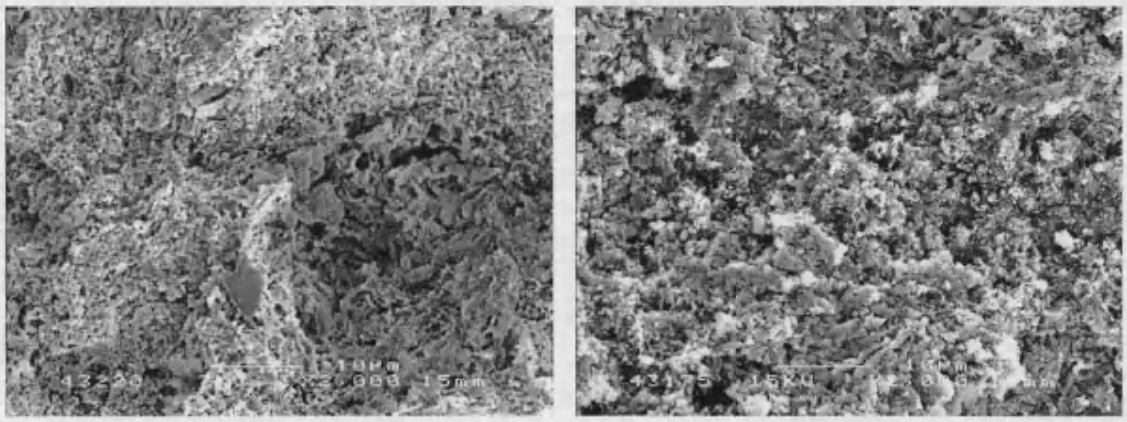

(a) Fresh **(b) Used**

Figure 4.63 – SEM image of the inner surface at the centre of a fractured catalyst pellet

Figure 4.63 (a) and (b) show the structure of the centre of a fresh and used catalyst particle respectively. Again, there is not any significant difference in the images.

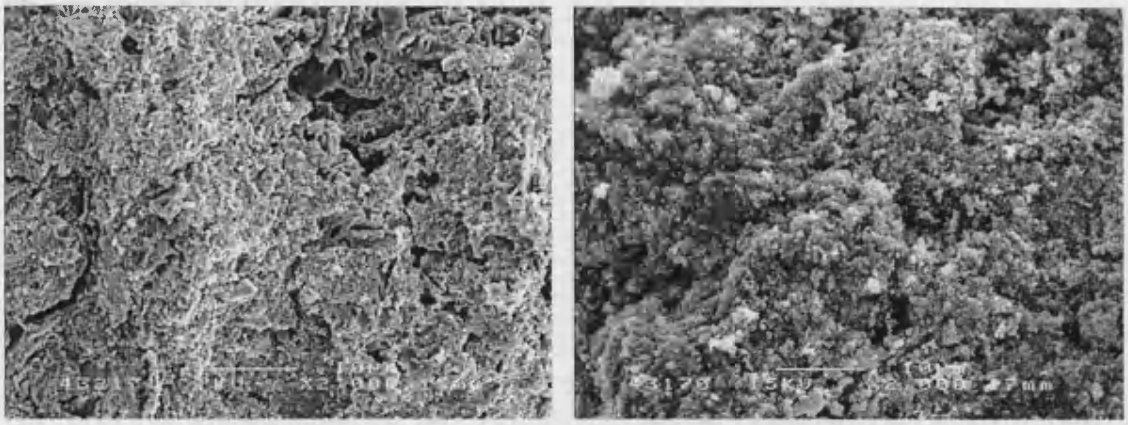

(a) Fresh (b) Used

Figure 4.64 – SEM image of the inner surface at the edge of a fractured catalyst pellet

At the edge of the catalyst pellet, there are small differences in the structure (see Figure 4.64). This is where the majority of the active catalyst material should be found, and is the area where reactions would have been taking place.

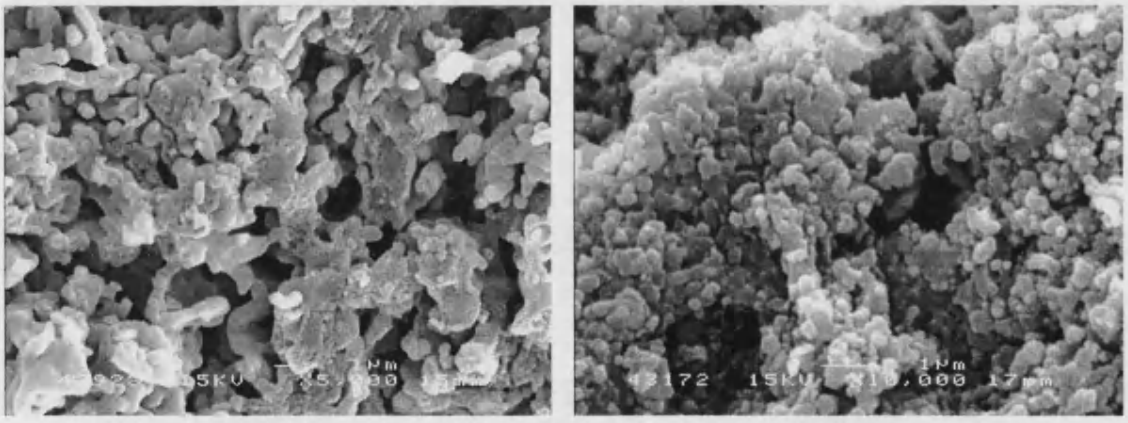

(a) Fresh (b) Used

Figure 4.65 – High magnification SEM image of the inner surface at the edge of a fractured catalyst pellet

To investigate further, images were taken at a higher magnification. Figure 4.65 (b) shows a "bobble-like" structure which is not present in the fresh catalyst, shown in Figure 4.65 (a). This could be carbon deposited on the surface, or the structure may have changed due to heating within the reactor.

To get an idea of the chemical constituents of the catalyst pellets, an x-ray diffraction analysis was carried out. Figure 4.66 and Figure 4.67 are the results of this analysis for the outside surface of the catalyst pellets.

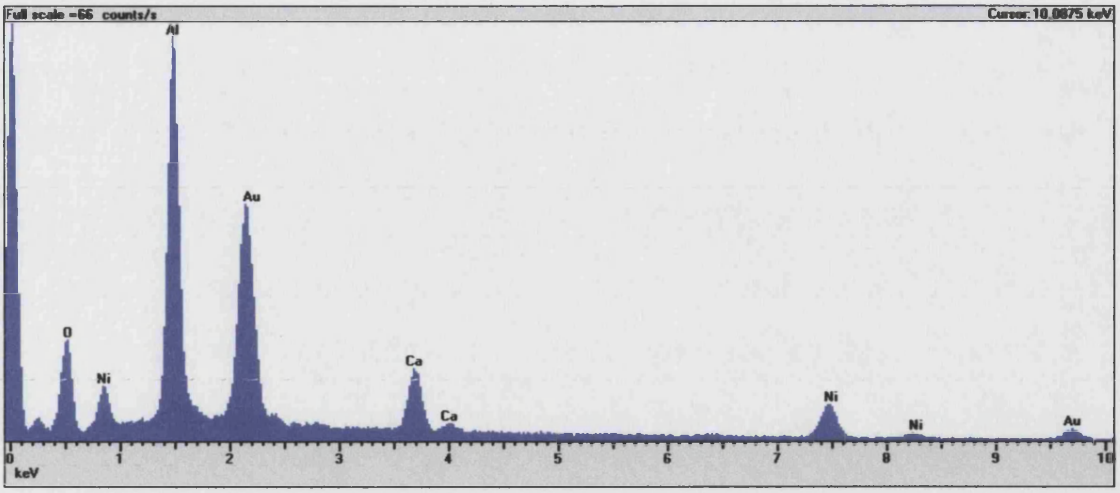

Figure 4.66 – X-ray diffraction plot for the outside surface of a fresh catalyst pellet

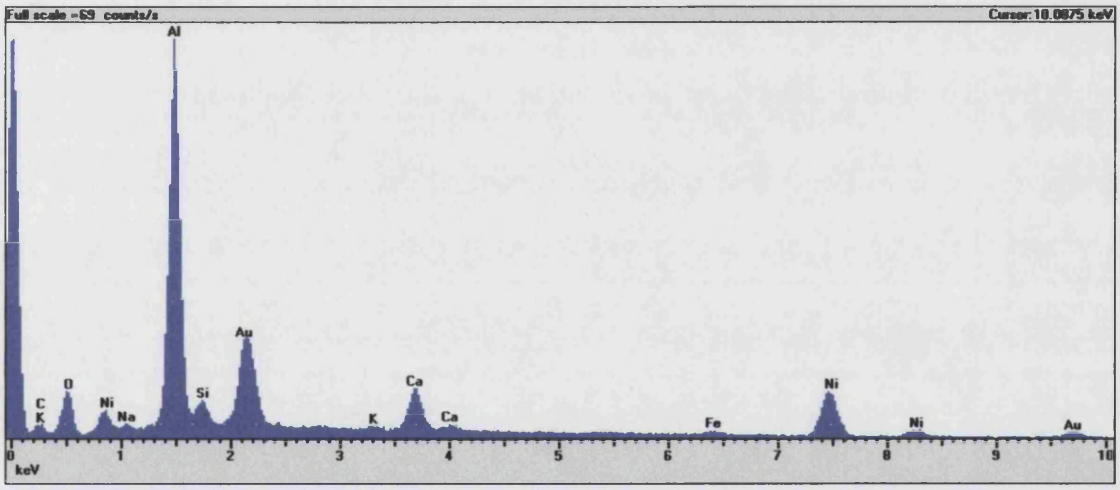

Figure 4.67 – X-ray diffraction plot for the outside surface of a used catalyst pellet

The spread of elements is very similar in both plots. This area of the used catalyst contained a small amount of silicon, probably from the packing material used in the reactor, and a small amount of iron, probably from the stainless steel reaction tube.

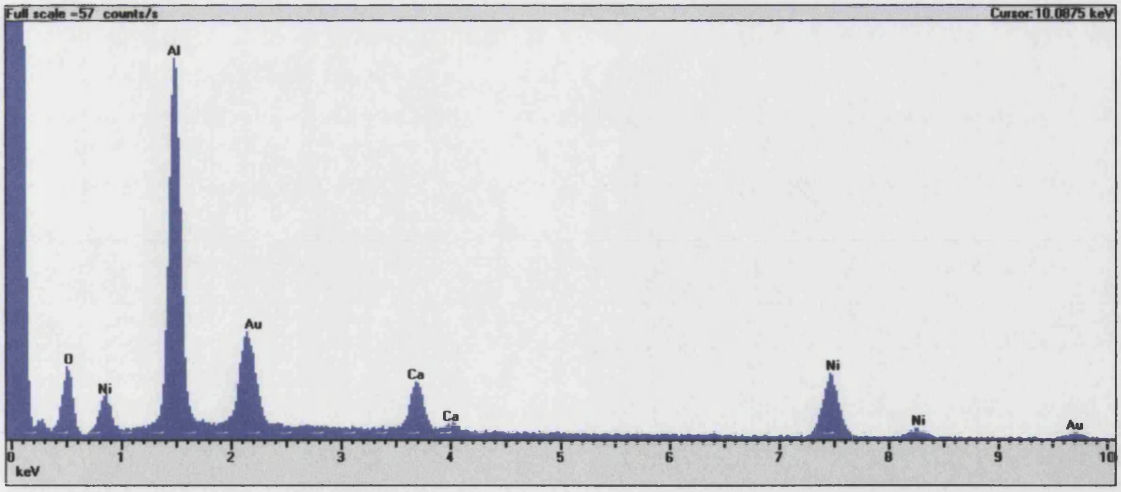

Figure 4.68 – X-ray diffraction plot for the inside surface of a fractured fresh catalyst pellet

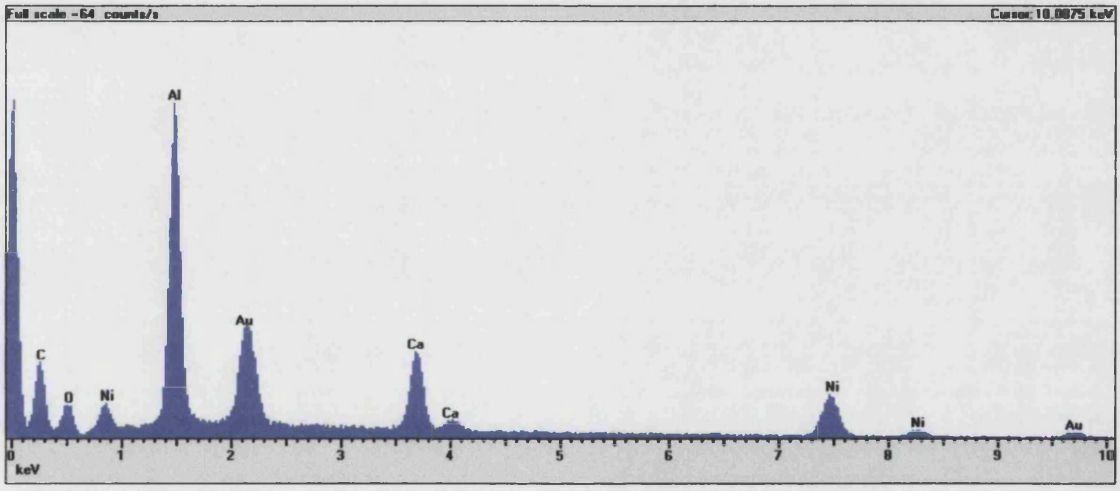

Figure 4.69 – X-ray diffraction plot for the inside surface of a fractured used catalyst pellet

The used catalyst examined in Figure 4.69 contained a relatively large quantity of carbon, and a relatively small quantity of oxygen, compared with the fresh catalyst examined in Figure 4.68. Clearly, carbon deposition has taken place here. Since the catalyst activity remained relatively constant over the course of the experiments, this may have occurred during the preliminary runs. The reduction in oxygen is probably due to the reduction of the nickel oxide to nickel during the catalyst preparation stage. The remaining oxygen does not necessarily mean that this process was incomplete however, since the support material is aluminium oxide.

4.6.12 Diffusion limitations within the rig

If low catalyst effectiveness factor is not entirely to blame for the poor results, perhaps they are due to a low overall effectiveness factor for the reaction system. It is possible that diffusion limitations within the tubes feeding the reactor limited the rate of reaction.

A series of runs with $SMR = 2$, $P = 6$ bar g and $T = 700°C$ were carried out in the rig in its original configuration, then repeated with a slightly different configuration. In the second series of runs, the side-tube connected to the reactor pressure gauge was replaced with one 25 cm in length (see Figure 4.70 and Figure 4.71). This approximately doubled the "dead volume" above the reactor. Runs were also carried out for a reaction time of 20 minutes in addition to those for 2, 4, 7 and 10 minutes. The results for the original run (Run 1) are shown in Figure 4.72, along with the new results. It can be seen that the original results are very similar to the new results for the system in its original configuration. This is further evidence for the good repeatability of the experimental results.

Three other details are apparent in Figure 4.72. Firstly, for the short tube, the rate of hydrogen production appears to remain constant over the 20 minute time span. If a longer residence time was allowed it could eventually reach equilibrium. Secondly, the amount of hydrogen produced when the longer tube was used is significantly less than that when the original tube was used. Obviously, some feature of the feed tubes or the "dead volume" is affecting the rate of reaction. Thirdly, for the longer tube, the rate of reaction has decreased at the 20 minute data point. Further increases in residence time would result in the approach to an asymptote that is below the equilibrium value.

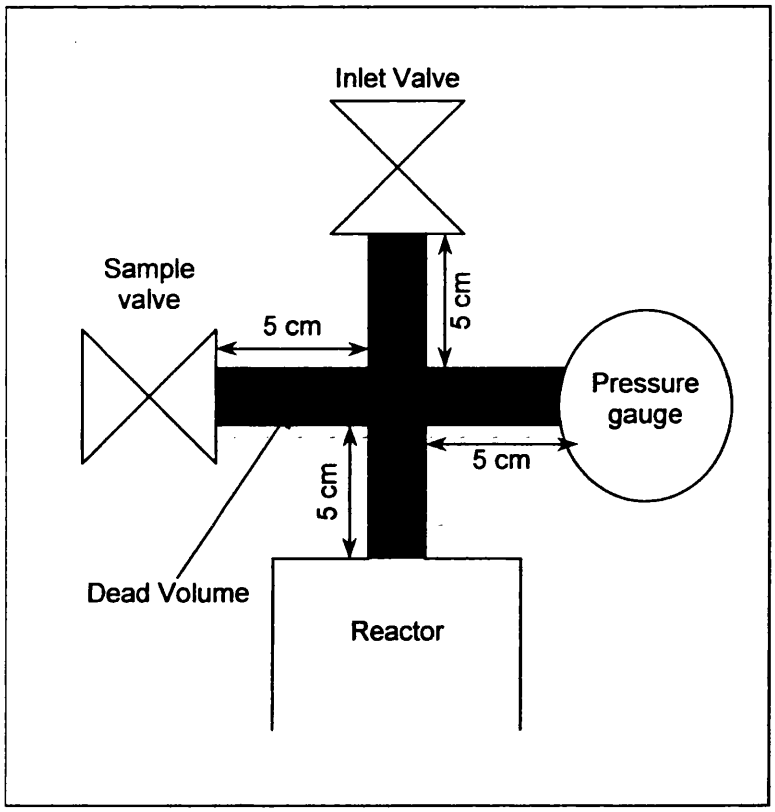

Figure 4.70 – Diagram showing regions of "dead volume" above the reactor

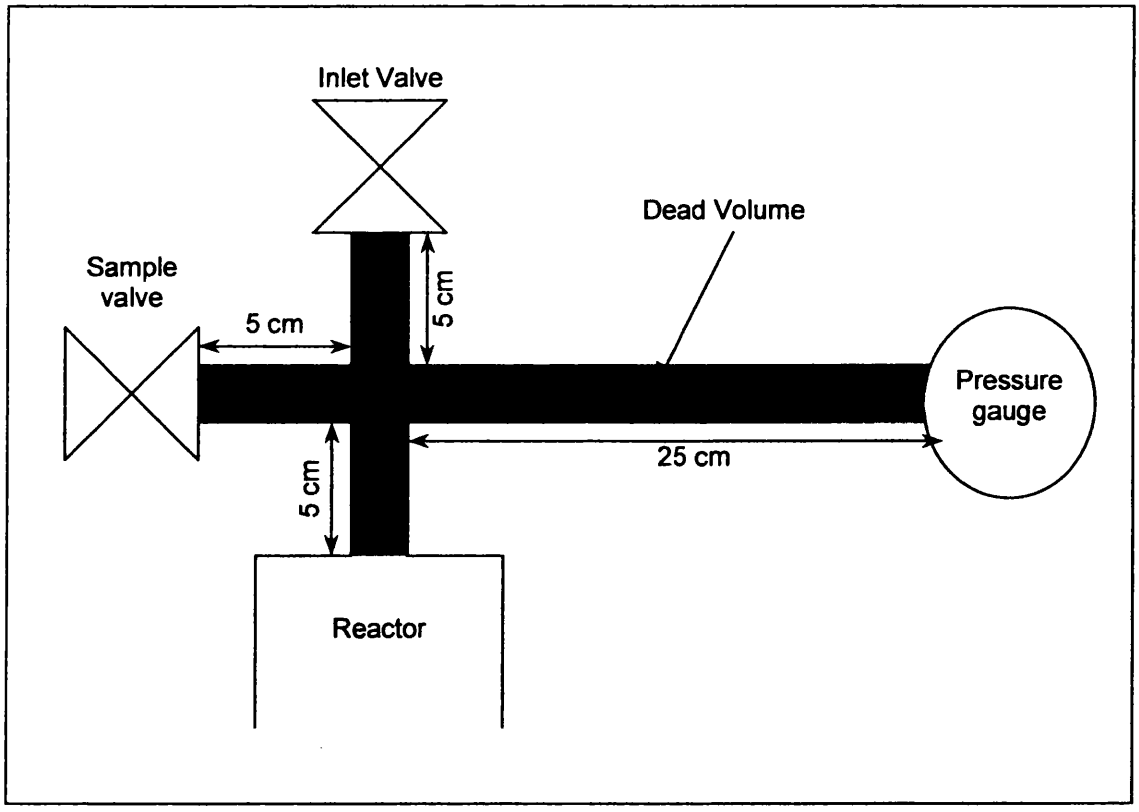

Figure 4.71 – Diagram showing tube extension used to test the effect of "dead volume" on reactor performance

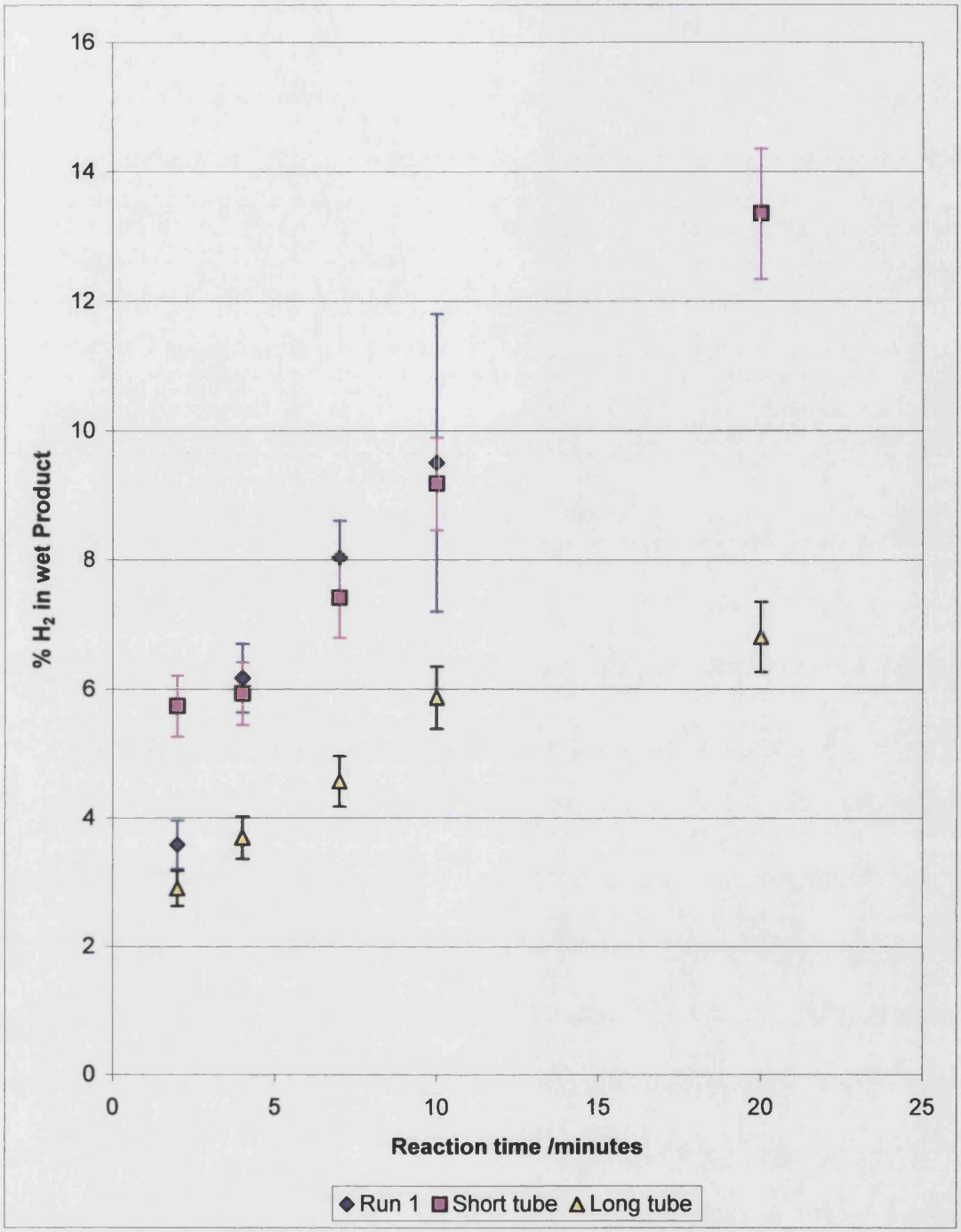

Figure 4.72 – Hydrogen production against time for different rig configurations

4.6.13 Simple diffusion model

In order to investigate whether the rate of diffusion in the tubes feeding the reactor could be partially responsible for its low conversion, a basic model was created. The purpose of the model was to determine whether it is feasible that the extent of the reaction was being reduced significantly by the time taken for reactants to diffuse from regions of dead

volume in connecting tubes into the reactor. An outline sketch indicating possible regions of dead volume that could have had a significant influence on the results is shown in Figure 4.70.

Initial assumptions

To obtain an estimate, a number of simplifying assumptions were made:

- Diffusion was initially modelled as 1-dimensional in a tube of uniform diameter.
- Equimolar counter diffusion was assumed, neglecting the change in the number of moles during the reaction.
- Pressure and temperature were assumed to be constant throughout.
- The starting condition was that the reactants were uniformly distributed throughout the tube, with no products present.
- The reaction was assumed to progress infinitely quickly, so that the concentrations of the various species at the interface between the tube and the reactor were at equilibrium concentrations.
- The effect of the diffusion rates of the products away from the reactor on the equilibrium composition was not considered.

Calculation of unsteady state diffusion rate

For unsteady state conditions, a material balance over a volume element yields Fick's Second Law (Coulson *et al.*, 1996, p. 500):

$$\frac{\partial C_A}{\partial t} = D_A \frac{\partial^2 C_A}{\partial z^2}$$

For a small time interval, Δt and distance, Δz, then with reference to Figure 4.73:

$$\frac{C_{Ai,j} - C_{Ai,j+1}}{\Delta t} = \frac{D_A}{\Delta z}\left[\left(\frac{C_{Ai,j} - C_{Ai-1,j}}{\Delta z}\right) - \left(\frac{C_{Ai+1,j} - C_{Ai,j}}{\Delta z}\right)\right] \qquad (4.50)$$

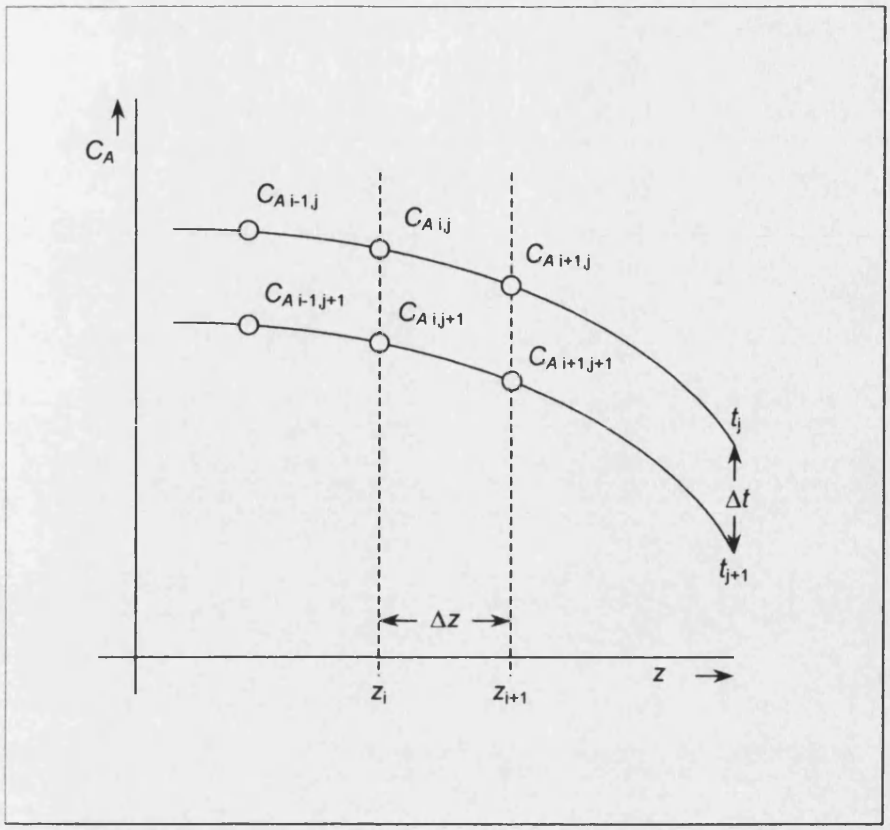

Figure 4.73 – Schematic showing change in concentration with distance and time

Equation (4.50) can be re-written:

$$C_{Ai,j+1} = C_{Ai,j} + \frac{D_A \Delta t}{(\Delta z)^2}\left[\left(C_{Ai+1,j} - C_{Ai,j}\right) - \left(C_{Ai,j} - C_{Ai-1,j}\right)\right] \tag{4.51}$$

Thus, the concentration at any point in the tube z_i, at time t_{j+1} can be estimated from the concentration at that point and at the adjacent points, z_{i-1} and z_{i+1}, at time t_j.

Determining the diffusivity

In order to use the equation above to model the system, a value for the diffusivity, D_A is required. In this case, a value for the diffusivity of CH_4 through a mixture of H_2O, CO, CO_2 and H_2 is required. The most favourable option is to use values that have been determined experimentally, since the errors are usually less than those of any estimate (Perry and Green, 1998, p. 5-48). In the absence of any experimental values, there are several different methods of estimating $D_{A,B}$, the binary diffusivity of species *A* in species *B*.

One of these is Gilliland's method, given below (Coulson *et al.*, 1996, p. 491):

$$D_{A,B} = \frac{4.3\times10^{-4} T^{1.5}\left((1/M_A)+(1/M_B)\right)^{0.5}}{P\left(V_A^{1/3}+V_B^{1/3}\right)^2} \tag{4.52}$$

V_A and V_B are the molecular volumes of species A and B, which may be determined from the Table 10.4 in Coulson *et al.* (1996) p. 492. M_A and M_B are the molecular mass of species A and B, T is the temperature in K, P is the pressure in Pa and $D_{A,B}$ is the diffusivity in m²/s.

It should be noted that this method implies that the diffusivity is inversely proportional to pressure and varies with temperature raised to the 1.5 power. There is evidence that this underestimates the temperature dependence. A more recent method is that of Fuller, Schettler and Giddings, which is described in Perry and Green (1998) p. 2-370 and is reproduced below:

$$D_{A,B} = \frac{0.01013T^{1.75}\left((1/M_A)+(1/M_B)\right)^{0.5}}{P\left(\left(\sum \upsilon_A\right)^{1/3}+\left(\sum \upsilon_B\right)^{1/3}\right)^2} \tag{4.53}$$

In this equation, υ_A and υ_B are atomic diffusion volumes, determined experimentally for different elements and molecules. They may be found in Table 5-16 in Perry and Green (1998) p. 5-49. Note that in this equation, diffusivity varies with temperature raised to the 1.75 power.

Experimental data are available for D_{CH_4,CO_2} and D_{CH_4,H_2} in Table 2-371 in Perry and Green (1998) p. 2-328. These data are for gases at 1 atm and 0°C and are in units of cm²/s. They may be converted to values in m²/s by dividing by 10^4. Values at the required temperature and pressure may then be estimated in the following way:

$$D_{T,P} = D_{273K,1atm}\frac{101325T^{1.75}}{273.15^{1.75}P} \tag{4.54}$$

where T is in K and P is absolute pressure in Pa. The values obtained for D_{CH_4,CO_2} and D_{CH_4,H_2} are given in Table 4.19:

Table 4.19 – Binary diffusion coefficients from Perry (1998), Table 2-371

A	B	$D_{A,B}$ at 1 atm and 0°C (cm²/s)	$D_{A,B}$ at 6 bar g and 700°C (m²/s)
CH_4	CO_2	0.153	2.04×10^{-5}
CH_4	H_2	0.625	8.34×10^{-5}

The values for D_{CH_4,H_2O} and $D_{CH_4,CO}$ were estimated using Equation (4.53). In order to verify the accuracy of Equation (4.53), values for D_{CH_4,CO_2} and D_{CH_4,H_2} were also calculated and compared with the experimental values in Table 4.19. The parameters used in the calculations and the results are given in Table 4.20 below:

Table 4.20 – Parameters in Equation (4.53) and calculated binary diffusion coefficients

A	B	M_A	M_B	$\Sigma\upsilon_A$	$\Sigma\upsilon_B$	$D_{A,B}$ at 6 bar g and 700°C (m²/s)
CH_4	H_2O	16.04	18.02	24.42	12.7	3.07×10^{-5}
CH_4	CO	16.04	28.01	24.42	18.9	2.48×10^{-5}
CH_4	CO_2	16.04	44.01	24.42	26.9	2.05×10^{-5}
CH_4	H_2	16.04	2.02	24.42	7.07	7.87×10^{-5}

The value of D_A for CH_4 in CO_2 is in very good agreement with the experimental value, while that for CH_4 in H_2 is within 6% of the experimental value. Therefore, Equation (4.53) is probably providing reasonable estimates of the unknown values.

The diffusivity of CH_4 in a mixture of H_2O, CO, CO_2 and H_2 may be calculated from the separate binary diffusivities and the mole fractions of the components in the mixture using Equation (4.55) below (Wilke, 1950):

$$D_{A,mix} = \frac{(1-y_A)}{\sum_{\substack{i \\ i\neq A}} y_i / D_{A,i}} \qquad (4.55)$$

Equation (4.55) was developed from the Stefan-Maxwell equations. In order to use it, it is now necessary to estimate the composition of the mixture through which the CH_4 is diffusing. The change in mole fraction of CH_4 between the initial composition and the equilibrium composition, present after an infinite amount of time, is given by Equation (4.56):

$$\Delta y_{CH_4,\infty} = y_{CH_4,initial} - y_{CH_4,equilibrium} \tag{4.56}$$

The change in mole fraction of CH_4 between the initial composition and the composition at time t is given by Equation (4.57):

$$\Delta y_{CH_4,t} = y_{CH_4,initial} - y_{CH_4,t} \tag{4.57}$$

The progress of the diffusion between $t = 0$ and $t = \infty$ may be characterised by the co-ordinate, θ_t, defined as:

$$\theta_t = \frac{\Delta y_{CH_4,t}}{\Delta y_{CH_4,\infty}} \tag{4.58}$$

In reality, the different gases present diffuse at different rates and are produced or consumed at different rates by the reactor. However, in order to simplify the calculation of D_A for CH_4 in the mixture, it is assumed that, at each point in the tube, the proportional change in mole fraction for each gas mirrors that of CH_4. Therefore, for H_2O we can write:

$$y_{H_2O,t} = y_{H_2O,initial} - \theta_t \Delta y_{H_2O,\infty} \tag{4.59}$$

For CO, CO_2 and H_2, $\Delta y_{i,\infty} = -y_{i,equilibrium}$ and $\Delta y_{i,t} = -y_{i,t}$, so Equation (4.59) can be re-written:

$$y_{i,t} = \theta_t y_{i,equilibrium} \tag{4.60}$$

At any point in the tube, the mole fraction of CH_4 can be found from the concentration of CH_4 at that point and the total molar concentration (calculated as the density of an ideal gas) at that point. This allows the composition of the gas at that point to be calculated using Equations (4.58), (4.59) and (4.60). The diffusivity of CH_4 in the mixture in the slice can then be calculated using Equation (4.55). The composition of the gas at one point may be different to the composition at the neighbouring point. In order to account for this, the average mole fraction of CH_4 between point z_i and point z_{i+1} is used to calculate D_A for the diffusion between these points, and the average mole fraction of CH_4 between points z_i and z_{i-1} is used to calculate D_A' for diffusion between these points. Therefore, Equation (4.51) is rewritten:

$$C_{Ai,j+1} = C_{Ai,j} + \frac{\Delta t}{(\Delta z)^2}\left[D_A\left(C_{Ai+1,j} - C_{Ai,j}\right) - D'_A\left(C_{Ai,j} - C_{Ai-1,j}\right)\right] \qquad (4.61)$$

Boundary conditions

For the first point, z_1, $(C_{Ai,j} - C_{Ai-1,j})$ is taken to be zero, since there is no point z_0 and mass transfer can only take place between z_1 and z_2. In calculating $D_{As,t}$ and $C_{An,j}$ for point z_n (the final point) the value of $C_{An+1,j}$ is assumed to be constant and equal to the equilibrium concentration.

Model improvement to take into account changing cross-sectional area

If the cross sectional area of the tube changes between one point and another, it will affect the rate of mass transfer between the points. In this case Equation (4.61) should be rewritten:

$$C_{Ai,j+1} = C_{Ai,j} + \frac{\Delta t}{(\Delta z)^2}\left[\frac{A_{i+1}}{A_i} D_A\left(C_{Ai+1,j} - C_{Ai,j}\right) - \frac{A_{i-1}}{A_i} D'_A\left(C_{Ai,j} - C_{Ai-1,j}\right)\right] \qquad (4.62)$$

where A_i is the cross-sectional area at point z_i, A_{i+1} is the area available for mass transfer between points z_i and z_{i+1}, and A_{i-1} is the area available for mass transfer between points z_i and z_{i-1}.

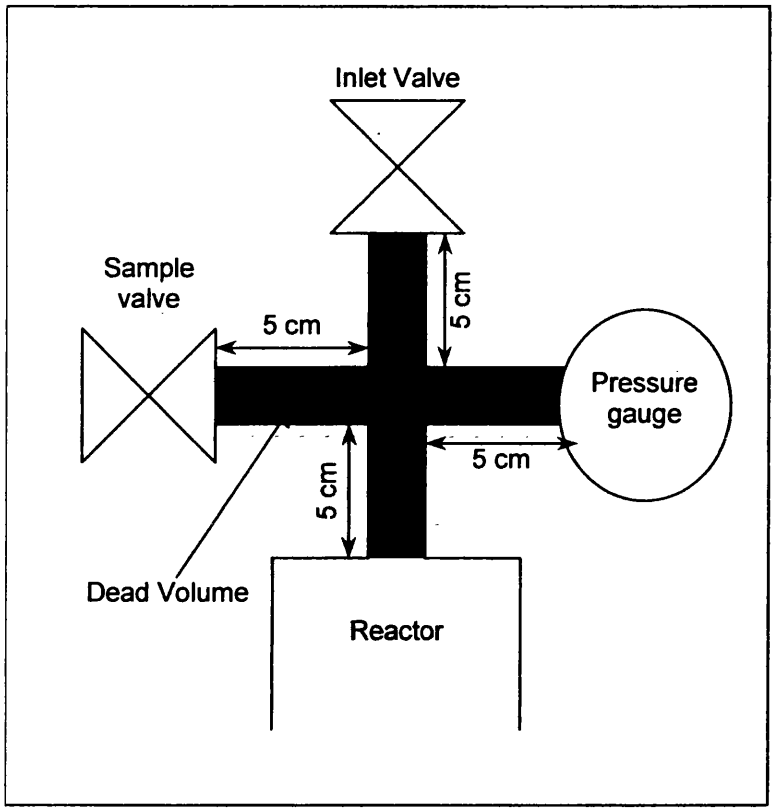

Figure 4.74 – Diagram of the layout of the tubes above the reactor

In order to more realistically model the experimental system, the fact that 4 tubes came together in a cross above the reactor was taken into account. Figure 4.74 shows the actual physical situation present in the experimental apparatus. The methane has to diffuse from the 3 upper tubes into the lower one leading to the reactor. All 4 tubes are the same length (5 cm) and diameter (1/4 inch (6.4 mm) o.d.). This was modelled as a single tube, 5 cm in length, connected to another tube of 5 cm length but 1/3 of the diameter. This is shown in Figure 4.75.

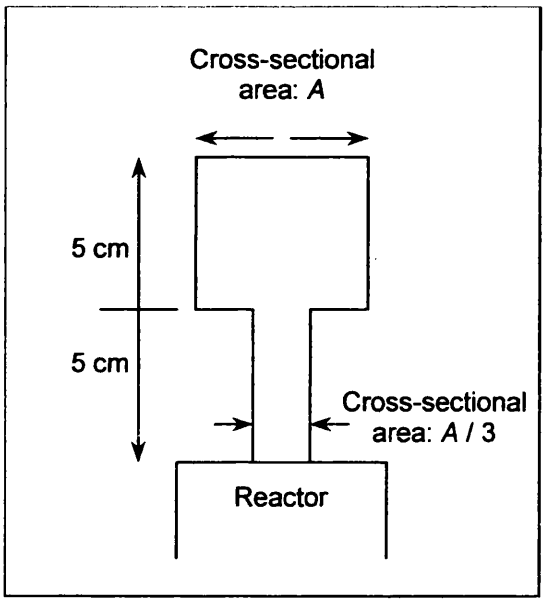

Figure 4.75 – Schematic of the layout used to model diffusion in the dead volume

For the point immediately before the cross-sectional are reduces (see Figure 4.76 below) the area available for diffusion from the previous point is the same as the cross-sectional area at the current point, whereas the area available for diffusion to the next adjacent point is reduced by a third. Thus, $A_{i-1} = A_i$ and $A_{i+1} = A_i / 3$.

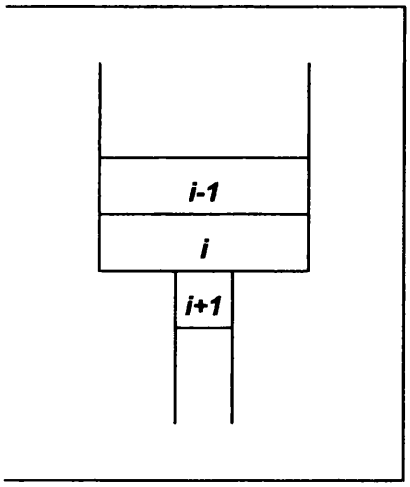

Figure 4.76 – Schematic showing the point before reduction in tube area

For the point immediately after the reduction in cross-sectional area (see Figure 4.77 below) the area available for diffusion is the same to both adjacent points, *i.e.* $A_{i-1} = A_i = A_{i+1}$.

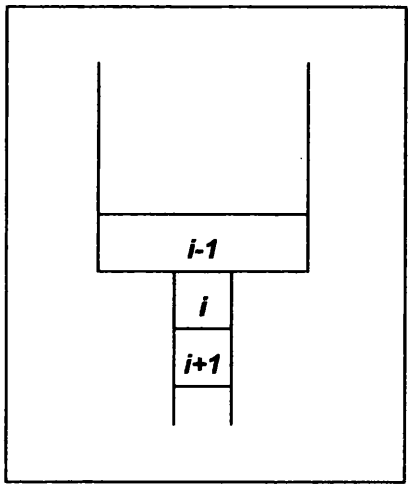

Figure 4.77 – Schematic showing the point after reduction in tube area

Diffusion model results

The calculations were performed in Excel using a Visual Basic macro, which is listed in Appendix C.

To match the experiments that were repeated with different lengths of tube, the conditions that were modelled were as follows:

- Steam to methane ratio of 2
- Temperature of 700°C
- Pressure of 6 bar g
- Reaction times of 2, 4, 7, 10 and 20 minutes

Under these conditions, the equilibrium mole fraction of methane is 0.106.

Single tube, uniform cross sectional area

The model was first run for a tube 15 cm in length. A time increment, Δt of 0.1 s was used and the number of slices, n was 40. The results are shown in Figure 4.78.

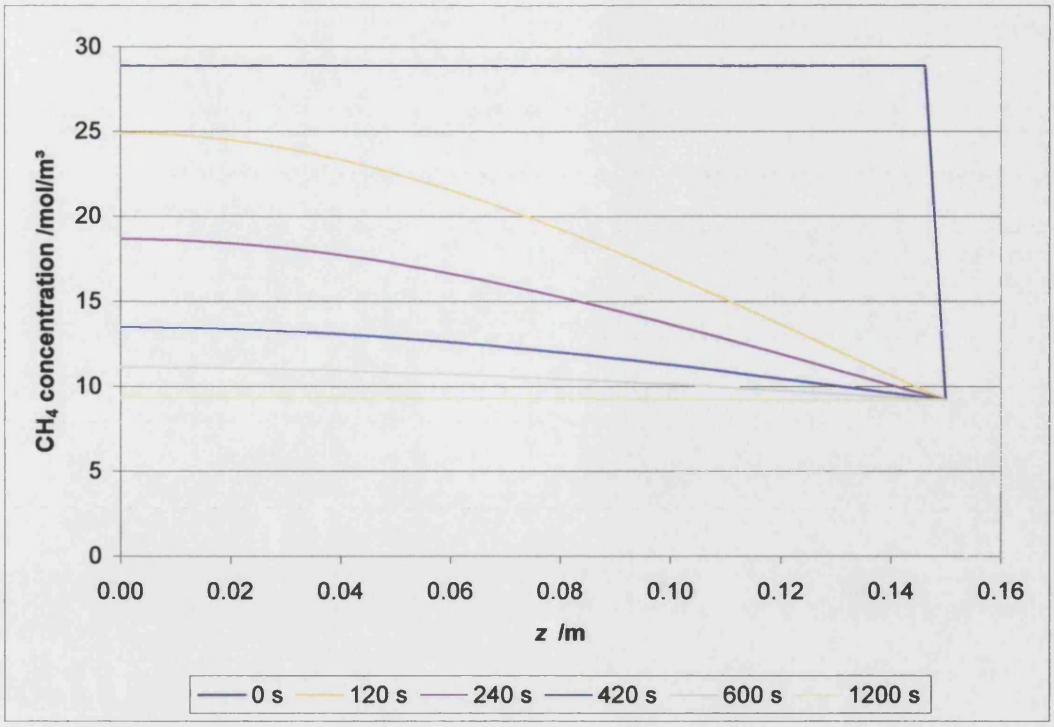

Figure 4.78 – l = 15 cm, Δt = 0.1 s, n = 40

Next, a tube length of 30 cm was used. The results of this model are shown in Figure 4.79. In order to check that the increase in Δz in the second run did not affect the results very much, the following run was for a tube length of 30 cm, using 80 points. These results are given in Figure 4.80.

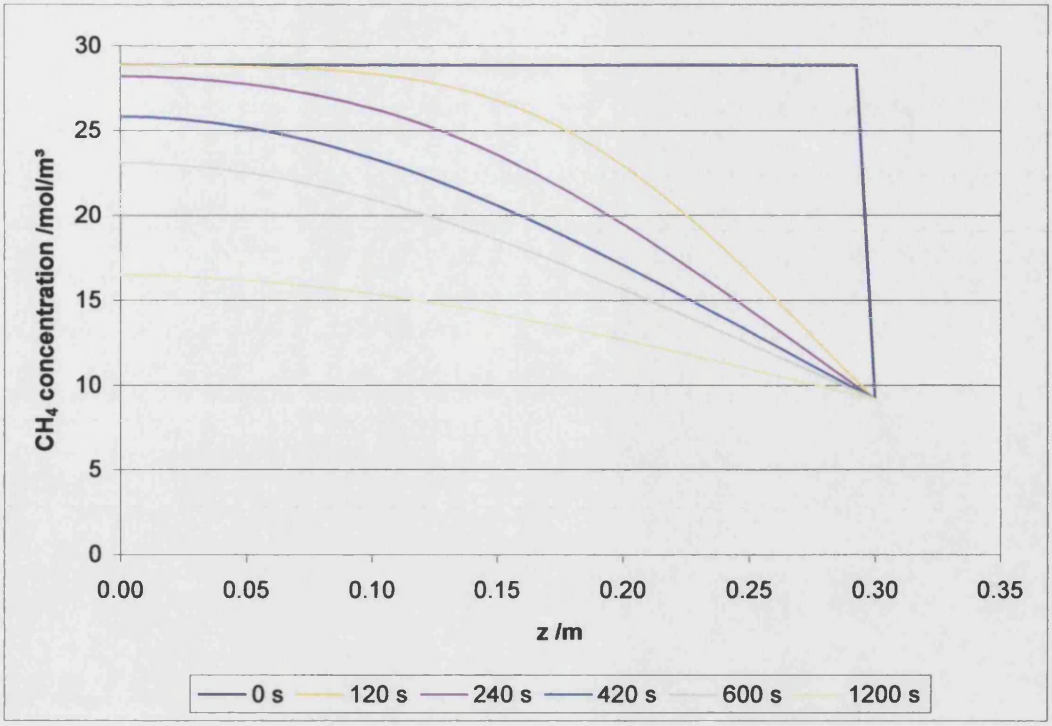

Figure 4.79 – $l = 30$ cm, $\Delta t = 0.1$ s, $n = 40$

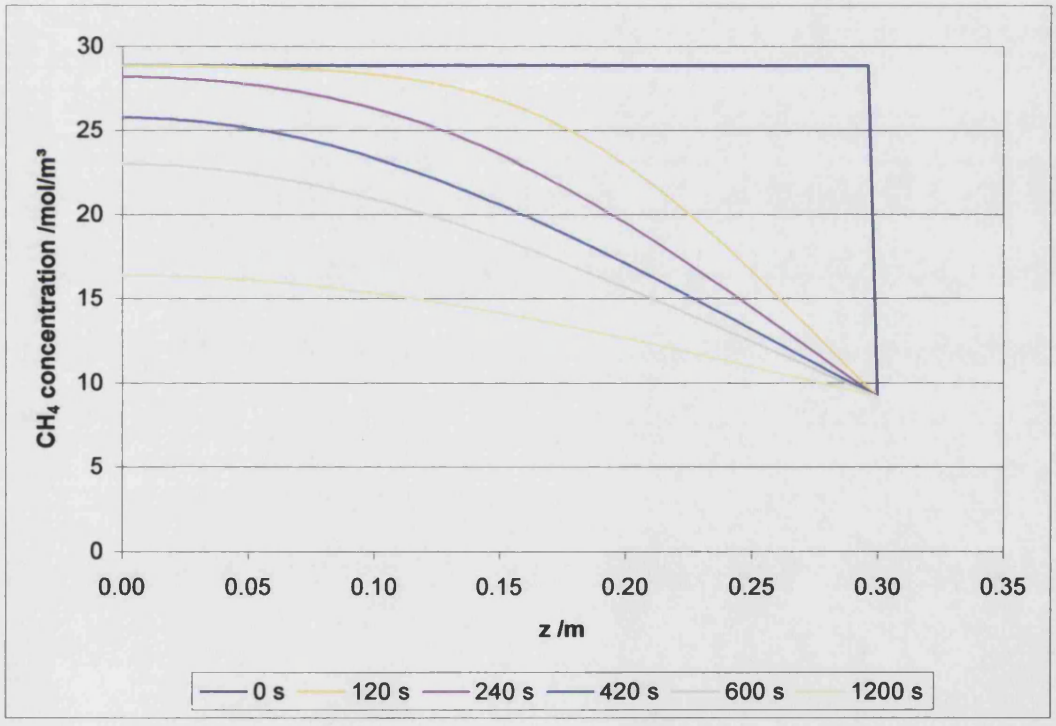

Figure 4.80 – $l = 30$ cm, $\Delta t = 0.1$ s, $n = 80$

Single tube with step reduction in cross sectional area

In this case, the area was reduced to a third of its original value after the slice at 5 cm. 20 points were used initially. Figure 4.81 shows the results.

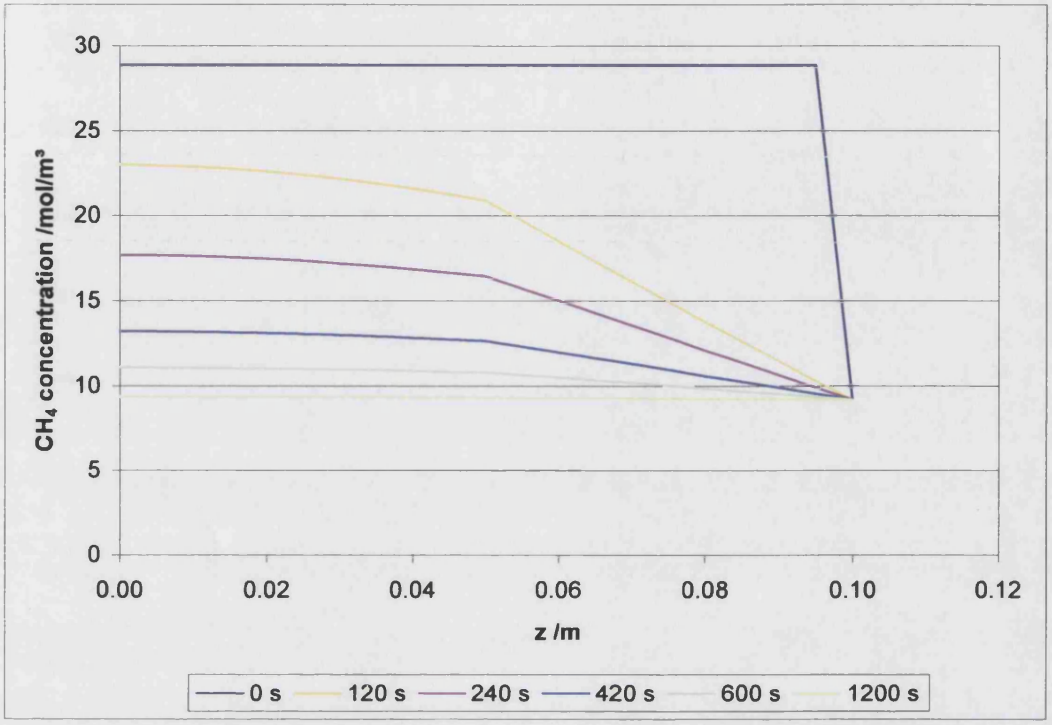

Figure 4.81 – l = 10 cm, Δt = 0.1 s, n = 20

In order to see whether there was much effect from reducing Δz further, the number of slices was increased to 40. This necessitated a decrease in Δt to 0.05 s, to prevent the model becoming unstable. This is because the instantaneous concentration gradient doubles with a halving of the Δz which can cause the change in C to be too large, unless Δt is suitably reduced. The results under these conditions are given in Figure 4.82.

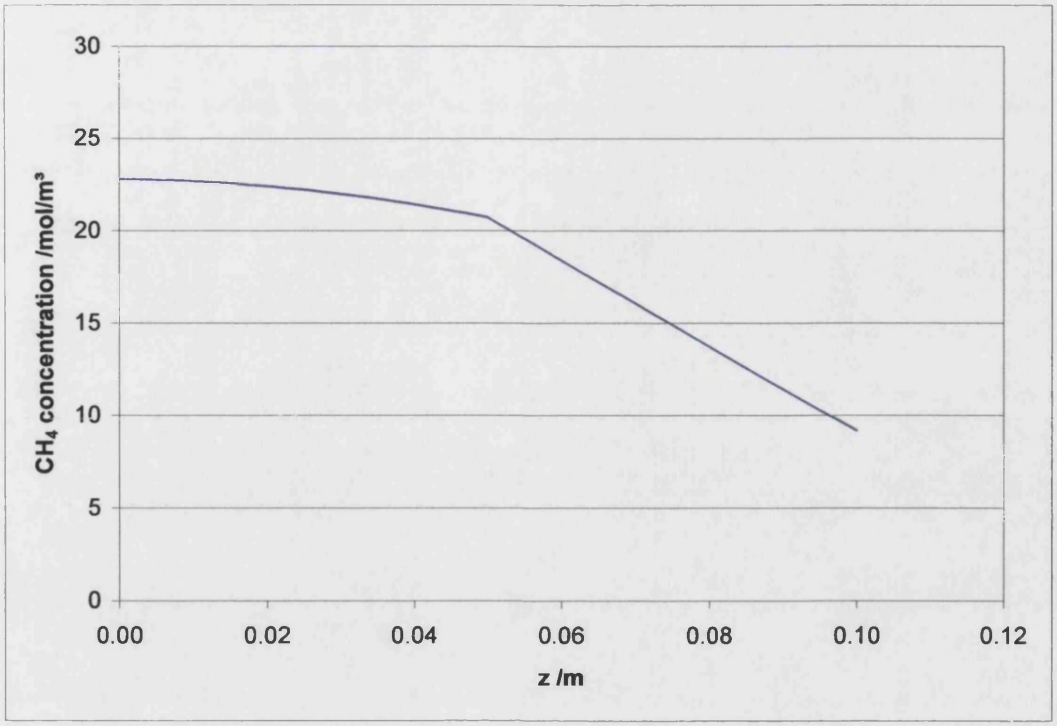

Figure 4.82 – l = 10 cm, Δt = 0.05 s, n = 40, final time = 120 s

Comparison of Figure 4.81 and Figure 4.82 reveals that there is little effect caused by reducing Δz, although the calculation time was significantly increased.

The results given in Table 4.21 are the average mole fractions of methane present in the tubes after a given length of time.

Table 4.21 – Results from basic model of diffusion in reactor feed tubes

	Average mole fraction of methane in tubes		
Time elapsed	Straight 15 ml tube	Straight 30 ml tube	4×5 ml tubes joined in cross piece
0 minutes	0.333	0.333	0.333
2 minutes	0.221	0.277	0.219
4 minutes	0.175	0.253	0.176
7 minutes	0.138	0.227	0.139
10 minutes	0.120	0.206	0.122
20 minutes	0.107	0.158	0.107

The volume of gas in the reactor is approximately 8 ml. The time taken for the reactants to diffuse into the reactor is likely to be significant for the shorter reaction periods. However, due to the relatively small volume of the reactor feed tubes (the length of tube

connected to each branch of the cross piece above the reactor is approximately 5 cm, thus the volume of the tubes is approximately 1 ml) this effect would not change the product concentration to a great degree. Certainly, for the long duration runs, the effect of slow diffusion in the tubes is unlikely to be significant.

4.6.14 Undesired condensation of steam

As diffusion in the tubes is not a major factor responsible the low conversion of methane observed in the reactor, there must be something else occurring in the reactor feed tubes. These tubes were insulated, but they were not trace heated like the reactant delivery tube. Perhaps some of the steam in the feed was condensing out in the feed tubes before it entered the reactor. It would not have been possible for a great deal of water to collect in the tubes, but if any were present there when the reactor was discharged, it could simply have been blown out into the sample bag. The temperature of the feed tubes was assumed to be high enough to prevent steam condensation, but perhaps the tube entering the pressure gauge was cool enough to allow a small amount of condensation. It would not require a great volume of water to condense to significantly affect the reactant composition. Even at 10 bar g, 1 mol of an ideal gas occupies 7.3 litres, whereas 1 mol of liquid water only occupies 18 ml. Any significant condensation of steam would have reduced the *SMR* and could have caused the coking of the catalyst that was observed. However, any condensation would have to have preceded very slowly (or very quickly, before the inlet valve was closed), otherwise a reduction in reactor pressure would have been observed.

4.6.15 Heat transfer within the reactor

Another possible cause of poor reaction rate would be poor heat transfer within the reactor. The steam reforming reaction is endothermic, so heat has to transfer from the block and through the tube walls to the catalyst inside. In order for the pellets lying in the centre of the reaction tube to be effective, heat must be transferred to the reaction sites on the catalyst surface. It is unlikely that the main source of heat transfer will be conduction from pellet to pellet. Due to the high temperatures involved, heat transfer is more likely to be in the form of radiation from the tube walls and adjacent pellets, combined with natural convection of the reactant mixture. If the reaction period were only a matter of

seconds, the heat transfer rate may have had a significant effect on the results. However, over the space of several minutes, all of the material inside the reactor would have reached the required temperature.

4.6.16 Most likely factors affecting reactor performance

The cause of the low rate of reaction in the experimental system is most likely to be a combination of the following processes:

- Some coking of the catalyst occurred, particularly during the initial runs, thus reducing the effectiveness factor.
- The dead volume in the tubes above the reactor reduced the reactor performance. Experiments showed that elimination of the dead volume could potentially double the hydrogen yield (see Figure 4.72). In addition, longer tubes caused a reduction in the equilibrium hydrogen yield. This could be due to partial condensation of steam in the feed tubes reducing the actual *SMR* of the feed to the reactor.
- The catalyst may not have had a very high activity to start with. This can only be ascertained by conducting tests on the catalyst using a conventional tubular reactor.

Chapter 5 - Conclusions and recommendations

5.1 Key conclusions drawn from the experimental work

Reactor performance

The hydrogen yield and methane conversion increased with higher reformer temperature, longer residence time and lower reformer pressure. This is as predicted by the thermodynamic analysis.

The reaction did not get close to equilibrium after a residence time of 10 minutes. This is at least an order of magnitude more time than predicted by kinetic analysis. The proportion of hydrogen in the product was between one third and one tenth of the equilibrium value after a residence time of 10 minutes. After 20 minutes, the hydrogen proportion was still increasing roughly linearly with time.

Reasons for the failure to approach equilibrium were discussed and the following aspects were considered:

- A significant amount of coking was observed on the used catalyst. Carbon deposition was confirmed by SEM analysis. However, catalyst deactivation over the course of the experiments was ruled out by comparison of data from repeated runs.
- Heat transfer limitations were ruled out due to the relatively long residence times.
- The amount of "dead volume" in the tubes feeding the reformer was found to adversely affect both the reaction rate and the equilibrium conversion (doubling the dead volume roughly halved the amount of hydrogen produced in a given time).
- A simple model ruled out diffusion limitations in the tubes for this effect. Another possibility is that steam was condensing inside the tubes (which were not at reaction temperature) thereby altering the reactant composition.

Reliability of data

The gas chromatograph that was used for the analysis of product gas was calibrated quite precisely, with errors in the computed response factors ranging from 0.1% to 2.6%. Despite measuring the hydrogen concentration in the dry sample gas directly with the GC, it was found that it could be calculated more accurately by material balance using the measured concentrations of CH_4 and CO_2. Using a basis of 1 mol CH_4 in the feed, the extents of reaction were calculated, and from these the composition of the product gas was determined for each experimental run. The estimated proportional error in the calculated hydrogen concentrations ranged from 7% to 24%, with the average being 14%.

The repeatability of the experiments was very good. The data from repeated experiments were identical to within estimated experimental error.

Reactor design

The reactor was able to operate at the temperatures and pressures required for this thesis.

The viability of using an electric cartridge heater to pre-heat the reactor was demonstrated. The temperature inside the reaction tubes reached 450°C after about 60 minutes and 500°C after about 120 minutes. This is a sufficiently high temperature to initiate a catalytic combustion reaction in one of the reaction tubes (Ma *et al.*, 1996).

Simulation of steam reforming reactions

Thermodynamic equilibrium analysis of the steam reforming reactions using various sources of data show good agreement with data produced by Aspen.

Simulations were set up in Aspen that showed that the low pressure compact steam reforming system is a feasible one. Simulations showed a significant increase in equilibrium conversion at lower pressures. Depending on the end use of the hydrogen gas, it may be far more efficient to run the steam reformer at a low pressure.

5.2 Recommendations for future work

Experiments should be conducted with the absolute minimum dead volume possible above the reactor. This could be achieved by using smaller diameter feed/exhaust tubes and minimising the lengths as much as possible. An increase in reactor volume would also have the effect of reducing the relative dead volume of the feed/exhaust tubes. The tubes above the reactor should be better insulated and trace heated.

A cartridge heater with high-temperature resistant cables should be specified for any future experiments. Otherwise, the specification should remain the same.

Experiments should be carried out on the catalytic combustion part of the system and the coupling of the combustion and reforming reactions should be investigated.

Experiments in which the methane and steam are added sequentially should be carried out to explore any advantage gained in reducing the chance of carbon formation.

The use of alternative catalysts such as platinum could be investigated. Also, different catalyst support materials could be tested.

If a platinum catalyst is used, would it be possible to use the same channel for reforming and combustion reactions by cycling the feed?

Would it be possible to use an enhanced oxygen feed to reduce gas flow for the combustion process? If so, could the steam-rich output be used as a feed for the reforming process?

Chapter 6 - References

Adris, A.M., Lim, C.J. and Grace, J.R. (1994). The fluidized bed membrane reactor system: A pilot scale experimental study. *Chemical Engineering Science,* **49**(24B), pp. 5833-5843.

Adris, A.M., Pruden, B.B., Lim, C.J. and Grace, J.R. (1996). On the Reported Attempts to Radically Improve the Performance of the Steam Methane Reforming Reactor. *The Canadian Journal Of Chemical Engineering,* **74**, pp. 177-186.

Aguiar, P., Lapeña-Rey, N., Chadwick, D. and Kershenbaum, L. (2001). Improving catalyst structures and reactor configurations for autothermal reaction systems: application to solid oxide fuel cells. *Chemical Engineering Science,* **56**, pp. 651-658.

Aguiar, P., Chadwick, D. and Kershenbaum, L. (2002). Modelling of an indirect internal reforming solid oxide fuel cell. *Chemical Engineering Science,* **57**, pp. 1665-1677.

Avcı, A.K., Trimm, D.L. and İlsen Önsan, Z. (2001). Heterogeneous reactor modelling for simulation of catalytic oxidation and steam reforming of methane. *Chemical Engineering Science,* **56**, pp. 641-649.

Batta, L.B. (1971). Selective adsorption process. *U.S. Patent 3,564,816.*

Björklund, A., Melaina, M. and Keoleian, G. (2001). Hydrogen as a transportation fuel produced from thermal gasification of municipal solid waste: an examination of two integrated technologies. *International Journal of Hydrogen Energy,* **26**, pp. 1209-1221.

Blue, R.W., Holm, V.C.F., Regier, R.B., Fast, E. and Heckelsberg, L.F. (1952). Effect of Granule Size in dehydrogenation of butane and in a hydrogen transfer reaction. *Industrial and Engineering Chemistry,* **44**(11), pp. 2710-2716.

Chum, H.L. and Overend, R.P. (2001). Biomass and renewable fuels. *Fuel Processing Technology,* **71**, pp. 187-195.

Coulson & Richardson's Chemical Engineering, Volume 1. (1996). Coulson, J.M., Richardson, J.F., with Backhurst, J.R. and Harker, J.H. 5th ed. Oxford: Butterworth-Heinemann.

DeLuchi, M.A. (1989). Hydrogen vehicles: An evaluation of fuel storage, performance, safety, environmental impacts, and cost. *International Journal of Hydrogen Energy,* **14**(2), pp. 81-130.

de Smet, C.R.H., de Croon, M.H.J.M., Berger, R.J., Marin, G.B. and Schouten, J.C. (2001). Design of adiabatic fixed-bed reactors for the partial oxidation of methane to synthesis gas. Application to production of methanol and hydrogen-for-fuel-cells. *Chemical Engineering Science,* **56**(16), pp. 4849-4861.

Dillon, A.C., Jones, K.M., Bekkedahl, T.A., Kiang, C.H., Bethune, D.S. and Heben, M.J. (1997). Storage of hydrogen in single-walled carbon nanotubes. *Nature,* **386**, pp. 377-379.

Dirksen, H.A. and Riesz, C.H. (1953). Equilibrium in the Steam Reforming of Natural Gas. *Industrial and Engineering Chemistry,* **45**(7), pp. 1562-1565.

Docter, A. and Lamm, A. (1999). Gasoline fuel cell systems. *Journal of Power Sources,* **84**, pp. 194-200.

Dudfield, C.D., Chen, R. and Adcock, P.L. (2001). A carbon monoxide PROX reactor for PEM fuel cell automotive application. *International Journal of Hydrogen Energy,* **26**, pp. 763-775.

Duonghong, D., Borgarello, E. and Grätzel, M. (1981). Dynamics of Light-Induced Water Cleavage in Colloidal Systems. *Journal of the American Chemical Society,* **103**(16), pp. 4685-4690.

Eisenstein, P. (2003). Kicking the oil habit. *Professional Engineering,* **16**(8), pp. 26-27.

Emonts, B. (1999). Catalytic radiant burner for stationary and mobile applications. *Catalysis Today,* **47**, pp. 407-414.

Emonts, B., Bøgild-Hansen, J., Lœgsgaard Jørgensen, S., Höhlein, B. and Peters, R. (1998). Compact methanol reformer test for fuel-cell powered light duty vehicles. *Journal of Power Sources,* **71**, pp. 288-293.

Farrell, A.E., Keith, D.W. and Corbett, J.J. (2003). A strategy for introducing hydrogen into transportation. *Energy Policy,* **31**, pp. 1357-1367

Felder, R.M. and Rousseau, R.W. (1986). *Elementary Principles Of Chemical Processes.* 2nd ed. New York: John Wiley & Sons.

Frauhammer, J., Eigenberger, G., Hippel, L.v. and Arntz, D. (1999). A new reactor concept for endothermic high-temperature reactions. *Chemical Engineering Science,* **54**, pp. 3661-3670.

Fuderer, A. and Rudelstorfer, E. (1976). Selective adsorption process. *U.S. Patent 3,986,849.*

Ghirardi, M.L., Zhang, L., Lee, J.W., Flynn, T., Seibert, M., Greenbaum, E. and Melis, A. (2000). Microalgae: a green source of renewable H_2. *Trends in Biotechnology,* **18**, pp. 506-511.

Guy, K.W.A. (2000). The Hydrogen Economy. *Transactions of the Institute of Chemical Engineers,* **78**(B), pp. 324-327.

Hacker, V. (2003). A novel process for stationary hydrogen production: the reformer sponge iron cycle (RESC). *Journal of Power Sources,* **118**, pp. 311-314.

Hacker, V., Fankhauser, R., Faleschini, G., Fuchs, H., Friedrich, K., Muhr, M. and Kordesch, K. (2000). Hydrogen production by steam-iron process. *Journal of Power Sources,* **86**, pp. 531-535.

Hayes, R.E. and Kolaczkowski, S.T. (1997). *Introduction to catalytic combustion.* Amsterdam: Gordon and Breach Science Publishers.

He, D., Bultel, Y., Magnin, J.-P., Roux, C. and Willison, J.C. (2005). Hydrogen photosynthesis by *Rhodobacter capsulatus* and its coupling to a PEM fuel cell. *Journal of Power Sources,* **141**, pp. 19-23.

Hickman, D.A., Haupfear, E.A. and Schmidt, L.D. (1993). Synthesis gas formation by direct oxidation of methane over Rh monoliths. *Catalysis Letters,* **17**, pp. 223-237.

Höhlein, B., Biedermann, P., Grube, T. and Menzer, R. (1999). Fuel cell power trains for road traffic. *Journal of Power Sources,* **84**, pp. 203-213.

Höhlein, B., Boe, M., Bøgild-Hansen, J., Bröckerhoff, P., Colsman, G., Emonts, B., Menzer, R. and Riedel, E. (1996). Hydrogen from methanol for fuel cells in mobile systems: development of a compact reformer. *Journal of Power Sources,* **61**, pp. 143-147.

Hou, K. and Hughes, R. (2001). The kinetics of methane steam reforming over a Ni/α-Al_2O catalyst. *Chemical Engineering Journal,* **82**, pp. 311-328.

Hufton, J.R., Mayorga, S. and Sircar, S. (1999). Sorption-Enhanced Reaction Process for Hydrogen Production. *AIChE Journal,* **45**(2), pp. 248-256.

ICI Catalysts brochure. Equilibrium Constants.

Iijima, S. (1991). Helical microtubes of graphitic carbon. *Nature,* **354**(11), pp. 56-58.

Ioannides, T. (2001). Thermodynamic analysis of ethanol processors for fuel cell applications. *Journal of Power Sources,* **92**, pp. 17-25.

Kalhammer, F.R., Prokopius, P.R., Roan, V.P., Voecks, G.E. (1998). *Status and prospects of fuel cells as automobile engines.* Sacramento, California. Fuel Cell Technical Advisory Panel.

Karakitsou, K.E. and Verykios, X.E. (1993). Effects of Altervalent Cation Doping of TiO_2 on Its Performance as a Photocatalyst for Water Cleavage. *The Journal of Physical Chemistry,* **97**(6), pp. 1184-1189.

Kawai, T. and Sakata, T. (1980). Conversion of carbohydrate into hydrogen fuel by a photocatalytic process. *Nature,* **286**, pp. 474 - 476.

Kolios, G., Frauhammer, J. and Eigenberger, G. (2002). Efficient reactor concepts for coupling endothermic and exothermic reactions. *Chemical Engineering Science,* **57**, pp. 1505-1510.

Lambert, J., Sorin, M. and Paris, J. (1997). Analysis of oxygen-enriched combustion for steam methane reforming (SMR). *Energy,* **22**(8), pp. 817-825.

Ledjeff-Hey, K., Formanski, V., Kalk, Th. and Roes, J. (1998). Compact hydrogen production systems for solid polymer fuel cells. *Journal of Power Sources,* **71**, pp. 199-207.

Lee, K.K., Han, G.Y., Yoon, K.J. and Lee, B.K. (2004). Thermocatalytic hydrogen production from methane in a fluidized bed with activated carbon catalyst. *Catalysis Today,* **93-95**, pp. 81-86.

Ma, L. and Trimm, D.L. (1996). Alternative catalyst bed configurations for the autothermic conversion of methane to hydrogen. *Applied Catalysis A: General,* **138**(2), pp. 265-273.

Ma, L., Trimm, D.L. and Jiang, C. (1996). The design and testing of an autothermal reactor for the conversion of light hydrocarbons to hydrogen I. The kinetics of the catalytic oxidation of light hydrocarbons. *Applied Catalysis A: General,* **138**(2), pp. 275-283.

Monnerat, B., Kiwi-Minsker, L. and Renken, A. (2001). Hydrogen production by catalytic cracking of methane over nickel gauze under periodic reactor operation. *Chemical Engineering Science,* **56**, pp. 633-639.

Moore, R.B. and Ramen, V. (1998). Hydrogen infrastructure for fuel cell transportation. *International Journal of Hydrogen Energy,* **23**(7), pp. 617-620.

Muradov, N.Z. and Veziroğlu, T.N. (2005). From hydrocarbon to hydrogen-carbon to hydrogen economy. *International Journal of Hydrogen Energy,* **30**, pp. 225-237.

Nakagawa, K., Nishitani-Gamo, M. and Ando, T. (2005). Hydrogen production from methane for fuel cell using oxidized diamond-supported catalysts. *International Journal of Hydrogen Energy,* **30**, pp 201-207.

Nielsen, A.T., Amandusson, H., Bjorklund, R., Dannetun, H., Ejlertsson, J., Ekedahl, L-G., Lundström, I. and Svensson, B.H. (2001). Hydrogen production from organic waste. *International Journal of Hydrogen Energy,* **26**, pp. 547-550.

Numaguchi, T. and Kikuchi, K. (1988). Intrinsic kinetics and design simulation in a complex reaction network. *Chemical Engineering Science,* **43**(8), pp. 2295-2301.

Ogden, J.M., Williams, R.H. and Larson, E.D. (2004). Societal lifecycle costs of cars with alternative fuels/engines. *Energy Policy,* **32**, pp. 7-27.

Panasyuk, V.V., Andreykiv, O.Y. and Gembara O.V. (2000). Hydrogen degradation of materials under long-term operation of technological equipment. *International Journal of Hydrogen Energy,* **25**, pp. 67-74.

Peña, M.A., Gómez, J.P. and Fierro, J.L.G. (1996). New catalytic routes for syngas and hydrogen production. *Applied Catalysis A: General,* **144**, pp. 7-57.

Perry's Chemical Engineers' Handbook. (1998). Perry, R.H. late ed. Green, D.W. ed. 7th ed. New York: McGraw Hill.

Peschka, W. (1998). Hydrogen: The future cryofuel in internal combustion engines. *International Journal of Hydrogen Energy,* **23**(1), pp. 27-43.

Poirier, M.G. and Sapundzhiev, C. (1997). Catalytic decomposition of natural gas to hydrogen for fuel cell applications. *International Journal of Hydrogen Energy,* **22**(4), pp. 429-433.

Polman, E.A., Der Kinderen, J.M. and Thuis, F.M.A. (1999). Novel compact steam reformer for fuel cells with heat generation by catalytic combustion augmented by induction heating. *Catalysis Today,* **47**, pp. 347-351.

Rohland, B. and Plzak, V. (1999). The PEMFC-integrated CO oxidation – a novel method of simplifying the fuel cell plant. *Journal of Power Sources,* **84**, pp. 183-186.

Rosen, M.A. (1996). Thermodynamic comparison of hydrogen production processes. *International Journal of Hydrogen Energy,* **21**(5), pp. 349-365.

Rosen, M.A. and Scott, D.S. (1998). Comparative efficiency assessments for a range of hydrogen production processes. *International Journal of Hydrogen Energy,* **23**(8), pp. 653-659.

Roy, S., Pruden, B.B., Adris, A.M., Grace, J.R. and Lim, C.J. (1999). Fluidized-bed steam methane reforming with oxygen input. *Chemical Engineering Science,* **54**, pp. 2095-2102.

Seo, Y.-S., Shirley, A. and Kolaczkowski, S.T. (2002). Evaluation of thermodynamically favourable operating conditions for production of hydrogen in three different reforming technologies. *Journal of Power Sources,* **108**, pp. 213-225.

Shangguan, W. and Yoshida, A. (2001). Synthesis and photocatalytic properties of CdS-intercalated metal oxides. *Solar Energy Materials & Solar Cells,* **69**, pp. 189-194.

Smith, J.M., Van Ness, H.C. and Abbott, M.M. (1996). *Introduction to Chemical Engineering Thermodynamics.* 5th ed. New York: McGraw-Hill. Chemical Engineering Series.

Soliman, M.A., Adris, A.M., Al-Ubaid, A.S. and El-Nashaie, S.S.E.H. (1992). Intrinsic Kinetics of Nickel/Calcium Aluminate Catalyst for Methane Steam Reforming. *Journal of Chemical Technology and Biotechnology,* **55**, pp. 131-138.

Stebar, R.F. and Parks, F.B. (1974). Emission Control with Lean Operation Using Hydrogen-Supplemented Fuel. *SAE Transaction Paper 740187, SAE Automotive Engineering Congress, Detroit, Mich. February 25 – March 1, 1974.*

Taylor, J.R. (1997). *An Introduction to Error Analysis. The Study of Uncertainties in Physical Measurements.* 2nd ed. Sausalito, California: University Science Books.

Taylor, J.D., Herdman, C.M., Wu, B.C., Wally, K. and Rice, S.F. (2003). Hydrogen production in a compact supercritical water reformer. *International Journal of Hydrogen Energy,* **28**, pp. 1171-1178.

Teagan, W.P., Bentley, J. and Barnett, B. (1998). Cost reductions of fuel cells for transport applications: fuel processing options. *Journal of Power Sources,* **71**, pp. 80-85.

Thomas, C.E., James, B.D., Lomax, F.D. and Kuhn, I.F. (2000). Fuel options for the fuel cell vehicle: hydrogen, methanol or gasoline? *International Journal of Hydrogen Energy,* **25**, pp. 551-567.

Tonkovich, A.Y., Perry, S., Wang, Y., Qui, D., LaPlante, T. and Rogers, W.A. (2004). Microchannel process technology for compact steam reforming. *Chemical Engineering Science,* **59**, pp. 4819-4824.

Venkataraman, K., Wanat, E.C. and Schmidt, L.D. (2003). Steam Reforming of Methane and Water-Gas Shift in Catalytic Wall Reactors. *AIChE Journal,* **49**(5), pp. 1277-1284.

Veziroğlu, T.N. and Barbir, F. (1992). Hydrogen: the wonder fuel. *International Journal of Hydrogen Energy,* **17**(6), pp. 391-404.

Webb, C. ed. (2002). Refining "offers solution on hydrogen". *The Chemical Engineer,* **733**, p. 8.

Weiss, M.A., Heywood, J.B., Drake, E.M., Schafer, A. and AuYeung, F.F. (2000). On the road in 2020. A life-cycle analysis of new automobile technologies.

Wiese, W., Emonts, B. and Peters, R. (1999). Methanol steam reforming in a fuel cell drive system. *Journal of Power Sources,* **84**, pp. 187-193.

Wilke, C.R. (1950). Diffusional properties of multicomponent gases. *Chemical Engineering Progress,* **46**(2), pp. 95-104.

Wu, X.B., Chen, P., Lin, J. and Tan, K.L. (2000). Hydrogen uptake by carbon nanotubes. *International Journal of Hydrogen Energy,* **25**, pp. 261-265.

Xiu, G.-h., Li, P. and Rodrigues, A.E. (2002). Sorption-enhanced reaction process with reactive regeneration. *Chemical Engineering Science,* **57**, pp. 3893-3908.

Xu, J. and Froment, G.F. (1989a). Methane Steam Reforming, Methanation and Water-Gas Shift: I. Intrinsic Kinetics. *AIChE Journal,* **35**(1), pp. 88-96.

Xu, J. and Froment, G.F. (1989b). Methane Steam Reforming: II. Diffusional Limitations and Reactor Simulation. *AIChE Journal,* **35**(1), pp. 97-103.

Yokota, O., Oku, Y., Sano, T., Hasegawa, N., Matsunami, J., Tsuji, M. and Tamaura, Y. (2000). Stoichiometric consideration of steam reforming of methane on Ni/Al_2O_3 catalyst at 650°C by using a solar furnace simulator. *International Journal of Hydrogen Energy,* **25**, pp. 81-86.

Zanfir, M. and Gavriilidis, A. (2001). Modelling of a catalytic plate reactor for dehydrogenation-combustion coupling. *Chemical Engineering Science,* **56**, pp. 2671-2683.

Zanfir, M. and Gavriilidis, A. (2003). Catalytic combustion assisted methane steam reforming in a catalytic plate reactor. *Chemical Engineering Science,* **58**, pp. 3947-3960.

Appendix A - Paper published by Seo, Shirley and Kolaczkowski (2002)

ELSEVIER

Journal of Power Sources 108 (2002) 213–225

JOURNAL OF POWER SOURCES

www.elsevier.com/locate/jpowsour

Evaluation of thermodynamically favourable operating conditions for production of hydrogen in three different reforming technologies

Y.-S. Seo[a,*], A. Shirley[b], S.T. Kolaczkowski[b]

[a]*Korea Institute of Energy Research, 71-2 Jang-dong Yusung-gu Taejon, 305-343, South Korea*
[b]*Department of Chemical Engineering, University of Bath, Bath BA2 7AY, UK*

Received 6 August 2001; accepted 2 January 2002

Abstract

With the aid of thermodynamic analysis using AspenPlus™, the characteristics of three different types of reforming process are investigated. These include: steam-methane reforming (SMR), partial oxidation (POX) and autothermal reforming (ATR). Thereby, favourable operating conditions are identified for each process. The optimum steam-to-carbon (S:C) ratio of the SMR reactor is found to be 1.9. The optimum air ratio of the POX reactor is 0.3 at a preheat temperature of 312 °C. The optimum air ratio and S:C ratio of the ATR reactor are 0.29 and 0.35, respectively at a preheat temperature of 400 °C. Simulated material and energy balances show that the CH_4 flow rates required to generate 1 mol s^{-1} of hydrogen are 0.364 mol s^{-1} for POX, 0.367 mol s^{-1} for ATR and 0.385 mol s^{-1} for the SMR. These results demonstrate that the POX reforming system has the lowest energy cost to produce the same amount of hydrogen from CH_4.

Keywords: Hydrogen; Steam reforming; Partial oxidation; Autothermal reforming; Thermodynamic analysis; Material and energy balance

1. Introduction

Today, hydrogen has emerged as an alternative clean energy source to existing fossil fuels [1]. Hydrogen can be directly combusted in an internal combustion engine or electrochemically converted to electricity in a fuel cell system. Neither of these processes produces carbon dioxide, soot or carbon monoxide. Vehicles which employ a fuel cell and a hydrocarbon fuel require an efficient and safe hydrogen generator. Such devices have been intensively developed [2–4]. Such activity is connected with increasing research world-wide in the field of polymer electrolyte membrane (PEM) fuel cells [5,6].

In general, technologies for the production of hydrogen from methane are based on one of the following three processes: steam-methane reforming (SMR); partial oxidation (POX); autothermal reforming (ATR). The SMR technology is the oldest and most widely used, but it has a disadvantage of slow start-up, which makes it more suitable for a stationary system rather than for a mobile system. Recently, catalytic POX reforming [7–10] and ATR reforming [11,12] appear to have attracted much interest. The POX consists of sub-stoichiometric oxidation of methane, while the ATR integrates POX with SMR. In general, both POX and ATR have low energy requirement and high gas-space velocity [13].

A reforming system is generally comprised of a pretreatment process, a reforming reactor, a shift reactor and a gas-purification process. A reforming system to produce hydrogen from liquefied natural gas (LNG) requires a desulphurisation unit as a pretreatment process. LNG usually contains a very low level of sulphur (lower than 10 ppm), but this sulphur can deactivate severely the catalysts used in reforming reactors and shift reactors, especially in the case of low catalyst operation temperatures. At less than 600 °C, the poisoning of catalysts by sulphur compounds becomes more significant. In general, the desulphurisation unit is installed before the reforming reactor. If the operating temperature of the reforming reactor is sufficiently high (more than 700 °C), however, then the unit can be installed between the reforming reactor and the shift reactor. The pretreatment unit has been excluded from the thermodynamic analysis performed in this study.

Synthesis gas produced from reforming reactions contains an appreciable amount of carbon monoxide. Therefore, it is further processed in a water–gas shift reactor where the carbon monoxide is converted into hydrogen by reaction

* Corresponding author. Tel.: +82-42-860-3612; fax: +82-42-860-3134.
E-mail address: ysseo@kier.re.kr (Y.-S. Seo).

0378-7753/02/$ – see front matter
PII: S0378-7753(02)00027-7

with steam. Water–gas shift reactors can be classified as one of two types according to their working temperature. A high-temperature shift reactor is operated at around 400 °C, while a low-temperature shift reactor is operated at around 200 °C.

After the shift reactor, the CO concentration is lower than 1.0%. In fact, many applications which utilise hydrogen require a lower CO concentration than this. For example, a PEM fuel cell (PEMFC) requires hydrogen with a CO concentration that is below 20 ppm [14]. To this end, the synthesis gas should be further cleaned to remove CO. This can be achieved by using preferential oxidation, selective methanation, adsorption or a membrane. Finally, pure hydrogen gas can be directly fed into a fuel cell, or a storage tank.

The purpose of this paper is to identify thermodynamically favourable operating conditions at which methane may be converted to hydrogen in the SMR, POX and ATR processes. First of all, the characteristics of each reforming reactor have been investigated by performing a thermodynamic equilibrium analysis for the products and reactants. This part of the investigation provides knowledge on how operating parameters such as input conditions of reactants and thermodynamic conditions in the reforming reactor affect the equilibrium. Each reforming reactor is expected to have its own favourable operating characteristics. As equilibrium is assumed, these may vary in a practical situation. Nevertheless, the results provide a valuable indication of the starting point for experimental research.

Next, the thermal energy required in each of the reforming systems, (which comprise a reforming reactor, a water–gas shift reactor, a steam generator and a heat exchanger), has been evaluated by performing material and energy balances for each system. The consumption of thermal energy is a key issue in the design of a reforming system.

2. Simulation methods

The thermodynamic equilibrium in a reforming reactor can be calculated in two ways. One is to use equilibrium constants, the other is to minimise the Gibbs free energy. It is well known that the former approach makes it difficult to analyse the solid carbon (graphite) which can be generated during the reforming process. Therefore, the method of minimising the Gibbs free energy is normally preferred in fuel-reforming analysis [15]. This method has been adopted in the study reported here. The following are operating parameters of the reformer: (i) preheat temperature of reactants; (ii) composition and flow rate of air, methane and water; (iii) pressure of the reforming reactor; (iv) temperature of the reforming reactor.

For given operating conditions, the equilibrium temperature of the reactor and the equilibrium compositions have been calculated. This calculation can be made with any commercially available software. In this study, AspenPlus™ [16] was used. In the simulation, the mole fraction composition of air was assumed to be 0.2095 O_2 and 0.7905 N_2. To analyse the reforming reactor effectively, two parameters, the air ratio and the steam-to-carbon ratio (S:C) were used. The former refers to the relationship between air and methane flow rates and the latter refers to the relationship between steam and methane flow rates. The parameters can be written as follows:

$$\text{air ratio} = 0.5\left(\frac{\text{molar flow rate of } O_2}{\text{molar flow rate of } CH_4}\right) \quad (1)$$

$$\text{steam-to-carbon ratio (S : C)} = \frac{\text{molar flow rate of steam}}{\text{carbon molar flow rate in } CH_4} \quad (2)$$

As a general goal, it is desirable to achieve a conversion which is as high as possible within allowable operating conditions. But in many cases if the fractional conversion approached a value of 1.0, then this could damage the durability of the reactor system. The durability of the reformer is governed by the thermal durability of the reforming catalysts and the deactivation of the catalysts by coke formation. In this analysis, the maximum allowable temperature of the catalysts is assumed to be 800 °C for all three reforming reactors. In reality, a certain catalyst for a reforming system might be able to be used at higher temperatures, but most commercially available catalysts have been operated at less than 800 °C to secure their thermal durability. Therefore, it is necessary to determine favourable operating conditions for each of the reforming reactors. These are defined as conditions at which the fractional conversion is more than 0.99 while the durability of the reformer system is secured.

Material and energy balances are then solved for each system, making use of AspenPlus™ software. It is assumed that each system consists of a steam generator, a preheating system, a reforming reactor, a heat exchanger and a water–gas shifter reactor. In order to compare the utilisation of thermal energy in the three systems, the operating conditions for each system are set to the favourable operating conditions identified in the equilibrium simulation. By comparing the energy utilisation in each reforming system, it is possible to evaluate that which system has the lowest energy cost.

3. Simulation results and discussion

3.1. Equilibrium analysis

3.1.1. SMR

To analyse the thermodynamic equilibrium of the SMR reactor, the general reforming reaction mechanism can be written in the following way:

$$CH_4 + \beta H_2O \Rightarrow \text{products} \quad (3)$$

The products can be CH_4, H_2O, H_2, CO, CO_2, C(s), H, O, OH, HO_2, HCO, CH or CH_2. C(s) refers to solid carbon (graphite) and H, O, OH, HO_2, HCO, CH, CH_2 are radicals

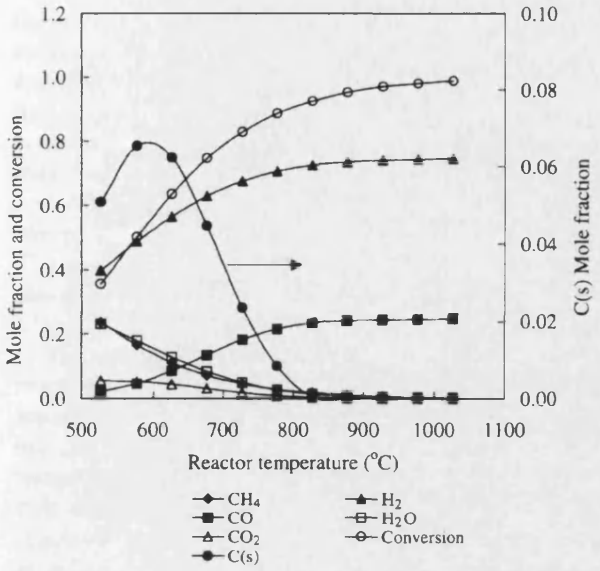

Fig. 1. Effect of reactor temperature on equilibrium compositions and conversion in SMR reactor. Reactor pressure, 1.0 bar; S:C ratio, 1.0.

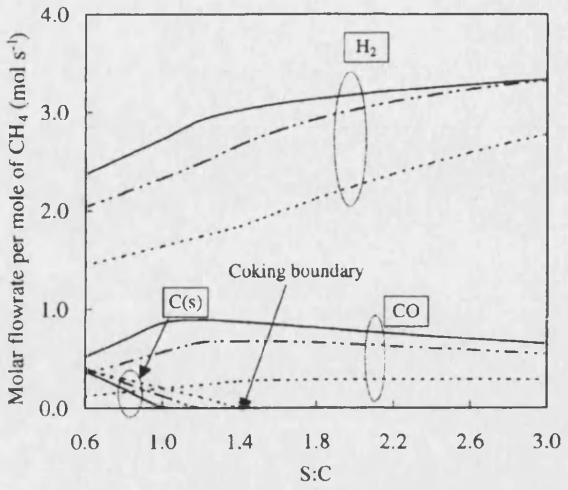

Fig. 2. Effect of S:C on equilibrium compositions in SMR reactor. Reactor pressure: 1.0 bar. Reactor temperature: (- - -) 600 °C; (– - - –) 700 °C; (—) 800 °C.

that could be produced in the reforming reaction. In the simulations, the concentration of radicals is found to be negligible compared with those of the other products. The stoichiometric coefficient, β, for H_2O is varied from 0.6 to 3.0, which corresponds to a S:C ratio range of 0.6–3.0. As the SMR is very endothermic, heat-transfer from the outside of the reactor controls the temperature of the SMR reactor. In this simulation, the temperature of the SMR reactor is varied in the range 500–1000 °C.

The reactor temperature is found to affect significantly the equilibrium compositions and, therefore, the conversion (see Fig. 1). As the reactor temperature is raised from 600 to 800 °C, the conversion increases from 0.56 to 0.90. If the operating temperature of the reactor is limited to less than 800 °C in order to maintain thermal durability of the catalyst, then it can be seen that it is difficult to obtain a satisfactory conversion that is greater than 0.99.

The reactor temperature also significantly affects the formation of solid carbon, C(s). It is generated at temperatures of less than 850 °C with a S:C of 1.0 and at 1.0 bar reactor pressure. This implies that in order to avoid coke formation, the reactor temperature should be maintained at temperatures that are greater than 850 °C. On the other hand, keeping the reactor temperature above 850 °C is likely to damage the thermal durability of the catalyst. Therefore, it is necessary to change other operating parameters in order to suppress coke formation in the temperature region below 850 °C. The formation of solid carbon might be caused by the following Boudouard reaction [17].

$$2CO \Rightarrow C + CO_2 \quad (4)$$

This is supported by the fact that CO_2 is generated only in the region in which C(s) exists (see Fig. 1). It is found, however, that the equilibrium compositions in the SMR reactor are independent of the preheat temperature of the reactants, as long as the reactor temperature is fixed at a certain value. This is because the temperature of the SMR reactor is determined by the external heat-transfer to the reactor. For the purpose of the thermodynamic calculations, the reactor temperature of the SMR reactor is given as an input parameter; hence the preheat temperature affects only the heat duty that is transferred to the SMR reactor.

The simulation results of the SMR reactor in terms of the S:C ratio are illustrated in Figs. 2 and 3. The data in Fig. 2 show that the formation of C(s) is strongly affected by the value of S:C. The coking boundary is defined as the limit condition within which the coke is generated. The coking boundary in the SMR reactor moves toward lower S:C values as the reactor temperature is raised. For example, if the reactor temperature is increased from 600 to 800 °C,

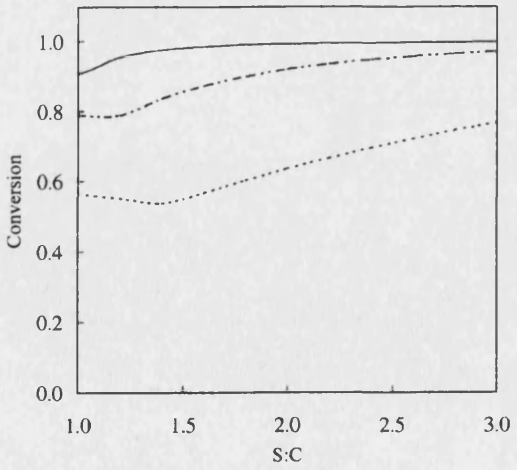

Fig. 3. Effect of S:C on conversion in SMR reactor. Reactor pressure: 1.0 bar. Reactor temperature: (- - -) 600 °C; (– - - –) 700 °C; (—) 800 °C.

the coking boundary moves from a S:C of 1.4 to 1.0. These results demonstrate that the formation of solid carbon can be avoided by increasing the reactor temperature and/or the S:C ratio. The maximum reactor temperature is restricted, however, by the thermal durability of the catalysts and the maximum value of S:C is limited according to the energy cost of the reactor system. A higher S:C incurs a higher energy cost because of the extra steam generation required. The molar flow rate of H_2 is increased and the molar flow rate of CO is decreased by increasing the S:C ratio. This is an advantage with using a higher S:C ratio.

The effects of the S:C ratio on the conversion of the SMR reactor at three reactor temperatures, 600, 700 and 800 °C, are shown in Fig. 3. Generally, the conversion is improved as the S:C value is increased, but in case of a low reactor temperature, viz., 600 °C, the complete conversion is difficult to obtain within a reasonable S:C range. If a SMR reactor is operated at 700 °C, the S:C should be maintained at greater than 2.5 in order to achieve a conversion of 0.95. In case of a reactor temperature of 800 °C, the conversion becomes greater than 0.95 when the S:C is more than 1.2. These simulation results demonstrate that both the S:C and the reactor temperature strongly affect conversion in the SMR reactor.

A sensitivity analysis has also been conducted with regard to the effect of varying the pressure of the SMR reactor. The effects of varying the pressure on the equilibrium compositions and the conversion in the SMR reactor are shown in Fig. 4. The simulation results reveal that the pressure of the reactor is one of the critical factors which affect the equilibrium state of the SMR reactor. As the pressure is increased, the conversion and mole fractions of H_2 and CO are rapidly reduced. Conversely, the mole fraction of H_2O increases with pressure. These results demonstrate that it is desirable to keep the pressure of the SMR reactor as low as possible. It is interesting to note,

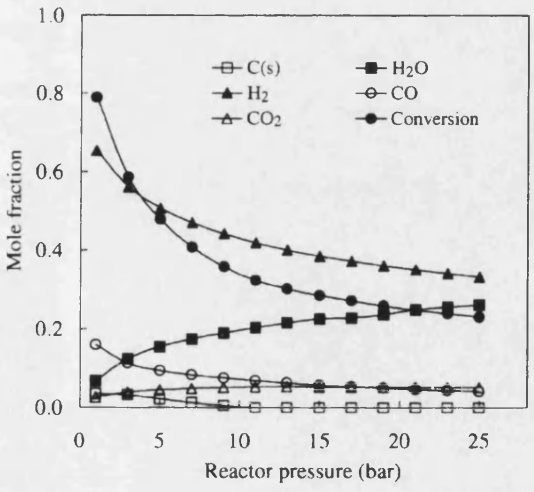

Fig. 4. Effects of the pressure on the equilibrium compositions and conversion in SMR reactor. Reactor temperature, 700 °C; S:C ratio, 1.0.

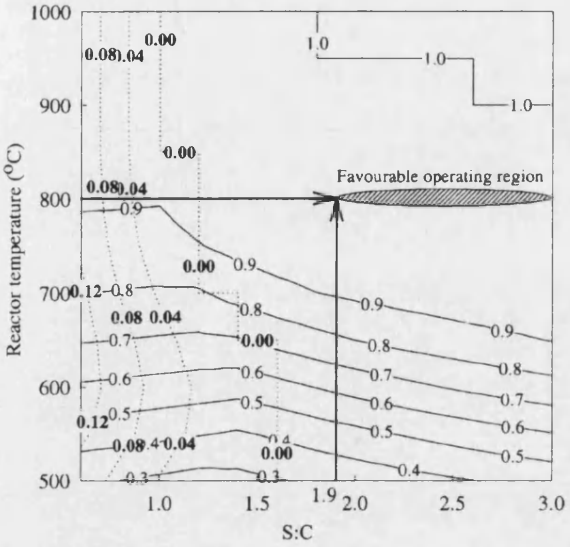

Fig. 5. Contour diagram of C(s) and conversion with regard to both reactor temperature and S:C ratio in SMR reactor. Reactor pressure, 1.0 bar; (- - -) C(s) mole fraction; (—) conversion.

however, that as the pressure is decreased, there is an increase in C(s) formation.

Favourable operating conditions in the SMR reactor can be ensured by the proper combination of reactor temperature, reactor pressure and S:C ratio. In the simulation of an SMR reactor, the pressure is fixed at 1.0 bar. A contour diagram that combines the conversion and C(s) mole fraction in terms of both the air ratio and the reactor temperature is shown in Fig. 5. This diagram provides the operation conditions that simultaneously satisfy the two conditions of no coke formation and a conversion of over 0.99 at a fixed reactor temperature of 800 °C. The result is shown in the Fig. 5 with thick arrows. Using this simulation, the optimum S:C ratio of the SMR reactor is found to be 1.9 or more. Under these operation conditions, the conversion of the reactor is calculated to be 0.99.

3.1.2. POX

The general reaction mechanism for the thermodynamic analysis of the POX reforming rector can be written as follows:

$$CH_4 + \alpha O_2 + 3.77\alpha N_2 \Rightarrow \text{products} \quad (5)$$

The stoichiometric coefficient of O_2, α, is varied from 0.0 to 1.2, which corresponds to an air ratio range of 0.0–0.6. The POX reforming reactor is modelled at adiabatic conditions during the calculation of the equilibrium state, which means that there is no heat-transfer to or from the POX reactor.

First, the POX reactor is simulated for various air ratios and reactant input temperatures. The equilibrium compositions of CH_4, C(s), H_2, CO, CO_2, H_2O are shown in Fig. 6 and have been calculated as a function of the air ratio over the range 0.0–0.6 at a preheat temperature of 200 °C and a

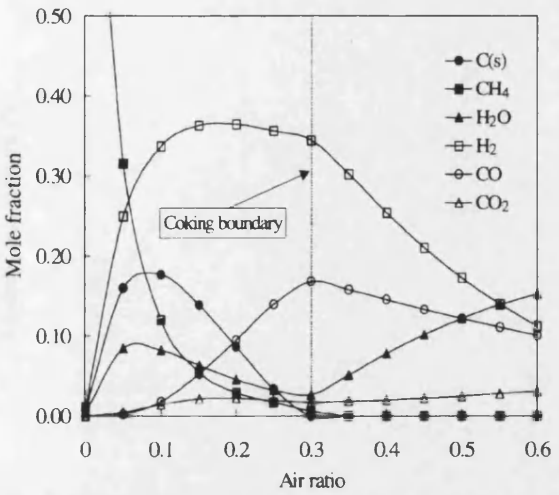

Fig. 6. Equilibrium composition of POX reactor with regard to air ratio. Preheat temperature of reactants (methane and air), 200 °C; reactor pressure, 1.0 bar.

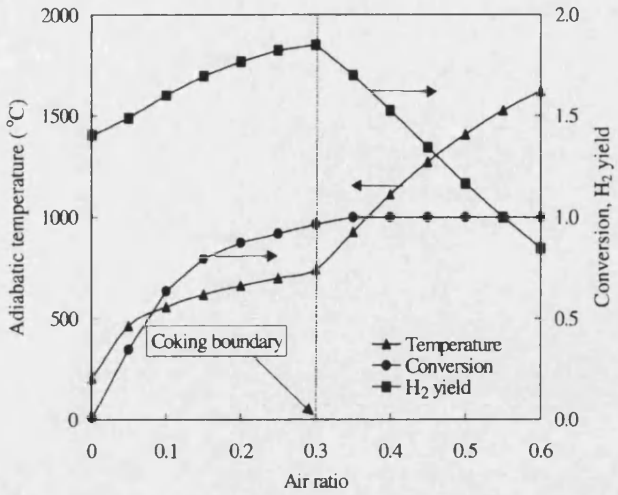

Fig. 7. Adiabatic temperature, conversion of methane and H_2 yield of POX reactor with regard to air ratio. Preheat temperature of reactants (methane and air), 200 °C; reactor pressure, 1.0 bar.

reactor pressure of 1.0 bar. The results have been sorted into two groups based on a coking boundary. The coking boundary is situated at an air ratio of 0.3. In the coking region, which corresponds to an air ratio range of 0.0–0.3, H_2 increases steeply with increasing air ratio. C(s) increases to a peak near an air ratio of 0.1, reduces gradually and finally drops to zero at an air ratio of 0.3. For an air ratio of more than 0.3, however, the H_2 concentration reduces rapidly with increasing air ratio, which leads to increased H_2O concentration. The CO also reduces with increased air ratio, but its rate of decrease is less than that of H_2. The decrease of H_2 and CO is contrary to the original aim of converting CH_4 completely into H_2 and CO. Therefore, operation of the POX reactor with an air ratio of greater than 0.3 is clearly undesirable.

The H_2 yield, conversion and adiabatic temperature of the POX reactor in terms of the air ratio are shown in Fig. 7. The H_2 yield is defined as:

$$H_2 \text{ yield} = \frac{[H_2]_{out}}{[CH_4]_{in} - [CH_4]_{out}} \quad (6)$$

The coking boundary is shown at an air ratio of 0.3 in the Fig. 7. At the coking boundary, the behaviour of both the H_2 yield and the adiabatic temperature drastically changes. The H_2 yield increases steadily with the air ratio in the region with the coking, but it decreases with the air ratio in the region without coke formation and this results in a lower quality of reformate. It is desirable for the reformed gas to contain as high a level of H_2 as possible. The adiabatic temperature of the reactor rises with the air ratio, but it increases more steeply in the region without coke formation. At the coking boundary, the adiabatic temperature and the H_2 yield are 743 and 0.97 °C, respectively.

The preheat temperature of reactants (CH_4 and air) can exert an important effect on the POX reactor. Reactants entering the POX reactor should be heated to a certain temperature to sustain the catalytic reaction of the reforming catalysts. The calculated results of the POX reactor with regard to the preheat temperature are presented in Figs. 8 and 9. The mole fractions of H_2 and CO are increased as the preheat temperature becomes higher (see Fig. 8). The behaviour of C(s) is, however, somewhat different from that of H_2 and CO. In the region of a very low air ratio (less than 0.1), the mole fraction of C(s) rises with increasing preheat temperature. By contrast, the mole fraction of C(s) reduces with the preheat temperature when the air ratio becomes greater than 0.1. The boundary line of coke formation hardly changes with respect to the preheat temperature. This demonstrates that to increase only the preheat temperature of reactants is not an effective way to avoid coke formation.

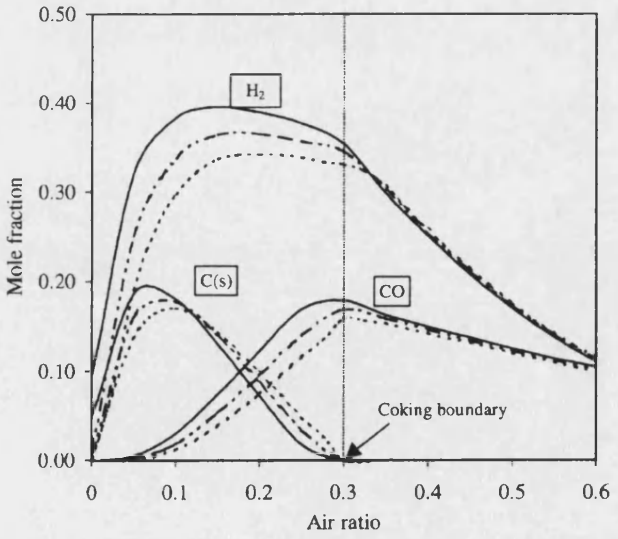

Fig. 8. Effects of preheat temperature of reactants on equilibrium compositions in POX reactor. Reactor pressure: 1.0 bar. Preheat temperature: (- - -) 20 °C; (– - - –) 200 °C; (—) 400 °C.

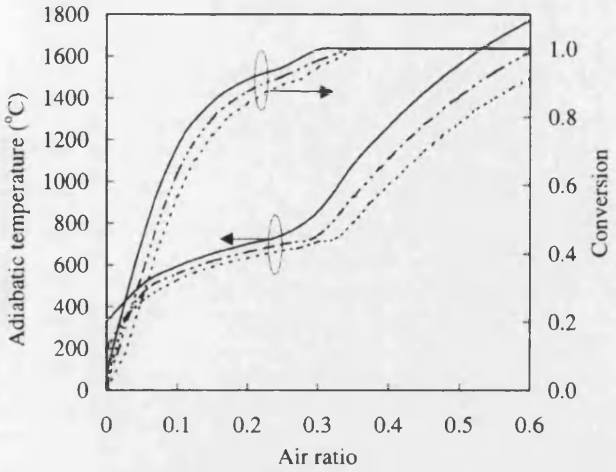

Fig. 9. Effects of preheat temperature of reactants on adiabatic temperature of POX reactor and conversion. Reactor pressure: 1.0 bar. Preheat temperature: (- - -) 20 °C; (– - - –) 200 °C; (—) 400 °C.

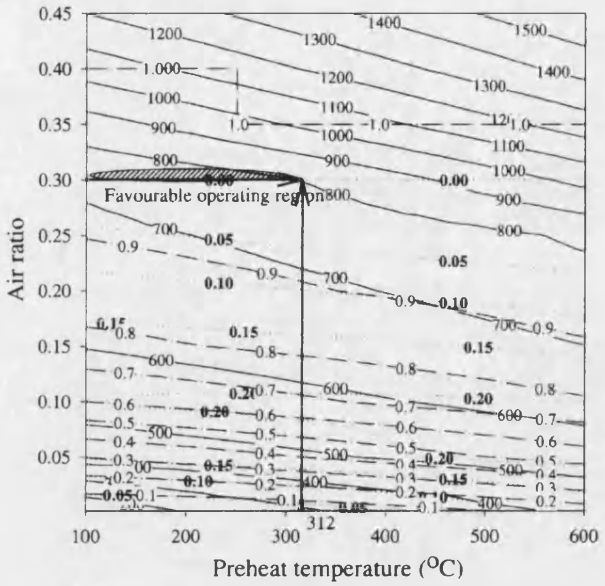

Fig. 10. Contour diagram of C(s), conversion and reactor temperature with regard to both air ratio and preheat temperature in POX reactor. Reactor pressure, 1.0 bar; (- - -) C(s) mole fraction; (– - –) conversion; (—) adiabatic reactor temperature (°C).

With an air ratio of more than 0.3, the mole fractions of H_2 and CO are hardly affected by the preheat temperature of the reactants. This trend becomes clearer as the air ratio is increased beyond 0.4.

The effects of the preheat temperature on the conversion and the adiabatic temperature of the POX reactor are shown in Fig. 9. Increasing the input temperature of the reactants causes both the conversion and the adiabatic temperature of the reactor to increase. To improve the conversion of the reformer, it is desirable to heat the reactants to a higher temperature, but this increases the adiabatic temperature of the POX reactor, which may cause deactivation of the catalysts. For example, the adiabatic temperature increases from 670 to 857 °C when the preheat temperature of the reactants is raised from 20 to 400 °C at an air ratio of 0.3. In the case of an air ratio of greater than 0.3, the adiabatic temperature rises steeply to more than 800 °C when the air ratio is increased by only a small amount. In reality, in order to operate the reactor with a high flow rate of reactants, it is necessary to heat the reactants sufficiently to maintain catalytic reaction. This thermodynamic analysis implies, however, that an excessive increase of the preheat temperature may cause the deactivation of the catalysts due to sintering at high-temperature.

To determine favourable operating conditions for the POX reactor, the C(s) formation, adiabatic reactor temperature and conversion have been calculated in terms of the air ratio and preheat temperature. The contour diagram that combines these results is given in Fig. 10. Favourable operation conditions are defined as those which simultaneously achieve no coke formation, an adiabatic reactor temperature of less than 800 °C and a conversion of over 0.99. These are indicated in Fig. 10 by the thick arrows. The optimum air ratio of the POX reactor is 0.3 at a preheat temperature of 312 °C. Under these operating conditions, the conversion of the reactor is calculated to be 0.99.

The preheat temperature of reactants is one of key operating parameters in the POX reactor. Thermodynamic analysis of the POX reactor shows that to increase the preheat temperature at a fixed air ratio makes both the reactor temperature and the conversion higher (see Fig. 10). If the temperature of catalyst is to be controlled within 800 °C, however, the air ratio should be altered to a lower value with increasing preheat temperature. When operating at a preheat temperature of over 312 °C, the formation of coke is inevitable if the reactor temperature is to be maintained at less than 800 °C. On the other hand, at a fixed preheat temperature, the conversion and the reactor temperature both increase with the air ratio, while the C(s) mole fraction is reduced. The favourable operating region in terms of the air ratio and preheat temperature is designated by the hatched area in Fig. 10.

3.1.3. ATR

The general reaction mechanism for the thermodynamic analysis of the ATR reactor can be written as follows:

$$CH_4 + \alpha O_2 + \beta H_2O + 3.77\alpha N_2 \Rightarrow \text{products} \quad (7)$$

The stoichiometric coefficient of O_2, α, is varied from 0.0 to 1.0, which corresponds to an air ratio range of 0.0–0.5. For each value of the air the ratio, the stoichiometric coefficient of H_2O, β, is varied from 0.0 to 1.2, which corresponds to a S:C ratio range of 0.0–1.2. As with the POX system, the ATR reactor is maintained under adiabatic conditions, which means that there is no heat-transfer to or from the reactor. The adiabatic temperature of the reactor is calculated with given input conditions of air ratio, S:C ratio, preheat temperature and reactor pressure.

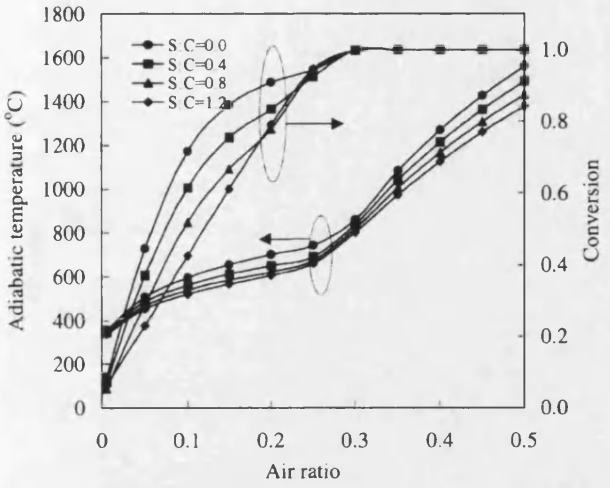

Fig. 11. Effect of air ratio and S:C ratio on adiabatic temperature and conversion in ATR reactor. Preheat temperature, 400 °C; reactor pressure, 1.0 bar.

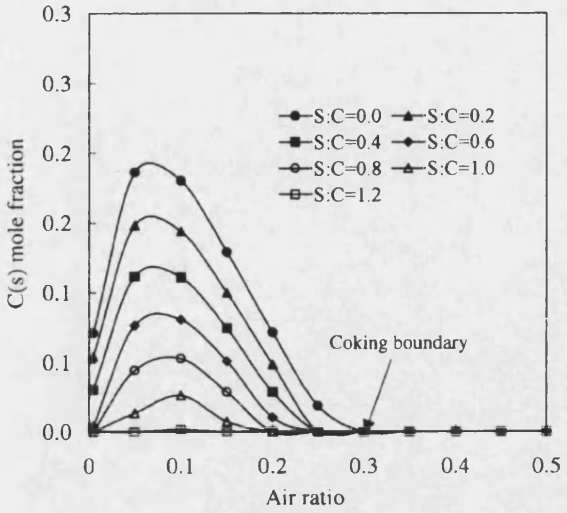

Fig. 12. Effect of air ratio and S:C ratio on C(s) formation in ATR reactor. Preheat temperature, 400 °C; reactor pressure, 1.0 bar.

The adiabatic temperature and the conversion in the ATR reactor in terms of the air ratio and the S:C ratio are shown in Fig. 11. The air ratio significantly affects the conversion and the adiabatic temperature. Conversion rapidly increases with the air ratio and reaches 1.0 at an air ratio of 0.3. For air ratios greater than 0.3, the adiabatic temperature continues to increase although the conversion remains at 1.0. This is due to oxidation of H_2 and CO into H_2O and CO_2 by excessive O_2 supply. The S:C ratio also affects both the conversion and the adiabatic temperatures of the ATR reactor. As the S:C ratio increases at a fixed air ratio, the conversion becomes lower and the adiabatic temperature decreases. When steam is supplied to the ATR reactor, the steam reforming reaction occurs, which is a strongly endothermic reaction. Therefore, a higher S:C results in a lower reactor temperature. As a result of the lower reactor temperature, the conversion is reduced.

The C(s) formation as a function of S:C ratio and air ratio is presented in Fig. 12. A higher S:C shifts the coking boundary to a lower air ratio and also reduces coke formation. As an example, the coking boundary moves from an air ratio of 0.3 to 0.2 if the S:C increases from 0.0 to 1.0. For a S:C of over 1.2, no coke is generated at any value of the air ratio. To avoid coke formation at a given air ratio, the optimum S:C can be derived from these results. The effects of the air ratio and S:C on the equilibrium compositions have also been investigated (see Fig. 13). The molar flow rates of H_2 and CO peak at an air ratio of 0.25 and 0.3, respectively. As S:C increases, the H_2 molar flow rate increases but, conversely, the CO mole flow rate decreases. This demonstrates that a higher S:C ratio causes the H_2:CO ratio to increase. On the other hand, if the air ratio is increased above 0.25, the H_2 molar flow rate drops more steeply when compared with the decrease in the CO molar flow rate. This is due to faster oxidation of H_2 than CO in the region of high air ratio.

To determine favourable operating conditions of the ATR reactor, the C(s) formation, adiabatic reactor temperature and conversion have been calculated in terms of the S:C ratio and air ratio. Contour diagrams that represent the results of these calculations are presented in Fig. 14. In the simulation to find the favourable operating conditions of the ATR reactor, the reactor pressure and the preheat temperature are set to 1 bar and 400 °C, respectively. From Fig. 14, the favourable operating conditions of the ATR reactor can be determined that simultaneously satisfy the requirements of no coke formation, a reactor temperature of 800 °C and a conversion of over 0.99. As a result, favourable operating conditions for the ATR reactor are found to be an air ratio of 0.29 and a S:C ratio of 0.35 at a preheat temperature of 400 °C. These conditions are shown in the Fig. 14 with thick arrows. The S:C ratio for this favourable operating region

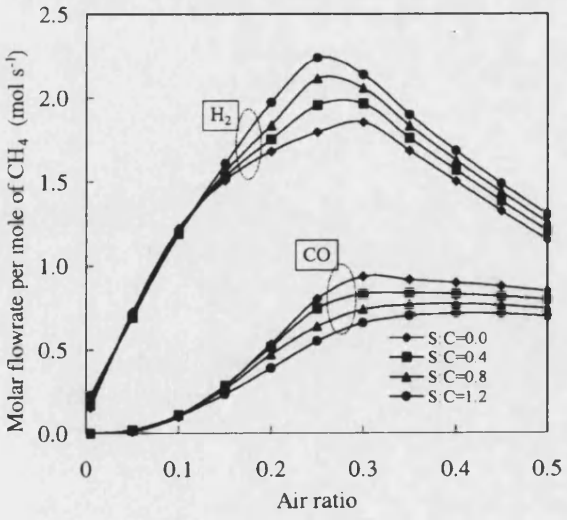

Fig. 13. Effect of air ratio and S:C ratio on mole fractions of H_2 and CO in ATR reactor. Preheat temperature, 400 °C; reactor pressure, 1.0 bar.

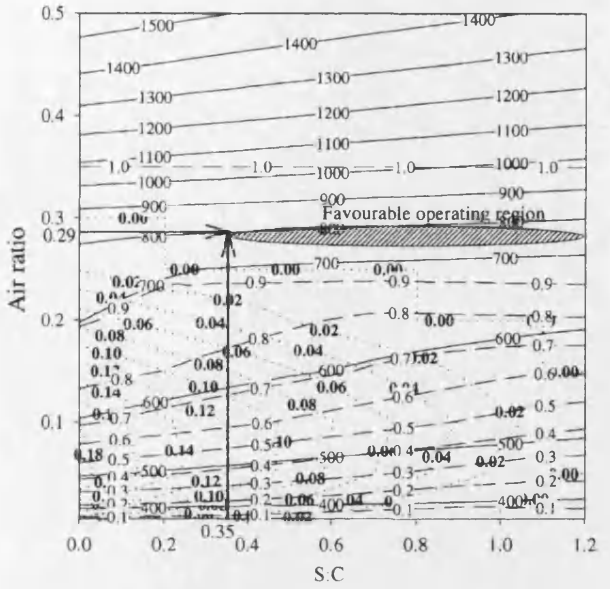

Fig. 14. Contour diagram of C(s), conversion and reactor temperature with regard to both air ratio and S:C ratio in ATR reactor. Reactor pressure, 1.0 bar; (- - -) C(s) mole fraction; (– – –) conversion; (—) adiabatic reactor temperature (°C).

can be extended beyond 0.35 when the air ratio is kept at 0.29. The hatched area shows the favourable operating region. It can be seen that the optimum air ratio exists within a very narrow range. On the other hand, the S:C ratio for the favourable operating region can be any value above 0.35. Nevertheless, the best S:C should be the lowest value, that is, 0.35, because a higher S:C incurs a greater energy cost in supplying the corresponding steam. In Table 1, a summary is provided of the favourable operating conditions for the three reforming reactors, SMR, POX and ATR. These data are used later to calculate the thermal energy requirements of each reforming system.

3.2. Analysis of thermal energy

It is useful to determine which of the three reforming systems is more efficient in terms of energy cost to generate a given amount of hydrogen. It is difficult, however, to compare each reforming system exactly because each has a different configuration to the others. For example, the SMR reforming system has a heat exchanger to supply the heat to the reforming reactor, while the POX and ATR reforming systems do not need any heat exchanger. Furthermore, the practical systems are composed of very complicated configurations in order to recover any available energy. In this study, the output flow rate of hydrogen is set to 1.0 mol s^{-1} in order to compare the three systems with one another. To this end, the calculation is iterated, changing the flow rate of reactants as an independent variable until the output flow rate of hydrogen reaches 1.0 mol s^{-1}. The data listed in Table 1 are used as input conditions for each reforming reactor. In order that the CH_4 conversion of each reforming reactor is kept at exactly the same level, viz., 0.991 ± 0.1%, the input conditions of the ATR reactor have to be slightly adjusted. The air ratio and S:C ratio in the ATR reactor are adjusted from 0.29 and 0.35, to 0.285 and 0.2, respectively. On the other hand, a water–gas shift reactor is normally used in practical systems to convert CO generated from the reforming reactor into hydrogen. Therefore, this simulation employs a water–gas shift reactor behind the reforming reactor.

Table 1
Favourable operation conditions of three reforming systems

	SMR	POX	ATR
Air ratio	–	0.3	0.29
S:C ratio	1.9	–	0.35
Preheat temperature (°C)	400	312	400
Reactor temperature (°C)	800	800	800
Reactor pressure (bar)	1.0	1.0	1.0
Fractional conversion of CH_4	0.99	0.99	1.00

The configuration of each reforming system is described in Tables 2–4. Basically, each system comprises a steam generator, a heater, a reforming reactor, a heat exchanger and a shift reactor. The input conditions of air, CH_4 and water are set to 20 °C and 1 bar. Steam generators are used to generate the steam required for both the reforming reactor and the shift reactor. All steam generators are run at 103 °C. The S:C data obtained through analysis of the favourable operating conditions (Table 1) are used to determine the water flow rate for each reforming reactor. The water flow rate for the shift reactor is determined based on the complete conversion of CO to hydrogen. Equilibrium analysis of the shift reactor shows that the S:C should be 2.0 to obtain a CO conversion of 0.99 or more. Therefore, the S:C for the shift reactor is set to 2.0 for all three systems.

A heater is employed to heat the reactants to a temperature sufficient to sustain the catalytic reaction in the reforming reactor. The outlet temperature of the heater is set to 400 °C for the SMR, 312 °C for the POX and 400 °C for the ATR system, according to the favourable operating conditions. The equilibrium of each reforming reactor is calculated using the same methods as those used before to investigate the equilibrium state. The synthesis gas (syngas) produced by each reforming reactor contains a large amount of CO together with hydrogen. To convert this CO to hydrogen, a water–gas shift reactor is used as described above. The simulation uses only one low-temperature shift reactor to simplify the comparison. It is assumed that this low-temperature shift reactor converts all CO to hydrogen with a conversion of over 0.99. Before the shift reactor, a heat exchanger is employed to cool down the temperature of syngas exhausted from the reforming reactor, which is around 800 °C. The syngas is cooled to the operating temperature of the shift reactor (200 °C). The shift reactor is modelled with the 'Requil' model in AspenPlus™. The material and energy balances for each system are listed in

Table 2
Material and energy balances of each stream in SMR reformer system

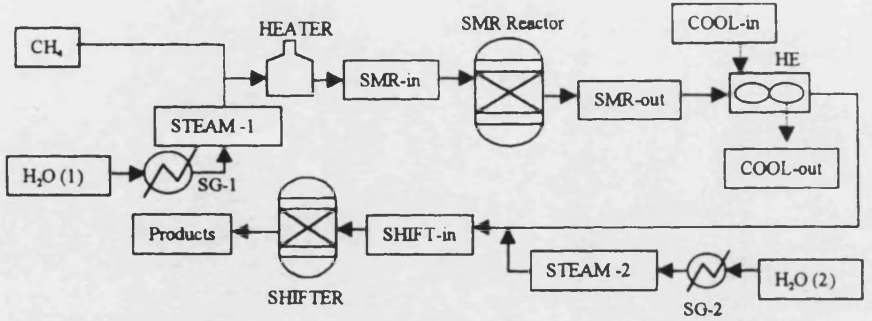

Stream	CH_4	H_2O (1)	STEAM-1	SMR-in	SMR-out	COOL-in	COOL-out	H_2O (2)	STEAM-2	SHIFT-in	Products
Mole flow (mol s^{-1})											
CH_4	0.2526	0	0	0.2526	2.283E−3	0	0	0	0	2.283E−3	2.283E−3
O_2	0	0	0	0	0	0	0	0	0	0	0
N_2	0	0	0	0	0	0	0	0	0	0	0
H_2	0	0	0	0	0.8002	0	0	0	0	0.8001	0.9991
H_2O	0	0.4799	0.4799	0.4799	0.1804	10.0	10.0	0.5052	0.5052	0.1803	0.4866
CO	0	0	0	0	0.2010	0	0	0	0	0.2010	2.155E−3
CO_2	0	0	0	0	0.0492	0	0	0	0	0.0492	0.2489
Mole fraction											
CH_4	1.00	0	0	0.3448	1.852E−3	0	0	0	0	1.852E−3	1.313E−3
O_2	0	0	0	0	0	00	0	0	0	0	0
N_2	0	0	0	0	0	0	0	0	0	0	0
H_2	0	0	0	0	0.6488	0	0	0	0	0.6488	0.5744
H_2O	0	1.00	1.00	0.6552	0.1462	1.00	1.00	1.00	1.00	0.1462	0.2798
CO	0	0	0	0	0.1630	0	0	0	0	0.1630	1.239E−3
CO_2	0	0	0	0	0.0399	0	0	0	0	0.0399	0.1431
Total flow (mol s^{-1})	0.2526	0.4799	0.4799	0.7325	1.2331	10.0	10.0	0.5052	0.5052	1.2331	1.7391
Temperature (K)	293	293	376	673	1073	293	324	293	376	473	473
Pressure (bar)	1.0	1.0	1.0	1.0	1.0	1.0	1.0	1.0	1.0	1.0	1.0
Enthalpy (J mol^{-1})	−7.469E+4	−2.862E+5	−2.394E+5	−1.695E+5	−4.463E+4	−2.862E+5	−2.838E+5	−2.862E+5	−2.394E+5	−6.393E+4	−1.185E+5

HE, heat exchanger; SG, steam generator.

Table 3
Material and energy balances of each stream in POX reformer system

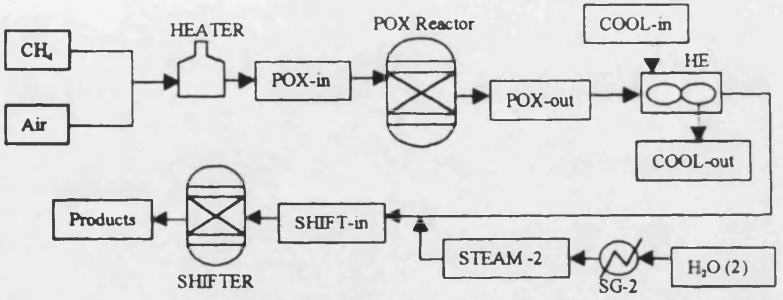

Stream	Air	CH_4	POX-in	POX-out	COOL-in	COOL-out	H_2O (2)	STEAM-2	SHIFT-in	Products
Mole flow (mol s^{-1})										
CH_4	0.0	0.3630	0.3630	3.203E−3	0	0	0	0	3.203E−3	3.203E−3
O_2	0.2178	0	0.2178	0.00	0	0	0	0	0.00	0.00
N_2	0.8218	0	0.8218	0.8218	0	0	0	0	0.8218	0.8218
H_2	0	0	0	0.6702	0	0	0	0	0.6702	1.0002
H_2O	0	0	0	0.0493	10.00	10.00	0.7260	0.7260	0.0493	0.4453
CO	0	0	0	0.3333	0	0	0	0	0.3333	3.389E−3
CO_2	0	0	0	0.0264	0	0	0	0	0.0264	0.3578
Mole fraction										
CH_4	0	1.00	0.2588	1.681E−3	0	0	0	0	1.681E−3	1.217E−3
O_2	0.2095	0	0.1552	0	0	0	0	0	0.00	0.00
N_2	0.7904	0	0.5859	0.4315	0	0	0	0	0.4321	0.3122
H_2	0	0	0	0.3519	0	0	0	0	0.3519	0.3800
H_2O	0	0	0	0.0259	1.00	1.00	1.00	1.00	0.0259	0.1692
CO	0	0	0	0.1750	0	0	0	0	0.1750	1.287E−3
CO_2	0	0	0	0.0138	0	0	0	0	0.0138	0.1359
Total flow (mol s^{-1})	1.0396	0.3630	1.4026	1.9043	10.00	10.00	0.7260	0.7260	1.9043	2.6318
Temperature (K)	293	293	585	1075	293	340	293	376	473	473
Pressure (bar)	1.0	1.0	1.0	1.0	1.0	1.0	1.0	1.0	1.0	1.0
Enthalpy (J mol^{-1})	−1.458E+2	−7.469E+4	−9.764E+3	−7.191E+3	−2.862E+5	−2.826E+5	−2.862E+5	−2.394E+5	−2.604E+4	−8.912E+4

HE, heat exchanger; SG, steam generator.

Table 4
Material and energy balances of each stream in ATR reformer system

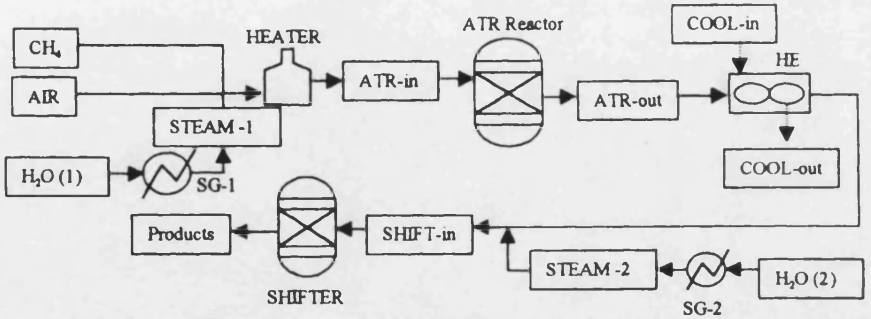

Stream	AIR	CH_4	H_2O (1)	STEAM-1	ATR-in	ATR-out	COOL-in	COOL-out	H_2O (2)	STEAM-2	SHIFT-in	Products
Mole flow (mol s^{-1})												
CH_4	0	0.3546	0	0	0.3546	2.797E−3	0	0	0	0	2.797E−3	2.797E−3
O_2	0.2021	0	0	0	0.2021	0	0	0	0	0	0	0
N_2	0.7627	0	0	0	0.7627	0.7627	0	0	0	0	0.7627	0.7627
H_2	0	0	0	0	0	0.6926	0	0	0	0	0.6926	0.9999
H_2O	0	0	0.07092	0.07092	0.07092	0.0818	10.00	10.00	0.7092	0.7092	0.0818	0.4837
CO	0	0	0	0	0	0.3103	0	0	0	0	0.3103	0.0030
CO_2	0	0	0	0	0	0.0414	0	0	0	0	0.0414	0.3502
Mole fraction												
CH_4	0	1.00	0	0	0.2550	1.478E−3	0	0	0	0	1.478E−3	1.075E−3
O_2	0.2094	0	0	0	0.1453	0	0	0	0	0	0	0
N_2	0.7905	0	0	0	0.5485	0.4031	0	0	0	0	0.4031	0.2930
H_2	0	0	0	0	0	0.3661	0	0	0	0	0.3661	0.3842
H_2O	0	0	1.00	1.00	0.0510	0.0432	1.00	1.00	1.00	1.00	0.0432	0.1858
CO	0	0	0	0	0	0.1640	0	0	0	0	0.1640	1.173E−3
CO_2	0	0	0	0	0	0.0219	0	0	0	0	0.0219	0.1345
Total flow (mol s^{-1})	0.9468	0.3546	0.07092	0.07092	1.3903	1.8918	10.00	10.00	0.7092	0.7092	1.8918	2.6025
Temperature (K)	293	293	293	376	673	1061	293	339	293	376	473	473
Pressure (bar)	1.0	1.0	1.0	1.0	1.0	1.0	1.0	1.0	1.0	1.0	1.0	1.0
Enthalpy (J mol^{-1})	−1.458E+2	−7.469E+4	−2.862E+5	−2.394E+5	−1.850E+4	−1.359E+4	−2.862E+5	−2.826E+5	−2.862E+5	−2.394E+5	−3.213E+4	−9.257E+4

HE, heat exchanger; SG, steam generator.

Tables 2–4. A summary of the material and energy balances for each reforming system is given in Table 5.

The term 'total net energy' in Table 5 means the summation of energy balances of all there units that comprise the reforming system together with consideration of their heat-transfer efficiency. Each unit in a reforming system may, in reality, have a different heat-transfer efficiency but the simulation assumes the same heat-transfer efficiency for all units to simplify the calculation. The term 'CH_4 equivalent' refers to a CH_4 flow rate, the combustion of which will release energy equivalent to the 'total net energy.' A combustion heat of 890 kJ/kmol of CH_4 is used to calculate the CH_4 equivalent from the total net energy. In the table, 'total CH_4' is the sum of 'input' CH_4 and 'CH_4 equivalent.' When considering only the input CH_4, the CH_4 flow rate required to produce 1 mol s^{-1} of hydrogen is 0.253 mol s^{-1} for the SMR, 0.363 mol s^{-1} for the POX and 0.355 mol s^{-1} for the ATR. The total CH_4 flow rate, including the CH_4 equivalent, required to generate 1 mol s^{-1} of hydrogen is 0.385 mol s^{-1} for the SMR, 0.364 mol s^{-1} for the POX and 0.367 mol s^{-1} for the ATR. The SMR reforming system has the highest CH_4 consumption rate and the POX system has the lowest CH_4 consumption rate. One interesting point is that the difference in the CH_4 consumption depends strongly on the heat-transfer efficiency of the heat-exchange units. The difference in CH_4 consumption between the SMR and POX systems becomes larger as the heat-transfer efficiency decreases. For example, when the heat-transfer efficiency is 0.8, the CH_4 consumption is 0.364 mol s^{-1} for the POX and 0.385 mol s^{-1} for the SMR. By contrast, when the heat-transfer efficiency is lowered to 0.7, the values change to 0.364 mol s^{-1} for the POX and 0.404 mol s^{-1} for the SMR.

Table 5
Comparison of material and energy balances of three reforming systems

	SMR	POX	ATR
Input (mol s^{-1})			
CH_4	0.253	0.363	0.355
O_2	–	0.218	0.202
N_2	–	0.822	0.763
H_2O (1)	0.480	–	0.071
H_2O (2)	0.505	0.726	0.709
Total	1.238	2.129	2.099
Output (mol s^{-1})			
CH_4	0.002	0.003	0.003
O_2	–	0.000	0.000
N_2	–	0.822	0.763
H_2O	0.487	0.445	0.484
CO	0.002	0.003	0.003
CO_2	0.249	0.358	0.350
H_2	1.000	1.000	1.000
CH_4 conversion	0.991	0.991	0.992
CO conversion	0.987	0.990	0.990
Energy balance (kW)			
Heater	9.6	13.6	17.9
Reforming reactor	69.2	0.0	0.0
Heat exchanger	−23.8	−35.9	−35.1
Shift reactor	−6.4	−11.2	−10.3
Steam generator (1)	22.5	0.0	3.3
Steam generator (2)	23.6	34.0	33.2
Heat-transfer efficiency	0.80	0.80	0.80
Total net energy (kW)	118.2	0.6	11.2
CH_4 equivalent (mol s^{-1})	0.133	0.001	0.013
Total CH_4 (input + CH_4 equivalent, mol s^{-1})	0.385	0.364	0.367

The results show that, in terms of energy cost, the POX reforming systems is superior to other systems for the production of the same amount of hydrogen from CH_4. If the heat-transfer efficiency of each unit in a reforming system can be improved, then the difference in the rate of CH_4 consumption between the three reforming systems will be reduced. As an extreme case, if the heat-transfer efficiency is 1.0, the SMR system has the lowest energy cost.

4. Conclusions

A thermodynamic analysis has been conducted to investigate the characteristics of three reforming rectors, namely, SMR, POX and ATR. This has allowed identification of the favourable operating conditions for each system. Material and energy balances have also been evaluated for the three reforming systems.

Favourable operating conditions have been determined, which simultaneously satisfy the requirements for no coke formation, a reactor temperature of up to 800 °C and a conversion of over 0.99. The optimum S:C ratio in the SMR reactor is found to be 1.9. For the POX reactor, the optimum conditions include an air ratio of 0.3 and a preheat temperature of 312 °C. The optimum air ratio and S:C ratio in the ATR reactor are 0.29 and 0.35, respectively, at a preheat temperature of 400 °C.

The material and energy balances which result from the simulations for each reforming system show that the total CH_4 flow rate required to generate 1 mol s^{-1} hydrogen is 0.364 mol s^{-1} for the POX, 0.367 mol s^{-1} for the ATR and 0.385 mol s^{-1} for the SMR. The SMR reforming system has the highest CH_4 consumption and the POX system has the lowest CH_4 consumption. The difference in CH_4 consumption between the three reforming systems depends strongly upon the efficiency of the heat exchangers. The difference in CH_4 consumption between the SMR and POX systems becomes larger as the efficiency of the heat exchangers decreases. When the heat-transfer efficiency is 0.8, the CH_4 consumption rates of the POX and SMR systems are 0.364 and 0.385 mol s^{-1} respectively. On the other hand, when the heat-transfer efficiency is lowered to 0.7, these values change to 0.364 mol s^{-1} for the POX and 0.404 mol s^{-1} for the SMR. These evaluations reveal that the POX reforming system is superior to the other systems in terms of the energy cost to produce the same amount of hydrogen from CH_4.

Acknowledgements

This work has been supported by a postdoctoral fellowships program from Korea Science and Engineering Foundation (KOSEF).

References

[1] M.A. Pena, J.P. Gomez, J.L.G. Fierro, Appl. Catal. A: Gen. 144 (1996) 7–57.
[2] R. Wegeng, L.R. Pederson, W.E. TeGrotenhuis, G.A. Whyatt, Fuel Cells Bull. 3 (2001) 8–13.
[3] G. Sattler, J. Power Sources 86 (2000) 61–67.
[4] B. Emonts, J.B. Hansen, H. Schmidt, T. Grube, B. Hohlen, R. Peters, A. Tschauder, J. Power Sources 86 (2000) 228–236.
[5] K.A. Starz, E. Auer, T. Lehmann, R. Zuber, J. Power Sources 84 (1999) 167–172.
[6] T. Susai, A. Kawakami, A. Hamada, Y. Miyake, Y. Azegami, Fuel Cells Bull. 3 (2001) 7–11.
[7] A. Piga, X.E. Verykio, Catal. Today 60 (2000) 63–71.
[8] S.S. Bharadwaj, L.D. Schmidt, Fuel Processing Technol. 42 (1995) 109–127.
[9] K.G. Marnasidou, S.S. Voutetakis, G.J. Tjatjopoulos, I.A. Vasalos, Chem. Eng. Sci. 54 (1999) 3691–3699.
[10] T. Wurzel, L. Mleczko, Chem. Eng. J. 69 (1998) 127–133.
[11] T. Rampe, A. Heinzel, B. Vogel, J. Power Sources 86 (2000) 536–541.
[12] S. Cavallaro, S. Freni, J. Power Sources 76 (1998) 190–196.
[13] V. Recupero, L. Pino, R.D. Leonardo, M. Lagana, G. Maggio, J. Power Source 71 (1998) 208–214.
[14] J. Han, I. Kim, K. Choi, J. Power Sources 86 (2000) 223–227.
[15] S.H. Chan, H.M. Wang, Fuel Processing Technol. 64 (2000) 221–239.
[16] Aspen Technology Inc., http://www.aspentech.com/.
[17] S. Freni, G. Calogero, S. Cavallaro, J. Power sources 87 (2000) 28–38.

Appendix B - Experimental Data

B.1 GC results using helium carrier gas

The following tables contain the integrated peak areas determined for carbon dioxide, oxygen, nitrogen, methane and carbon dioxide present in each sample. Multiple data sets for each experiment number were obtained by testing the same sample with the GC multiple times. This was to enable an estimate to be made of the precision of the data.

Table B.1 – Peak areas for Run 1, using helium carrier gas

Experiment number	Carbon dioxide	Oxygen	Nitrogen	Methane	Carbon monoxide
1	21196	2283	4824	583546	4154
1	21259	2183	4519	581680	2488
2	9455	10758	39281	584705	2392
2	9484	10585	38990	584377	2260
3	8029	2178	5797	630722	2486
3	8000	1983	5335	629520	1185
4	19671	7002	22528	566415	4285
4	19632	6944	22328	566728	4190
5	6995	1397	4121	616624	2282
5	7005	1388	4133	616851	2370
6	9057	17369	63187	566678	1212
6	9114	17385	63244	566886	1170
7	19863	2841	7401	561104	4712
7	19881	2892	7488	561006	4700
8	6211	1739	6334	607666	2081
8	6177	1779	6376	608842	2186
9	11794	11489	40929	576818	2200
9	11846	11424	40885	576912	2015
10	24949	22129	78504	504172	5055
10	24984	22132	78639	504247	5035
11	3474	6091	22797	596616	1894
11	3474	6192	22991	596705	1763
12	18345	7627	27618	567929	2271
12	18201	7821	27713	567375	1165

Table B.1 continued

Experiment number	Carbon dioxide	Oxygen	Nitrogen	Methane	Carbon monoxide
13	10988	3458	8874	526549	7766
13	10930	3482	8932	526970	7826
14	7858	11558	40215	546903	7378
14	7866	11545	40183	544227	5310
15	11340	1455	3965	574912	6382
15	11399	1459	4020	574660	6398
16	10675	3355	12239	486682	8435
16	10600	3379	12150	488065	8467
17	9176	2008	4715	549877	6315
17	9221	1986	4648	552615	8586
18	35080	2716	9282	517973	12268
18	34883	2660	9036	517758	9724
19	10737	9385	32807	457767	12607
19	10760	9465	32996	455076	9752
20	12016	1290	5726	522646	9965
20	11560	1416	5943	524045	10029
21	13689	7820	27812	528547	9332
21	13708	7559	27262	530259	9363
22	22964	3144	10644	426166	19981
22	22981	3184	11007	426121	20168
23	21416	2260	6837	487665	10646
23	21488	2239	6696	488330	10704
24	7965	1493	3890	545646	7533
24	7871	1229	2991	544460	5441
25	7872	3217	9592	437100	23331
25	7904	3313	9653	437000	23321
26	14309	2394	6281	484173	25197
26	14293	2248	6113	484997	25346
26	14180	2214	6063	486453	25399
27	6840	6259	17056	495990	15955
27	6948	5757	16415	498400	15941
27	7026	5404	16083	499040	16077
27	6696	5349	16100	497431	15988
28	7418	1975	4302	403365	25195
28	7406	2106	4357	403132	25176
29	24362	2475	7513	461377	36862
29	23463	3043	8363	459924	36887

Table B.1 continued

Experiment number	Carbon dioxide	Oxygen	Nitrogen	Methane	Carbon monoxide
30	3345	3432	10796	510329	11181
30	3330	3530	10979	510980	11235
31	8560	8182	27367	348458	30599
31	8584	8150	27267	353095	35760
32	96849	15148	51897	401345	40357
32	78768	20909	62034	400340	41759
32	97884	13337	48006	408777	40607
33	7503	13775	49450	476065	20705
33	7377	14169	50265	473943	17720
34	10500	3825	7310	335033	38450
34	10515	3931	7293	334966	38415
35	195126	3655	13574	449399	16080
35	194703	3725	13763	452647	16118
36	12524	4372	13925	449979	24147
36	12351	4327	13671	450322	24175
37	4929	2402	7605	370222	43804
37	4912	2470	7525	370461	43855
37	4892	2368	7453	370507	43797
38	1932	1652	4103	449537	19258
38	1922	1585	4085	450606	19309
39	1795	1562	4776	474269	15043
39	1800	1530	4655	475819	15061
40	4770	2851	12128	317313	53929
40	4773	2834	11968	312856	47471
40	4802	2916	12171	318099	54046
41	3083	2071	7408	410787	26582
41	3076	2143	7604	416354	30968
42	773	8277	30051	430362	9149
42	785	8362	30269	430911	9175
43	5845	3054	10968	267427	60713
43	5813	3011	10931	267384	60650
43	5837	2978	10791	267338	60662
44	4274	2910	4528	396517	34130
44	4286	2769	4080	401249	39154
45	997	2230	6605	438296	11292
45	1039	1912	5898	442288	13706

Table B.1 continued

Experiment number	Carbon dioxide	Oxygen	Nitrogen	Methane	Carbon monoxide
46	8866	36064	132198	229295	78556
46	8820	36055	132606	229831	78605
46	8839	36209	133065	229717	78484
47	9005	6578	23574	339949	47999
47	9127	6616	23900	340257	48064
48	701	4755	15753	424935	8950
48	721	5052	16237	427044	10874
49	13220	5347	12854	597012	2182
49	13203	5352	12877	596887	2642
49	13227	5384	12973	597022	2344
50	6988	4213	10477	619214	1846
50	6924	4195	10302	618736	1722
50	6945	4304	10541	618797	1517
51	5447	4031	12364	636850	1674
51	5463	3999	12344	637422	1519
51	5465	3984	12315	637458	1504
52	31430	5370	10693	558561	3333
52	31494	5334	10736	558546	3672
52	31402	5333	10707	558448	3281
53	15092	5921	33455	578086	1944
53	15124	5866	33354	578024	2046
53	15110	5946	33436	578053	2217
54	6219	12609	27429	613755	1841
54	6237	12637	27494	613777	1772
54	6248	12656	27527	613794	1745
55	47051	4744	12143	500208	4033
55	47154	4759	12160	501243	4003
55	47226	4905	12114	502110	3933
56	22103	15750	57843	546353	2461
56	22185	15713	57896	546394	2780
56	22149	15835	58114	546182	2322
57	9003	2173	5757	630867	1923
57	9015	2246	5829	631116	2079
57	8979	2252	5825	631170	1881

Table B.1 continued

Experiment number	Carbon dioxide	Oxygen	Nitrogen	Methane	Carbon monoxide
58	50887	5408	15213	488900	4938
58	50909	5399	15141	488985	4688
58	50821	5500	15298	488965	4819
59	5307	1652	6610	612175	1674
59	5395	1658	6552	611066	614
59	5340	1705	6637	612935	1875
60	11278	1381	3080	623532	1981
60	11332	1422	3071	623628	1910
60	11340	1432	3106	623734	2129
61	12208	4962	14165	546574	9757
61	12169	4918	14101	546505	10019
61	12209	4903	14098	546291	9777
62	8506	2604	6615	589069	6594
62	8461	2616	6639	588563	6465
62	8508	2677	6736	588816	6604
63	6978	2100	3929	612595	5676
63	6975	2004	3761	612744	5435
63	6957	2037	3864	612692	5555
64	17439	3661	8165	507668	13385
64	17493	3663	8056	507374	13148
64	17526	3743	8205	507437	13412
65	12259	1926	5833	566048	7667
65	12312	1942	5761	566303	7922
65	12294	1961	5820	566227	7828
66	5567	1608	3208	604617	5022
66	5569	1641	3168	604825	5121
66	5568	1635	3519	604965	5225
67	30658	5056	12804	459138	18490
67	30606	5102	12789	459242	18542
67	30637	5133	12855	459694	18828
68	8045	7575	30445	519596	6707
68	8049	7691	30828	519096	6517
68	8050	7878	31470	518972	6732
69	7805	765	2073	582735	6196
69	7867	848	2002	583558	6018
69	7895	804	2029	583884	5776

Table B.1 continued

Experiment number	Carbon dioxide	Oxygen	Nitrogen	Methane	Carbon monoxide
70	37037	12042	38787	423265	20542
70	37043	11819	38353	423432	20713
70	36955	11961	38675	423302	20909
71	14615	1694	13443	512220	8632
71	14619	1662	13446	512374	8517
71	14655	1775	13556	512754	8753
72	15847	1797	5631	559652	8131
72	15894	1710	5445	559664	7932
72	15808	1755	5411	559845	8095
73	10174	3682	10792	479841	26907
73	10097	3730	11246	479867	26482
73	10120	3791	11635	480211	27009
74	3488	1100	3029	533574	12406
74	3457	1081	2996	533350	12497
74	3475	1126	2968	532938	12211
75	2319	1142	1936	575448	9745
75	2336	1168	2078	575239	9467
75	2300	1240	1963	575518	9565
76	6478	4103	10687	437751	27592
76	6473	4128	10629	437487	27379
76	6489	4142	10740	437021	27367
77	4016	1354	4455	504701	13718
77	4030	1380	4323	506685	13964
77	4020	1378	4343	507021	13912
78	2269	1659	4015	556855	9579
78	2283	1686	4098	557150	9734
78	2299	1685	4082	557143	9613
79	6138	10184	34505	386231	29148
79	6184	10284	34632	386078	29139
79	6155	10338	34936	385837	29506
80	6602	914	3710	471780	18335
80	6593	949	3956	472948	18512
80	6596	921	3946	472819	18558
81	2698	1502	3312	537952	10600
81	2706	1455	3176	539193	10340
81	2717	1509	3375	539408	10477

Table B.1 continued

Experiment number	Carbon dioxide	Oxygen	Nitrogen	Methane	Carbon monoxide
82	49293	4946	25462	287465	70459
82	49298	4895	25407	287866	70904
82	49331	5021	25667	287753	70658
83	33406	3804	16277	404431	39857
83	33449	3882	16428	405621	39648
83	33501	3908	16413	405276	39745
84	5293	4621	14958	501104	14609
84	5325	4655	14948	501483	14251
84	5324	4604	15056	501872	14680
85	3055	1845	5545	417371	36917
85	3077	1792	5379	416811	36481
85	3069	1923	5682	417262	36960
86	1694	1224	3847	487148	20121
86	1710	1238	3825	487777	20298
86	1715	1258	3858	487572	20309
87	2247	1338	2532	519824	21662
87	2225	1424	2736	519411	21773
87	2212	1380	2600	519414	21552
88	4312	2493	8651	352714	51536
88	4318	2560	8932	352673	51740
88	4323	2569	8910	352687	51734
89	3548	2161	7865	429075	30772
89	3541	2164	7852	430107	30528
89	3504	2254	7915	430626	30996
90	2114	1604	3801	490751	21247
90	2089	1653	3718	490670	21347
90	2154	1659	3937	490563	21170
91	7048	3861	12084	297045	63916
91	6707	3829	12133	296820	63324
91	6713	3889	12344	297192	63638
92	2574	1523	4488	422296	27748
92	2572	1455	4397	422609	27418
92	2604	1517	4566	422668	27666
93	1477	850	2262	458623	17103
93	1460	886	2351	453420	12130
93	1510	1025	2355	458738	17481

Table B.1 continued

Experiment number	Carbon dioxide	Oxygen	Nitrogen	Methane	Carbon monoxide
94	10054	1784	7582	230601	85004
94	10091	1721	7586	230469	85681
94	10077	1724	7527	221274	72755
95	3964	5040	18279	384906	33671
95	3996	5030	18333	386555	33975
95	3958	5091	18466	386068	34068
96	1698	1112	3409	437650	18674
96	1697	1156	3242	432401	13564
96	1762	1183	3373	437390	18719

Table B.2 – Peak areas for Run 2 (selected experiments), using helium carrier gas

Experiment number	Carbon dioxide	Oxygen	Nitrogen	Methane	Carbon monoxide
26	2908	17197	62301	515374	7446
26	2895	17279	62657	519312	11152
26	2899	17395	62846	514857	7481
29	3322	2245	6245	518163	12920
29	3362	2207	6197	514794	8966
29	3349	2295	6301	515016	8941
32	4790	1389	3840	480986	10478
32	4735	1371	3855	481349	10490
32	4740	1380	3867	481759	10540
35	20117	6278	22068	437213	23403
35	20118	6306	22134	438408	23479
35	20176	6297	22200	443593	29689
39	1585	2671	5441	508634	12830
39	1642	2685	5542	508473	12792
39	1618	2735	5601	508462	12732
42	1684	1675	2077	486378	14055
42	1678	1658	2063	486519	14081
42	1668	1663	2076	491067	18586
45	1582	10769	35926	455723	18365
45	1600	10830	36166	451644	14108
45	1626	11001	36405	451479	14161

Table B.2 continued

Experiment number	Carbon dioxide	Oxygen	Nitrogen	Methane	Carbon monoxide
48	1023	2100	6517	425943	14161
48	1040	2067	6333	426252	13976
48	1052	2106	6425	422837	10797
74	11413	4005	11704	527921	21103
74	11411	4048	11840	527872	21083
74	11460	4113	11937	528256	20774
77	6252	3687	11757	513510	17026
77	6168	3704	11806	514041	17187
77	6213	3758	11991	514391	17363
80	5635	2137	5780	492457	17006
80	5598	2164	5681	492366	16984
80	5626	2223	5749	492322	17207
83	6359	1480	3135	470460	19021
83	6412	1564	3116	470481	19059
83	6371	1506	3178	470311	19233

Table B.3 – Peak areas for Run 3 (selected experiments), using helium carrier gas

Experiment number	Carbon dioxide	Oxygen	Nitrogen	Methane	Carbon monoxide
74	4528	2717	8270	538835	13985
74	4533	2703	8210	538146	14028
74	4556	2726	8317	538207	14120
77	5110	3288	10690	510540	15808
77	5088	3241	10586	510355	15586
77	5139	3275	10667	510207	15696
80	5894	1521	3697	492049	17779
80	5935	1544	3827	491769	17985
80	5914	1504	3649	491858	17849
83	6684	1406	4063	464911	19893
83	6729	1350	3970	465425	19832
83	6655	1388	4014	465285	19767

Table B.4 – Peak areas for Run 4 (selected experiments), using helium carrier gas

Experiment number	Carbon dioxide	Oxygen	Nitrogen	Methane	Carbon monoxide
74	4179	4037	11768	545542	14077
74	4199	4065	11871	545698	14153
74	4132	4076	12082	546242	14356
77	4401	6317	20783	514210	14960
77	4335	6352	20852	514222	14857
77	4372	6428	21091	514231	14867
80	4800	2071	5963	493637	16861
80	4799	2100	5977	493206	16405
80	4851	2147	5970	493356	16474
83	5608	4132	14571	467989	18116
83	5570	4059	14359	468382	17973
83	5565	4109	14536	468053	18299

Table B.5 – Peak areas for Run 5 (selected experiments), using helium carrier gas

Experiment number	Carbon dioxide	Oxygen	Nitrogen	Methane	Carbon monoxide
74	4716	1473	4094	539851	14851
74	4700	1481	4245	539848	14580
74	4689	1645	4486	539761	14716
77	4868	1716	4603	513858	15310
77	4829	1730	4752	514030	15449
77	4841	1741	4763	514358	15446
80	4952	1671	4737	493808	15985
80	4922	1669	4793	494227	16047
80	4956	1664	4877	494559	16049
83	6026	3328	10866	460531	18287
83	6009	3415	11054	460604	18073
83	6015	3394	10904	460255	18480

During the following runs, the configuration of the rig was changed to investigate the effect of the "dead volume" above the reactor. Experiment numbers 36.5 and 36.5a refer to experiments with a reaction duration of 20 minutes, with other conditions the same as those of experiment number 35.

Table B.6 – Peak areas for repeat runs with original configuration, using helium carrier gas

Experiment number	Carbon dioxide	Oxygen	Nitrogen	Methane	Carbon monoxide
26	3984	2000	8814	505285	13051
26	3969	2005	8963	505402	13227
26	3982	2001	8781	505737	12627
29	3927	1418	5786	505738	13803
29	3969	1412	5809	505475	13889
29	3925	1436	5744	505126	13841
32	7898	1078	2905	473536	20203
32	7886	1104	2830	473511	20225
32	7926	1135	2881	473150	19895
35	8076	2026	5804	447024	21922
35	8055	1889	5666	447806	21852
35	8069	1963	5819	447341	21863
36.5	12635	1418	4433	389804	28646
36.5	12673	1374	4308	389711	28572
36.5	12655	1423	4319	389897	28463

Table B.7 – Peak areas for repeat runs with "long tube" configuration, using helium carrier gas

Experiment number	Carbon dioxide	Oxygen	Nitrogen	Methane	Carbon monoxide
26a	2535	2493	5189	578272	7990
26a	2549	2498	5351	578532	7970
26a	2593	2476	5369	578676	8136
29a	3083	1959	3926	563242	9650
29a	3034	2025	3910	562999	9420
29a	3051	2075	3952	562593	9633

Table B.7 continued

Experiment number	Carbon dioxide	Oxygen	Nitrogen	Methane	Carbon monoxide
32a	3426	3527	10002	539699	10442
32a	3432	3524	10006	539823	10524
32a	3425	3546	10163	539605	10573
35a	2554	6544	23878	510851	9834
35a	2538	6591	24024	510322	9495
35a	2541	6631	24108	510071	9427
36.5a	2451	2255	5874	501862	10106
36.5a	2445	2197	5821	501826	9889
36.5a	2505	2270	5975	501056	10445

B.2 GC results using argon carrier gas

Using argon carrier gas (and therefore reference gas) allowed hydrogen to be detected. The other peaks were very small and were not integrated.

Table B.8 – Hydrogen peak areas for Run 1

Experiment number	Hydrogen	Experiment number	Hydrogen	Experiment number	Hydrogen
1	22062	8	13493	15	22060
1	20737	8	13539	15	22665
2	9099	8	13601	16	49564
2	9113	9	12636	16	49502
3	8152	9	13443	17	32227
3	9065	10	29821	17	31900
4	20948	10	29273	18	33239
4	21027	11	14647	18	32873
5	11267	11	14172	19	63277
5	11221	12	18815	19	63182
6	10468	12	18913	20	39505
6	10650	13	36763	20	40157
7	28141	13	36243	21	28386
7	28078	14	24683	21	28106
		14	24665		

Table B.8 continued

Experiment number	Hydrogen	Experiment number	Hydrogen	Experiment number	Hydrogen
22	70394	37	92797	51	5478
22	70929	37	93156	51	5472
23	46520	37	92933	51	5461
23	47436	38	65142	52	25668
24	32770	38	65216	52	25715
24	32861	39	55628	52	25712
25	68139	39	56216	53	12090
25	68237	40	119213	53	11998
25	68153	40	119474	53	12030
26	46118	40	119268	54	6866
26	46046	41	77707	54	6879
27	43305	41	77832	54	6849
27	43673	42	64456	55	35359
27	43342	42	64887	55	35293
28	86024	43	140300	55	35353
28	85998	43	140491	56	19183
29	52007	43	140305	56	19268
29	51883	44	86430	56	18953
30	44537	44	86246	57	8788
30	44627	45	77457	57	8763
31	97377	45	77613	57	8758
31	97276	46	141254	58	39207
32	37402	46	141875	58	39295
32	36556	46	141559	58	39225
33	39300	47	88420	59	15014
33	39392	47	88144	59	14986
34	113488	48	79238	59	14993
34	113235	48	79597	60	11424
34	113407	49	14385	60	11407
35	20971	49	14430	60	11389
35	20651	49	14396	61	29793
35	20708	50	10030	61	29849
36	60039	50	8984	61	29836
36	60250	50	8896		

Table B.8 continued

Experiment number	Hydrogen	Experiment number	Hydrogen	Experiment number	Hydrogen
62	18856	74	35157	85	72912
62	18891	74	35074	86	51607
62	18934	74	35022	86	51444
63	14784	75	26433	86	51487
63	14773	75	26474	87	43025
63	14829	75	26434	87	42949
64	42904	76	73232	87	43014
64	43003	76	73274	88	90841
64	42981	76	73459	88	90845
65	25690	77	44474	88	90715
65	25743	77	44655	89	70527
65	25701	77	44571	89	70564
66	17785	78	31671	89	70441
66	17816	78	31606	90	54415
66	17819	78	31614	90	54351
67	57864	79	93777	90	54344
67	57964	79	93587	91	117716
67	57951	79	93684	91	117674
68	27550	80	56023	91	117729
68	27519	80	56041	92	79020
68	27463	80	56057	92	78903
69	21689	81	37960	92	78824
69	21732	81	37944	93	65078
69	21526	81	37920	93	65342
70	67333	82	96331	93	65277
70	67302	82	96240	94	147601
70	67256	82	96080	94	147240
71	37233	83	64113	94	147442
71	37223	83	64107	95	81438
71	37251	83	63909	95	81694
72	26158	84	41868	95	81495
72	26126	84	41851	96	73798
73	38504	84	41800	96	73518
73	38495	85	72955	96	73399
73	38482	85	72931		

Table B.9 – Hydrogen peak areas for Run 2

Experiment number	Hydrogen	Experiment number	Hydrogen	Experiment number	Hydrogen
26	23573	39	50340	74	29664
26	23968	39	50291	74	29638
26	23896	39	50363	74	29596
29	44664	42	59321	77	37174
29	44809	42	59675	77	37172
29	44537	42	59517	77	37218
32	57693	45	72162	80	47997
32	57668	45	72371	80	48021
32	57477	45	72371	80	48002
35	54955	48	81052	83	57525
35	55067	48	81172	83	57586
35	54800	48	81298	83	57516

Table B.10 – Hydrogen peak areas for Runs 3, 4 and 5

Run 3		Run 4		Run 5	
Experiment number	Hydrogen	Experiment number	Hydrogen	Experiment number	Hydrogen
74	31754	74	31812	74	31285
74	31799	74	31856	74	31338
74	31793	74	31905	74	31370
77	38454	77	40192	77	39101
77	38435	77	40278	77	39169
77	38440	77	40191	77	39143
80	50501	80	51341	80	46639
80	50492	80	51351	80	46647
80	50496	80	51250	80	46682
83	59217	83	58012	83	55709
83	59186	83	57872	83	55686
83	59178	83	57654	83	55682

During the following runs, the configuration of the rig was changed to investigate the effect of the "dead volume" above the reactor. Experiment numbers 36.5 and 36.5a refer to experiments with a reaction duration of 20 minutes, with other conditions the same as those of experiment number 35.

Table B.11 – Hydrogen peak areas for repeated runs on rig in original and "long tube" configurations

Original configuration		"Long tube" configuration	
Experiment number	Hydrogen	Experiment number	Hydrogen
26	38516	26a	20486
26	38502	26a	20486
26	38482	26a	20434
29	39951	29a	26097
29	39979	29a	26132
29	39946	29a	26093
32	49872	32a	32085
32	49892	32a	32046
32	49911	32a	31992
35	59211	35a	42083
35	59220	35a	42023
35	59252	35a	42065
36.5	84926	36.5a	49399
36.5	85004	36.5a	49417
36.5	85041	36.5a	49405

Appendix C - Diffusion calculations

C.1 Calculation flowchart

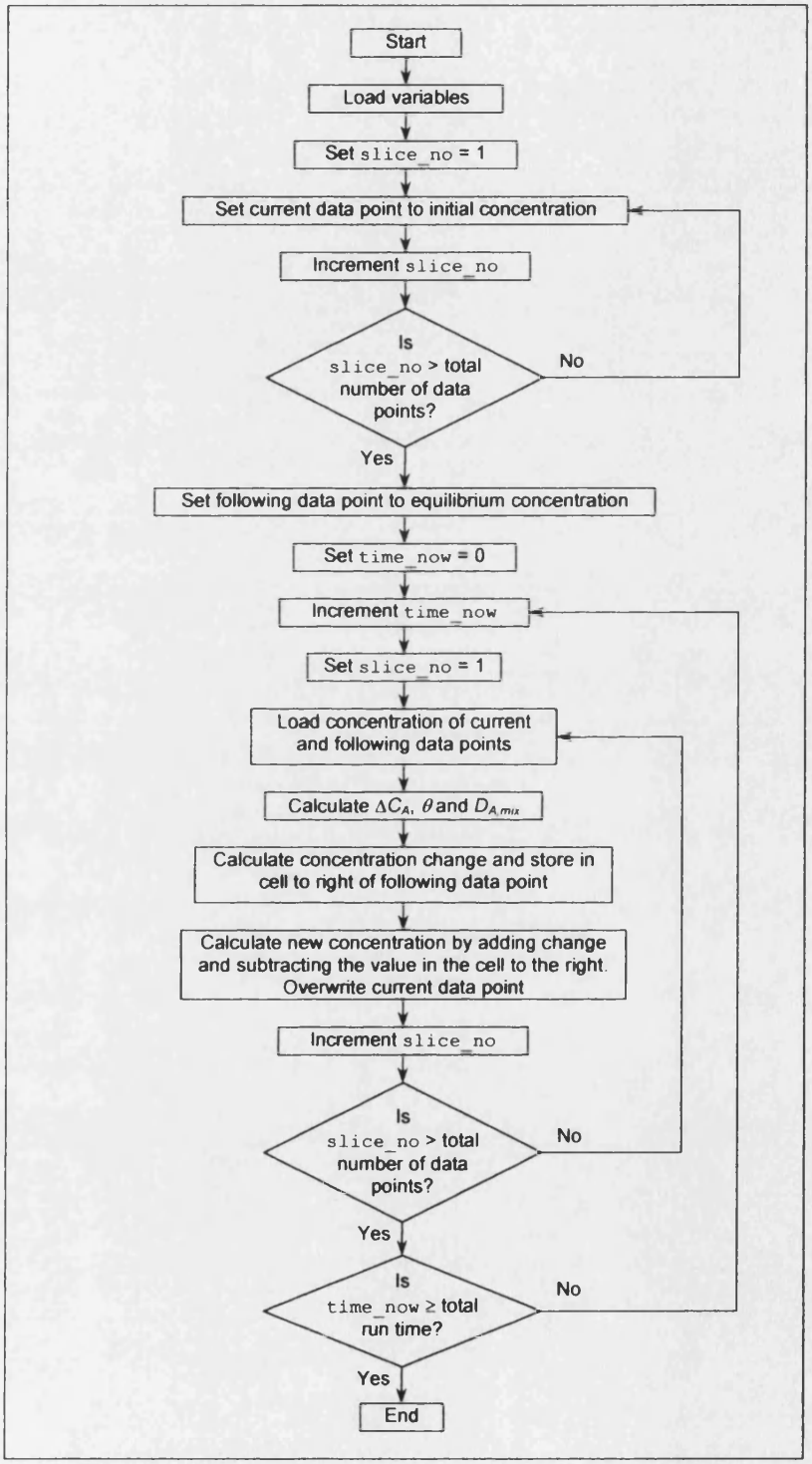

Figure C.1 – Flowchart for basic diffusion calculation

C.2 Macro listings

C.2.1 Single tube, uniform cross sectional area

```
Sub run_calcs2()
    Application.ScreenUpdating = False
    y_CH4_init = Sheets("Sheet2").Range("B2")
    y_H2O_init = Sheets("Sheet2").Range("B3")
    y_CH4_eqm = Sheets("Sheet2").Range("B34")
    y_H2O_eqm = Sheets("Sheet2").Range("B35")
    y_CO_eqm = Sheets("Sheet2").Range("B36")
    y_CO2_eqm = Sheets("Sheet2").Range("B37")
    y_H2_eqm = Sheets("Sheet2").Range("B38")
    C_init = Sheets("Sheet2").Range("B9")
    C_eqm = Sheets("Sheet2").Range("B11")
    C_total = Sheets("Sheet2").Range("B13")
    tube_length = Sheets("Sheet2").Range("B16")
    total_slices = Sheets("Sheet2").Range("B20")
    delta_t = Sheets("Sheet2").Range("B21")
    run_time = Sheets("Sheet2").Range("B22")
    D_H2O = Sheets("Sheet3").Range("B28")
    D_CO = Sheets("Sheet3").Range("D28")
    D_CO2 = Sheets("Sheet3").Range("J5")
    D_H2 = Sheets("Sheet3").Range("J9")
    delta_l = tube_length / total_slices
    time_now = 0
    Columns("D:F").ClearContents
    Sheets("Sheet2").Range("E25") = time_now
    slice_no = 1
    Sheets("Sheet2").Range("D27") = 0
    Do Until slice_no > total_slices
        length_now = delta_l * slice_no
        Sheets("Sheet2").Range("E27").Cells(slice_no, 1) = C_init
        Sheets("Sheet2").Range("D28").Cells(slice_no, 1) = length_now
        slice_no = slice_no + 1
    Loop
    Sheets("Sheet2").Range("E27").Cells(slice_no, 1) = C_eqm
    Do Until time_now >= run_time
        time_now = time_now + delta_t
        Sheets("Sheet2").Range("E25") = time_now
        slice_no = 1
        Do Until slice_no > total_slices
            C_i = Sheets("Sheet2").Range("E27").Cells(slice_no, 1)
            C_ii = Sheets("Sheet2").Range("E27").Cells(slice_no + 1, 1)
            delta_C = C_ii - C_i
            C_av = (C_i + C_ii) / 2
            y_CH4 = C_av / C_total
            prop_extent = (y_CH4_init - y_CH4) / (y_CH4_init -
y_CH4_eqm)
            y_H2O = y_H2O_init - (prop_extent * (y_H2O_init -
y_H2O_eqm))
            y_CO = prop_extent * y_CO_eqm
            y_CO2 = prop_extent * y_CO2_eqm
            y_H2 = prop_extent * y_H2_eqm
            D_mix = (1 - y_CH4) / ((y_H2O / D_H2O) + (y_CO / D_CO) +
(y_CO2 / D_CO2) + (y_H2 / D_H2))
            C_change = (D_mix * delta_t * delta_C / (delta_l * delta_l))
```

```
            Sheets("Sheet2").Range("E27").Cells(slice_no, 1) = C_i +
C_change
            Sheets("Sheet2").Range("E27").Cells(slice_no + 1, 2) =
C_change
            Sheets("Sheet2").Range("E27").Cells(slice_no, 1) =
Sheets("Sheet2").Range("E27").Cells(slice_no, 1) -
Sheets("Sheet2").Range("E27").Cells(slice_no, 2)
            slice_no = slice_no + 1
        Loop
    Loop
    Application.ScreenUpdating = True
End Sub
```

C.2.2 Single tube with step reduction in cross sectional area

```
Sub run_calcs3()
    Application.ScreenUpdating = False
    y_CH4_init = Sheets("Sheet2").Range("B2")
    y_H2O_init = Sheets("Sheet2").Range("B3")
    y_CH4_eqm = Sheets("Sheet2").Range("B34")
    y_H2O_eqm = Sheets("Sheet2").Range("B35")
    y_CO_eqm = Sheets("Sheet2").Range("B36")
    y_CO2_eqm = Sheets("Sheet2").Range("B37")
    y_H2_eqm = Sheets("Sheet2").Range("B38")
    C_init = Sheets("Sheet2").Range("B9")
    C_eqm = Sheets("Sheet2").Range("B11")
    C_total = Sheets("Sheet2").Range("B13")
    tube_length = 0.1
    total_slices = 40
    delta_t = Sheets("Sheet2").Range("B21")
    run_time = Sheets("Sheet2").Range("B22")
    D_H2O = Sheets("Sheet3").Range("B28")
    D_CO = Sheets("Sheet3").Range("D28")
    D_CO2 = Sheets("Sheet3").Range("J5")
    D_H2 = Sheets("Sheet3").Range("J9")
    delta_l = tube_length / total_slices
    time_now = 0
    Columns("D:F").ClearContents
    Sheets("Sheet2").Range("E25") = time_now
    slice_no = 1
    Sheets("Sheet2").Range("D27") = 0
    Do Until slice_no > total_slices
        length_now = delta_l * slice_no
        Sheets("Sheet2").Range("E27").Cells(slice_no, 1) = C_init
        Sheets("Sheet2").Range("D28").Cells(slice_no, 1) = length_now
        slice_no = slice_no + 1
    Loop
    Sheets("Sheet2").Range("E27").Cells(slice_no, 1) = C_eqm
    Do Until time_now >= run_time
        time_now = time_now + delta_t
        Sheets("Sheet2").Range("E25") = time_now
        slice_no = 1
        Do Until slice_no > total_slices
            If slice_no = 1 Then
                A_ratio = 0
                ElseIf slice_no = 21 Then
                A_ratio = Sheets("Sheet2").Range("B19")
                Else
                A_ratio = 1
            End If
```

```
            C_i_prev = Sheets("Sheet2").Range("E27").Cells(slice_no - 1,
1)
            C_i = Sheets("Sheet2").Range("E27").Cells(slice_no, 1)
            C_ii = Sheets("Sheet2").Range("E27").Cells(slice_no + 1, 1)
            delta_C = C_ii - C_i
            delta_C_prev = C_i - C_i_prev
            C_av = (C_i_prev + C_i) / 2
                y_CH4 = C_av / C_total
                prop_extent = (y_CH4_init - y_CH4) / (y_CH4_init -
y_CH4_eqm)
                y_H2O = y_H2O_init - (prop_extent * (y_H2O_init -
y_H2O_eqm))
                y_CO = prop_extent * y_CO_eqm
                y_CO2 = prop_extent * y_CO2_eqm
                y_H2 = prop_extent * y_H2_eqm
            D_mix_prev = (1 - y_CH4) / ((y_H2O / D_H2O) + (y_CO / D_CO)
+ (y_CO2 / D_CO2) + (y_H2 / D_H2))
            C_av = (C_i + C_ii) / 2
                y_CH4 = C_av / C_total
                prop_extent = (y_CH4_init - y_CH4) / (y_CH4_init -
y_CH4_eqm)
                y_H2O = y_H2O_init - (prop_extent * (y_H2O_init -
y_H2O_eqm))
                y_CO = prop_extent * y_CO_eqm
                y_CO2 = prop_extent * y_CO2_eqm
                y_H2 = prop_extent * y_H2_eqm
            D_mix_next = (1 - y_CH4) / ((y_H2O / D_H2O) + (y_CO / D_CO)
+ (y_CO2 / D_CO2) + (y_H2 / D_H2))
            If A_ratio <= 1 Then
                C_change = (delta_t * (D_mix_next * delta_C - D_mix_prev
* A_ratio * delta_C_prev) / (delta_1 * delta_1))
            Else
                C_change = (delta_t * ((1 / A_ratio) * D_mix_next *
delta_C - D_mix_prev * delta_C_prev) / (delta_1 * delta_1))
            End If
            Sheets("Sheet2").Range("E27").Cells(slice_no, 2) = C_i +
C_change
            slice_no = slice_no + 1
        Loop
        Range("F27:F66").Copy
        Range("E27").Select
        ActiveSheet.Paste
    Loop
    Application.ScreenUpdating = True
End Sub
```